Multiscale modeling of the hydromechanical behavior of fractured reservoirs

Ana Carolina Loyola Caetano Rios

École des Ponts
ParisTech

UnB

THÈSE DE DOCTORAT
de l'École des Ponts ParisTech et
Universidade de Brasília

Multiscale modeling of the hydromechanical behavior of fractured reservoirs

École doctorale 531, Sciences, Ingeniérie et Environnement (SIE)

Géotechnique

Thèse préparée au laboratoire Navier et au Programa de Pós-Graduação em Geotecnia

Ana Carolina LOYOLA CAETANO RIOS

Composition du jury:

Titre, établissement	*Président*
Chloé, ARSON Professor, Georgia Tech	*Rapporteur*
Leonardo José, GUIMARÃES Professor, Universidade Federal de Pernambuco	*Rapporteur*
Amade, POUYA Professor, Université Gustave Eiffel	*Examinateur*
Flávia, FALCÃO Doctor, Petrobras	*Examinateur*
Márcio, MUNIZ DE FARIAS Professor, Universidade de Brasília	*Examinateur*
Rebecca, LUNN Professor, University of Strathclyde	*Examinateur*
Jean-Michel, PEREIRA Professor, École des Ponts ParisTech	*Directeur de thèse*
Manoel, PORFÍRIO CORDÃO NETO Professor, Universidade de Brasília	*Directeur de thèse*

Multiscale modeling of the hydromechanical behavior of fractured reservoirs

Ana Carolina LOYOLA

Acknowledgements/Agradecimentos

I would like to thank all of those who developed the open-source tools used in this thesis. I appreciate the belief on cooperation to go further, and I can only hope that the things developed here will be useful to someone someday.

A big obrigada, merci, gracias and thanks to my colleagues and friends at the École des Ponts for the warm reception. I am grateful to have spent the end of my thesis in such good company.

Thank you to Chloé Arson, Leonardo Guimarães, Márcio Muniz, Flávia Falcão, Rebecca Lunn and Amade Pouya for being part of the juri of my thesis and for raising very interesting points of discussion.

I should continue this acknowledgements in Portuguese, as it is the language I communicate with all the other wonderful people I have something to thank for.

Obrigada aos meus colegas e amigos que me acompanharam nesses anos de tese. A Letícia e Jordana, pelas conversas e cafézinhos na nossa sala do SG-12. Aos meus amigos Henrique, Júlia, Juliana, Laura e Pedro, por se fazerem presentes quando eu estive longe e por me animarem quando eu precisei.

Obrigada aos meus pais, Max e Regina, e à minha irmã, Jéssica, pelo amor incondicional, pelo suporte aos meus sonhos como se fosse seus, por entederem minha mania de ficar longe de casa e por serem a melhor família que eu poderia ter.

Obrigada aos professores do Progama de Pós-graduação em Geotecnia da UnB, que me ensinaram muito do que eu sei e me deram a base pra aprender tantas outras coisas.

Obrigada ao CNPq e à CAPES que financiaram, respectivamente, o período desta tese no Brasil e o doutorado sanduíche na França, que mais tarde se transformou nesta tese em cotutela.

Obrigada ao meu orientador Jean-Michel, que desde que entrou na minha tese esteve presente, disponível e interessado. Agradeço pela confiança, pelas discussões e pelo olhar cuidadoso aos problemas que enfrentei durante este trabalho, assim como pela gentileza e pela recepção no laboratório Navier.

Obrigada ao meu orientador Manoel por todas as coisas que eu nunca serei capaz de retribuir. Ao longo dos anos foram muitos os incentivos que vieram de todas as formas: recursos computacionais, financeiros, cafeína, muito aprendizado e aquilo pelo qual sou grata acima de todas estas outras coisas: as motivações constantes e a preocupação com o bem estar dos seus alunos.

Esta tese se iniciou na Universidade de Brasília, que pra mim é uma casa. Os momentos dos mais corriqueiros no Campus Darcy Ribeiro são especiais na minha memória: os pós-aulas no Minhocão, depois as tardes na Faculdade de Tecnologia e por fim o mestrado e o doutorado no SG-12, com as pausas estratégicas no Café das Letras. Por causa da pandemia, não pude voltar à Universidade até então, mas fica aqui a expressão da minha gratidão e das minhas saudades.

Abstract

A significant part of petroleum, gas, and geothermal reservoirs contain natural fractures that impact their performance. When these discontinuities fall on the sub-seismic scale, it is a challenge to incorporate them into numerical models, because the computational costs of their explicit representation are usually too high. Popular solutions that deal with the effect of these small-scale fractures are the dual-porosity approaches and classical flow-based upscaling. However, while the dual-porosity models disregard the geometrical complexity of real fracture networks, traditional upscaling can not capture the dynamic influence of the fractures, whose permeabilities change continuously during the reservoir's productive life. This thesis is dedicated to the multiscale hydro-mechanical modeling of reservoirs containing complex fracture networks. The adopted multiscale method is an adaptation of the multi-level Finite Element Method (FEM), which solves both the macroscale and the microscale numerically and couples them according to the principles of homogenization. The modification proposed here is called the multi-level Box method because it replaces the FEM with the Box method, also called the control-volume FEM. Contrary to upscaling techniques, this method can capture the dynamic influence of the heterogeneities on the large-scale behavior without the need of defining equivalent constitutive laws. At the level of the REV, the fractures are generated stochastically and represented by interface elements. Major modifications were made to an open-source code to make the hydro-mechanical simulation of elastoplastic fractures possible. A new statistics-based methodology based on the Central Limit Theorem was proposed to define the REV of random fractured media. Also, two methods used to impose periodic boundary conditions on periodic and non-periodic meshes were adapted to domains containing interface elements. The developed tools and methods were applied to a synthetic case of depletion inspired by a real naturally fractured chalk reservoir. The multiscale method was able to represent the loss of productivity caused by depletion and the anisotropic evolution of the pore pressure field.

Resumo

Uma parte significativa dos reservatórios geotérmicos e de petróleo e gás possuem fraturas naturais que impactam sua performance. Quando essas discontituidades se encontram na escala sub-sísmica, sua incorporação aos modelos numéricos é desafiadora, pois os custos computacionais de sua representação explícita são geralmente proibitivos. As soluções mais populares que consideram o efeito dessas fraturas de pequena escala são os modelos de dupla porosidade e o cálculo de propriedades equivalentes (upscaling). No entanto, enquanto os modelos de dupla porosidade consideram geometrias muito idealizadas e pouco representativas de redes de fraturas reais, as técnicas tradicionais de upscaling não são capazes de capturar a influência dinâmica das fraturas, cujas permeabilidades mudam continuamente durante a vida produtiva do reservatório. Esta tese desenvolve métodos e ferramentas computacionais para a modelização multiescala do comportamento hidro-mecânico de reservatórios contendo redes complexas de fraturas. O método multiescala adotado é uma adaptação do Médoto dos Elementos Finitos (MEF) multi-nível, em que a microescala e a macroescala são resolvidas simultaneamente com o FEM e acopladas de acordo com os princípios da homogenização. A modificação aqui proposta é denominada método Box multi-nível, pois o MEF foi substituído pelo método Box. Ao contrário das técnicas convencionais de upscaling, este método captura os efeitos dinâmicos das heterogeneidades sem a necessidade de definir modelos constitutivos para a macroescala. No nível do Volume Elementar Representativo (VER), as fraturas são geradas de maneira estocástica e representadas por elementos de interface. Um programa de código aberto foi estendido para comportar simulações hidromecânicas em meios fraturados elastoplásticos. Uma nova metodologia estatística baseada no Teorema do Limite Central para definir o tamanho do VER de meios fraturados estocásticos foi proposta. Além disso, dois métodos para a imposição de condições de contorno periódicas foram adaptados para meios contendo elementos de interface. Os métodos e ferramentas desenvolvidos foram aplicados em um caso sintético de depleção de um reservatório inspirado em um carbonato fraturado real. O método multiescala foi capaz de representar a perda de produtividade causada pelo fechamento das fraturas e a evolução anisotrópica dos campos de poropressão.

Résumé

Une partie importante des réservoirs de pétrole, de gaz et géothermiques contient des fractures naturelles qui ont un impact sur leur performance. Lorsque ces discontinuités se situent à l'échelle sub-sismique, leur incorporation aux modèles numériques pose un défi, car le coût de calcul de leur représentation explicite est généralement trop élevé. Les solutions populaires qui traitent de l'effet de ces fractures à petite échelle sont les approches à double porosité et l'obtention de propriétés constitutives équivalentes par changement d'échelle (upscaling). Pourtant, alors que les modèles à double porosité ne tiennent pas compte de la complexité géométrique des réseaux de fractures réels, les techniques traditionnelles de changement d'échelle ne peuvent pas capturer l'influence dynamique des fractures, dont la perméabilité change continuellement pendant l'exploitation du réservoir. Cette thèse est dédiée à la modélisation hydromécanique multi-échelle de réservoirs contenant des réseaux de fractures complexes. La méthode multi-échelle adoptée est une adaptation de la méthode des éléments finis au carré, qui résout numériquement à la fois la macro-échelle et la micro-échelle et les couple selon les principes d'homogénéisation. La modification proposée ici s'appelle la méthode Box multi-niveaux car elle remplace la méthode des éléments finis par la méthode Box. Contrairement au changement d'échelle conventionnel, cette méthode permet de capturer l'influence dynamique des hétérogénéités sur le comportement à grande échelle sans qu'il soit nécessaire de définir des lois constitutives pour la macro-échelle. Au niveau du Volume Élémentaire Représentatif (VER), les fractures sont générées de manière stochastique et représentées par des éléments d'interface. Des modifications majeures ont été apportées à un code open-source pour permettre la simulation hydro-mécanique des milieux fracturés élastoplastiques. Une nouvelle méthodologie statistique basée sur le théorème de la limite centrale a été proposée pour définir le VER de milieux fracturés aléatoires. De plus, deux méthodes utilisées pour imposer des conditions aux limites périodiques sur des maillages périodiques et non-périodiques ont été adaptées aux domaines contenant des éléments d'interface.

Contents

List of Figures

List of Tables

List of Symbols

Symbol	Description	Dimension*	Unit SI
b	Biot's coefficient	Scalar	-
c	Cohesion	Scalar	Pa
$\boldsymbol{\delta}$	Kronecker's delta		-
E	Young's modulus	Scalar	N/m^2
ε	Scale factor	-	-
$\boldsymbol{\varepsilon}$	Strains tensor	2 x 2	m/m
ε_v	Volumetric strain	Scalar	m/m
$\boldsymbol{F}$	Oda's crack tensor	2 x 2	m
G	Shear modulus	Scalar	N/m^2
φ	Friction angle	Scalar	rad
$\boldsymbol{k}$	Permeability tensor	2 x 2	m^2
K_n	Fracture normal stiffness	Scalar	Pa/m
K_t	Fracture tangent stiffness	Scalar	Pa/m
m	Mass	Scalar	kg
M	Biot's modulus	Scalar	1/Pa
$\boldsymbol{\nabla}$	Gradient vector ($\{\frac{\partial}{\partial x}\frac{\partial}{\partial y}\}$)	2 x 1	1/m
p	Fluid pressure	Scalar	N/m^2
ψ	Angle of dilation	Scalar	rad
q	Mass flow rate	Scalar	kg/s
ρ	Density	Scalar	kg/m^3
S	Degree of saturation	Scalar	m^3/m^3
$\boldsymbol{\sigma}$	Stress tensor	2 x 2	N/m^2
S	Degree of saturation	Scalar	m^3/m^3
ν	Poisson's ratio	Scalar	-
ϕ	Porosity	Scalar	m^3/m^3
t	Time	Scalar	s
$\boldsymbol{u}$	Displacement vector	2 x 1	m
Υ	Storage term	-	kg/m^3
$\boldsymbol{v}$	Velocity vector	2 x 1	m/s
V	Volume	Scalar	m^3
w	Fracture aperture	Scalar	m

* Dimensions for 2D problems

Notation for tensor operations

$\boldsymbol{a} \cdot \boldsymbol{b}$	Dot product of two vectors
$\boldsymbol{a} : \boldsymbol{b}$	Double contraction of two tensors
$\boldsymbol{a} \otimes \boldsymbol{b}$	Dyadic product of two vectors

Chapter 1

Introduction

1.1 Fractured reservoirs

Naturally Fractured Reservoirs (NFR) make up a significant part of the world's reserves and production of petroleum and gas (Firoozabadi, 2000; Bourbiaux, 2010). While practically all hydrocarbon reservoirs contain natural fractures, the concept of NFR is more restrictive, since it connotes that the fractures have or are expected to have a considerable effect on the performance during oil production (Nelson, 2001). A sufficiently dense and connected network of fractures affects important aspects of oil recovery planning such as the production rates, water breakthrough and the stability of wells.

The term fracture used here refers to any planar discontinuity that occurs in rocks, except for seismic faults, which have lengths above hundreds of meters and are not in the scope of this research. In opposition to the geological classifications, which adopt different terminologies for these discontinuities according to their originating events and stresses, they are regarded here from an engineering perspective. Thus, they are differentiated by their geometrical features and hydromechanical properties, which make them either barriers or preferential paths for fluid flow and planes of weakness for geomechanical analyses.

Reservoir fractures can be identified and characterized by a variety of methods, such as seismic techniques, well logging, core samples, borehole testing, analysis of outcrops and aerial photographs. The seismic techniques have a limited resolution and are only able to capture large discontinuities, while from core samples it may be possible to identify small cracks. The so-called sub-seismic fractures, whose lengths range from meters to tenths of meters, are more problematic since they are not identifiable by seismic methods and well data provide, at most, limited information on them. They are known, however, to have the potential of being highly influential on reservoirs fluid flow (Matthäi et al., 2007; Lohr et al., 2008). Additional information on this kind of fracture may be obtained with geological investigations of outcrop analogues, which are increasingly popular. It is impossible, however, to remove uncertainties from the characterization of subsurface fracture networks, because of the lack of data outside the measurement locations, the difficulty in obtaining measures in

three dimensions and doubts on how well the analogues represent the reservoir conditions, for example. Thus, geological modeling relies largely on extrapolation and subjective decisions (Berkowitz, 2002). Nonetheless, with the aid of geostatistical methods, it is possible to build detailed geological models, which can be calibrated during the reservoirs life.

After a good geological model is available, the predictability of the performance during recovery depends on the proper modeling and simulation of the reservoir. The impact of fractures on the global performance of the reservoir is related to a variety of physical phenomena, such as capillarity (Firoozabadi, 2000), anisotropy, localized flow, compaction and shear failure. Thus, the early identification of fractures and their consideration in the recovery planning can significantly improve the production of fluids. Failing in recognizing the possible influence of these discontinuities has led to unexpected early water breakthroughs and causes a reported variability of oil recovery in NFRs (Bourbiaux, 2010).

The scientific, technological and economical importance of reservoir simulations led to great advancements in the field of flow modeling, including the development of techniques to scale up the effects of heterogeneities. Despite of the limitations of the geological models, there is a general recognition that they have a much finer resolution than the conventional simulators; in fact, their sizes commonly differ by orders of magnitudes (Christie, 1996; Aarnes, 2004).

Usually, it is only feasible to explicitly represent the existing fractures in numerical models of reservoirs when the fractures are large faults or when the domain of simulation is restricted to near-well regions. Otherwise, the computational cost of representing smaller fractures in large-scale simulations tends to be prohibitive.

Upscaling techniques emerged as the most common way of dealing with the problem of considering small heterogenities in reservoir simulation. They are part of the broader area of homogenization methods, which scale up properties from a fine scale to a coarser scale that is treated as homogeneous. This thesis focuses on a different class of homogenization: the multiscale methods. Although multiscale approaches have not been extensively explored for the simulation of reservoirs, they present characteristics that overcome some robustness issues of upscaling and are more adequate to represent phenomena that are hard to describe with equivalent constitutive laws.

1.2 Upscaling and multiscale methods

Homogenization methods are used to model heterogeneous media as simpler equivalent homogeneous media under the assumption that the problem at the large-scale domain happens on a separate, much bigger scale than the problem at the level of the microstructure. There are two scales of interest: the macroscale, which is the coarser scale and the microscale, which is the scale at which the small heterogeneities are described in detail. We present here two classes of homogenization techniques: upscaling and multiscale methods. In both cases the homogenization is performed over a domain that must be representative of the

microscale, which is usually called the Representative Elementary Volume (REV).

1.2.1 Upscaling

Upscaling applied to fractured reservoirs has received distinct early contributions that are still very popular, such as the sugar cube model (Figure 1.1) by Warren and Root (1963) and the tensor method to evaluate the permeability of discontinuous media by Oda (1985). Although the term upscaling may refer to a variety of different techniques, it will be used here as a synonym of calculating homogenized or equivalent properties to be used in large-scale simulations. The equivalent properties are computed with analytical methods or with numerical experiments on samples where the heterogeneities are explicitly represented. Then, the large scale problem is solved by considering that the domain is homogeneous and its materials respect the previously computed equivalent constitutive laws. In reservoir simulation, most of the efforts are directed to deriving an equivalent permeability, but other fields of study have advanced a lot in upscaling complex mechanical behavior of fractured domains.

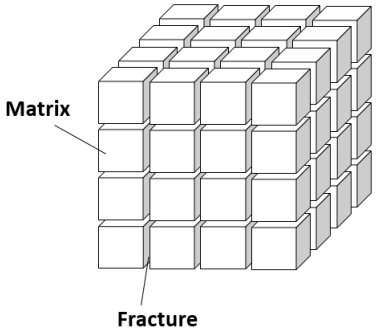

Figure 1.1: The sugar cube geometry assumed in the dual-porosity model by Warren and Root (1963).

Some researches report the limitations of the traditional upscaling methods. For instance, Salimi and Bruining (2010) compared the sugar cube model and the equivalent permeability approach with a more rigorous solution that uses the theory of periodic homogenization. They showed that the accuracy of both methods depends on the time required to imbibe the porous matrix with water and the travel time of water in the fracture system. Matthäi et al. (2007) computed two-phase flow in different fractured media to observe flow patterns and to upscale relative permeability; the upscaled relative permeabilities were radically different from those predicted by van Genuchten (Van Genuchten, 1980) or Brooks-Corey (Brooks and A.T., 1966) functions, which means that a new calibrated equation, dependent on the fractures geometry, would have to be used in the large-scale simulations. Chen et al. (2003) observed that traditional upscaling is not very accurate for highly heterogeneous porous media where the fluids follow tortuous paths and flow is channelized. Although they studied heterogeneities in porosity, fractures produce the same effects of channelized flow, since they

form preferential paths for the fluids. Zareidarmyian et al. (2021) compared the fine-scale and the upscaled solution of water injection in an elastoplastic fractured domain; they concluded that upscaling may not be capable of accurately representing the preferential direction of yielding and the pressure fields.

The problems of upscaling can be resumed to lack of robustness. Once an equivalent property is obtained, the medium is treated as homogeneous. Thus, the information of any physical interaction that would occur at the scale of the heterogeneities during flow is lost. Multiscale methods can overcome this limitation, at the cost of additional computational efforts.

1.2.2 Multiscale

In multiscale methods, both the macroscale and the microscale are solved numerically for every step of the simulation and are coupled by information that they send to one another. Figure 1.2 illustrates a multiscale method called multi-level Finite Element Method (FEM) or finite element squared (FE^2). In the FE^2, each integration point at the macroscale corresponds to a microscale domain (i.e. a REV), and both are solved with the FEM.

In the multi-level FEM, the strains and hydraulic gradients at the macroscale are imposed to the REV in the form of essential boundary conditions that are calculated using a localization rule. As for the stresses and fluxes at the integration points of the macroscale, they are obtained from the averaging of the microscale after the resolution of a boundary-value problem at the REV scale.

In one-scale simulations, stresses and velocities are defined based on a constitutive law. Since in multiscale methods these quantities are computed from the simulation of the microscale, they do not require the definition of any constitutive law for the large-scale. The constitutive behavior arises naturally from the simulation at the microscale. Also, since the boundary conditions of the REV problem arise from the macroscale, it is guaranteed that they are representative of the large-scale problem. And as the microscale is solved at every step of the problem, the physical phenomena at the level of the heterogeneities are updated and continuously modify the large scale behavior. For these reasons, multiscale methods are more robust than upscaling techniques.

The so-called global upscaling techniques (e.g. Chen et al., 2003) also solve both scales numerically and use the macroscale solution to define the boundary conditions at the microscale; for this trait, they can be referred to as multiscale (e.g. Aarnes, 2004). Applications of global upscaling to reservoir simulation showed that the coupled numerical solution of micro and macroscale yields more accurate results for highly heterogeneous porous media (Chen et al., 2003) and fractured media (Li et al., 2015). Thus, it is expected that multiscale simulations also return good results, with the advantage of not requiring assumptions on the constitutive behavior of the macroscale.

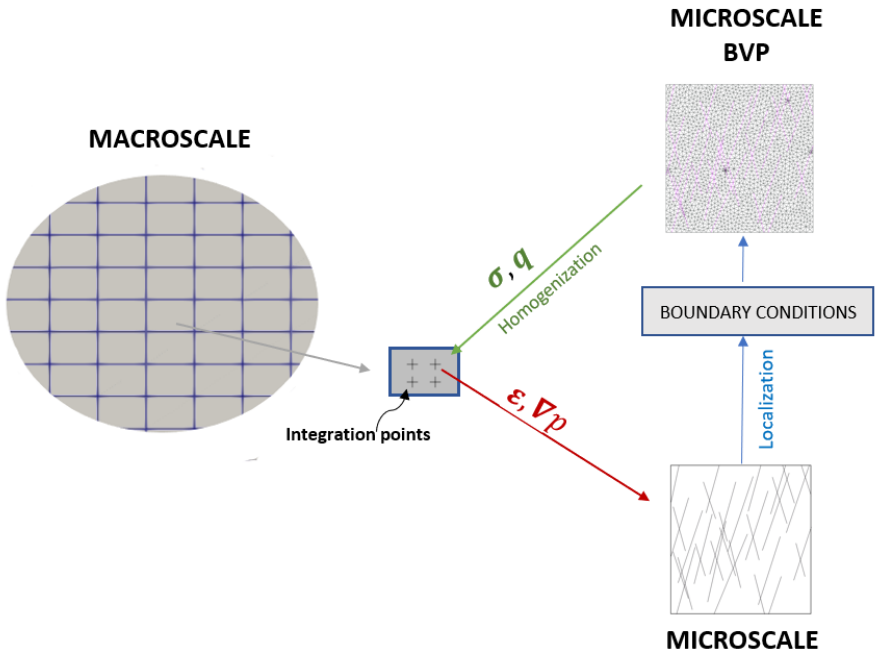

Figure 1.2: Schematic representation of the FE^2 method. The Boundary Value Problems (BVP) at the macro and microscale are coupled by homogenization and localization rules.

1.3 Hydromechanical coupling in fractured reservoirs

Many notable experimental works have showed that permeability, stiffness and strength of joints are strongly coupled to the stress-strain conditions of the rock mass (e.g Witherspoon et al., 1980; Barton et al., 1985; Teufel et al., 1993). Because of this coupling, the fracture properties change with the stress state, and so they are expected to have a dynamic impact on the overall behavior of geological structures submitted to time-dependent field variations. The terms "dynamic behavior" or "dynamic impact" will be used hereinafter to refer to this temporal change of the constitutive properties of the fractures and should not be confused with inertial effects.

There are several implications of this dynamic behavior to the performance of sufficiently fractured reservoirs. For example, the shear mobilization induced by primary or secondary recovery may compromise well stability and influence the fracture propagation behavior (Rahman and Rahman, 2013).

Another effect of major importance is the evolution of the fractures permeability during the reservoir's productive life. There are at least three important mechanisms related to this phenomenon. The first one is the loss of permeability induced by depletion, by which the fractures close progressively and become less permeable as pore pressure decreases. In reservoirs where the fractures are much more conductive then the intact rock, they are the

main source of permeability in the early stages of production, so this closure can have a significant impact on productivity. A second and opposite impact is the elastic opening of fractures when submitted to pore pressure increases that arise, for example, from stimulation methods such as the injection of water.

Thirdly, some reservoirs can have their permeability enhanced by shear dilation, which is the fracture opening induced by shear yielding; in this case, the dilated apertures are irreversible because the asperities of the fractures surfaces resist to their sliding back. The geothermal and petroleum industries currently use this mechanism as a stimulation method for reservoirs; by injecting at the proper pressure, it is possible to provoke the shear dilation of the fractures without the need of proppants to keep them open, as is the case in conventional hydraulic fracturing (Rahman et al., 2002). There are also reservoirs where depletion itself is sufficient to induce differential stresses that will make the fractures slip and dilate (e.g Teufel and Rhett, 1991).

Considering these impacts, the inclusion of coupled hydromechanics at the level of the fractures is sometimes beneficial to the predictability of reservoir simulations and to the efficiency of the recovery plans. This was firstly achieved by adding geomechanics to classical dual-porosity (sugar-cube) models (e.g. Chen and Teufel, 1997; Bagheri and Settari, 2008), and then to more complex fracture networks (e.g. de Sousa Junior et al., 2016).

Some researches focus on the comparison of the production forecasts when a dynamic, i.e. coupled, and a static fracture permeability is considered. Bagheri and Settari (2008) compared the dual-porosity model with static and dynamic permeabilities for depletion and injection scenarios. They reported that during depletion the static permeability approach significantly overestimates the production, while there is a considerable underestimation of the flux rates during injection. Also, they showed that static permeabilities can not capture the anisotropic pressure fields that surge when adopting different mechanical parameters for the distinct fracture sets in the sugar-cube model. de Sousa Junior et al. (2016) made a similar comparison for three case studies of a limestone reservoir that contains large fractures represented with an Embedded Discrete Fracture Model (EDFM). Their simulations showed that considering a geomechanics-sensitive permeability and a shear strength model for the fractures can significantly alter the forecasts of water breakthrough and oil production.

The role of stress state on the dynamic behavior of the fractures in reservoirs has also been investigated. It is well acknowledged that the reservoir's permeability may be damaged or enhanced depending on the initial stress conditions and the stress path followed during production. This was demonstrated, for example, in the experiments conducted by Teufel et al. (1993), for which the evolution of fracture permeability depended strongly on the imposed ratio between horizontal and vertical stresses. Tao et al. (2011) captured these effects in their numerical model, which is made of a combination of the Finite Differences Method (FDM) and the displacement discontinuity method (DDM). Their methodology was applied to a synthetic case, composed of two regular persistent and perpendicular sets of fractures. They verified the sensitivity of the decline in production to the fractures stiffness, as well as the effect of an anisotropic in-situ stress, which induced shear failure, and thus an

increase in permeability at some of the fractures.

Coupled hydromechanical simulations have also been used to evaluate production strategies in fractured reservoirs. For instance, Gan and Elsworth (2016) studied different plans of stimulation of a heavily fractured geothermal reservoir; they concluded that the best strategy is to place the injector and producer wells aligned with the major principal stresses, but the orientation of the fractures also impacts significantly the efficiency of the stimulation. Bertrand et al. (2020) used the finite element squared method to simulate a fractured coal reservoir. At the level of the microscale, they model the adsorption-induced shrinkage and swelling of coal and the consequent changes of apertures in the fractures; as a result, fracture permeability varies during depletion, and so does the reservoir's productivity. Their REV is made of regular and perpendicular sets of elastic fractures.

Most of these studies that apply coupled hydromechanics to fractured reservoirs either use simple idealized geometries, usually consisting of perpendicular and regular sets of fractures like in a sugar cube pattern, or represent the fractures explicitly, but are dedicated to large faults of tenths to hundreds of meters. The integration of smaller fractures that have tenths of centimeters to meters, with consideration of their real geometry, has not been much explored. These fractures are usually treated with an equivalent medium (upscaling) approach, which disregards the evolution of their properties. This simplification is questionable, because although these fractures are small, they tend to be much more frequent than the larger ones; so they do not necessarily have a less considerable influence on the reservoir's overall behavior.

Some upscaling techniques try to capture the dynamic nature of the properties by defining the equivalent stiffness and permeability of fractured media as a function of meaningful state variables such as the mean effective stresses (e.g Daley et al., 2006). However, experimental and numerical studies show that the evolution of the fracture properties is a result of the interplay between fracture orientation, mean effective stress and deviatoric stresses. So, even these more elaborate equivalent properties functions are unlikely to well capture the complexity of this behavior.

1.4 Description of the problem

Contrary to classical upscaling techniques, multiscale methods can represent the dynamic hydro-mechanical behavior of the fracture networks while maintaining a high fidelity to the complexity of their geometries.

For this reason, the main problem that this work explores is: how to apply a multiscale method like the finite element squared in the simulation of reservoirs containing complex networks of subseismic fractures. We should approach this problem by making the procedures of the multiscale modeling as general as possible and taking in consideration well-established practices in reservoir simulation.

This thesis works on three specific problems that need to be addressed to establish gen-

eral protocols and methods for the multiscale modeling of reservoirs that have small-scale fractures. They are:

- Numerical homogenization with the finite element squared usually employs periodic boundary conditions to homogenize the REV. When the mesh of the domain does not have symmetrical nodes at the boundaries, as is often the case when fractures are present, the imposition of this type of periodic boundary condition is not trivial and requires sophisticated methods. This problem is explored in Chapter 4.

- The size of the REV of stochastic random media has been extensively studied and conclusions were drawn for individual fracture networks, but there is a lack of mathematically rigorous rules that are general, i.e., could be applied to any fracture network. This problem is explored in Chapter 5.

- The original finite element squared uses a classical Galerkin formulation. As such, it is not locally conservative, i.e. it does not conserve mass at the level of the finite elements. This is a problem in reservoir simulation, because the lack of mass conservation leads to errors when dealing with saturation fronts and other phenomena that are typical of the production in reservoirs. For this reason, reservoir simulators usually adopt Finite Volume (FV) methods or adaptations of the FEM that makes it locally conservative. This problem is explored in Chapter 6.

Apart from these issues of theoretical and scientific nature, there is another issue concerning the computational tool. We used in this work the version 3.2 of DuMu^X (Koch et al., 2020), an open-source software for solving flow and elastic mechanical problems with FV methods. The original code already supports flow in fractured media and elastic problems in non-fractured domains, but it requires extensions and modifications to be used in the hydro-mechanical multiscale modeling of elastoplastic fractured domains. This problem is explored in Chapter 3.

1.5 Objectives

The general objective of this thesis is to develop methods and tools for the multiscale modeling of reservoirs that contain sub-seismic fracture networks.

Considering the specific problems described above, the specific objectives of this thesis are:

- Adapt the open-source software DuMu^X 3.2 to support hydro-mechanical coupled problems on elastic and elastoplatic fractured domains where the fractures are represented with lower-dimensional interface elements.

- Define general protocols for the definition of the size of the fractured REV and for the hydromechanical coupling in the simulation of the REV.

- Define a methodology to impose periodic boundary conditions on periodic and non-periodic meshes with interface elements.
- Develop a locally conservative multiscale method to be applied in reservoir simulation by adapting the finite element squared.
- Apply a multiscale method to simulate the production of a reservoir containing a complex network of subseismic fractures and observe the influence of the evolution of the fractures permeability on productivity.

1.6 Outline

This thesis is structured in 8 chapters.

Chapter 2 is dedicated to the boundary value problem of the REV. It presents a theoretical review on homogenization applied to hydromechanical problems, some of the current research on the homogenization of fractured rocks and the numerical methods employed to model the REV.

Chapter 3 presents the open-source code used to perform the simulations in this thesis, the extensions made to the code and their validation.

Chapter 4 presents the methods used to impose periodic boundary conditions on finite element meshes containing interface elements.

Chapter 5 proposes a statistics-based methodology to define the geometrical, hydraulic and mechanical REV of random fractured media.

Chapter 6 presents a method that was entitled multi-level Box, which is an adaption of the finite element squared, and validates its implementation.

Chapter 7 presents a synthetic case study where the tools and methods developed in the previous chapters were applied to model the production of a fractured reservoir.

Finally, Chapter 8 contains the conclusions and perspectives of this work.

Chapter 2

REV of fractured rocks: modeling and homogenization

In Section 1.2 the upscaling and multiscale methods were presented as techniques to transfer information between two scales: the microscale and the macroscale. The homogenization of quantities at the microscale was vaguely said to be obtained from the simulation of a Representative Elementary Volume (REV), a domain that must follow a few requirements for the macroscale to be considered homogeneous.

This chapter is dedicated to the boundary value problem of the REV and the theoretical aspects that it implicates. Firstly, Sections 2.1 and 2.2 present the definition of REV and some fundamentals of homogenization applied to hydro-mechanical problems. Then, Section 2.3 reviews the current research on the topic of modeling and numerical homogenization of fractured REVs. Finally, Section 2.4 presents the equations of the problem and the numerical and computational methods adopted to model the microscale.

2.1 What is a REV ?

The numerical testing of heterogeneous materials is used to study the impact of the microstructure on their overall behaviour and to homogenize properties for large-scale simulations. The selected equivalent properties must have been obtained from an adequate sample of the material, that is, a REV.

The REV is usually defined as a domain that is large enough to be statistically representative of the material; thus, it must contain a sampling of all of the existing types of heterogeneity (Kanit et al., 2003). Additionally, when the REV is used to obtain an equivalent constitutive behavior, this volume should also be large enough for the equivalent properties or the averaged response not to suffer size effects.

The term averaged response refers to the volume average $\langle . \rangle$ over a volume V:

$$\langle \cdot \rangle = \frac{1}{V} \int_V \cdot dV \tag{2.1}$$

In the case of the so called periodic media, the concept of REV is replaced by the concept of unit cell. Periodic media contain a pattern of heterogeneities that repeats itself within a distance interval called the period. In periodic media, the most appropriate sample is the unit cell, which is the smallest domain to contain the repeating pattern of heterogeneities that characterizes the microstrucure. The sugar cube model in Figure 1.1, for example, is a periodic structure. Figure 2.1 shows the definition of a proper unit cell for a sugar-cube like bi-dimensional structure.

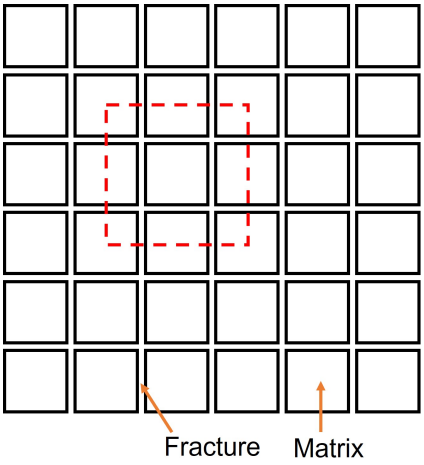

Figure 2.1: The domain delimited by the dashed red line shows a proper unit cell for a periodic strucute like the sugar cube model, where the porous matrix is intercepted by reguarly spaced and perpendicular sets of fractures.

In the case of non-periodic media, it is a standard approach to test increasing sample sizes and to define the minimum dimensions of the REV as those for which the equivalent properties seem to stabilize. The REV size for the geometrical and constitutive properties are not necessarily the same, as will be discussed in the following sections and in Chapter 5. The REV size depends on the physical phenomena at play, so it tends to be different for different constitutive properties.

A REV is considered adequate for homogenization if separation of scales exists, that is, if the dimensions of the REV are substantially smaller than the characteristic length of the macroscale problem. This guarantees that the principles of continuum mechanics are respected and the homogenized properties can be used to model the macroscale. The separation of scales solves what Hudson and Harrison (2000) call a paradox in using REVs to measure stress or any other quantity that is a property of a point, i.e. a sample with zero volume: if this separation exists, the REV can be treated as a point in the large scale domain.

The mathematical form of the principle of separation of scales is expressed through the definition of the scale factor ε:

$$\varepsilon = \frac{l_c}{L_c} \ll 1 \tag{2.2}$$

The length l_c is the characteristic length of the REV and L_c is the macroscopic length, which considers two characteristics: one purely geometrical, related to the spatial dimensions of the macroscopic domain, and one related to the characteristic length of the studied phenomenon. Usually, this latter is defined in terms of the macroscopic gradient $\frac{\partial \langle \Psi \rangle}{\partial x_i}$ of the homogenized variable $\langle \Psi \rangle$ that describes the phenomenon:

$$L_c = \frac{\langle \Psi \rangle}{\frac{\partial \langle \Psi \rangle}{\partial x_i}} \tag{2.3}$$

where x_i is a directional component of the coordinate system $\boldsymbol{x}$ at the microscale. Equation 2.2 then becomes:

$$\varepsilon = \frac{l_c}{L_c} = \frac{l_c \frac{\partial \langle \Psi \rangle}{\partial Y}}{\langle \Psi \rangle} \ll 1 \tag{2.4}$$

The basic principle of the homogenization method described in Figure 1.2 is that quantities such as strains and pressure gradients at a point of the macroscale can be imposed to the REV to obtain an averaged response in terms of stresses and fluxes. The term $l_c \frac{\partial \langle \Psi \rangle}{\partial Y}$ in (2.4) gives an estimation of the variation of $\langle \Psi \rangle$ inside the REV. If the imposed macroscopic quantities vary considerably at the microscale, it is hard to set a proper value to be imposed to the REV and to obtain a reliable averaged response.

For random materials, it follows from (2.4) that the volume average of a property Ψ must satisfy the stationarity condition (Auriault et al., 2009):

$$\int_{V_1} \Psi dV = \int_{V_2} \Psi dV \tag{2.5}$$

where V_1 and V_2 are two volumes of characteristic dimension l_c, taken from the same large-scale domain and for which the distance between them is of the order of l_c. In other words, the stationarity condition imposes the translational invariance of $\langle \Psi \rangle$. Note that the fulfillment of this condition depends both on the size l_c, which must be large enough for the averaged response of both REVs to be approximately the same, and on the gradient $\frac{\partial \langle \Psi \rangle}{\partial Y}$, which can not be so large that $\langle \Psi \rangle$ changes significantly with a translation of the order of l_c.

The larger the separation of scales is, the better are the results obtained from homogenization; although there is no exact way of estimating a limit value for the scale factor ε, it is generally considered that homogenization is effective for $\varepsilon < 0.1$ (Auriault et al., 2009).

2.2 Homogenization of hydro-mechanical properties

This section presents the principles behind the homogenization applied to hydro-mechanical problems. In what follows, the subscripts M and m will refer to the macroscale and the microscale, respectively. The position $\boldsymbol{y}$ locates a point on the macroscale's coordinate system, and the position $\boldsymbol{x}$ locates a point on the microscale's coordinate system.

For the problem at the REV to be consistent with the problem at the macroscale, energetic constraints need to be enforced. For the mechanical problem, the classic form of this constraint is the Hill-Mandel principle, which states:

$$\boldsymbol{\sigma}_M(\boldsymbol{y},t) : \dot{\boldsymbol{\varepsilon}}_{\boldsymbol{M}}(\boldsymbol{y},t) = \langle \boldsymbol{\sigma}_m(\boldsymbol{x},t) : \dot{\boldsymbol{\varepsilon}}_{\boldsymbol{m}}(\boldsymbol{x},t) \rangle \tag{2.6}$$

where $\boldsymbol{\sigma}$ and $\boldsymbol{\varepsilon}$ are the stress and strain tensors, respectively. Equation (2.6) imposes the energy rate at the macroscale to be equal to the volume average of the microscale's energy rate.

The stress tensor at the macroscale $\boldsymbol{\sigma}$ is the volume average of the stresses at the microscale:

$$\boldsymbol{\sigma}_M(\boldsymbol{y},t) = \langle \boldsymbol{\sigma}_m(\boldsymbol{x},t) \rangle \tag{2.7}$$

The same applies to the deformation tensor $\boldsymbol{F}_M$, defined here in terms of the displacements at the microscale, $\boldsymbol{u}_m$:

$$\boldsymbol{F}_M(\boldsymbol{y},t) = \boldsymbol{I} + \frac{1}{V}\int_V \nabla_m \otimes \boldsymbol{u}_m(\boldsymbol{x},t) dV \tag{2.8}$$

where $\boldsymbol{I}$ is the identity tensor and ∇_m is the gradient operator vector for the microscale. The macroscale strain tensor $\boldsymbol{\varepsilon}_M$ is defined as:

$$\boldsymbol{\varepsilon}_M(\boldsymbol{y},t) = \frac{1}{2}({\boldsymbol{F}_M}^T + \boldsymbol{F}_M) - \boldsymbol{I} \tag{2.9}$$

The following relationship forms the system that yields the upscaled stress-strain constitutive matrix, $\boldsymbol{C}_M$:

$$\boldsymbol{\sigma}_M(\boldsymbol{y},t) = \boldsymbol{C}_M(\boldsymbol{y},t) : \boldsymbol{\varepsilon}_M(\boldsymbol{y},t) \tag{2.10}$$

For fluid flow problems, the energetic bridge between microscale and macroscale is usually established by the consistency of the dissipation energy i.e., the specific energy dissipated by viscous friction, proposed by Indelman and Dagan (1993). This latter considers the flux at the REV to be stationary. Khoei and Hajiabadi (2018) proposed the following extension to consider the possibility of non-stationary flow at the microscale:

$$-(\boldsymbol{G}_{M\alpha}(\boldsymbol{y},t))^T \,.\boldsymbol{v}_{M\alpha}(\boldsymbol{y},t) + p_{M\alpha}\dot{\Theta}_{M\alpha} = \langle -(\nabla_m p_{m\alpha}(\boldsymbol{x},t))^T \,.\, v_{m\alpha}(\boldsymbol{x},t) + p_{m\alpha}\dot{\Theta}_{m\alpha} \rangle \tag{2.11}$$

where the subscript α refers to a fluid phase, p is fluid pressure, $\boldsymbol{G}$ is the macroscale pressure gradient vector, $\boldsymbol{v}$ is the fluid's velocity or specific flux and Θ is the fluid's volumetric content.

The specific flux $\boldsymbol{v}_{M\alpha}$ of the phase α at the macroscale is:

$$\boldsymbol{v}_{\alpha M}(\boldsymbol{y},t) = \langle \boldsymbol{v}_{\alpha m}(\boldsymbol{x},t) - \boldsymbol{x}\dot{\Theta}_{m\alpha} \rangle \tag{2.12}$$

and the pressure gradient $\boldsymbol{G}_\alpha$ is defined as a function of the pressure p_α at the microscale:

$$\boldsymbol{G}_{M\alpha}(\boldsymbol{y},t) = \langle \nabla_m p_{m\alpha}(\boldsymbol{x},t) \rangle \tag{2.13}$$

In transient flow problems, the mass flux per unit volume is given by the storage term Υ; at the macroscale, it is computed from the fields of fluid density ρ_α and volumetric content Θ_α at the microscale:

$$\Upsilon_{M\alpha}(\boldsymbol{y},t) = \langle \Upsilon_{m\alpha}(\boldsymbol{x},t) \rangle = \langle \rho_{m\alpha}(\boldsymbol{x},t)\Theta_{m\alpha}(\boldsymbol{x},t) \rangle \tag{2.14}$$

Assuming Darcian flow and ignoring gravitational effects, the following relationship can be established between the homogenized properties and the upscaled permeability tensor $\boldsymbol{K}_M$:

$$\boldsymbol{v}_{\alpha M}(\boldsymbol{y},t) = \boldsymbol{K}_{M\alpha}(\boldsymbol{y},t) \cdot \boldsymbol{G}_{M\alpha}(\boldsymbol{y},t) \tag{2.15}$$

The homogenized variables presented above are outcomes of the solution of the equilibrium of forces and mass conservation equations (presented in Item 2.4.3) at the REV. The resulting pressures p_m and displacements $\boldsymbol{u}_m$ at the REV can be decomposed in two parts: the linear components $\boldsymbol{u}_l$ and p_l related to their gradient at the corresponding point $\boldsymbol{y}$ of the macroscale, and the fluctuation components $\tilde{p}$ and $\tilde{\boldsymbol{u}}$, which capture their spatial variations due to the existence of small-scale heterogeneities. Hence, the pressures and displacements at the microscale can be defined as:

$$\boldsymbol{u}_m(\boldsymbol{x},t) = (\boldsymbol{F}_M(\boldsymbol{y},t) - \boldsymbol{I}) \;.\; \boldsymbol{X} + \tilde{\boldsymbol{u}}(\boldsymbol{x},t) = \boldsymbol{u}_l(\boldsymbol{x},t) + \tilde{\boldsymbol{u}}(\boldsymbol{x},t) \tag{2.16}$$

$$p_{m\alpha}(\boldsymbol{x},t) = \boldsymbol{G}_{M\alpha}(\boldsymbol{y},t) \;.\; \boldsymbol{X} + \tilde{p}_\alpha(\boldsymbol{x},t) = p_l(\boldsymbol{x},t) + \tilde{p}_\alpha(\boldsymbol{x},t) \tag{2.17}$$

where $\boldsymbol{X}$ denotes the position of point $\boldsymbol{x}$ in reference to an arbitrary reference point of the REV. Considering (2.8) and (2.13), it can be inferred from (2.16) and (2.17) that the integral of the fluctuation components over the contour of the REV is null:

$$\int_{\partial V} \tilde{\boldsymbol{u}}(\boldsymbol{x},t) \otimes \boldsymbol{n} \; d\partial V = \boldsymbol{0} \tag{2.18}$$

$$\int_{\partial V} \tilde{p}_\alpha(\boldsymbol{x},t) \;.\; \boldsymbol{n} \; d\partial V = \boldsymbol{0} \tag{2.19}$$

where $\boldsymbol{n}$ is the outward unit outer vector of boundary ∂V. Along with the energy consistency requirements in (2.6) and (2.11), equations (2.18) and (2.19) constrain the microscale problem to be used in homogenization-based methods.

2.2.1 Numerical homogenization: boundary conditions

Dormieux et al. (2006) presents analytical solutions for the homogenization of porous materials with simple geometries. For complex microstructure geometries or highly non-linear behaviour, Equations 2.10 and 2.15 can be solved numerically by defining a boundary value problem at the REV scale. The adopted boundary conditions usually fall on one of the three main categories described below:

(a) Linear Dirichlet boundary conditions

The homogenization of properties with Dirichlet boundary conditions consists in imposing displacements and pressures at the boundaries for mechanical and flow problems, respectively. To upscale the equivalent constitutive tensors, a set of linearly independent deformations or pressure gradients must be imposed. The numerical solution of the REV for each boundary value problem yields the averaged stress $\boldsymbol{\sigma}_M$ or the averaged specific flux, $\boldsymbol{v}_M$.

The most common type of Dirichlet boundary conditions used in the upscaling of permeability is the linear pressure configuration proposed by Long et al. (1982), which is illustrated in Figure 2.2 for 2D problems. It consists in applying, for each pair of opposite boundaries at a time, an injection pressure at one side and zero pressure at the other; on the other pairs of opposite boundaries, pressure is an equal linear function of the position, so there is no pressure gradient in the directions normal to them. The pressures p at the boundaries of the REV are a function of the imposed constant pressure gradient vector $\overline{\boldsymbol{G}}$:

$$p = \overline{\boldsymbol{G}} \cdot \boldsymbol{x} \tag{2.20}$$

If the injection pressure P_{inj} is applied to a side that is normal to the direction i and the sides parallel to i have length L_i: $G_j = P_{inj}/L_i$ if $j = i$ and $G_j = 0$ if $j \neq i$. From Equation 2.20, it follows that the macroscopic pressure gradient $\boldsymbol{G}_{M\alpha}$ (Equation 2.13) is equal to the imposed gradient $\overline{\boldsymbol{G}}$:

$$\boldsymbol{G}_{M\alpha} = \overline{\boldsymbol{G}} \tag{2.21}$$

A similar configuration of linear displacements can be used to impose a constant displacement gradient tensor $\overline{\boldsymbol{F}}$, as illustrated in Figure 2.3, so the displacements $\boldsymbol{u}$ at the boundaries are defined by:

$$\boldsymbol{u} = \overline{\boldsymbol{E}} \cdot \boldsymbol{x} \tag{2.22}$$

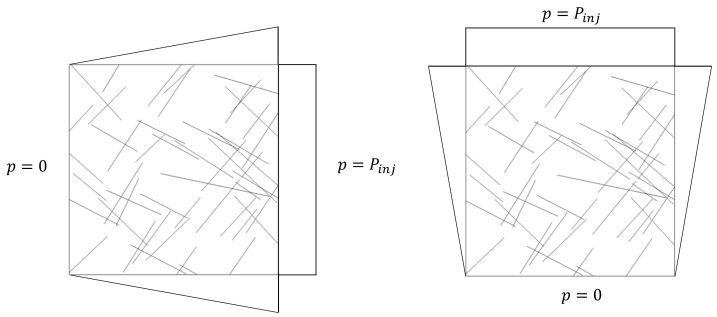

Figure 2.2: Linear pressure boundary conditions for upscaling in flow problems: imposition of pressure gradient with respect to directions x (left) and y (right) independently.

where $\overline{\boldsymbol{E}}_{ij} = {}^{\partial u_i}/_{\partial x_j}$. It is thus straightforward to conclude that:

$$\boldsymbol{\varepsilon}_M = \frac{1}{2}(\overline{\boldsymbol{E}} + \overline{\boldsymbol{E}}^T) \tag{2.23}$$

The displacements in Figure 2.3 are applied in such a way that, at each step of the upscaling procedure, only one of the components $\boldsymbol{\varepsilon}_{xx}$, $\boldsymbol{\varepsilon}_{yy}$ and $\boldsymbol{\gamma}_{xy}$ of the strain vector assumes a non-zero value. This allows all the components of the equivalent stiffness tensor to be easily retrieved.

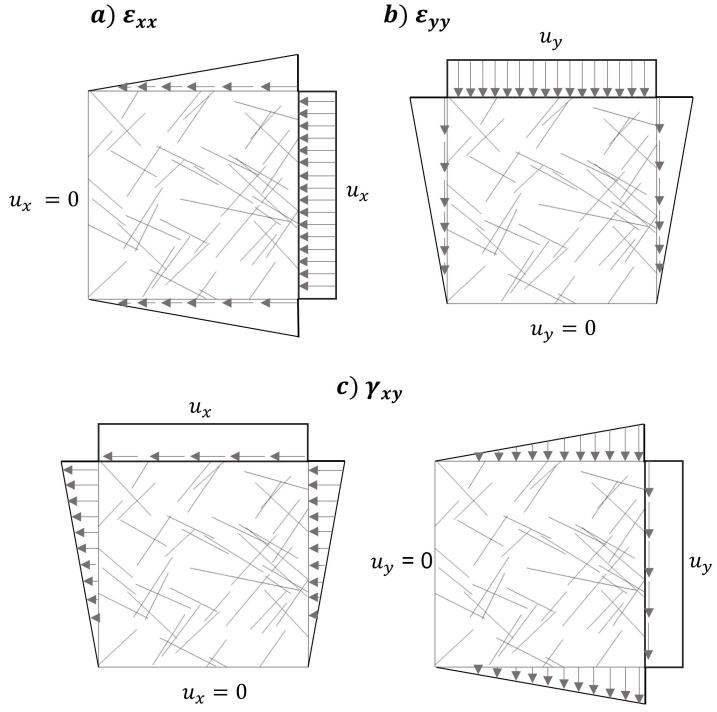

Figure 2.3: Linear displacement boundary conditions for upscaling in mechanical problems: imposition of pure compressive strains $\boldsymbol{\varepsilon}_{xx}$ (a) and $\boldsymbol{\varepsilon}_{yy}$ (b) and of pure shear strain $\boldsymbol{\gamma}_{xy}$.

(b) Neumann boundary conditions

The homogenization of hydro-mechanical properties is also feasible using Neumann boundary conditions, which means the imposition of stresses and flux at the boundaries.

A common set of flux boundary conditions used for the homogenization of hydraulic properties are the so-called no-flow boundary conditions (Figure 2.4), on which a specific flux $\boldsymbol{Q}_{inj}$ is applied to one boundary, while a null flux is imposed to the others, except for its opposite side. As a consequence, the homogenized macroscale velocity $\boldsymbol{v}_M$ is:

$$\boldsymbol{v}_M = \boldsymbol{Q}_{inj} \tag{2.24}$$

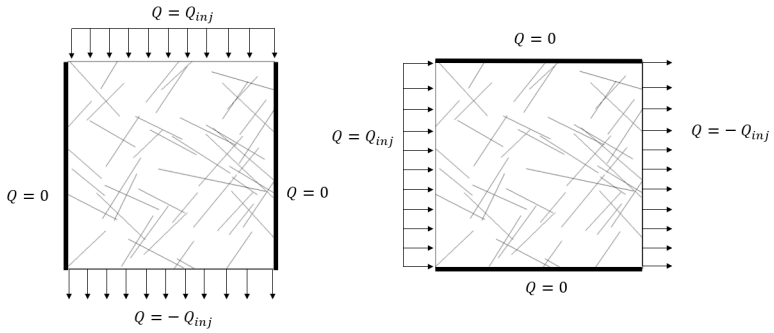

Figure 2.4: No flow boundary conditions for upscaling in flow problems.

Figure 2.5 illustrates commonly adopted sets of linearly independent stresses $\boldsymbol{\Sigma}$, for which the homogenized stress tensor $\boldsymbol{\sigma}_M$ is:

$$\boldsymbol{\sigma}_M = \boldsymbol{\Sigma} \tag{2.25}$$

The configuration in Figure 2.5 allows the assessment of the influence of each stress component on the homogenized deformation, and thus the equivalent compliance tensor can be easily obtained.

(c) Periodic boundary conditions

Consider any two symmetrical points on opposite sides of the REV, like the ones illustrated in Figure 2.6. Periodic boundary conditions are imposed by enforcing the fluctuation of the primary variables to be equal at these points:

$$\tilde{p}(\boldsymbol{x}^+) = \tilde{p}(\boldsymbol{x}^-) \tag{2.26}$$

$$\tilde{\boldsymbol{u}}(\boldsymbol{x}^+) = \tilde{\boldsymbol{u}}(\boldsymbol{x}^-) \tag{2.27}$$

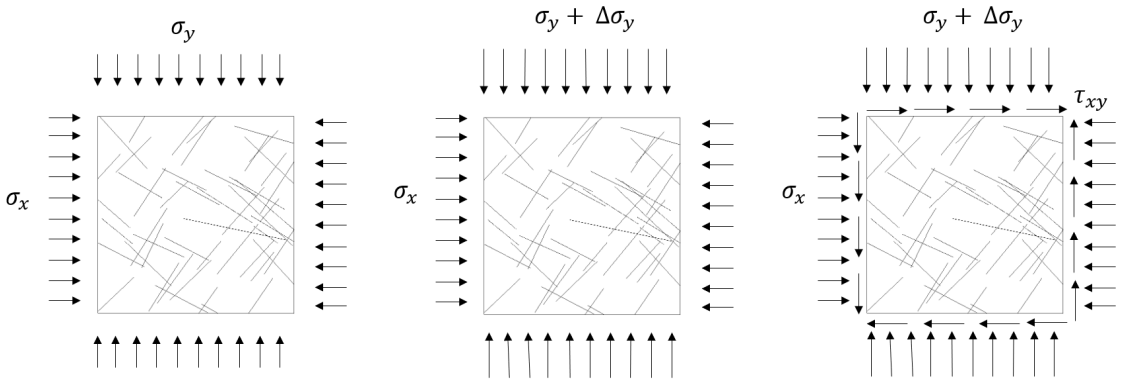

Figure 2.5: Stress boundary conditions for upscaling in mechanical problems.

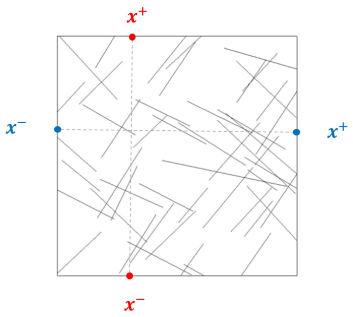

Figure 2.6: Examples of pairs of symmetric points $\boldsymbol{x}^-$ and $\boldsymbol{x}^+$ that are located at opposite boundaries of the REV; such pairs are mapped to define the periodic boundary conditions.

Considering an imposed macroscopic pressure gradient $\overline{\boldsymbol{G}}$ and an imposed macroscopic displacement gradient tensor $\overline{\boldsymbol{E}}$, it can be concluded from (2.26) and (2.27) that:

$$p(\boldsymbol{x}^+) = p(\boldsymbol{x}^-) + \overline{\boldsymbol{G}} \,.\, (\boldsymbol{x}^+ - \boldsymbol{x}^-) \tag{2.28}$$

$$\boldsymbol{u}(\boldsymbol{x}^+) = \boldsymbol{u}(\boldsymbol{x}^-) + \overline{\boldsymbol{E}} \,.\, (\boldsymbol{x}^+ - \boldsymbol{x}^-) \tag{2.29}$$

As a consequence of the imposition of periodic pressures and displacements, the resulting flow rates Q and tractions T are anti-periodic, that is:

$$Q(\boldsymbol{x}^+) = -Q(\boldsymbol{x}^-) \tag{2.30}$$

$$\boldsymbol{T}(\boldsymbol{x}^+) = -\boldsymbol{T}(\boldsymbol{x}^-) \tag{2.31}$$

Equations (2.28), (2.29), (2.30) and (2.31) provide additional relationships that make the solution of the microscale problem unique. Chapter 4 presents in detail the solution of the REV using periodic boundary conditions and their imposition when non-symmetric mesh geometries and interface elements are used. As the directly imposed variables are pressure

gradients and strains, Equations (2.21) and (2.23) apply to periodic boundary conditions.

Appendix A presents a review on how to retrieve the equivalent elastic tensors using the boundary conditions mentioned above for plane-strain conditions.

These three categories of boundary conditions are widely used and are known to respect the constraints in Equations (2.6) and (2.11) and (2.18)-(2.19), as was demonstrated, for example, by Liu and Reina (2016) for mechanics and by Pouya and Fouché (2009) for fluid percolation.

It was shown that depending on the chosen boundary conditions, either the homogenized gradients of the essential primary variables (Equations 2.21 and 2.23) or the homogenized stresses/flux (Equations 2.24 and 2.25) are directly obtained. Their associated homogenized variables depend on the solution of the boundary-value problem. If the divergence theorem is applied to Equations 2.7 – 2.13, the volumetric averages of the properties are more easily taken by accessing the solutions at the boundaries only. For Equations 2.8 and 2.13, the divergence theorem yields:

$$\int_V \nabla a_m(\boldsymbol{x}) dv = \int_{\partial V} a_m(\boldsymbol{x}) \cdot \boldsymbol{n}(\boldsymbol{x}) \; d\partial V \tag{2.32}$$

where the variable a is a general representation of fluid pressure or of a directional component of the displacement vector. For Equations 2.7 and 2.12:

$$\int_V \boldsymbol{b}_m(\boldsymbol{x}) dv = \int_{\partial V} (\boldsymbol{b}_m(\boldsymbol{x}) \cdot \boldsymbol{n}(\boldsymbol{x}))\boldsymbol{x} \; d\partial V \tag{2.33}$$

where b is a general representation of boundary forces and specific flux. Equation 2.33 was proposed by Pouya and Fouché (2009) as a rigorous form of calculating the homogenized unit flux, in opposition to the initial formulation by Long et al. (1982), who calculated the flux only at one boundary based on erroneous premises. It can be regarded as a general form of the multi-boundary upscaling later proposed by Chen et al. (2015), since the former is valid for any domain shape and the latter assumes a rectangular REV.

It is well acknowledged that the upscaled properties depend on the chosen boundary conditions. As was demonstrated by Chalon et al. (2004), Pouya and Fouché (2009) and others, linear Dirichlet boundary conditions provide an upper bound for the permeability and stiffness tensors, while Neumann boundary conditions give a lower bound for these properties and periodic boundary conditions provide intermediate values. These differences are explored in Chapter 4.

As the REV size increases, the differences between the various categories of boundary value problems tend to zero. The REV size may be defined as the size for which this difference becomes insignificant; but it is more common to select one type of boundary conditions that returns conservative estimations. The vast majority of the works on the upscaling of the mechanical constitutive tensor of fractured rocks uses stress boundary conditions. As for flow problems, the adequate choice between a lower bound and an upper bound of permeability

depends on whether high flux rates are alarming or desirable.

2.3 State-of-the-art review

This section reviews some relevant results, concepts, discussions and techniques in the literature on the homogenization of fractured rocks and on the modeling and definition of their REV.

The first step to define a proper REV is to guarantee that the volume is statistically homogeneous with respect to the geometrical patterns of the discontinuities. This is a challenge that starts on the field, since the geological methods to characterize fracture sets always carry some uncertainty. The selected geometrical REV can then be used as a reference volume to study scale effects on the mechanical and hydraulic properties. The homogenization of such properties has been approached with empirical (e.g Hoek and Brown, 1997) and analytical (e.g Duncan and Goodman, 1968; Oda, 1985) methods. Although these methods remain relevant, upscaling with numerical experiments have been used more frequently for relying on physically consistent models where the geometry and the properties of the fractures are controllable. For that reason, they are the focus of this review.

2.3.1 Geometrical REV

The definition of a geometrical REV for fractured rocks requires a decision on which parameters will be used to quantify geometry. This is not a straightforward task, since fracture networks can be a complex combination of sets that differ in their geological history and in the statistical characterization of their various features, such as orientation, spacing and size. Another important choice is the scale of study. Since rock masses contain discontinuities whose size might range from micrometers to hundreds of meters or even kilometers, the geometrical REV is surely different if the considered heterogeneities are micro-cracks or sub-seismic faults, for example. Hence, due to the impossibility of considering all discontinuities, the REV should be representative of those that are relevant to the selected scale. A consequence of that for numerical modeling is that fractures that are bigger than the scale of the REV are not accounted for in the homogenization and should be modeled explicitly in the macroscale.

A variety of geometrical measurements has been used to determine the REV size of rock masses, such as: average length (e.g. Oda, 1988), average spacing (e.g. Xia et al., 2016), orientation (e.g. Zhang et al., 2011) and fracture intensity (e.g. Liu et al., 2018). Although these quantities are frequently analyzed separately, they can be accounted for altogether in the crack tensor proposed by Oda (1982).

The crack tensor provides an overall measure that considers the density, the size and the orientation of all the fractures in the REV. Zhang and Einstein (2000) removed the arbitrary non-dimensionalization of Oda's formulation and proposed the following equation

for the crack tensor:

$$F_{ij} = \frac{1}{V} \sum_{k=1}^{n_f} S^{(k)} {n_i}^{(k)} {n_j}^{(k)} \tag{2.34}$$

where V is the volume of the rock mass, $S^{(k)}$ is the area of the k^{th} discontinuity, and $n_i^{(k)}$ and $n_j^{(k)}$ are the components of the normal vector of the k^{th} discontinuity with respect to the directions $i, j = x, y, z$. In this formulation, the first invariant I_1 of F_{ij} has a clear physical meaning because it corresponds to the fracture intensity:

$$I_1 = F_{xx} + F_{yy} + F_{zz} = \frac{1}{V} \sum_{k=1}^{n_f} L^{(k)} \tag{2.35}$$

where $L^{(k)}$ is the length of the k^{th} fracture. As for the second invariant, it is related to the orientation of the fractures and can be used to evaluate the degree of anisotropy of the system (Kulatilake et al., 1993).

An alternative formulation that takes aperture into account was derived by Oda (1985) to calculate the permeability of fractured media based on the cubic law (Equation 2.68). The components of this new tensor $\boldsymbol{P}$ are the components of $\boldsymbol{F}$ multiplied by the cube of the aperture w:

$$P_{ij} = \frac{1}{V} \sum_{k=1}^{n_f} (w^{(k)})^3 S^{(k)} {n_i}^{(k)} {n_j}^{(k)} \tag{2.36}$$

The selection of a proper size for the geometrical REV guarantees that the relevant heterogeneity types are well represented, but does not ensure that this volume is sufficient to represent the average constitutive behavior. Although the pattern of the fractures influences the behaviour of the rock masses, the geometrical REV may be different from the REVs for the equivalent hydraulic and mechanical properties.

2.3.2 Mechanical REV and upscaling of mechanical properties

The presence of fractures in rock masses is linked to many relevant mechanical responses, such as high compressibility, anisotropy and brittle failure. Their impact on the equivalent constitutive behaviour can be assessed with numerical experiments modeled with continuous or discrete methods.

Numerical homogenization has been used to assess the elastic parameters, strength and failure modes of fractured media. Pouya and Ghoreychi (2001) developed a method to obtain an oriented strength criterion for highly fractured rocks using FEM experiments. Min and Jing (2003) and Yang et al. (2014) estimated the equivalent elastic compliance tensor and its associated REV size using the Distinct Element Method (DEM) and FEM, respectively. Wang et al. (2013) used a DEM model to reproduce the mechanical behavior observed on

their compression tests on granite, including fracturing events measured *via* acoustic emissions. Rasmussen et al. (2018) extended the Rigid Body Spring Network (RBSN) method to reproduce brittle failure and obtained accurate estimations for the elastic and strength properties of the Lac du Bonnet granite. JianPing et al. (2015) also represented the progressive failure of fractured rocks by implementing a damage evolution model in a FEM code; they studied the anisotropy and REV size for the equivalent strength. These studies adopt methods that can be applied to the investigation of any rock mass, but their results are specific to the tested rocks.

More general rules can be inferred from works that investigate the role of the geometry of the fractures on the mechanical properties. Kulatilake and co-authors conducted numerical and laboratory experiments on fractured samples and showed that the elastic parameters (Kulatilake et al., 1993) and the compression strength (Kulatilake et al., 2001; Wu and Kulatilake, 2012) are strongly related to the directional components F_{ii} of the fracture tensor. Other authors also showed that strength has a clear relationship with fracture intensity (e.g Harthong et al., 2012).

The observed responses can only be considered to reproduce the average behaviour of a material if the experiment is conducted on a representative sample. Thus, the size of the mechanical REV is naturally a topic of interest and an important outcome of the homogenization process. Some researchers used one generation of the fractures network to define the REV as the volume for which the equivalent mechanical properties stabilize (e.g. JianPing et al., 2015; Yang et al., 2014). In an attempt to account for the stochastic nature of the fractures, other authors tested multiple samples to define the mechanical REV size based on the coefficient of variation (COV) of the properties (e.g. Min and Jing, 2003; Esmaieli et al., 2010; Farahmand et al., 2018). Using a large number of simulations, Loyola et al. (2021) proposed a general methodology to define the REV size based on the statistical theory of samples. This methodology is detailed in Chapter 5.

In order to create general rules that avoid numerical simulations, there were also attempts to define the mechanical REV size as a function of geometrical features such as spacing (e.g. Chalhoub and Pouya, 2008) and fracture length (Ni et al., 2017). The existing comparisons between the mechanical and the geometrical REVs could indicate whether the latter can be consistently used as a close, or at least conservative, estimation of the former. This question remains unclear since some authors concluded that the geometrical REV is larger (Loyola et al., 2021), while others concluded the opposite (e.g. Esmaieli et al., 2010; Ni et al., 2017).

2.3.3 Hydraulic REV and upscaling of permeability

Fractures can alter the seepage in porous media by acting either as conductive preferential paths or by blocking the passage of fluids, if they contain an impermeable material. Since a basic concern of any percolation problem is to make good estimations of the flow rates, there is a rich literature on the calculation of equivalent permeabilities for heterogeneous rocks. Shahbazi et al. (2020) present a comprehensive review of the existing empirical, analytical

and numerical methods to assess the permeability of fractured media. The numerical techniques consist in solving flow on discrete fracture models and are generally called flow-based upscaling. An important distinction is made with respect to the imposed boundary conditions; these can be local, when arbitrary boundary conditions are assumed, or global, when the boundary conditions of the REV are taken from the solution of the large-scale problem.

The upscaled intrinsic permeability of heterogeneous media has been assessed using linear pressure (e.g. Min et al., 2004a), constant flux (e.g. Matthäi et al., 2007) and periodic boundary conditions (e.g. Durlofsky, 1991). Since the calculated permeability depends on the chosen boundary conditions, global upscaling techniques (e.g Chen et al., 2003) were developed to guarantee that the boundary value problem at the REV scale represents the conditions in the large-scale simulation.

For multiphase flow, it is often possible to build proper large-scale models with only the upscaled intrinsic permeability (Durlofsky, 2005). Sometimes, however, it is necessary to upscale multiphase parameters like relative permeability and capillary pressure. Multiphase upscaling can be realized using steady-state or dynamic techniques. In the former, time derivatives are ignored and boundary value problems are solved for different constant values of capillary pressure or fractional flow to obtain the equivalent relative permeability as a function of the averaged saturation (Christie, 2001). In contrast, dynamic techniques do not work with the assumption of capillary or gravity equilibrium (Barker and Dupouy, 1999); they require transient solutions to compute relative permeability based on the saturation changes over time.

Flow-based upscaling has been used not only to transfer information for large scale simulations, but also to investigate how the geometry of the fractures affects permeability. The idea of defining permeability as a function of the crack tensor was introduced by Oda (1985) with an analytical approach. Based on that, Panda and Kulatilake (1999) used numerical experiments to show that there is a strong relationship between directional permeability and the crack tensor for connected joints; this relation was shown to be a linear function for blocks containing mainly persistent discontinuities and a power function for blocks containing minor discontinuities. Kulatilake and Panda (2000) performed more tests on blocks containing non-persistent discontinuities to confirm this relationship and showed that, when rotating the test, the directional variations of the permeability and the fracture tensor components are related.

As the permeability of a fracture depends strongly on its aperture, recent studies assessed the effects of aperture and its spacial variability on the upscaled permeability of fractured rock masses. De Dreuzy et al. (2012) observed a reduction of this permeability when the heterogeneity of the aperture is considered, but concluded that at sufficiently large scales the fractured medium can be reasonably described by a proper constant aperture. Lei et al. (2014) considered stress-dependent apertures and observed significant discrepancies with models where the variability of aperture is ignored; and Bisdom et al. (2016) considered the variability of aperture within a single fracture and concluded that a unique averaged aperture can provide a similar upscaled permeability when most fractures contribute to flow.

Geometry does not whatsoever control flow in fractured media alone. In fact, geometrical aspects should ideally be analyzed within the geomechanical context, since the acting stresses may dictate the fluid paths and the evolution of permeability, specially for sets of non-persistent fractures (Lei et al., 2017). For example, Bisdom et al. (2016) showed that, if the fractures are ideally oriented with respect to the major principal stresses, upscaled permeability can be higher than that of blocks containing higher fracture density and connectivity, but less favorable orientations. Massart and Selvadurai (2012) assessed the permeability evolution in quasi-brittle materials under shear; cohesive interfaces were employed at the level of the REV to simulate the evolution of damage, which increases the local permeability. They observed that the damage is more important on fractures that are parallel to the direction of the deviatoric loading and assessed the influence of the confinement pressure on the evolution of permeability. Several other studies can be found in the state-of-the-art review by Lei et al. (2017), which is focused on the geomechanical effects on the flow in fractured media. The existing researches point the orientation of principal stresses, dilation, crack propagation and the opening and closure of the fractures as factors that alter the fluid pathways and promote localized flow channels. The equivalent permeability is thus dependent on mechanical conditions; for instance, it decreases until a residual value when normal stress increases, and it increases when deviatoric stresses are high enough to provoke shear dilation (Min et al., 2004b).

Lastly, many works on upscaled permeability inevitably pass through the definition of the REV's size. This leads to a deeper question on whether the REV exists, which was addressed in early publications and remains as a topic of discussion. Clauser (1992) compiled data for the permeability of fractured rocks on three different scales: laboratory (1 to 10 centimeters), borehole (1 to 100 meters) and regional (1 to 100 kilometers); they show that permeability increases by orders of magnitude from laboratory to borehole scale, but this increase does not seem to hold from borehole scale to regional scale. Based on this, Neuman (1994) proposed a scaling law for permeability; he defends that statistical homogeneity for log permeability occurs intermittently over intervals of the scale spectrum; this corroborates what was stated in section 1.2.1 about the importance of defining a scale of study.

These investigations on the existence of a REV for the permeability of fractured media advanced with the development of numerical tools. Kulatilake and Panda (2000) affirm that an equivalent continuum is difficult to obtain for blocks containing persistent discontinuities, but this task is possible for rocks consisting mainly of minor discontinuities; they obtained the REV for some blocks in this second category and concluded that its size varies from 10 to 30 times the first invariant of the fracture tensor. Several other works could define a REV for permeability using deterministic or statistical approaches (e.g. Min et al., 2004a; Wang et al., 2018). Most of the conclusions were drawn under the assumption of constant aperture, but Baghbanan and Jing (2007) evaluated the REV size and the existence of a permeability tensor when heterogeneous aperture is considered. Their results show that, as the variance of aperture increases, the REV gets significantly larger and it becomes harder to obtain a proper equivalent permeability tensor.

2.4 Equations of the problem and simulation methods

As previously seen, numerical upscaling requires the resolution of the physical problem at the microscale, where it is assumed to be better known. The microscale problem of interest here is the coupled hydro-mechanical simulation of elastic and elastoplastic fractured media. The process of modeling the fractured REV involved decisions regarding the discretization schemes and coupling techniques.

Zero-thickness interface elements were selected to introduce the strong discontinuities in the problem and the Box method was selected for the discretization of the domain. These techniques will be presented in the following items; also, this Section presents the equations that describe the mass conservation of fluids and the equilibrium of momentum, as well as the resulting weak formulations for the selected discretization scheme. A final item dedicated to hydro-mechanical coupling presents the terms that couple the flux and mechanical models, reviews the existing coupling schemes and presents the coupling algorithm adopted in this work.

2.4.1 Fracture representation: DFNs and Interface Elements

Discrete Fracture Networks (DFNs) are computational models that explicitly represent the geometrical features of each fracture; they can be created from geological mapping, stochastic generation, geomechanical simulation or a combination of these approaches (Lei et al., 2017). Fractures are represented as straight lines or curves in 2D domains and as planar discs or polygons in 3D domains. In the stochastic approach, the geometrical attributes of each fracture are treated as variables and are randomly generated according to a best-fit probability distribution for data measured in the field. The location of the fractures is usually randomly attributed by using a Poisson process to generate their barycenters. Lei et al. (2017) point out that these assumptions may lead to unrealistic models that disregard patterns observed in the field such as clustering, curved and irregular fractures.

Discrete and continuous methods can incorporate DFNs to solve hydromechanical problems. For continuous methods such as the Finite Element Method (FEM), the most common available techniques to solve models with DFNs are the embedded discontinuity approaches, nodal enrichment (which is the basis of the extended FEM) and zero-thickness interface elements, also called lower-dimensional elements. The latter poses a challenge concerning remeshing when crack propagation is considered, so it is preferred for fixed discontinuities (Dias-Da-Costa et al., 2010).

Interface elements were introduced by Goodman et al. (1968) to capture strong discontinuities on mechanical elastic problems. Since then, new types of interface elements, as well as formulations that apply them to hydromechanical analyses (e.g. Segura and Carol, 2008; Pouya, 2015) were developed. Figure 2.7 illustrates triple-nodded interfaces, which are popular when fluid flow is considered. In hydromechanical simulations, displacements are evaluated at the top and bottom nodes, while fluid pressure is also evaluated at the middle

nodes. This allows the consideration of a pressure drop across the matrix-fracture interface as well as the longitudinal flow through the fracture.

The interface elements are created by duplicating the nodes at edges that contain fractures. The original and clone nodes have the same coordinates, so aperture is not explicitly represented, but is a property of the element that can be updated as deformations occur.

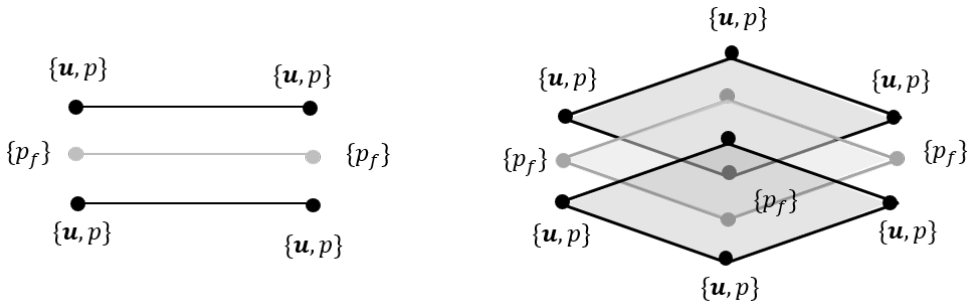

Figure 2.7: Triple-nodded interface elements for 2D (left) and 3D (right) problems: displacements ($\boldsymbol{u}$) are computed at the extremities and pressure (p_f) is also evaluated at the middle nodes.

2.4.2 Box Method

Helmig (1997) proposed the Box method, also called the Control Volume Finite Element Method, to combine the advantages of the FEM and of the finite volume method (FVM) to model fluid flow. From the FEM, it inherits the finite-element shape functions and the geometrical flexibility, since it can be applied on unstructured grids; from the FVM, it inherits the property of local mass conservation, which means that the mass of the fluids is conserved at the level of the elements.

The Box method is a type of vertex centered FVM, that is, the control volumes are built around the nodes of the primary FEM mesh. There are different methodologies to define the dual mesh; the control volume around a node can be defined by joining the cirscumcentres of the elements (Voronoi diagrams), by connecting the barycenters of adjacent elements with straight lines (centroid-dual grid) or by connecting the barycenters of the elements to the mid-points of their edges (median-dual grid). Figure 2.8 illustrates the median-dual method, which is the most flexible approach, since it supports different element shapes in two or three dimensions (Szymkiewicz, 2013). The control volumes (CVs) are constituted of subcontrolvolumes (SCVs) and are delimited by faces. At the faces, the pressure gradients are calculated using the finite element shape functions to compute the flux that enters or leaves the SCV. The configuration of the grid is such that velocity is continuous across the faces, while this is not true at the boundaries of the finite elements (Geiger et al., 2004); for that reason, the box method is locally conservative, and as other formulations of this type it is more accurate and more stable for the solution of flow at saturation fronts than the classical Galerkin FEM (Helmig, 1997).

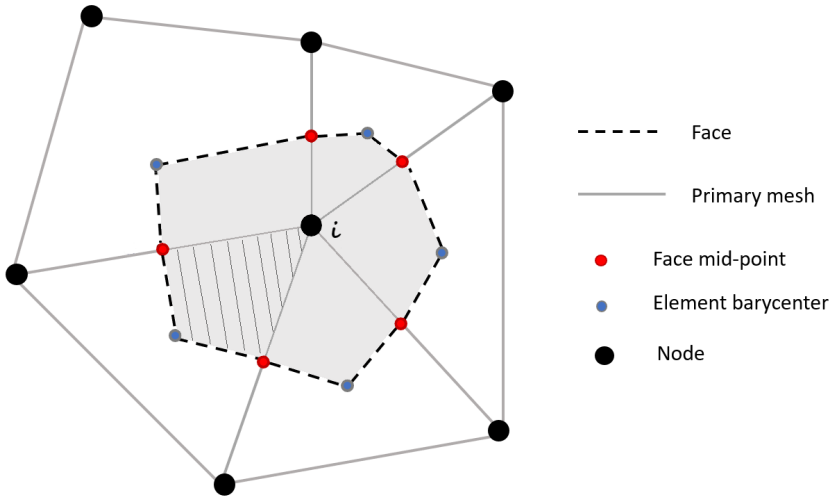

Figure 2.8: Creation of a control volume (in grey) around a node i in the primary mesh. The hatched area indicates a sub-control volume.

2.4.3 Equations of the problem and discretization

Considering a control volume B_i assigned to a node i, the primary variables a at a point P with coordinates $\boldsymbol{x}$ are approximated from the nodal values $\hat{a}$ using the shape functions N_j as:

$$\tilde{a}(\mathbf{x}) = \sum_{j \in \zeta_i} N_j(\boldsymbol{x}) \hat{a}_j \tag{2.37}$$

where $\tilde{a}(\mathbf{x})$ is the approximation of a, ζ_i is the set of nodes that belong to the finite element ξ for which $P \in \xi$. Similarly, the gradients of a at P are approximated by:

$$\nabla \tilde{a}(\boldsymbol{x}) = \sum_{j \in \zeta_i} \hat{a}_j \nabla N_j(\boldsymbol{x}) \tag{2.38}$$

The main procedures for discretization with the box method will be shown for the mass conservation equation of one fluid phase α:

$$\frac{\partial \Upsilon_\alpha}{\partial t} + \nabla \cdot (\rho_\alpha \mathbf{v}_\alpha) - q_\alpha = 0 \tag{2.39}$$

where Υ_α denotes the mass of the fluid per unit volume of the porous medium, and ρ_α and $\mathbf{v}_\alpha$ are the density and the velocity vector of the fluid and q_α is a source term. In (2.39), the first term is called the storage term, the second term is the flux term and the third term is the source term. The storage term can be further defined by:

$$\frac{\partial \Upsilon_\alpha}{\partial t} = \frac{\partial (\rho_\alpha S_\alpha \phi)}{\partial t} \tag{2.40}$$

where S_α is the degree of saturation of phase α and ϕ is the porosity of the medium.

The weak formulation of (2.39) is obtained with a weighted residual method, which means that the integral of (2.39) multiplied by a weighting function $W(\mathbf{x})$ must be equal to zero:

$$\int_\Omega \left(\frac{\partial \Upsilon_\alpha}{\partial t} + \nabla(\rho_\alpha \mathbf{v}_\alpha) - q_\alpha \right) W(\mathbf{x}) d\Omega = 0 \tag{2.41}$$

where Ω is the solution domain discretized in CVs. For the Box method, the weighting function $W_i(\mathbf{x})$ for a control volume B_i is:

$$W_i(\mathbf{x}) = \begin{cases} 1, & \text{if } x \in B_i \\ 0, & \text{if } x \notin B_i \end{cases} \tag{2.42}$$

After applying the Gauss theorem to the divergence operator in (2.41), we arrive at:

$$\int_\Omega \frac{\partial \Upsilon_\alpha}{\partial t} W(\mathbf{x}) d\Omega - \int_\Omega \rho_\alpha \mathbf{v}_\alpha \nabla W(\mathbf{x}) d\Omega + \int_\Gamma \rho_\alpha \boldsymbol{n} \cdot \boldsymbol{v}_\alpha W(\mathbf{x}) d\Gamma - \int_\Omega q_\alpha W(\mathbf{x}) d\Omega = 0 \tag{2.43}$$

where Γ is the boundary of domain Ω and $\mathbf{n}$ is the unit vector normal to Γ. From (2.42) it can be concluded that $\nabla W_i(\mathbf{x}) = 0$; thus, (2.43) can be reduced to the final weak formulation:

$$\int_\Omega \frac{\partial \Upsilon_\alpha}{\partial t} W(\mathbf{x}) d\Omega - \int_\Gamma \rho_\alpha \boldsymbol{n} \cdot \boldsymbol{v}_\alpha W(\mathbf{x}) d\Gamma - \int_\Omega q_\alpha W(\mathbf{x}) d\Omega = 0 \tag{2.44}$$

It can be observed in (2.44) that the flux is calculated at the boundaries of the control volume, i.e., the faces. Thus, during a certain time interval, the net volume of fluid that enters the CV through the faces must be balanced by the variation of fluid stored within the CV and an eventual source of flux. The integration of the flux term over a control volume B_i associated to node i is given by:

$$\int_{\Gamma_{B_i}} \rho_\alpha \mathbf{n} \cdot \mathbf{v}_\alpha W(\mathbf{x}) d\Gamma_{B_1} = \sum_{F \in B_i} |F| {\rho_\alpha}^{(f_c)} \mathbf{n}_F \cdot \tilde{\boldsymbol{v}}_\alpha{}^{(f_c)} \tag{2.45}$$

where F denotes a face, $\mathbf{n}_F$ is the unit outer normal to this face, and f_c denotes the face's mid-point, where velocity and unit weight are evaluated. And the integral of the storage term over B_i is approximated by:

$$\int_\Omega \frac{\partial \Upsilon_\alpha}{\partial t} W(\mathbf{x}) d\Omega = \sum_{V \in B_i} |V| \frac{\partial {\Upsilon_\alpha}^{(V)}}{\partial t} = \sum_{V \in B_i} |V| \frac{\partial}{\partial t} (\phi^{(V)} {S_\alpha}^{(i)} {\rho_\alpha}^{(i)}) \tag{2.46}$$

where V is a sub-control volume, $\phi^{(V)}$ is the porosity of V and ${S_\alpha}^{(i)}$ and ${\rho_\alpha}^{(i)}$ are the fluid's saturation and unit weight evaluated at node i.

This concludes the spatial discretization of 2.39 with the Box method, but the problem also requires discretization in time. Using a finite difference scheme, the solution of Equation 2.39 for a given control volume in a time step of size Δt that starts at time t assumes the

following general form:

$$\frac{\Upsilon_\alpha{}^{t+\Delta t} - \Upsilon_\alpha{}^{t}}{\Delta t} = F(a^{t+\theta\Delta t}) = F(\theta a^{t+\Delta t} + (1-\theta)a^t) \quad \text{with } 0 \leq \theta \leq 1 \tag{2.47}$$

where the source and flux terms are generalized as a function F of the variables a, which are evaluated at point $t + \theta\Delta t$ of the time step by interpolating between a^t and $a^{t+\Delta t}$. When $\theta = 0$, the temporal solution scheme is called explicit and the flux is evaluated using the solution of the previous time step. When $\theta = 1$, the scheme is fully implicit and the variables are evaluated at the end of the time step. Explicit schemes have the advantage of not requiring an iterative solution, but they are stable only until a certain time step size; on the other side, fully implicit schemes are unconditionally stable, but require an iterative linearization method (Zienkiewicz and Taylor, 2000). Alternatively, one can use partially implicit schemes, for which $0 < \theta < 1$. While this type of scheme has been shown to provide more accurate solutions than fully implicit solutions (Blunt and Rubin, 1992; Zienkiewicz and Taylor, 2000), they also allow for bigger time steps than the explicit scheme.

2.4.3.1 Formulation for fractures and coupling with the matrix domain

The Box method has been adapted to media containing fractures represented by lower-dimensional elements. Reichenberger et al. (2006) presented a Box formulation for two-phase flow in fractured media. Their method captures the possible discontinuity of the saturation of the non-wetting phase at the matrix-fracture interface, and thus accounts for the transfer of fluids caused by capillary non-equilibrium. For the pressure of the wetting phase, they make the common assumption of continuity, which makes their method invalid for blocking fractures, as was demonstrated in the benchmark applications proposed by Flemisch et al. (2018). This is a good assumption for a wide range of problems that deal with fractures that are more conductive than the porous medium; but, if the consideration of blocking fractures is needed, a simple solution is to use two-nodded or three-nodded interface elements, which can capture transverse pressure drops.

The mass conservation equation for the fractures is the following:

$$\frac{\partial(\Upsilon_{f\alpha} w)}{\partial t} + \frac{\partial(\rho_\alpha v_{l\alpha} w)}{\partial l} - q_{f\alpha} = 0 \tag{2.48}$$

where l is a local coordinate that is longitudinal to the fracture, $\Upsilon_{f\alpha}$ is the fluid mass per unit volume in the fracture, $v_{l\alpha}$ is the longitudinal component of the velocity of the phase α, $q_{f\alpha}$ is the source term and w is the fracture's effective aperture. The storage term can be defined as:

$$\frac{\partial(\Upsilon_{f\alpha} w)}{\partial t} = \frac{\partial(\rho_\alpha S_\alpha w)}{\partial t} \tag{2.49}$$

The spatial discretization of the flux term in 2.48 results in 2.45, with $|\digamma| = wZ$, being

Z the out-of-plane width of the face, usually considered equal to unity in bi-dimensional problems. Note in Figure 2.9 that the normal to a face $\digamma_f$ of the lower-dimensional element is colinear to the fracture; thus, the dot product $\mathbf{n} \cdot \mathbf{v}_\alpha$ in 2.45 returns v_l.

The spatial discretization of the storage term results in:

$$\int_{\Omega_f} \frac{\partial(\Upsilon_{f\alpha} w)}{\partial t} W(\mathbf{x}) d\Omega_f = \sum_{V_f \in C_i} |V_f| \frac{\partial \Upsilon_{f\alpha}{}^{(V_f)}}{\partial t} = \sum_{V_f \in C_i} |V_f| \frac{\partial}{\partial t} (w^{(V_f)} S_\alpha{}^{(i)} \rho_\alpha{}^{(i)}) \tag{2.50}$$

where Ω_f is the domain of lower-dimensional elements, C_i is a lower-dimensional control volume, V_f is a sub-control volume with surface area $|V_f| = ZL$, where L is the length of the lower-dimensional element and Z the out-of-plane width.

The introduction of a triple nodded element in the Box method is illustrated in Figure 2.9. The edges of the bulk elements that coincide with a fracture have their nodes duplicated and become faces where an exchange flux q_c is evaluated; as for the fracture, it is represented by a lower-dimensional element that contains the middle nodes illustrated in Figure 2.7. The flux q_c accounts for the fluid exchanges between the porous matrix and the fractures. Assuming Darcian flow, the flux from a face $\digamma$ of a bulk control volume B_i to a sub-control volume V_f of the middle lower-dimensional element is given by:

$$q_c = |\digamma| \rho_\alpha{}^{(f_c)} \boldsymbol{n}_\digamma \cdot \tilde{\boldsymbol{v}}_\alpha^{(f_c)} = |\digamma| \rho_\alpha \frac{k_t}{\mu_\alpha} \boldsymbol{n}_\digamma (\nabla \tilde{p}^{(f_c)} - \rho_\alpha{}^{(f_c)} \boldsymbol{g}) \tag{2.51}$$

where $\boldsymbol{g}$ is the gravity vector, k_t is the fractures transversal permeability, μ_α is the fluid's viscosity and the pressure gradient ∇p is given by:

$$\nabla \tilde{p}^{(f_c)} = \frac{\tilde{p}_f^{(v_c)} - \tilde{p}_m^{(f_c)}}{0.5 w^{(f_c)}} \boldsymbol{n}_\digamma \tag{2.52}$$

where f_c and v_c denote the mid-points of $\digamma$ and V_f, w is the facet's aperture, p is the pressure and the subscripts m and f refer to the matrix and the facet domains, respectively. For the matrix domain, q_c corresponds to a flux term, since it is evaluated at the CVs faces. For the facet domain, it is a source term, since it is integrated over a SCV.

2.4.3.2 Formulation of the mechanical problem

Box method can also be applied to discretize the equilibrium equation, given by:

$$\nabla \cdot \boldsymbol{\sigma} + \boldsymbol{b} = 0 \tag{2.53}$$

where $\boldsymbol{\sigma}$ is the total stress tensor and $\boldsymbol{b}$ is the body force vector. The procedure detailed in this section leads to the following weak formulation for the Box method:

$$\int_\Gamma \mathbf{n} \cdot \boldsymbol{\sigma} W(\mathbf{x}) d\Gamma + \int_\Omega \boldsymbol{b} W(\mathbf{x}) d\Omega = 0 \tag{2.54}$$

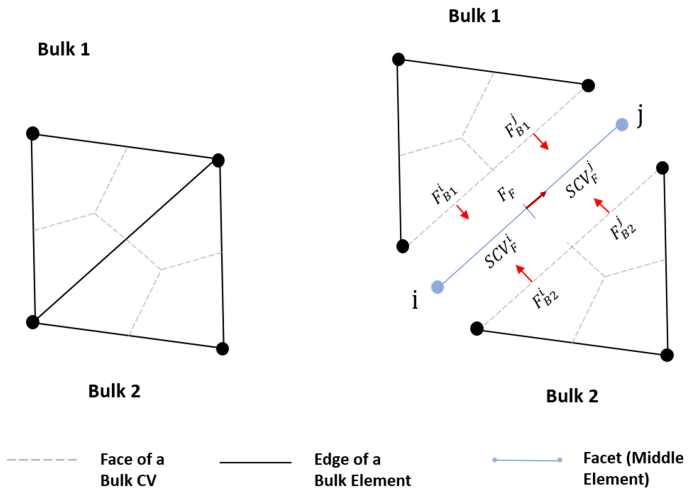

Figure 2.9: Finite volume discretization for adjacent elements with no fractures (left) and with a fracture between them (right). The fracture is represented by a lower-dimensional middle element (facet) and bulk nodes are duplicated to achieve the form of a three-noded interface element.

Thus, similarly to the velocity in (2.44), the stresses are evaluated at the faces and then integrated to compute the corresponding forces. For a control volume B_i, (2.54) leads to:

$$\sum_{F \in B_i} |F| \mathbf{n}_F \cdot \boldsymbol{\sigma} + \sum_{V \in B_i} |V| \boldsymbol{b} = 0 \tag{2.55}$$

When interface elements are introduced to solve problems in fractured media, a configuration similar to the one illustrated in Figure 2.9 is set, with the exception that the lower-dimensional middle element is not used. At the faces that coincide with a fracture, there is an acting traction $\boldsymbol{t_c}$ given by:

$$\boldsymbol{t_c} = \boldsymbol{n} \cdot {\boldsymbol{\sigma'}_c}^{(f_c)} \tag{2.56}$$

If the fractures are elastic, the effective stresses ${\boldsymbol{\sigma'}_c}^{(f_c)}$ are evaluated at the face's midpoint f_c and depend on the displacement discontinuities in the following manner:

$$\boldsymbol{\sigma_c}^{(f_c)} = \begin{pmatrix} \sigma_n \\ \sigma_t \end{pmatrix} = \begin{pmatrix} K_n & K_{nt} \\ K_{nt} & K_t \end{pmatrix} \begin{pmatrix} [\![u_n]\!] \\ [\![u_t]\!] \end{pmatrix} \tag{2.57}$$

where σ_n is the normal stress, σ_t is the shear stress, $[\![u_n]\!]$ and $[\![u_t]\!]$ are the normal and shear displacement jumps across the interface, K_n and K_t are the normal and shear stiffnesses of the fracture and K_{nt} accounts for the fracture's dilation. Considering a face F_1 sharing the evaluated fracture with a face F_2 that belongs to a different bulk element, the displacement jump vector is given by:

$$[\![\boldsymbol{u}]\!] = \boldsymbol{u}^{(f_{c1})} - \boldsymbol{u}^{(f_{c2})} \tag{2.58}$$

where f_{c1} and f_{c1} denote the locations of the mid-points of Γ_1 and Γ_2, respectively. The displacements are interpolated at these locations using their nodal values and the finite element shape functions (Equation 2.38). Note that the Equation 2.57 provides a general form of coupling two bulk elements when there is a strong discontinuity between them. The specificity of the Box Method is the location of the evaluation of the displacement jumps and stresses.

2.4.4 Hydromechanical coupling

The resulting pressure fields from fluid percolation affect the acting stresses and strains on the domain and vice-versa. To account for this inter-dependency, hydromechanical coupling can be introduced to the fluid flow and equilibrium problems by adding coupling terms to Equations (2.39),(2.48) and (2.53).

In the equilibrium equation (2.53), the pressure fields are introduced by means of the effective stress principle, which, considering tension to be positive and compression to be negative, is given by:

$$\boldsymbol{\sigma} = \boldsymbol{\sigma}' - bp\boldsymbol{\delta} = \boldsymbol{C} : \boldsymbol{\varepsilon} - bp\boldsymbol{\delta} \tag{2.59}$$

for the matrix domain, where $\boldsymbol{\sigma}$ is the total stress tensor, $\boldsymbol{\sigma}'$ is the effective stress tensor, p is the pore pressure, $\boldsymbol{C}$ is the stiffness constitutive tensor, $\boldsymbol{\varepsilon}$ is the matrix strain tensor and b is the matrix Biot's coefficient, defined by:

$$b = 1 - \frac{K_{dr}}{K_s} \tag{2.60}$$

where K_{dr} is the material's bulk drained modulus and K_s is the bulk modulus of the solid grains.

For the fracture domain, the effective stress principle can be written as:

$$\boldsymbol{\sigma} = \boldsymbol{\sigma}' - b_f p\boldsymbol{m} = \boldsymbol{C_f}.[\![\boldsymbol{u}]\!] - b_f p\boldsymbol{m} \tag{2.61}$$

where $\boldsymbol{m} = (1\ 0)$, $\boldsymbol{C_f}$ is the fracture constitutive tensor defined in (2.57) and b_f is the fractures Biot's coefficient. The second terms in (2.59) and (2.61) are the coupling terms of the equilbrium equation.

The mechanical effects in the fluid mass conservation manifest in the storage terms (2.40) and (2.49). For the matrix, the variation in porosity $d\phi$ is a function of the volumetric strain variation $d\boldsymbol{\varepsilon}_v$:

$$d\phi = bd\boldsymbol{\varepsilon}_v + \frac{1}{M}dp \tag{2.62}$$

The Biot's modulus M defines the ratio of the fluid volume variations to pore pressure; it considers the compressibility of the fluid and of the solid grains:

$$\frac{1}{M} = \frac{\phi}{K_f} + \frac{b - \phi_0}{K_s} \tag{2.63}$$

where ϕ is the porosity and K_f is the fluid's bulk modulus.

The first term in (2.62) is related to the deformation of the porous matrix and thus it depends directly on the displacements of the domain, since:

$$\boldsymbol{\varepsilon}_v = tr(\boldsymbol{\varepsilon}) = tr(\frac{1}{2}(\nabla \otimes \boldsymbol{u} + (\nabla \otimes \boldsymbol{u})^T)) \tag{2.64}$$

For the fractures domain, the aperture variation dw to be considered in (2.49) can similarly be defined as:

$$dw = b_f d[\![u_n]\!] + \frac{w}{M_f} dp_f \tag{2.65}$$

where b_f and M_f are the Biot's coefficient and module for the fractures, dp_f is the fracture pressure variation and $d[\![u_n]\!]$ is the variation in the normal displacement jump $[\![u_n]\!]$ across the discontinuity, which is a component of the vector $[\![\boldsymbol{u}]\!]$. The Biot's coefficient and Biot's modulus of a discontinuity depend on the roughness of the surface, the stress state and the filling material, but for clean discontinuities b_f can be assumed to be equal to unity and M_f equal to the inverse of the fluid compressibility multiplied by the aperture (Segura and Carol, 2008).

The volumetric strains and normal displacement jumps can also be defined in terms of volumetric stress σ_v and pore pressure p with the following relationships:

$$K_{dr}\boldsymbol{\varepsilon}_v = \sigma_v + bp \tag{2.66}$$

$$K_n[\![u_n]\!] = \sigma_v + b_f p_f \tag{2.67}$$

where the subscript f indicates the fractures domain, K_{dr} is the drained bulk modulus and K_n is the fractures normal stiffness. A second type of dependency of the fluid flow on the mechanics is usually introduced in (2.48) by defining the matrix intrinsic permeability as a function of the porosity (for example, the well known Kozeny-Karman equation) and the fractures intrinsic permeability k_f as a function of aperture. This latter function is usually the cubic law:

$$k_f = \frac{w^2}{12} \tag{2.68}$$

2.4.4.1 Coupling strategies

The coupling between the hydraulical and mechanical problems on fractured media is fully established by relationships (2.59), (2.61), (2.62), (2.64) and (2.65). These terms introduce displacements to (2.39) and (2.48) and pore pressures to (2.53). The resulting system of equations can be solved numerically with different coupling strategies, which can be categorized as fully coupled or partially coupled. Figure 2.10 presents the main existing coupling schemes using the nomenclature that is the most common in reservoir simulation.

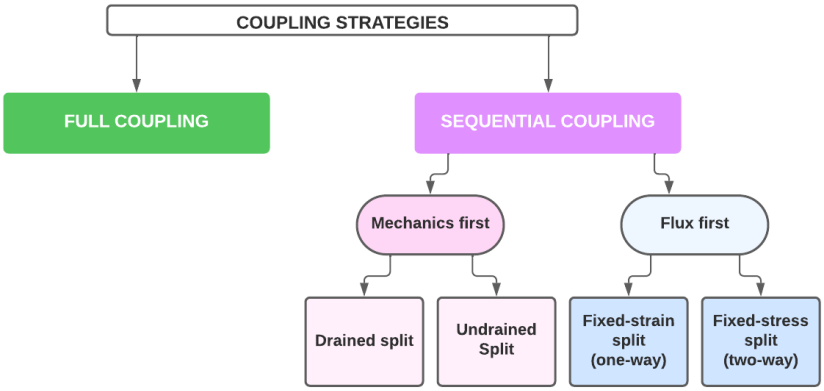

Figure 2.10: Coupling strategies used in reservoir simulation.

In a fully coupled approach, the flow and mechanical equations are solved as a monolithic system, while partially coupled approaches consist in solving them separately and sequentially. Among the partial coupling schemes, a first differentiation can be made regarding which equation is solved first within a time step. The two main schemes for which geomechanics is solved first are the drained split and undrained split. The strategies where flux is solved first can be generally defined as fixed-strain split and fixed-stress split. The fixed-strain split and drained split are types of one-coupling, which means that only one of the equations is influenced by the results of the other. As for the undrained split and the fixed-stress split, they are types of two-way coupling, where both the mechanical and the flow equations receive information from one another. The focus of this review are the strategies where flux is solved first for two main reasons. Firstly, because among the one-way coupling schemes, the fixed-strain split is the one to be usually employed in reservoir simulation. And secondly, because the fixed-stress split is more stable and converges faster that the other coupling schemes(Kim et al., 2011). From now on, the terms one-way coupling and two-way coupling will be used as synonyms for the fixed-strain and the fixed-stress splits, respectively.

In a one-way coupling scheme, the pore pressures obtained from the flux model are introduced into the stress equations, but mechanical effects due to the volumetric strains are not considered in the flux model. The flow chart for one-way coupling is described in Figure 2.11: for a given time step, the flow equation is solved first (assuming a fixed solid

skeleton); next, the resulting pore pressures are used to compute stress variations; then, the equilibrium problem is solved and the solution proceeds to the next time step.

In a two-way coupling or fixed-stress split scheme, both the flow and the geomechanical models transmit information to each other, as showed in the flow chart of Figure 2.11. The time step starts by solving the flow equation with consideration of the strains obtained from the previous solution of the mechanical problem. These strains are used to compute the storage terms and permeabilities. Then, the resulting pore pressures are used to solve the equilibrium equation. If this process is done repeatedly within a time-step until a convergence criterion for the displacements and forces is reached, the process is called an implicit two-way coupling. If each equation is solved only once for each time step, the two-way coupling is called explicit.

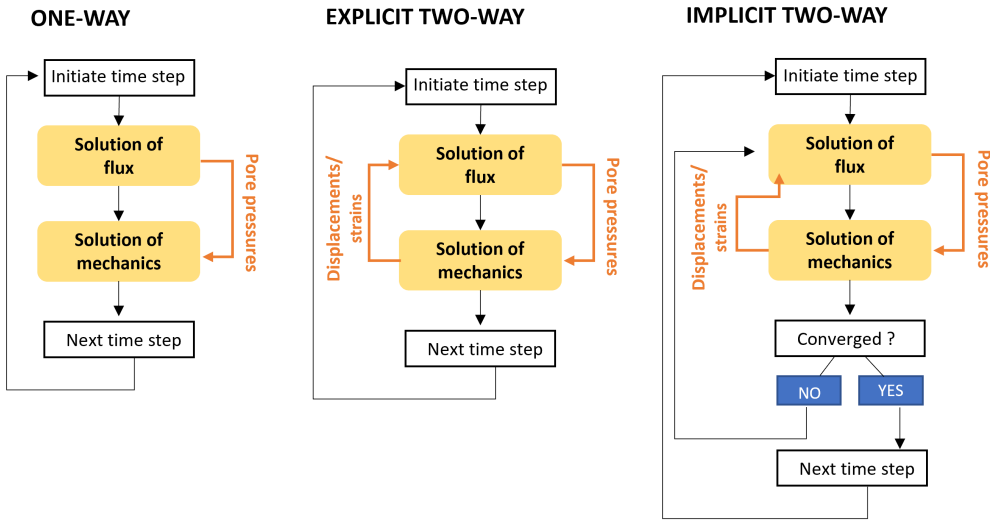

Figure 2.11: Algorithms of the one-way, explicit two-way and implicit two-way coupling schemes.

Several studies compare the existing coupling schemes for features such as stability, convergence properties, accuracy and computation time (e.g. Kim et al., 2011; Dean et al., 2013; Preisig and Prevost, 2011; Beck et al., 2020). The full-coupling is unconditionally stable and highly accurate (Kim et al., 2011); however, its implementation is more complex, since the need for an unified simulator for flow and mechanics compromises the modularity of the code and the derivation of the coupling terms for complex models can be cumbersome. Also, full coupling may be associated to spurious oscillations when an equal-order approximation is used for the pressures and displacements, which requires solutions like the use of different discretization schemes for the coupled problems (Beck et al., 2020).

Kim et al. (2011) made a comprehensive comparative study of the partial coupling approaches. Using examples of fluid injection and production in elastic media, they showed that the two-way coupling is unconditionally stable, converges with fewer iterations than other schemes and is accurate. On the other side, one-way coupling is only conditionally

stable and the literature on the subject shows that it may fail in providing accurate results for all steps of the simulation. For example, Preisig and Prevost (2011) showed that the one-way coupling was not capable of reproducing the analytic solution of the Mandel problem (Mandel, 1953); and, in the study case of CO_2 injection in a reservoir, the one-way coupling underestimated the lateral extent of the uplift dome by up to 30 %, when compared to a full coupling. Also using the full coupling as a reference solution, Beck et al. (2020) simulated the injection of CO_2 in a heterogeneous faulted reservoir using implicit and explicit two-way coupling. The explicit coupling underestimated the pressures close to the injection point and predicted the arrival of the gas to the fault 50 days later than the full-coupling. On the other hand, the implicit scheme was shown to converge to the fully coupled solution after a few iterations.

When it comes to computation time, it is not obvious which coupling strategy is more efficient. It is common to think of the full coupling as more demanding, since it requires the solution of a larger system and the time required by conventional solvers is known to be proportional to the square of the system's size (Beck et al., 2020). However, as the full coupling is unconditionally stable, it can be used with bigger time steps than one-way coupling and explicit schemes to provide a similar or better accuracy. As for the implicit two-way coupling, it may be slower than fully coupled solutions when convergence is only reached after a high number of iterations, which can happen if the coupling between the problems is very strong (Segura and Carol, 2008).

Since the analysis of efficiency also takes accuracy into consideration, one-way coupling should be avoided or used with caution. As for the full coupling and two-way coupling, on the other hand, they have similar properties of accuracy and stability, and there is no general rule to define which one is faster, since this depends on the problem. So, the coupling strategies used in this work were selected according to what is more convenient in terms of code implementation and simplicity of the solution algorithms. For the coupled problem at the REV scale, the two-way coupling or fixed-stress split was selected; the algorithm is presented below. Regarding the macroscale, a full-coupling is adopted; the solution of this monolithic system is described in Chapter 7.

2.4.4.2 Fixed-stress split

Using Equations 2.46, 2.47, 2.50, and considering one-phase flow and a fully implicit time discretization, that is, $\theta = 1$, the general discrete forms of the mass conservation equations for a time step of size Δt that starts at time t and finishes at time $t + 1$ are:

$$\frac{\phi^{t+1}\rho^{t+1} - \phi^t\rho^t}{\Delta t} = F(p^{t+1}) \tag{2.69}$$

for the matrix domain, and:

$$\frac{w^{t+1}\rho^{t+1} - w^t\rho^t}{\Delta t} = F({p_f}^{t+1}) \tag{2.70}$$

for the fracture domain.

The functions F are a general representation of the flux and source terms combined. The hydro-mechanical coupling may appear in these terms if the permeabilities and/or fluid densities are solution-dependent. The subscript f denotes the fracture domain, and although these equations are presented separately, they are solved altogether and coupled by the exchange flux in (2.51).

The coupling terms (2.62) and (2.65) are used to update the porosity and aperture variations at a new iteration k:

$$d\phi^{k,t} = \frac{dp^k}{M} + bd\varepsilon^k = \frac{p^{k,t} - p^{k-1,t}}{M} + b(\varepsilon^{k,t} - \varepsilon^{k-1,t}) \tag{2.71}$$

$$dw^{k,t} = \frac{dp_f{}^k}{M_f} + b_f du_n{}^k = \frac{p_f{}^{k,t} - p_f{}^{k-1,t}}{M_f} + b_f(u_n^{k,t} - u_n^{k-1,t}) \tag{2.72}$$

In a fixed-stress split, the coupled problems are solved sequentially and, since the flux is solved first, $\varepsilon^{k,t}$ and $u_n^{k,t}$ can not be obtained from the solution of the mechanical problem. Thus, $d\varepsilon^k$ and $du_n{}^k$ are replaced by the predictor estimators $\hat{d\varepsilon}^k$ and $\hat{du_n}^k$. Using Equations 2.66 and 2.67, these estimators are related to changes in volumetric stress ($d\sigma_v$) and pore-pressures (dp) by:

$$K_{dr}\hat{d\varepsilon}^k = \sigma_v^k - \sigma_v^{k-1} + b(p^k - p^{k-1}) \tag{2.73}$$

$$K_n\hat{du_n}^k = \sigma_v^k - \sigma_v^{k-1} + b_f(p_f{}^k - p_f{}^{k-1}) \tag{2.74}$$

The fixed-stress split, as the name suggests, consists in enforcing volumetric total stress conservation to solve the flux problem, that is, $\sigma_v^k - \sigma_v^{k-1} = 0$. Thus, estimators $\hat{d\varepsilon}^k$ and $\hat{du_n}^k$ read:

$$\hat{d\varepsilon}^k = \frac{b(p^k - p^{k-1})}{K_{dr}} \tag{2.75}$$

$$\hat{du_n}^k = \frac{b_f(p_f{}^k - p_f{}^{k-1})}{K_n} \tag{2.76}$$

and Equations 2.71 and 2.72 become:

$$\hat{d\phi}^{k,t} = (\frac{1}{M} + \frac{b^2}{K_{dr}})(p^{k,t} - p^{k-1,t}) \tag{2.77}$$

$$\hat{dw}^{k,t} = (\frac{1}{M_f} + \frac{b_f{}^2}{K_n})(p_f{}^{k,t} - p_f{}^{k-1,t}) \tag{2.78}$$

The adequate bulk modulus K_{dr} depends on the problem and will determine how efficient is the convergence of the solution (Kim et al., 2011). For one-dimensional poroelastic

problems, the optimal choice is the uniaxial drained bulk modulus ${K_{dr}}^{(1D)}$:

$$ {K_{dr}}^{(1D)} = \frac{E(1-\nu)}{(1+\nu)(1-2\nu)} \tag{2.79} $$

where E is the Young's modulus and ν is the Poisson's ratio. For two-dimensional plane strain problems, the most adequate choice is the bulk drained modulus ${K_{dr}}^{(2D)}$:

$$ {K_{dr}}^{(2D)} = \frac{{K_{dr}}^{(1D)}}{2(1-\nu)} \tag{2.80} $$

In elasto-plasticity, if the material is yielded, the tangent modulus ${K_{dr}}^{(ep)}$ is evaluated from the elastoplastic constitutive matrix $\boldsymbol{D}_{ep}$ (Kim et al., 2011):

$$ \frac{1}{{K_{dr}}^{(ep)}} = \frac{1}{4}\mathbf{1}^T \boldsymbol{D}_{ep} \mathbf{1} \tag{2.81} $$

where, for plane-strain conditions, $\boldsymbol{D}_{ep}$ has dimensions 3 x 3 and $\mathbf{1} = \{1\ 1\ 0\}$. The iterative nature of the fixed-stress split comes from the difference in the calculated volumetric strains and apertures between the coupled problems: in the lack of the updated displacements vector, the flow model uses the predictor estimators, which are then corrected by the solution of the geomechanical model. The fixed-stress split coupling algorithm for a time step t is the following:

1. Time step initialization: For the first iteration $k = 1$, set the previous pressures $p^{k-1,t}$ and displacements $\boldsymbol{u}^{k-1,t}$ as those from the last time step:

$$ \boldsymbol{p}^{k-1,t} = \boldsymbol{p}^{t-1}, \text{ k = 1} \tag{2.82} $$

$$ \boldsymbol{u}^{k-1,t} = \boldsymbol{u}^{t-1}, \text{ k = 1} \tag{2.83} $$

2. Solve the flow equations by using estimators in (2.77) and (2.78) to update the porosities ${\phi_{flow}}^{k,t}$ and apertures ${w_{flow}}^{k,t}$ as:

$$ {\phi_{flow}}^{k,t} = {\phi_{flow}}^{k-1,t} + d\hat{\phi}^{k,t} \tag{2.84} $$

$$ {w_{flow}}^{k,t} = {w_{flow}}^{k-1,t} + d\hat{w}^{k,t} \tag{2.85} $$

3. Using the resultant pressures $\boldsymbol{p}^{k,t}$ in the computation of stresses with (2.59) and (2.61), solve the mechanical problem for the displacements $\boldsymbol{u}^{k,t}$.

4. Update the volumetric strains $\varepsilon^{k,t}$ and displacement jumps $[\![\boldsymbol{u}]\!]^{k,t}$.

5. Update the porosities ${\phi_{mech}}^{k,t}$ and apertures ${w_{mech}}^{k,t}$ for the geomechanics model:

$$ {\phi_{mech}}^{k,t} = \phi^{t-1} + \frac{1}{M}(p^{k,t} - p^{t-1}) + b(\varepsilon^{k,t} - \varepsilon^{t-1}) \tag{2.86} $$

$$ {w_{mech}}^{k,t} = \frac{1}{M_f}({p_f}^{k,t} - {p_f}^{k-1,t}) + b_f({u_n}^{k,t} - {u_n}^{k-1,t}) \tag{2.87} $$

6. Set ${\phi_{flow}}^{k,t} = {\phi_{mech}}^{k,t}$. Given a threshold ε_{tol}, proceed to the next time step if:

$$ \frac{\|\boldsymbol{p}^{k,t} - \boldsymbol{p}^{k-1,t}\|}{\|\boldsymbol{p}^{k,t}\|} \leq \varepsilon_{tol} \tag{2.88} $$

and

$$ \frac{\|\boldsymbol{u}^{k,t} - \boldsymbol{u}^{k-1,t}\|}{\|\boldsymbol{u}^{k,t}\|} \leq \varepsilon_{tol} \tag{2.89} $$

Otherwise, begin a new iteration $k+1$, starting from step 2 .

As the convergence of the displacements and pressures vectors is approached, the differences between the calculated porosities and apertures for the flow and mechanics models vanish to zero and should approach the results of a fully coupled solution.

2.5 Conclusions of the chapter

The REV is a sample that must be large enough to well represent the heterogeneities and the average constitutive behavior of a material; at the same time, it must be small enough to respect the principle of separation of scales. The homogenization of the REV is based on the volume average of the problem's variables and on the respect of energy consistency conditions.

The theoretical review of this chapter focused on the geometrical and hydro-mechanical REVs of fractured media. A useful quantity to verify if the geometry of the fracture network is properly represented is the crack tensor, which is known to be related to the constitutive behavior of fractured rock masses; as for the hydro-mechanical properties, they can be assessed by means of numerical experiments, which can be performed using different kinds of boundary conditions.

In this work, the numerical modeling of the REV aims the solution of two equations: the equilibrium of momentum and the mass conservation of the fluid. The Box method was selected to solve these problems, combined with lower-dimensional interface elements to discretize the fractures. The fixed-stress split was selected to promote the coupling between both problems; this is a sequential coupling technique known to be accurate and stable, while it also maintains the flexibility and easy maintenance of codes.

The computational tool used to perform the simulations is an open-source code to which major additions were made. The code and its validations are presented in the next chapter.

Chapter 3

Computational tool: DuMu^X 3

DuMu^X (Koch et al., 2020) is a free and open-source simulator for flow and transport in porous media. It is based on the Distributed Unified Numerics Environment (DUNE), a toolbox for solving partial differential equations with grid-based methods. Both codes are written in C++. DuMu^X possesses a modular design that takes advantage of well-known principles for objected-oriented design, modern C++ features and generic programming techniques.

Thanks to that, the code is very flexible and easily extensible. The problems are built by combining the existing modules and the objects are instantiated at compile-time based on tags defined by the user. For example, a mandatory definition is the spatial discretization method, which can be a variety of cell-centered schemes and the Box, if the tag `BoxModel` is used. As a consequence of this choice, the classes used for the creation of the finite volume (FV) mesh, the calculation of residuals and other procedures that depend on the discretization scheme are specialized for the chosen method.

This chapter presents the main features of DuMu^X, with focus on solutions with the Box method. The Box was chosen for its mesh flexibility and for being the only technique available in DuMu^X that can be used to solve mechanical problems. If the Box is used, the original code allows for the solution of stress-strain problems on domains constituted of elastic materials. To attain the objectives of this thesis, five major additions were made to the code: the inclusion (i) of methods to handle elastoplastic analyses, (ii) of strong discontinuities to geomechanical problems, (iii) of new coupling manager classes that handle the hydro-mechanical coupling in domains with interfaces, (iv) of new classes to impose periodic boundary conditions, and (v) an entire new module for multiscale simulations.

3.1 Modules

The original modules in DuMu^X handle all the steps for the solution of multi-phase, multi-component and multi-domain flow and geomechanics, among others. The main dependencies on DUNE are related to the primary mesh generation, the elements shape functions and the linear algebra operations. The most relevant modules are described below:

- **Module** `IO`: contains the classes that manage the instantiating of grid entities (nodes, elements and boundaries) and handles the creation of output files.
- **Module** `Common`: contains geometry-related methods and the definition of properties that are common to all kind of problems.
- **Module** `Discretization`: contains the classes where the FV mesh is created according to the selected discretization method. Also, this module manages the grid variables.
- **Module** `Material`: contains the classes that handle the spatial distribution and definition of material properties.
- **Module** `Flux`: contains classes used to calculate flux or stress according to a number of constitutive laws and the chosen discretization method. The sub-module Box includes a class that computes flux with Darcy's law (BoxDarcysLaw), a class that computess stress with the Hooke's law (HookesLaw) and a class that computes effective stresses (EffectiveStressLaw).
- **Module** `Material` **Porous Medium Flow**: contains classes that handle the computation of volume residuals for a given CV. Also, it contains the base class for flow problems.
- **Module** `Geomechanics`: contains the classes that handle the computation of force residuals for a given CV. Also, it contains the base class for geomechanical problems.
- **Module** `Linear`: handles the solution of linear systems.
- **Module** `Non Linear`: handles the solution of non-linear systems with Newton's method.
- **Module** `MultiDomain`: handles the coupling of multiple domains. The sub-module Facet is of interest to this thesis. Facet is the designation employed for lower-dimensional elements that occur at the edges of bulk elements. This sub-module contains classes that are in charge of the mapping and coupling of the facets and their adjacent bulk elements. Also, this module handles the assembly of the system for multi-domain problems. For fractured media, the term multi-domain problem refers to the solution of two overlapping and coupled domains: the porous matrix domain, with elements of dimension d and the fractures domain, formed by elements of dimension $d-1$ called facets.

3.1.1 Design of a Multi-Domain Flux Problem

The steps to build a multi-domain flow simulation in DuMu^X are illustrated in Figure 3.1. This workflow is also applicable to the definition of problems containing only one domain if the steps 6 and 9 are removed; those are specific to multi-domain problems.

The definition of the model starts by setting a combination of tags for each sub-domain. Besides the tags for the definition of the spatial discretization method, DuMu^X contains tags to define the type of flow, for example one-phase or two-phase. Several properties are automatically defined from these tags. The steps 2 and 3 require the user to create classes to handle the spatial parameters, where constitutive models are defined, and to create classes to configure the problem, where initial values and boundary conditions are set. DuMu^X allows for boundary conditions and material properties to be solution-dependent.

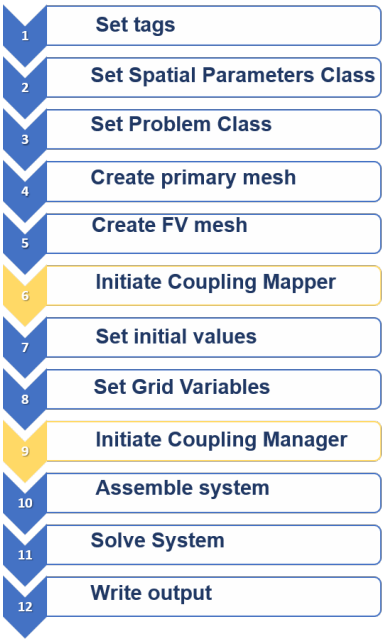

Figure 3.1: General workflow for the definiton of a flow simulation in DuMu^X. The steps in yellow are specific to multi-domain problems.

The primary mesh (step 4) is created by DUNE dependencies and the FV grid is created by defining control volumes as illustrated in Figure 2.8, if the Box Method is chosen. A particularity of the multi-domain problems is the initiation of the coupling mapper (step 6), which is responsible for tracking the correspondences between bulk elements and their adjacent facets and for storing these information. Also, this class is responsible for duplicating the nodes at the edges of bulk elements that coincide with facets. With this procedure, the configuration of interfaces that contain facets is similar to the one in Figure 2.7, where the facets contain the middle nodes of a triple-nodded interface element.

The process used by DuMu^X to duplicate nodes is illustrated in Figure 3.2. If the fracture does not terminate at a boundary of the domain, no new node is created at the tip (a and b), but only at the intermediary nodes; otherwise the node at the tip is duplicated (c). The changes in the elements connectivities are illustrated for a node that: (a) is intercepted by one fracture, (b) is intercepted by several fractures and (c) is at the boundary of the domain. This separation between two adjacent elements prevents pressure from being continuous across the edge they used to share. Since the configuration of the CVs is different when two

bulk elements have a facet between them (Figure 2.9), they are decoupled from each other and instead are coupled to the facet between them.

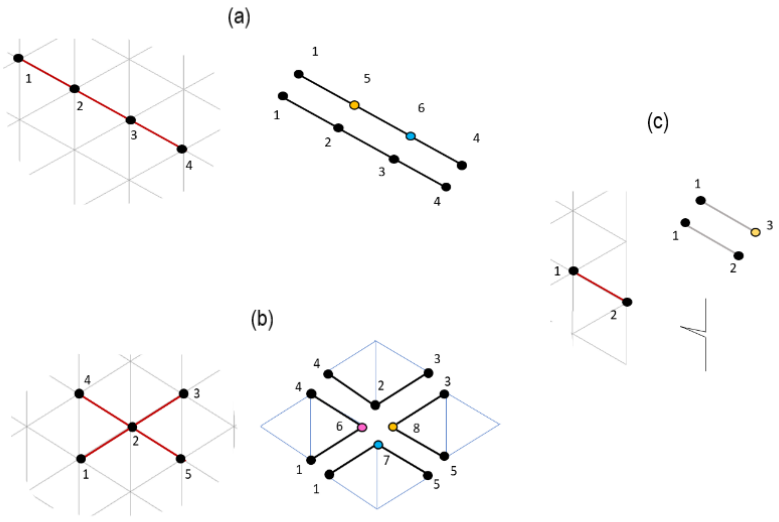

Figure 3.2: Duplication of nodes and change of connectivity for surrounding bulk elements in three possible scenarios: a) one fracture b) several intercepting fractures c) fracture at the boundary of the domain (Loyola et al., 2021).

The so-called grid variables include the solution of the problem, the gradient of the shape functions and other variables that are associated to the grid entities. After their initiation (step 8), multi-domain problems require the Coupling Manager to be set (step 9). The Coupling Manager couples the grid variables of the facets and the corresponding bulk elements. At an edge that contains a fracture, the mid-point of a bulk face corresponds to the mid-point of a sub-control volume of the adjacent facet (Figure 2.9). The variables at these points are associated by the coupling manager to calculate, using Equation 2.51, the flux q_c (red vector in Figure 2.9) that couples both domains.

The assembly of the system (step 10) includes the assembly of the residual vector and of the Jacobian matrix using implicit or explicit schemes. The residuals are calculated element by element and the Jacobian for each subdomain is computed with a classical perturbation method by using forward, backward or central finite differences. The final system for flow models in fractured media has size $n_f + n_m$, where n_f is the number of degrees of freedom in the facet domain and n_m is the number of degrees of freedom in the matrix domain.

The system is solved using the Newton-Raphson method (step 11) and the results can be written in an output file in VTK format (step 12).

3.1.2 Extensions to the original code

The extensions made to the original code of version 3.2 of DuMu^X incorporate two new possibilities for geomechanical models: elastoplastic analyses and interface elements.

Elastoplastic analyses:

To include elastoplastic behaviour in the analyses, the following additions are required: a return function to correct the elastic stress trials; the storage of the previous stress state for each integration point; functions to calculate stress invariants; a class for plastic parameters and plastic constitutive models.

For that, the new classes described in Figure 3.3 were created. Some of them inherit from existing DuMu^X classes. The new base classes `FVSpatialParamsPlastic` and `FVSpatialParamsPoroPlastic` inherit from the spatial parameters classes for elastic and poroelastic models. Additionally to the functions that return elastic parameters and models, there are new functions that return the yield function, the flow function and the normal vectors to the yield and flow function surfaces. Also, a perfectly plastic isotropic Mohr-Coulomb model was added as class `MohrCoulomb`. Both associated and non-associated plastic flow are supported. For simplicity, this model will be called only Mohr-Coulomb from now on; it is the only plastic model added to DuMu^X so far.

The plasticity-related functions depend on the current stress state. DuMu^X does not store stresses from a previous step to calculate the next one. This functionality was added by creating the class `StressHistoryCache`, which inherits from `StressVariablesCache`, a class that manages grid variables in elastic problems. The class `StressHistoryCache` has a function that allows the stress vector to be stored for each integration point. This update must be made by the user at the end of each time step. Also, three new classes were added to calculate stress invariants.

Finally, the template class `PlasticCorrection` was added to calculate the elastic stress trials using the existing classes for elastic problems and return them to the yield function, if necessary, using the new class `ReturnAlgorithm`. This latter is a template class containing two specializations; one for the Mohr-Coulomb model, where the two-vector return algorithm proposed by Crisfield (1987) is implemented, and the other for plastic models that do not contain singularities, which is empty. So, the current code does not support other models than Mohr-Coulomb, but can be easily extended to do so. Two new tags that are associated with the new classes were added for elastoplastic problems: `Plastic`, which can be used for purely mechanical problems, and `Poroplastic`, which incorporates pore pressures in the calculations of stresses using the effective stress principle. The modifications described here essentially change the way of calculating force residuals, which are based on corrected stresses when plasticity-related tags are used. Thus, they mainly affect the step 10 of the workflow in Figure 3.1.

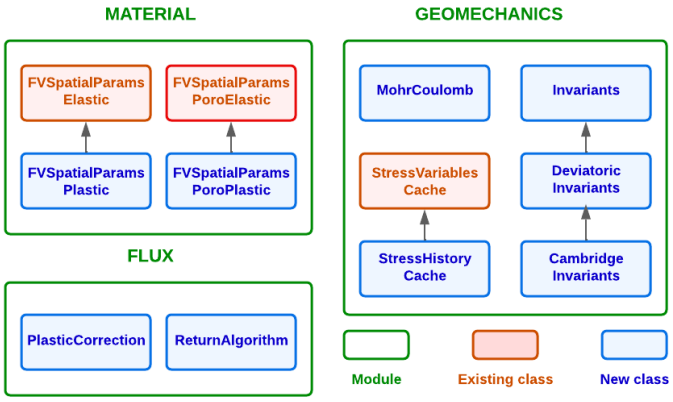

Figure 3.3: Extensions made to the original code DuMu^X to account for elastoplastic analyses.

Interface elements for mechanical analyses:

The Multidomain Module does not support mechanical problems. Also, the original coupling manager can not be used in mechanical problems as it is because the intermediary facet elements are not used to compute displacements (Figure 2.7). Thus, the coupling manager should couple two bulk elements that share a facet with each other. Also, the system for a mechanical problem containing interfaces is only the size of the bulk problem, since there are no variables at the facets. The new implementations that address this issues are illustrated in Figure 3.4.

The first major change is the creation of a new coupling manager class called `InterfaceBulkCouplingManager`, which couples the variables of two bulk elements that share a facet. These coupling information is used in the new class `BoxFacetCouplingElasticLaw` to compute the stresses $\boldsymbol{\sigma_c}$ using Equations 2.56–2.58 for faces that coincide with facets.

Also, a new class called `GeomechanicsMultiDomainTraits` was created to define the size of the system for geomechanical multi-domain models as equal to the number of degrees of freedom in the bulk domain only. As a result, system assembly is also different for mechanical multi-domain problems. So, the classes called `GeomechanicsMultiDomainAssembler` and `InterfaceBulkBox LocalAssembler` were created to assemble the bulk domain system using the coupling manager. Finally, the tags `GeomechanicsBoxFacetCouplingModel` and `PoromechanicsBoxFacetCoupli ngModel` were created for geomechanical problems with interfaces.

The class `HydroMechCouplingManager` (Figure 3.4) promotes the coupling between independent flux and mechanical problems in multi-domains containing interface elements. It is responsible for transmitting pore pressures at the faces to the mechanical problem and passing updated porosities and fracture apertures to the flux problem. This class employs the fixed-stress split method described in Section 2.4.4.2.

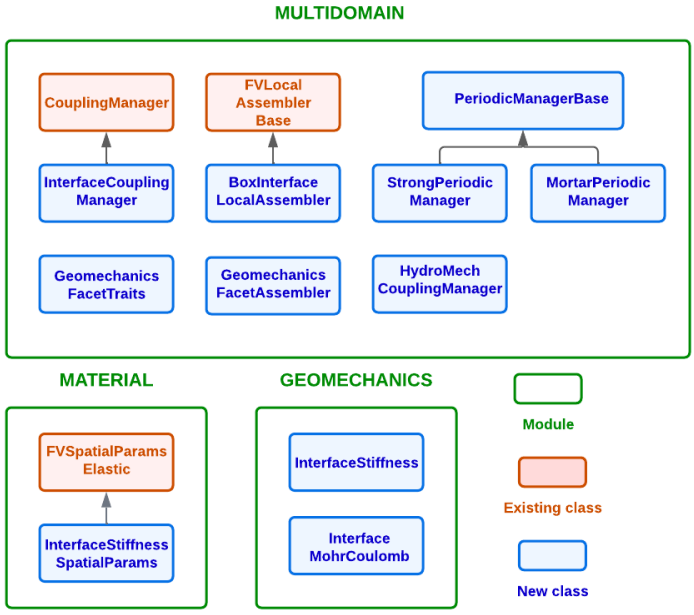

Figure 3.4: Extensions made to the original code of DuMu^X to add interface elements to geomechanical problems

A final requirement of the microscale problems to be incorporated in a multiscale framework is the imposition of periodic boundary conditions; DuMu^X does not contain this option for multi-domains. So, the class `PeriodicManagerBase` and its child classes were created to handle the imposition of periodic boundary conditions on media containing interface elements; their mathematical foundations will be discussed in detail in Chapter 4. Likewise, a new module called `Multiscale` will be presented further on, in Chapter 7.

3.1.3 Validations

This section presents the validations of the new implementations in DuMu^X. Apart from the algorithm for the multiscale solution, which is validated in Chapter 7, there are three major extensions that need to be verified: geomechanical problems with interface elements; addition of elastoplasticity, with the implementation of the return algorithm for the Mohr-Coulomb model; and the fixed-stress split coupling scheme applied to the solution of hydro-mechanical problems in fractured porous media.

3.1.3.1 Mechanics with fractures: elasticity

The implementation of the elastic model for the fractures and of the system assemblage for mechanical problems with interface elements was verified against the analytic solution for the stiffness tensor of fractured media presented in Duncan and Goodman (1968). The tested

domain is a rock mass containing two perpendicular sets of persistent fractures (Figure 3.5). By means of tensor rotation, the equivalent elastic tensor can be calculated for different orientations β of the fractures. Figure 3.5 presents the comparison between the analytical solution and the numerical results for different angles β and ratios K_t/K_n, where K_n and K_t are the fractures normal and tangent stiffnesses, respectively. A maximum error of 0.5 % was observed for the ratio of the equivalent Young modulus (E) to the Young modulus of the intact rock (E_r).

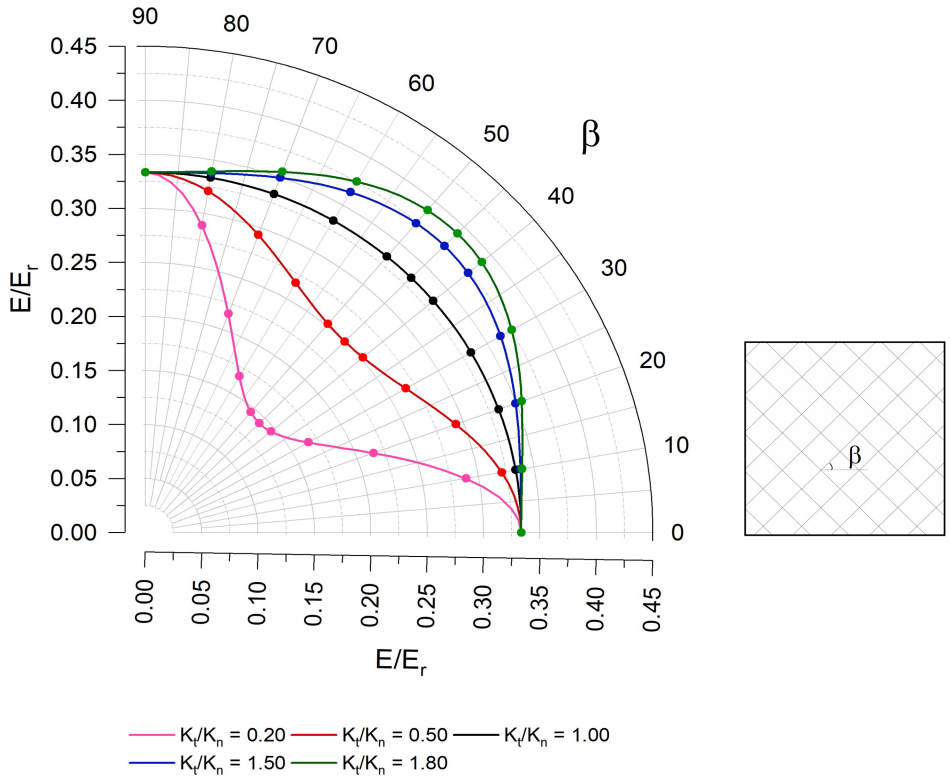

Figure 3.5: Validation of the new code for geomechanics with elastic fractures: comparison between the analytical (lines) and numerical (dots) solutions of E/E_r, where E is the equivalent Young modulus of the fractured rock mass and E_r is the Young modulus of the intact rock.

3.1.3.2 Plasticity

A verification of the new implementations required by the so-called Mohr-Coulomb model is made with the classical problem of a rigid strip footing resting on an elastoplastic soil; this is a common benchmark because it has an analytical solution and allows the verification of the return algorithm when the singularities of the yielding surface are crossed. Figure 3.6 illustrates the simulated problem: at the location of the strip footing of half-width B, a downward vertical displacement of $0.005B$ is applied in 100 steps. Horizontal and

vertical displacements are restricted at the lateral and bottom boundaries, respectively. The mesh contains 225 linear quadrangular elements. Table 3.1 lists the parameters and problem definitions, which are the ones employed by Sloan (1987). The exact solution for the collapse pressure is $14.83c$, where c is the soil's cohesion. Figure 3.6 shows the load-deformation curve obtained in DuMu^x; the load is the averaged pressure under the footing strip, and it is normalized by the cohesion. An ultimate load of $14.4c$ was obtained, which differs from the exact solution by 3.0 %.

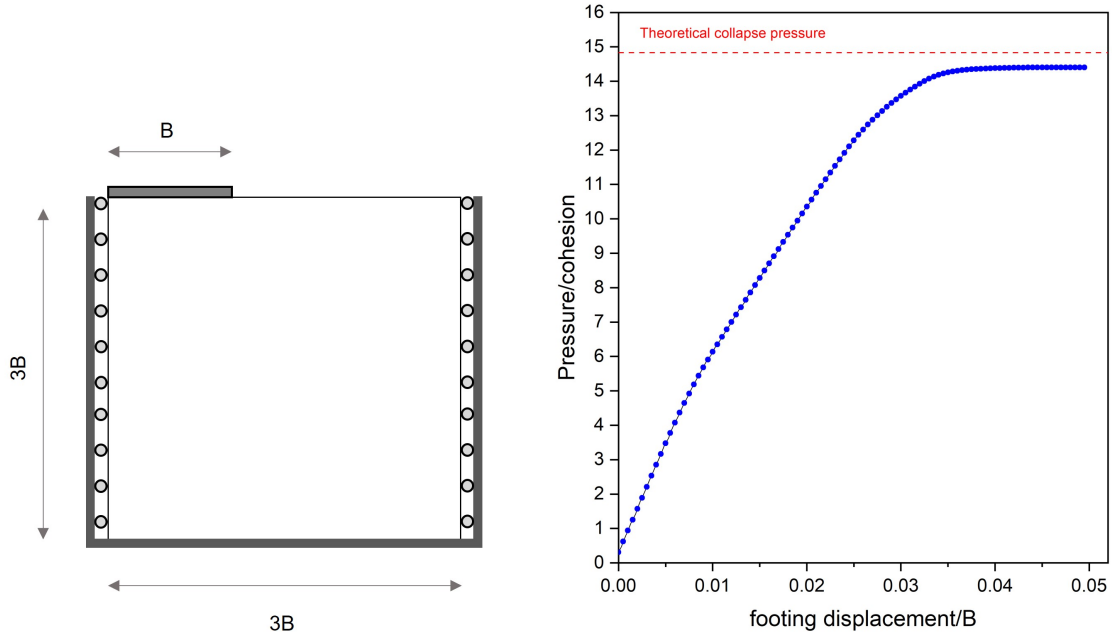

Figure 3.6: Validation of the new module for plasticity: simulation of the problem of a rigid strip footing on a material that follows the Mohr-Coulomb model (left) and comparison of the theoretical and calculated collapse pressures (right).

Table 3.1: Simulation parameters and definitions used in the strip footing problem in Figure 3.6.

Quantity	Unity	Value
Young's modulus (E)	kPa	5200
Poisson's ratio (ν)	-	0.30
Cohesion (c)	kPa	5.0
Friction Angle (ϕ)	°	20
Dilation Angle (ψ)	°	20
Half width of the footing (B)	m	3

3.1.3.3 Hydro-mechanical coupling

Matrix

The implementation of the fixed-stress scheme for the hydro-mechanical coupling is first verified for the matrix domain against two analytic solutions: Terzaghi's one-dimensional consolidation and Mandel's problem (Mandel, 1953). For both cases a convergence criterion $\varepsilon_{tol} = 0.001$ was adopted for the fixed-stress scheme (Equations 2.88 and 2.89).

Figure 3.7 presents the geometry and the boundary conditions of Terzaghi's problem. On the upper boundary of the column, a load q is applied; vertical displacements are restrained at the bottom and horizontal displacements are restrained on the sides, so the problem is essentially one-dimensional. Drainage is allowed to occur only at the top by the imposition of a zero pressure boundary condition. At any point of the domain, the initial pore pressure is $P_0 = q$. The mesh has 20 linear quadrangular finite elements, the total time of the simulation is 600 s and the time step size is 1 s. The modulus K_{dr} in (2.75) is equal to ${K_{dr}}^{(1D)}$ (Equation 2.79), which allows a faster convergence for Terzaghi's problem (Castelletto et al., 2015). The adopted parameters are described in Table 3.2.

Figure 3.7 compares the analytical and numerical solutions for the pressure distribution along the y-axis for different non-dimensional time factors T_v, defined by:

$$T_v = \frac{C_v t}{L^2} \tag{3.1}$$

where C_v is the one-dimensional coefficient of consolidation and t is time. Convergence is reached within two iterations per time step and the maximum error observed for the pore pressure is 0.1%.

Table 3.2: Simulation parameters and definitions used for the validation of Terzaghi's problem.

Hydro-mechanical parameters			Problem definitions		
Quantity	Unity	Value	Quantity	Unity	Value
Young's modulus (E)	kPa	1000	q	kPa	10.0
Poisson's ratio (ν)	-	0.25	L	m	1.0
Permeability (k_s)	m/s	1.16×10^{-5}			
Biot's coefficient (b)	-	1.0			
Biot's modulus (M)	kPa	∞			

Mandel's problem consists in a rectangular domain compressed both at the top and bottom boundaries by a load q; drainage is allowed to occur at the sides (Figure 3.8). The initial pore pressure is $P_0 = -q/3(1 + \nu_u)$, where ν_u is the undrained Poisson's ratio. The variables of the problem are described in Table 3.3 and are the same as those used by Preisig and Prevost (2011). Due to the symmetry of the problem, only a quarter of the domain

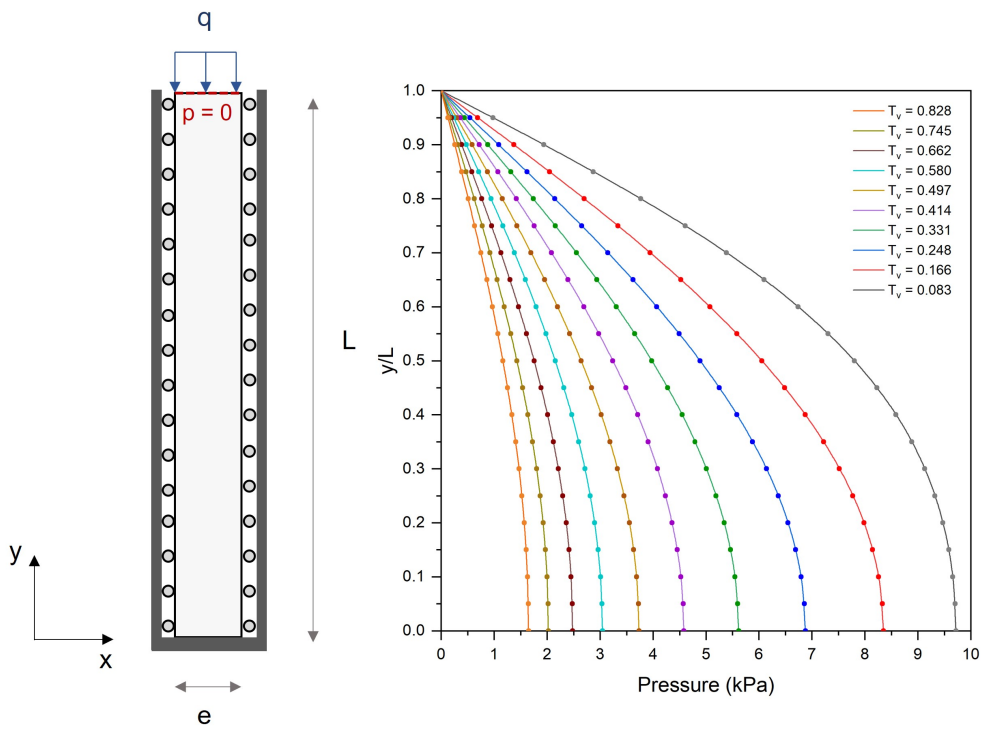

Figure 3.7: Scheme of Terzaghi's one-dimensional consolidation problem (left) and comparison of the analytical solution (lines) and the results from the numerical simulation (dots) using the fixed-stress split (right).

needs to be simulated. The mesh has 400 linear quadrangular elements and the total time of the simulation is 1 s, which is divided in 200 steps. The modulus K_{dr} in (2.75) is equal to ${K_{dr}}^{2D}$ (Equation 2.80), which allows for convergence to be attained within two iterations per time step. Figure 3.8 compares the analytical solution for the distribution of the pressure along the line $y = 0.5a$ and the pressure at the symmetry axis ($x = 0$), which is the same for any position y, for different non-dimensional time factors T_v. A maximum error of 1.3% was observed in the early stages of the simulation.

Table 3.3: Simulation parameters and definitions used for the validation of Mandel's problem.

Hydro-mechanical parameters			Problem definitions		
Quantity	Unity	Value	Quantity	Unity	Value
Young's modulus (E)	kPa	1.0	q	kPa	1.0
Poisson's ratio (ν)	-	0	a	m	1.0
Undrained Poisson's ratio (ν_u)	-	0.5	b	m	1.0
Permeability (k_s)	m/s	1.0			
Biot's coefficient (b)	-	1.0			
Biot's modulus (M)	kPa	∞			

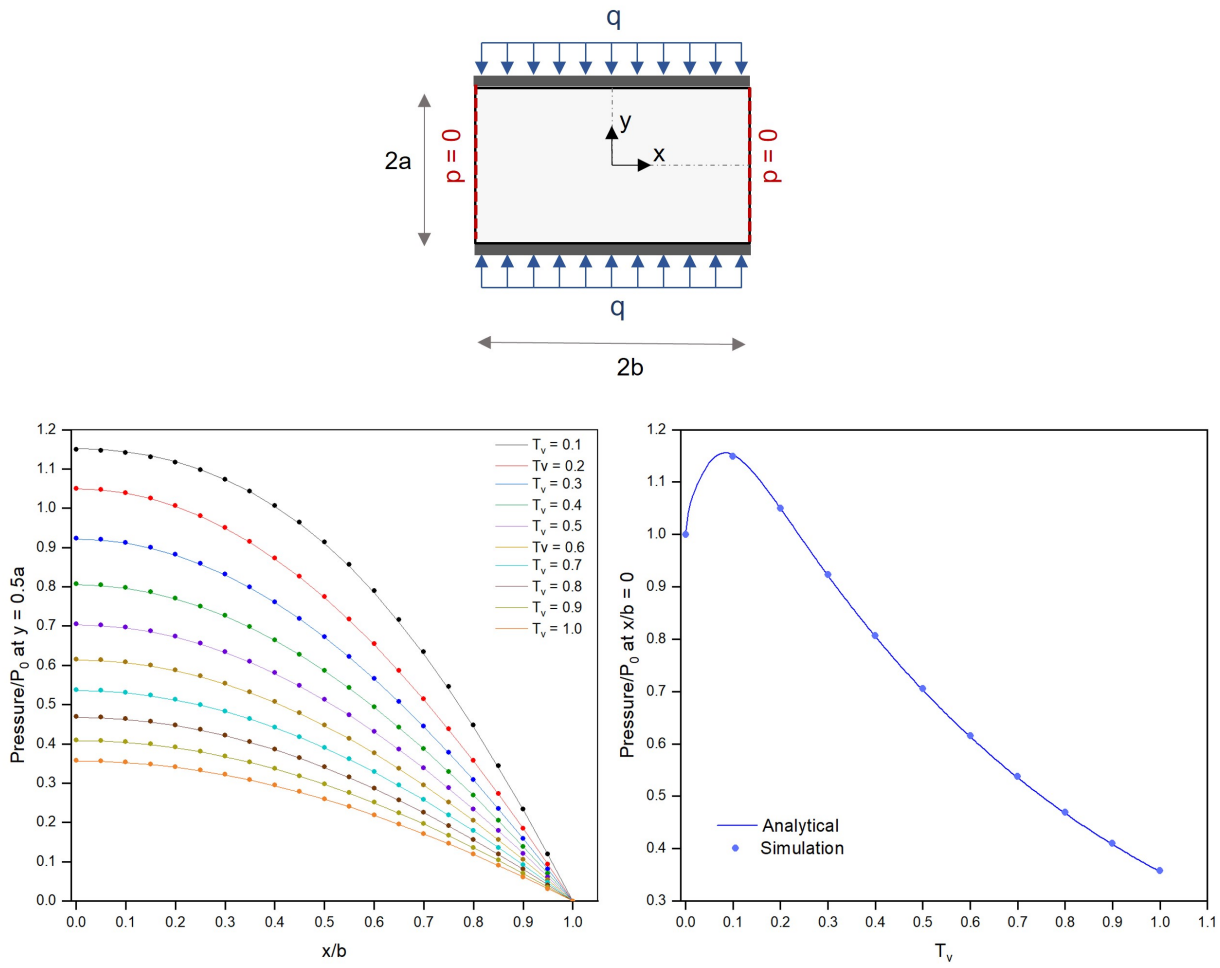

Figure 3.8: Scheme of Mandel's consolidation problem (top) and comparisons of the analytical solution (lines) and the results from the numerical simulation (dots) using the fixed-stress split (bottom). The graph on the left compares the spatial distribution of the normalized pore pressure at the position 0.5a and the graph on the right compares the normalized pore pressure history at the symmetry axis (x/b = 0).

Fractured domain

The algorithm for the fixed-stress split was also validated for fractured domains; in the absence of a closed-form solution, the test proposed by Segura and Carol (2008) and illustrated in Figure 3.9 was used here for verification. It consists in a two-dimensional domain with boundary and initial conditions similar to the Terzaghi's consolidation problem, but with a vertical fracture in the middle. The mesh contains 400 triangular bulk elements and 10 lower-dimensional linear elements to represent the fracture. A time step of 0.5 s was adopted.

Segura and Carol (2008) compared a sequential and a fully coupled scheme to verify one against the other. The parameters they adopted are described in Table 3.4. Two

scenarios were simulated: one where the fracture's permeability is constant and one where the longitudinal permeability is a function of the aperture by the cubic law (Equation 2.68), with k_l in Table 3.4 being its initial value. It has to be pointed out that they employ for the flow problem the double-nodded interface element earlier proposed by Segura and Carol (2004). This element accounts for transverse fluid, but suppresses the middle element of the triple-nodded interface with the assumption that the pressure at the fracture's mid-plane is the average of the pressures at the corresponding opposite matrix nodes. This has proven to be a good assumption when the transversal conductivity is high, but the comparison with a triple-nodded element showed significant discrepancies as the transversal conductivity becomes low and the fracture act as a flow barrier.

Figure 3.9a compares the results for the constant permeability case; the pressures along the fracture are displayed at the four different times selected by Segura and Carol (2008): 0.0007, 0.0021, 0.0035 and 0.007 days. In their work, these pressures are the average of the pressures obtained at the matrix faces, while here they are taken directly from the lower-dimensional elements. The results match very well; since the fracture permeability is very high, no appreciable differences arise from the use of different interface elements. As the vertical fracture is very conductive, it would rapidly drain its initial excess pore-pressure; but since it is much more permeable than the rest of the domain, it constantly receives an exchange flux from the matrix and act as a preferential path for flow.

The opposite happens when the permeability is assumed to be a function of the aperture. Already at the early stages of the simulation, the top portion of the fracture closes stops contributing to the drainage. Figure 3.9b compares the normalized pressures on the fracture for this scenario. While there is a good overall agreement, the differences are more significant than in the first scenario, specially during early stages at the top of the fracture, where the permeability rapidly becomes very low. This is due to the different interface elements; while the interface element used by Segura and Carol (2008) constrains the pressures on the fracture to be equal to the average of the pressures at the matrix faces, the results in DuMu^x with the triple-nodded interface element show that actually the pressure at the fracture becomes slightly higher than the pressures at the matrix. Thus, the fracture not only looses its drainage capacity, but is starts to transfer fluid to the matrix. Although these small discrepancies exist, they have a clear explanation and the new classes in DuMu^x were shown to be capable of handling coupled problems on fractured domains.

Elastoplastic material

Finally, the accuracy of the results obtained with the fixed-stress split was verified for a hydro-mechanical problem where the material is elastoplatic and follows the Mohr-Coulomb criterion. This validation was made by comparing the results from DuMu^x with those obtained using Sigma/W by GeoStudio, a well-known commercial software that solves hydro-mechanical problems with a fully coupled scheme. The problem is illustrated in Figure 3.10: it consists in a square of size 0.1 m and initial confinement stress of 200 kPa, which is loaded

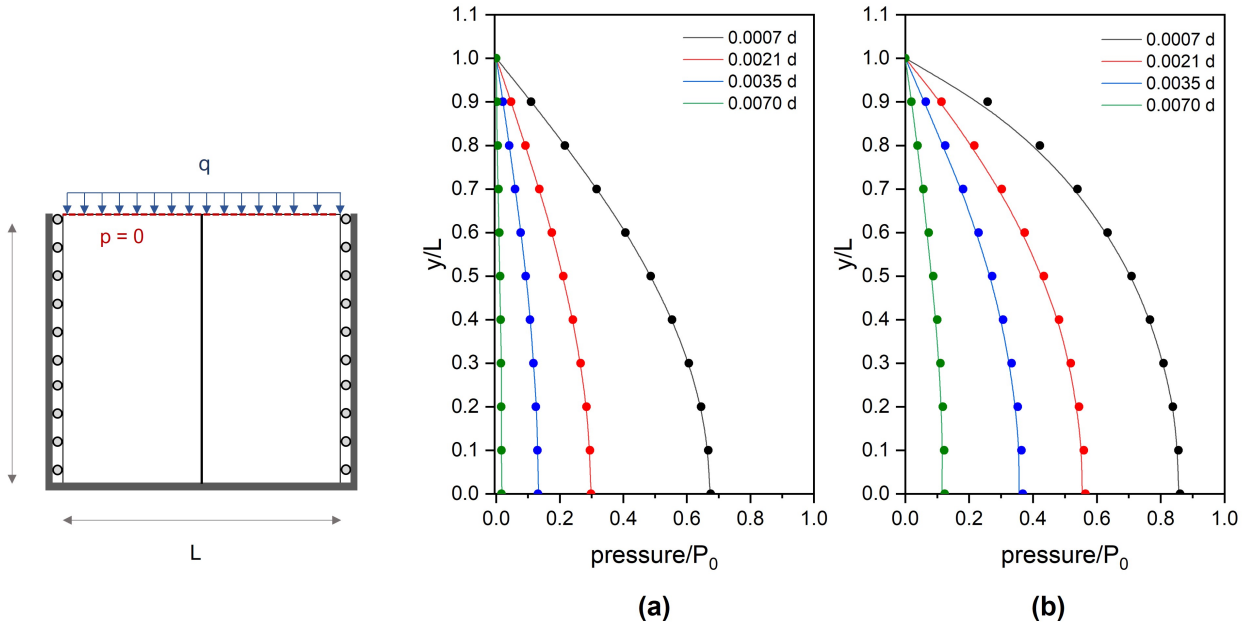

Figure 3.9: Scheme of the consolidation problem on a domain with a vertical fracture by Segura and Carol (2008) (left) and a) comparison of their results (lines) with the results obtained in DuMu^x (dots) for the constant permeability case b) comparison of their results (lines) with the results obtained in DuMu^x (dots) when the permeability is a function of aperture.

Table 3.4: Simulation parameters and definitions used by Segura and Carol (2008) on their test for the consolidation of a fractured domain.

Hydro-mechanical parameters			Problem definitions		
Quantity	Unity	Value	Quantity	Unity	Value
Matrix Young's modulus (E)	kPa	1000	q	kPa	10.0
Matrix Poisson's ratio (ν)	-	0.25	L	m	1.0
Matrix Permeability (k_s)	m/s	1.16×10^{-5}			
Matrix Biot's coefficient (b)	-	1.0			
Matrix Biot's modulus (M)	kPa	∞			
Fracture Normal Stiffness (K_n)	kPa/m	20000			
Fracture Tangent Stiffness (K_t)	kPa/m	1000			
Fracture Transversal Permeability (k_t)	m^2/s	1.15×10^{-6}			
Fracture Longitudinal Permeability* (k_l)	m^2/s	1.15×10^{-6}			
Fracture Biot's coefficient (b_f)	-	1.0			
Fracture Biot's modulus (M_f)	kPa	∞			

by a vertical displacement that linearly increases from 0 to -0.01 m in 9000 seconds. Table 3.5 presents the problem definitions and input data. In both softwares, the mesh contains 25 quadrangular elements and the adopted time step is 9 s. For the fixed-stress split scheme,

the estimator in (2.75) is calculated using ${K_{dr}}^{2D}$ (Equation 2.80) for elastic behavior, and then using ${K_{dr}}^{ep}$ (Equation 2.81) if the current stresses reach the yield surface.

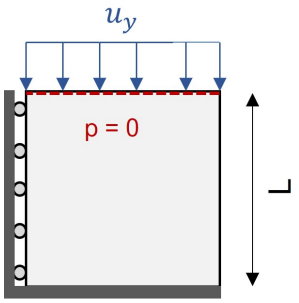

Figure 3.10: Test used to validate the hydro-mechanical coupling when the material is elasto-plastic and modeled with the Mohr-Coulomb criterion.

Two values of permeability were tested: 1×10^{-8} m/s and 1×10^{-9} m/s. Figures 3.11 and 3.12 compare the results for the pore pressure and vertical displacement distributions along the axis $x = 0$ and the time evolution of the pore pressure at the lower left corner. There is a very good match between these results. Also, they show the stress paths of the sample in terms of mean effective stresses and deviatoric stresses; these were calculated using the volume averages of the major and minor principal stresses, $\boldsymbol{\sigma_1}$ and $\boldsymbol{\sigma_3}$. It can be observed that the return algorithm is effective and returns the stresses to the Mohr-Coulomb surface once yielding occurs.

Table 3.5: Simulation parameters and definitions used in the validation problem of Figure 3.10.

Hydro-mechanical parameters			Problem definitions		
Quantity	Unity	Value	Quantity	Unity	Value
Young's modulus (E)	kPa	1000	L	m	0.1
Poisson's ratio (ν)	-	0.25	u_y	m	-0.01
Permeability (k_s)	m/s	1×10^{-8} ; 1×10^{-9}	Time	s	9000 s
Biot's coefficient (b)	-	1.0			
Biot's modulus (M)	kPa	∞			
Cohesion (c)	kPa	5.0			
Friction Angle (ϕ)	°	30			
Dilation Angle (ψ)	°	0			

3.2 Conclusions of the chapter

The computational tool used to perform the simulations is DuMu^x, an open-source code to which major additions were made. These extensions address the following requirements for

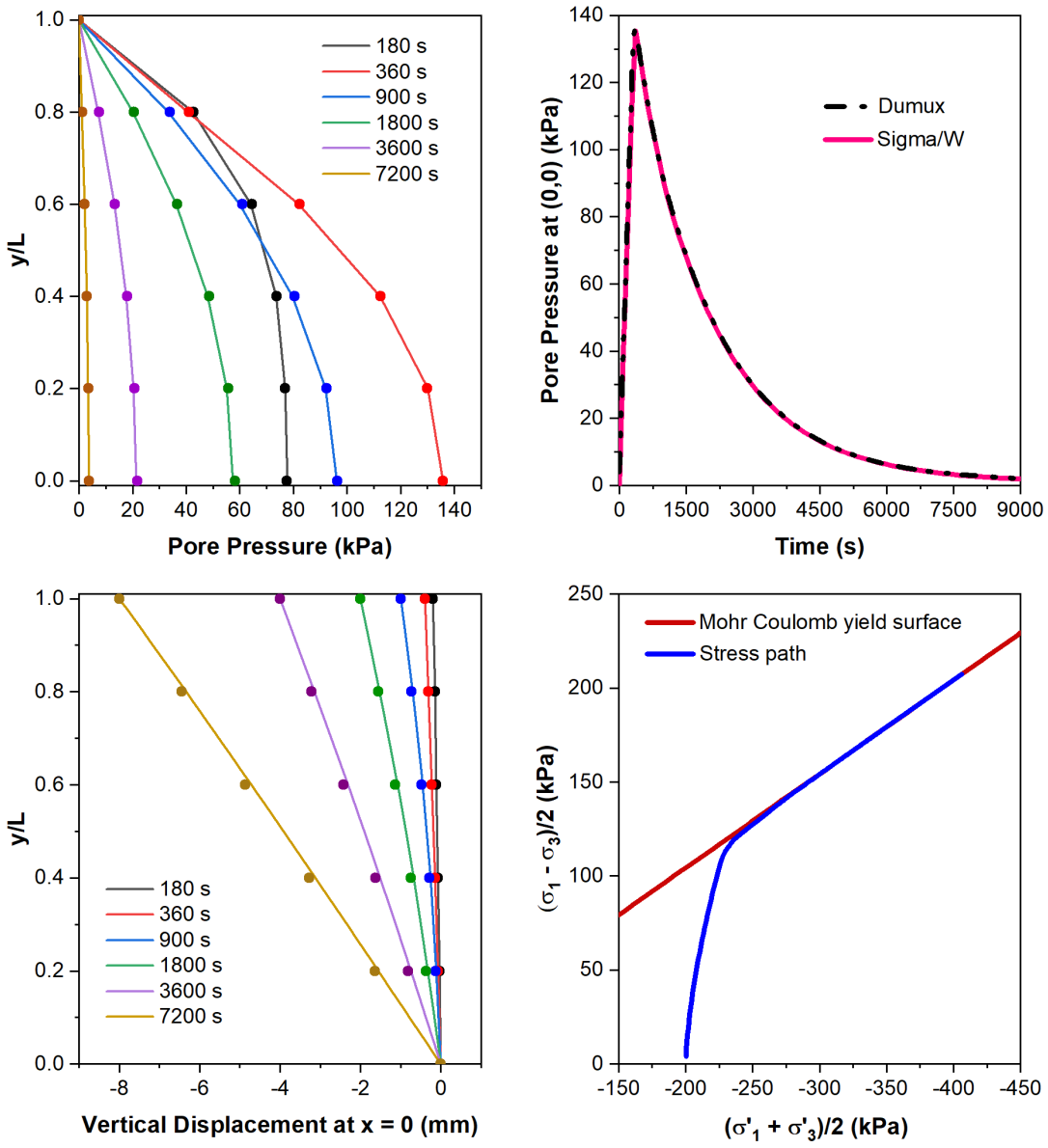

Figure 3.11: Comparison of the results obtained in Sigma/W (lines) and Dumux (dots) for the poroplastic problem in Figure 3.10 using $k_s = 1 \times 10^{-8}$ m/s. The lower right graph presents the averaged stress path of the sample and the Mohr-Coulomb surface.

a hydro-mechanical multiscale simulation on fractured media that were not present in the original code:

(a) Elastic and elastoplastic geomechanical problems in media containing interface elements;

(b) Hydro-mechanical coupling in media containing interface elements;

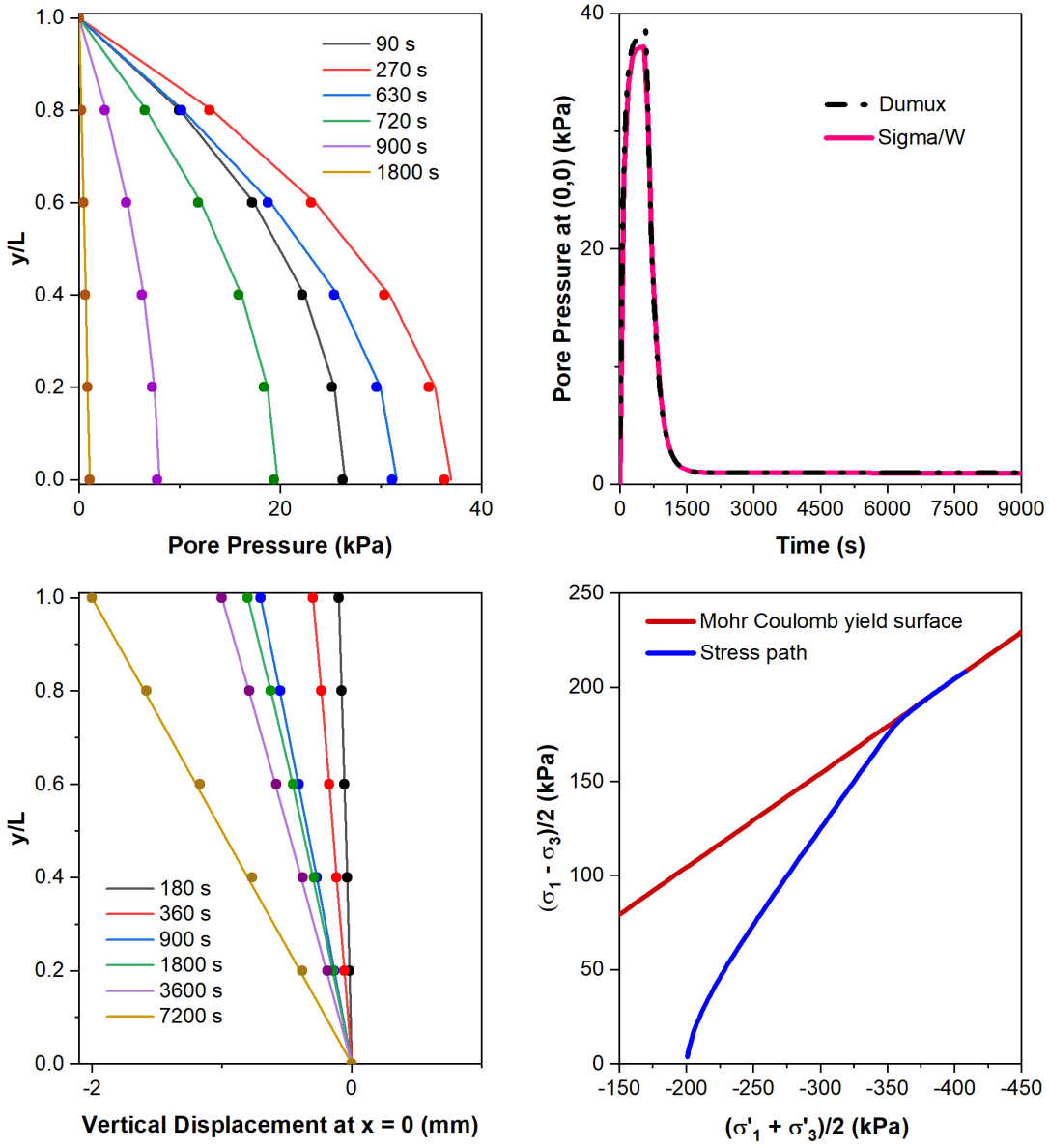

Figure 3.12: Comparison of the results obtained in Sigma/W (lines) and Dumux (dots) for the poroplastic problem in Figure 3.10 using $k_s = 1 \times 10^{-9}$ m/s. The lower right graph presents the averaged stress path of the sample and the Mohr-Coulomb yield surface.

(c) Imposition of periodic boundary conditions on media containing interface elements;

(d) Multiscale simulations.

The additions in (a) and (b) were validated against well-known closed-form solutions or other verified numerical results. The additions (c) and (d) are verified in Chapters 4 and 7 after the theoretical review on which their algorithms are founded.

Chapter 4

Imposing periodic boundary conditions on fractured domains

Works on the application of multiscale methods traditionally use periodic boundary conditions to solve the microscale's numerical problem (e.g. Özdemir et al., 2008; Feyel and Chaboche, 2000) even when the material is not periodic, since they are known to provide a faster convergence for the effective properties as the sample size increases (Terada et al., 2000; Miehe, 2003).

This chapter presents the methods that were implemented in DuMu^x to impose periodic boundary conditions on fractured domains. As it can be seen in Figure 3.4, there are two child classes dedicated to the periodic boundary conditions; they handle two possible scenarios: periodic and non-periodic meshes. For both cases, the existence of interface elements required some adaptions to the original methods.

4.1 Periodicity and stationarity

A material has a periodic geometry when it contains a pattern of heterogeneities that repeats itself within a distance called the period. In this case, the REV reduces to the unit cell, and its characteristic length l_c (Equation 2.2) is equal to the period.

The theory of periodic homogenization shows that the periodicity of the geometry leads to the periodicity of the physical quantities. Hence, it is unsurprising that in this case the imposition of periodic boundary conditions in numerical upscaling problems leads to optimum results. For truly periodic materials, the application of periodic boundary conditions on one unit cell only yields the final effective properties, while linear Dirichlet and Neumann boundary conditions require a sample with a certain number of unit cells to converge to this same result (Svenning et al., 2016).

It may not be as intuitive that the periodic boundary conditions are also useful and efficient when dealing with random media. As was mentioned in Section 2.1, a proper REV for random media needs to follow the stationarity condition (Equation 2.5). Auriault

et al. (2009) show that from a macroscopic point of view periodicity and stationarity are equivalent because they both lead to the translational invariance of the averaged quantities. It thus follows that the assumption of periodicity on random media is possible. Although the structure is not really periodic, if the REV is representative of the average constitutive behavior, it can be treated as so.

Actually, the imposition of periodic boundary conditions on random media is not only theoretically logical, but is also known to provide a faster convergence of the mean value of the equivalent properties. For example, Kanit et al. (2003) showed that the means of the thermal and elastic properties of random composites do not change significantly with size when periodic boundary conditions are employed, while linear Dirichlet and Neumann boundary conditions need larger REVs for those values to stabilize. On the other side, they observed a higher dispersion for the data obtained with periodic boundary conditions; thus, they would require a larger REV if a criterion based on the standard deviation of the properties was to be used. In the context of fractured media, a similar comparison was made by Svenning et al. (2016), who also demonstrated that the average of effective elastic properties converge faster for periodic boundary conditions, but did not make any remarks on their standard deviations.

4.2 Imposition of periodic boundary conditions

As was mentioned in Section 2.2.1, periodic boundary conditions are applied by imposing relationships between opposite sides of the REV. We divide here the REV boundary Γ into a positive part Γ_+ and a negative part, Γ_- (Figure 4.1), so that $\Gamma = \Gamma_+ \cup \Gamma_-$. Either Γ_- or Γ_+ can be taken as the dependent boundary for which the variables will be described as a function of the opposite, independent, sides via Equations (2.26)-(2.31). For convenience, these equations are recalled below:

$$\tilde{p}(\boldsymbol{x}^+) = \tilde{p}(\boldsymbol{x}^-) \tag{2.26}$$

$$\tilde{\boldsymbol{u}}(\boldsymbol{x}^+) = \tilde{\boldsymbol{u}}(\boldsymbol{x}^-) \tag{2.27}$$

$$p(\boldsymbol{x}^+) = p(\boldsymbol{x}^-) + \overline{\boldsymbol{G}} \,.\, (\boldsymbol{x}^+ - \boldsymbol{x}^-) \tag{2.28}$$

$$\boldsymbol{u}(\boldsymbol{x}^+) = \boldsymbol{u}(\boldsymbol{x}^-) + \overline{\boldsymbol{E}} \,.\, (\boldsymbol{x}^+ - \boldsymbol{x}^-) \tag{2.29}$$

$$Q(\boldsymbol{x}^+) = -Q(\boldsymbol{x}^-) \tag{2.30}$$

$$\boldsymbol{T}(\boldsymbol{x}^+) = -\boldsymbol{T}(\boldsymbol{x}^-) \tag{2.31}$$

where p and $\boldsymbol{u}$ are pressure and displacement vectors at a point, the superscript $\sim$ indicates their fluctuation components, the tensors $\overline{\boldsymbol{G}}$ and $\overline{\boldsymbol{E}}$ have their imposed macroscopic gradients, and Q and $\boldsymbol{T}$ are flux and traction forces, respectively.

In the context of numerical homogenization using a finite element discretization, these relationships are established between nodes on opposite boundaries of the mesh. Their enforcement on the system can be done with the Lagrange multiplier method or directly by constraint eliminations (Nguyen et al., 2012). This latter will be employed here. The implications of periodicity on the solution of the problem will be shown for the systems of general forms:

$$\boldsymbol{K_e u} = \boldsymbol{f} \tag{4.1}$$

$$\boldsymbol{K_f p} = \boldsymbol{q} \tag{4.2}$$

where $\boldsymbol{K_e}$ and $\boldsymbol{K_f}$ are the tangent matrices for the mechanical equilibrium and flux problems respectively, $\boldsymbol{u}$ is the nodal displacements vector, $\boldsymbol{p}$ is the nodal pressures vector, $\boldsymbol{f}$ is the nodal forces vector and $\boldsymbol{q}$ is the nodal fluxes vector. The displacements and pressure vectors can be decomposed as:

$$\boldsymbol{u}^T = \{\boldsymbol{u}^i \ \boldsymbol{u}^+ \ \boldsymbol{u}^- \ \boldsymbol{u}^p\} \tag{4.3}$$

$$\boldsymbol{p}^T = \{\boldsymbol{p}^i \ \boldsymbol{p}^+ \ \boldsymbol{p}^- \ \boldsymbol{p}^p\} \tag{4.4}$$

where the superscript i denotes internal nodes, $+$ and $-$ denote nodes on Γ_+ and Γ_-, respectively and p indicates nodes where the variables are prescribed. As a consequence, the systems in (4.1) and (4.2) can be reorganized as:

$$\begin{bmatrix} \boldsymbol{K}_e^{ii} & \boldsymbol{K}_e^{i+} & \boldsymbol{K}_e^{i-} & \boldsymbol{K}_e^{ip} \\ \boldsymbol{K}_e^{+i} & \boldsymbol{K}_e^{++} & \boldsymbol{K}_e^{+-} & \boldsymbol{K}_e^{+p} \\ \boldsymbol{K}_e^{-i} & \boldsymbol{K}_e^{-+} & \boldsymbol{K}_e^{--} & \boldsymbol{K}_e^{-p} \\ \boldsymbol{K}_e^{pi} & \boldsymbol{K}_e^{p+} & \boldsymbol{K}_e^{p-} & \boldsymbol{K}_e^{pp} \end{bmatrix} \begin{Bmatrix} \boldsymbol{u}^i \\ \boldsymbol{u}^+ \\ \boldsymbol{u}^- \\ \boldsymbol{u}^p \end{Bmatrix} = \begin{Bmatrix} \boldsymbol{f}^i \\ \boldsymbol{f}^+ \\ \boldsymbol{f}^- \\ \boldsymbol{f}^p \end{Bmatrix} \tag{4.5}$$

$$\begin{bmatrix} \boldsymbol{K}_f^{ii} & \boldsymbol{K}_f^{i+} & \boldsymbol{K}_f^{i-} & \boldsymbol{K}_f^{ip} \\ \boldsymbol{K}_f^{+i} & \boldsymbol{K}_f^{++} & \boldsymbol{K}_f^{+-} & \boldsymbol{K}_f^{+p} \\ \boldsymbol{K}_f^{-i} & \boldsymbol{K}_f^{-+} & \boldsymbol{K}_f^{--} & \boldsymbol{K}_f^{-p} \\ \boldsymbol{K}_f^{pi} & \boldsymbol{K}_f^{p+} & \boldsymbol{K}_f^{p-} & \boldsymbol{K}_f^{pp} \end{bmatrix} \begin{Bmatrix} \boldsymbol{p}^i \\ \boldsymbol{p}^+ \\ \boldsymbol{p}^- \\ \boldsymbol{p}^p \end{Bmatrix} = \begin{Bmatrix} \boldsymbol{q}^i \\ \boldsymbol{q}^+ \\ \boldsymbol{q}^- \\ \boldsymbol{q}^p \end{Bmatrix} \tag{4.6}$$

These systems have a solution if, at each node, either the pressures/displacements or the fluxes/forces are prescribed. However, in the case of periodic boundary conditions, these quantities are not directly prescribed at the boundaries, but the system becomes solvable by adding additional relationships between opposite points. These relationships force the fluctuation parts of the pressure and displacements at opposite nodes to be equal (Equations

(2.26) and (2.27)), and the forces and fluxes to be equal but opposite in sign (Equations (2.30) and (2.31)).

Two scenarios will be explored in the following sections. The first one is the imposition of strong periodic boundary conditions on periodic meshes, that is, meshes where every node on the boundary has a symmetric corresponding node on the opposite side (Figure 4.1). Then, the method used here to impose periodic boundary conditions on non-symmetric mesh geometries will be presented. For both cases, adaptions were made to the original algorithms to account for the existence of interface elements. They will also be presented in this Chapter, along with the additions made to DuMu^X to allow for the imposition of periodic boundary conditions on fractured domains in hydro-mechanical analyses.

4.2.1 Strong periodicity

The term strong periodicity means that relationships 2.28, 2.29, 2.30 and 2.31 hold point-wise on the boundary Γ. The imposition of such constraints require the mesh to be periodic. As a consequence, in the absence of discontinuities, the mapping between opposite boundaries is straightforward since each node has one exact correspondent at the opposite side (Figure 4.1).

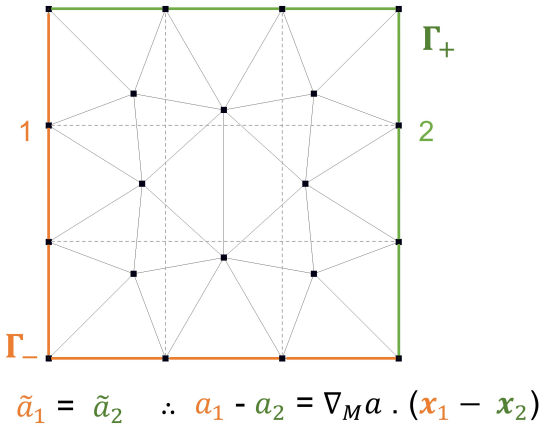

Figure 4.1: Example of a periodic mesh and definition of boundaries Γ_+ and Γ_-. Each pair of symmetrical nodes such as 1 and 2 is constrained to have an equal fluctuation part $\tilde{a}$ of a given physical quantity of interest a.

Here, the subscripts m and s will refer to the master (independent) and slave (dependent) boundaries Γ_m and Γ_s, which can be either Γ_- or Γ_+. The vector $\boldsymbol{a}$ will refer generally to the primary variable vectors $\boldsymbol{p}$ and $\boldsymbol{u}$.

Equations 2.28 and 2.29 define that the difference in the value of a primary variable a between two opposite points of the REV comes from the imposed macroscopic gradients only, since their fluctuation part is equal (Equations 2.26 and 2.27). These relationships are defined for each pair of opposite nodes, providing a mapping that can be organized in matrix form as:

$$\boldsymbol{T}\boldsymbol{a}^{\Gamma} = [\![\boldsymbol{a}]\!]_s \tag{4.7}$$

The matrix $\boldsymbol{T}$ has dimensions $n_{\Gamma_s} \times n_{\Gamma}$, where n_{Γ_s} is the number of nodes on Γ_s and n_{Γ} is the number of nodes on Γ. The vector $\boldsymbol{a}^{\Gamma}$ is a vector containing the nodal values of a on Γ; it has size n_{Γ} and can be decomposed as follows:

$$\boldsymbol{a}_{\boldsymbol{\Gamma}}{}^{T} = \{\boldsymbol{a}^s \ \boldsymbol{a}^m\} \tag{4.8}$$

where $\boldsymbol{a}^s$ and $\boldsymbol{a}^m$ contain the nodal values of a on Γ_s and Γ_m, respectively. The vector $[\![\boldsymbol{a}]\!]_s$ has size n_{Γ_s} and contains the jumps in a across opposite boundaries of the REV, which depend on the imposed macroscopic gradients only. For a slave node on Γ_s the component $[\![a]\!]_s$ is defined as:

$$[\![a]\!]_s(\boldsymbol{x}_s) = a^s(\boldsymbol{x}_s) - a^m(\boldsymbol{x}_m) = \{\nabla_M a \cdot (\boldsymbol{x}_s - \boldsymbol{x}_m)\} \tag{4.9}$$

where $\nabla_M a$ is the imposed macroscopic gradient of a, $\boldsymbol{x}_s$ denotes the coordinates of the slave node on Γ_s and $\boldsymbol{x}_m$ gives the coordinates of its mirror (master) node at the opposite side of the REV.

If i denotes a node on Γ_s whose mirror node on Γ_m is k, the component T_{ij} is given by:

$$T_{ij} = \begin{cases} 1, & \text{if } j = i \\ -1, & \text{if } j = k \\ 0, & \text{otherwise} \end{cases} \tag{4.10}$$

Systems 4.5 and 4.6 are undetermined as they are because both the primary variables and the right hand side vectors for the nodes on Γ are unknown. The introduction of the periodic constraints makes the solution unique; this is achieved by: a) adding the lines corresponding to the dependent or slave nodes to the lines of their master nodes and b) introducing the constraint (4.8) into the system; although it is possible to remove the slave nodes completely and condensate the system (e.g Nguyen et al., 2012; Reis and Andrade Pires, 2014), we opt here to replace the lines of the slave nodes by their corresponding lines in (4.7); this avoids changes in the way the original code of DuMu^x sets the system's size. Also, it is necessary to prescribe the unknowns of at least one node in the boundary. So, the primary variables at the lower left corner node are prescribed and, as a consequence of the mesh periodicity, the primary variables at all the other corner nodes are also prescribed and can be calculated from their values at the master corner node.

After these manipulations, the systems 4.5 and 4.6 become:

$$\begin{bmatrix} \boldsymbol{K}_e^{ii} & \boldsymbol{K}_e^{is} & \boldsymbol{K}_e^{im} & \boldsymbol{K}_e^{ip} \\ \boldsymbol{0} & \boldsymbol{T} & \boldsymbol{T} & \boldsymbol{0} \\ \boldsymbol{K}_e^{mi} + \boldsymbol{T}^T \boldsymbol{K}_e^{si} & \boldsymbol{K}_e^{ms} + \boldsymbol{T}^T \boldsymbol{K}_e^{ss} & \boldsymbol{K}_e^{mm} + \boldsymbol{T}^T \boldsymbol{K}_e^{sm} & \boldsymbol{K}_e^{mp} + \boldsymbol{T}^T \boldsymbol{K}_e^{sp} \\ \boldsymbol{0} & \boldsymbol{0} & \boldsymbol{0} & \boldsymbol{I}_p \end{bmatrix} \begin{Bmatrix} \boldsymbol{u}^i \\ \boldsymbol{u}^s \\ \boldsymbol{u}^m \\ \boldsymbol{u}^p \end{Bmatrix} = \begin{Bmatrix} \boldsymbol{f}^i \\ [\![\boldsymbol{u}]\!]_s \\ \boldsymbol{0} \\ \overline{\boldsymbol{u}} \end{Bmatrix} \tag{4.11}$$

$$\begin{bmatrix} \boldsymbol{K}_f^{ii} & \boldsymbol{K}_f^{is} & \boldsymbol{K}_f^{im} & \boldsymbol{K}_f^{ip} \\ \boldsymbol{0} & \boldsymbol{T}^{ss} & \boldsymbol{T}^{sm} & \boldsymbol{0} \\ \boldsymbol{K}_f^{mi} + \boldsymbol{T}^T \boldsymbol{K}_f^{si} & \boldsymbol{K}_f^{ms} + \boldsymbol{T}^T \boldsymbol{K}_f^{ss} & \boldsymbol{K}_f^{mm} + \boldsymbol{T}^T \boldsymbol{K}_f^{sm} & \boldsymbol{K}_f^{mp} + \boldsymbol{T}^T \boldsymbol{K}_f^{sp} \\ \boldsymbol{0} & \boldsymbol{0} & \boldsymbol{0} & \boldsymbol{I}_p \end{bmatrix} \begin{Bmatrix} \boldsymbol{p}^i \\ \boldsymbol{p}^s \\ \boldsymbol{p}^m \\ \boldsymbol{p}^p \end{Bmatrix} = \begin{Bmatrix} \boldsymbol{q}^i \\ [\![\boldsymbol{p}]\!]_s \\ \boldsymbol{0} \\ \overline{\boldsymbol{p}} \end{Bmatrix} \tag{4.12}$$

where $\boldsymbol{I}_p$ is the identity tensor of size equal to the number of corners and $\overline{\boldsymbol{u}}$ and $\overline{\boldsymbol{p}}$ are the vectors of prescribed displacements and pressures, respectively. In the right hand vectors, the null vectors on the third line come from the sums $\boldsymbol{f}^s + \boldsymbol{f}^m$ and $\boldsymbol{q}^s + \boldsymbol{q}^m$; since boundary tractions and fluxes are anti-periodic (Equations 2.30 and 2.31), these sums vanish.

Strong periodicity on domains with interface elements

Since opposite boundaries of zero-thickness interface elements have equal coordinates, it is possible, for non-periodic geometries, that a node on the boundary has more than one symmetric node on the opposite side of the REV. Thus, the imposition of strong periodicity on fractured domains needs to consider the three different scenarios illustrated in Figure 4.2, where the master boundary is considered to be Γ_-:

(a) Both the opposite sides have an intercepting interface element at the same position; in this case, the masters of matrix nodes M_1 and M_2 are nodes M_3 and M_4, respectively, and the master of fracture node F_1 is F_2;

(b) A node M_7 on the dependent side is symmetric to the interface nodes M_5, M_6 and F_3 that intercept the master boundary; in this case, M_5 is the only master node. The primary variables in M_6, M_7 and F_3 are constrained to be a function of M_5 according to (4.8). The fluxes and forces at the slave nodes are distributed to the master node, so their anti-periodicity leads to: $q_{M_5} + q_{M_6} + q_{M_7} + q_{F_3} = 0$ and $f_{M_5} + f_{M_6} + f_{M_7} = 0$. Note that the fracture node F_3 is not used in the mechanical problem.

(c) The nodes M_9, M_{10} and F_4 at the dependent boundary are symmetric to a matrix node M_8 only; in this case, the variables at M_9, M_{10} and F_4 are equal and are mapped from M_8 via (4.9) and (4.10). The anti-periodicity of fluxes and forces lead to $q_{M_8} + q_{M_9} + q_{M_{10}} + q_{F_4} = 0$ and $f_{M_8} + f_{M_9} + f_{M_{10}} = 0$.

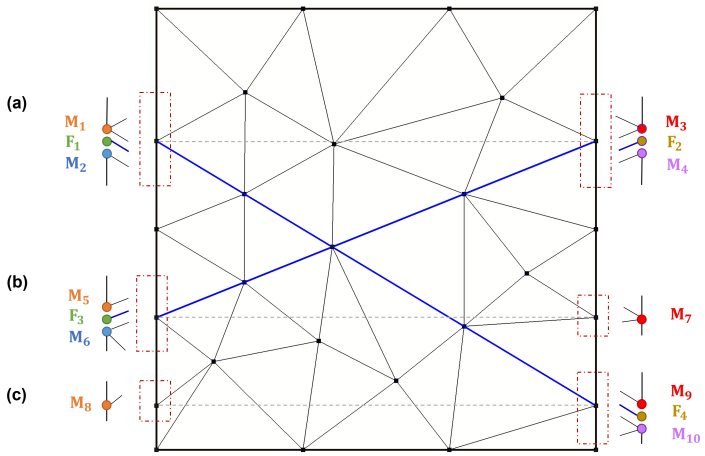

Figure 4.2: Three possible scenarios for periodic meshes containing interface elements: a) periodic fracture b) fracture on the independent side corresponding to a matrix node on the dependent side and c) matrix node on the dependent side at the same position than a fracture on the independent side.

The practical changes of these considerations on systems 4.11 and 4.12 is that there are interface nodes on the master side that will be treated as slave nodes when building the system.

Note from cases b) and c) that pressure and displacement discontinuities at the boundaries are prevented when the geometry of the fractures is not periodic. The prevention of displacement discontinuities was reported by Svenning et al. (2016) to significantly overestimate the equivalent stiffness for smaller sizes of the REV. The method that will be presented in the following section does not prevent discontinuities, so it may be more efficient for non-periodic fracture geometries, and is specially useful for non-conforming meshes.

4.2.2 Weak periodicity: the mortar method

Although it is possible to generate periodic meshes on non-periodic materials, this task becomes harder when the geometry of the heterogeneities becomes complex, as is often the case with DFNs. To gain flexibility in the homogenization of complex microstructures, several different techniques were developed to impose periodic boundary conditions on non-periodic meshes. They include the polynominal interpolation method by Nguyen (2014) and the technique proposed by Larsson et al. (2011a), which is based on an independent discretization of the boundary tractions to enforce weak periodicity; this latter was adapted by Svenning et al. (2016) to upscale the mechanical properties of fractured domains.

Another class of technique is the mortar method, which was already well established for contact problems before it was applied by Reis and Andrade Pires (2014) to the imposition of periodic boundary conditions; a later work presents a more detailed description of the implementation of these mortar periodic conditions (Rodrigues Lopes et al., 2021). We will

first present this method without considering the existence of fractures; then, the modifications proposed here to incorporate triple-nodded interface elements in the problem will be detailed.

The mortar method is used to enforce a weak continuity across the interface of non-conforming meshes, instead of the point-wise continuity that arises naturally from conforming meshes. This also applies to the imposition of periodicity, which is weak in the sense that it does not hold point-wise, while the boundary integral of the pressures and displacements will still result on the imposed macroscopic gradients.

The first step to apply the mortar method is the definition of the non-mortar (dependent) side and the mortar (independent) side, which can be chosen to be either Γ_+ or Γ_-. The subscripts m and n that will be used below refer to the mortar and the non-mortar sides, respectively.

We consider here a vector $\boldsymbol{a}$ that is a general representation of the pressure and displacement vectors in (4.5) and (4.6) ($\boldsymbol{u}$ and $\boldsymbol{p}$). The vector $\boldsymbol{a}$ can be decomposed in a vector $\boldsymbol{a}^i$ for the internal nodes and a vector $\boldsymbol{a}^\Gamma$ for the boundary nodes. This latter can be further decomposed as:

$$\boldsymbol{a}^\Gamma = \{\boldsymbol{a}^m \ \boldsymbol{a}^n\} \tag{4.13}$$

The component a represents either a fluid pressure or a directional displacement. Recall from (2.16) and (2.17) that a is composed of a linear part a_l, calculated from the imposed macroscopic gradients, and a fluctuation part $\tilde{a}$, that is:

$$a = \tilde{a} + a_l \tag{4.14}$$

We will first work with the imposition of the weak periodicity of $\tilde{a}$ (Equations (2.26) and (2.27)), and then will derive constraints in terms of a.

The enforcement of periodic boundary conditions requires the integration domains of opposite mortar and non-mortar sides to be compatible. Here this is achieved by the construction of virtual integration lines (Reis and Andrade Pires, 2014). As illustrated in Figure 4.3 for bi-dimensional problems, a virtual integration line is built for each pair of opposite sides of the REV: it contains the projection of all of their nodes.

Consider the functions π_n and π_m that project variables on the non-mortar and mortar sides, respectively, on the integration line Γ_i. The objective of the mortar method is to enforce weakly a null jump of the variable between the mortar and non-mortar boundaries by means of the following condition:

$$\int_{\Gamma_i} (\pi_n(\tilde{a}^n) - \pi_m(\tilde{a}^m))\psi_n d\Gamma_i = 0 \tag{4.15}$$

where ψ_n is a test function contained in the space of non-mortar elements.

The integral (4.15) is computed using the Gaussian quadrature rule. The local coordinates on the virtual line, on the mortar and on the non-mortar sides will be denominated

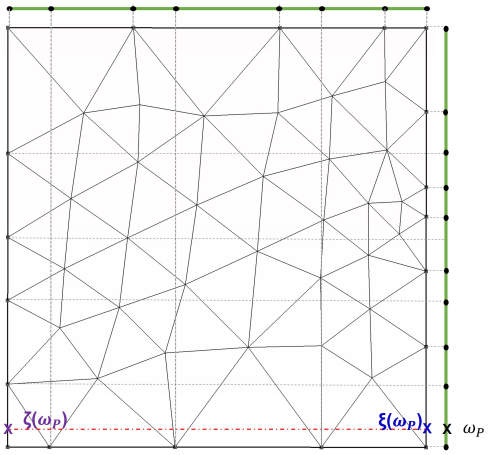

Figure 4.3: Construction of the virtual integration lines, in green, for two-dimensional problems and mapping of an integration point ω_p of the virtual line into the mortar and non-mortar boundaries.

ω, ζ and ξ, respectively. Consider a Gauss point ω_p on the integration line that can be mapped into the local coordinates $\xi(\omega_p)$ and $\zeta(\omega_p)$ located on the segments δ_n and δ_m of the non-mortar and mortar sides, respectively (Figure 4.3). The mapping functions in (4.15) assume the following forms at ω_p:

$$\pi_m(\tilde{a}^m(\omega_p)) = \sum_{j \in d\delta_m} N_{m,j}(\zeta(\omega_p))\tilde{a}_j \tag{4.16}$$

$$\pi_n(\tilde{a}^n(\omega_p)) = \sum_{j \in d\delta_m} N_{n,j}(\xi(\omega_p))\tilde{a}_j \tag{4.17}$$

where $\boldsymbol{N}_m$ and $\boldsymbol{N}_n$ are the finite element shape functions on the mortar and non-mortar spaces, respectively and $\tilde{a}_j$ is the value of $\tilde{a}$ at node j.

Considering its finite element approximation, the mortar condition (4.15) can be written in matrix form as:

$$\boldsymbol{A}^n\tilde{\boldsymbol{a}}^n - \boldsymbol{A}^m\tilde{\boldsymbol{a}}^m = 0 \tag{4.18}$$

where:

$$\boldsymbol{A}^n_{ij} = \sum_{\omega_p \in \Gamma_i} M_i(\xi(\omega_p))N_j(\xi(\omega_p))|\boldsymbol{J}_p|w_p \tag{4.19}$$

$$\boldsymbol{A}^m_{ij} = \sum_{\omega_p \in \Gamma_i} M_i(\xi(\omega_p))N_j(\zeta(\omega_p))|\boldsymbol{J}_p|w_p \tag{4.20}$$

and $\boldsymbol{M}$ are Lagrange multipliers selected to be the test functions ψ_n in (4.15), $\boldsymbol{J}_p$ is the Jacobian matrix evaluated at ω_p and w_p is the integration weight at ω_p.

The non-mortar variables $\tilde{a}^n$ can then be written in terms of the mortar variables $\tilde{a}^m$ as:

$$\tilde{\boldsymbol{a}}^n = (\boldsymbol{A}^n)^{-1}(\boldsymbol{A}^m\tilde{\boldsymbol{a}}^m) = \boldsymbol{A}\tilde{\boldsymbol{a}}^m \tag{4.21}$$

where $\boldsymbol{A} = (\boldsymbol{A}^n)^{-1}(\boldsymbol{A}^m)$. There are some possible formulations for the Lagrange multipliers, but Reis and Andrade Pires (2014) employ the dual shape functions that were originally incorporated to the mortar method by Wohlmuth (2000); they are presented in Table 4.1 for linear two-dimensional elements. These functions are convenient because they are such that:

$$\int_{\Gamma_n} M_i(\xi)N_j(\xi)d\Gamma_n = \boldsymbol{\delta}_{ij}\int_{\Gamma_n} N_j(\xi)d\Gamma_n \tag{4.22}$$

which makes $\boldsymbol{A}^n$ a diagonal matrix, and thus easily inversible. The corner nodes that are located at non-mortar segments are prescribed to $\tilde{a} = 0$. As a consequence, the Lagrange multipliers need to be adapted for segments that contain these prescribed corner nodes; the modifications proposed by Rodrigues Lopes et al. (2021) are also presented in Table 4.1.

Table 4.1: Dual functions for the Lagrange multipliers $\boldsymbol{M}$ when linear two-dimensional elements are employed and $\xi \in [-1, 1]$.

Regular equations	$M_1 = \frac{1}{2}(1-3\xi)$	$M_2 = \frac{1}{2}(1+3\xi)$
Prescribed corner at $\xi = -1$	$M_1 = 0$	$M_2 = 1$
Prescribed corner at $\xi = 1$	$M_1 = 1$	$M_2 = 0$

The coordinates $\boldsymbol{x}_c$ of the corner node that joins the two existing non-mortar boundaries in a bi-dimensional REV can be taken as the reference point to calculate the linear part a_l of the variable a as:

$$a_l(\boldsymbol{x}) = \nabla_M a(\boldsymbol{x} - \boldsymbol{x}_c) \tag{4.23}$$

If the non-mortar boundary is Γ_+, this reference point is the upper right corner; if it is Γ_-, this reference point is the lower left corner.

Since the objective here is to solve the vector $\boldsymbol{a} = \boldsymbol{p}, \boldsymbol{u}$, (4.14) can be inserted into (4.21) to obtain the following relationship:

$$\boldsymbol{a}^n - \boldsymbol{A}(\boldsymbol{a}^m - \boldsymbol{a}_l^m) - \boldsymbol{a}_l^n = 0 \tag{4.24}$$

or

$$\boldsymbol{a}^n - \boldsymbol{A}\boldsymbol{a}^m = [\![\boldsymbol{a}_l]\!]_\Gamma \tag{4.25}$$

where $[\![\boldsymbol{a}_l]\!]_\Gamma = \boldsymbol{a}_l^n - \boldsymbol{A}\boldsymbol{a}_l^m$.

Now consider the force and flux vectors $\boldsymbol{f}$ and $\boldsymbol{q}$, which will be generally represented by $\boldsymbol{b}$. In order to impose the anti-periodicity of these variables (Equations 2.30 and 2.31), the mortar condition becomes:

$$\int_{\Gamma_i} (\pi_{\Gamma_{n,\delta_i}}(b^n) + \pi_{\Gamma_{m,\delta_i}}(b^m))\psi_n d\Gamma_i = 0 \tag{4.26}$$

which results in the following relationship between the mortar and non-mortar flux and force vectors:

$$\boldsymbol{b}^m + \boldsymbol{A}^T \boldsymbol{b}^n = 0 \tag{4.27}$$

The component $\boldsymbol{A}_{ij}$ is a coefficient that will be used to distribute part of the fluxes or forces at the slave node i to the master node j. Equations 4.25 and 4.27 can be added to systems (4.6) and (4.5) as constraints that make their solutions unique. Similarly to what was done in the previous section, the dependent (non-mortar) nodes have their corresponding lines in the system replaced by (4.25). As for their corresponding master nodes, they have $\boldsymbol{A}^T \boldsymbol{b}_n$ added to their lines, so (4.27) is enforced:

$$\begin{bmatrix} \boldsymbol{K}_m^{ii} & \boldsymbol{K}_m^{in} & \boldsymbol{K}_m^{im} & \boldsymbol{K}_m^{ip} \\ \boldsymbol{0} & \boldsymbol{I}_n & -\boldsymbol{A} & \boldsymbol{0} \\ \boldsymbol{K}_m^{mi} + \boldsymbol{A}^T \boldsymbol{K}_m^{ni} & \boldsymbol{K}_m^{mn} + \boldsymbol{A}^T \boldsymbol{K}_m^{nn} & \boldsymbol{K_m}^{mm} + \boldsymbol{A}^T \boldsymbol{K}_m^{nm} & \boldsymbol{K}_m^{mp} + \boldsymbol{A}^T \boldsymbol{K}_m^{np} \\ \boldsymbol{0} & \boldsymbol{0} & \boldsymbol{0} & \boldsymbol{I}_p \end{bmatrix} \begin{Bmatrix} \boldsymbol{u}^i \\ \boldsymbol{u}^n \\ \boldsymbol{u}^m \\ \boldsymbol{u}^p \end{Bmatrix} = \begin{Bmatrix} \boldsymbol{f}^i \\ [\![\boldsymbol{u}_l]\!] \\ \boldsymbol{0} \\ \overline{\boldsymbol{u}} \end{Bmatrix} \tag{4.28}$$

$$\begin{bmatrix} \boldsymbol{K}_f^{ii} & \boldsymbol{K}_f^{in} & \boldsymbol{K}_f^{im} & \boldsymbol{K}_f^{ip} \\ \boldsymbol{0} & \boldsymbol{I}_n & -\boldsymbol{A} & \boldsymbol{0} \\ \boldsymbol{K}_f^{mi} + \boldsymbol{A}^T \boldsymbol{K}_f^{ni} & \boldsymbol{K}_f^{mn} + \boldsymbol{A}^T \boldsymbol{K}_f^{nn} & \boldsymbol{K_f}^{mm} + \boldsymbol{A}^T \boldsymbol{K}_f^{nm} & \boldsymbol{K}_f^{mp} + \boldsymbol{A}^T \boldsymbol{K}_f^{np} \\ \boldsymbol{0} & \boldsymbol{0} & \boldsymbol{0} & \boldsymbol{I}_p \end{bmatrix} \begin{Bmatrix} \boldsymbol{p}^i \\ \boldsymbol{p}^n \\ \boldsymbol{p}^m \\ \boldsymbol{p}^p \end{Bmatrix} = \begin{Bmatrix} \boldsymbol{q}^i \\ [\![\boldsymbol{p}_l]\!] \\ \boldsymbol{0} \\ \overline{\boldsymbol{p}} \end{Bmatrix} \tag{4.29}$$

Domains with interface elements

When interface elements exist at the mesh boundaries, some considerations have to be made about the imposition of periodic boundary conditions using the mortar method.

In the case of the mechanical problem, the method can be applied using the original formulation described above. The mapping of the integration points on the virtual line naturally allows for displacement discontinuities when interface elements are present on any side of the REV. Contrarily to what happens in the strongly periodic case, no enforcement needs to be made regarding the displacement jumps across the boundary interfaces. The mapping of master and salve nodes through the virtual integration line naturally causes the duplicated nodes at a fracture to have different masters, so their primary variables will have different values.

The case of the flux problem here is different because it uses the middle interface elements

to evaluate the pressures at the fractures. We propose some adaptions to make it solvable.

The pressure in any fracture node at the boundary is mapped from the mortar matrix nodes through:

$$\boldsymbol{p}_f^{\Gamma} - \boldsymbol{\alpha}\boldsymbol{p}^m - [\![\boldsymbol{p_f}]\!]_{\Gamma} = 0 \tag{4.30}$$

The subscript f indicates fracture and the superscript Γ indicates that the node is located on the boundary; $\boldsymbol{\alpha}$ is a matrix of dimensions $n_f \times n_m$, which are the number of fracture nodes on the boundary and the number of nodes on the mortar boundary, respectively.

Equation 4.30 will always be used to enforce the pressure at the fracture nodes to be equal to the average of the pressure at their coupled matrix nodes. This enforcement will have different implications on $\boldsymbol{\alpha}$ depending on the fracture being on the mortar or on the non-mortar side, as will be discussed below. Prescribing the fracture to have the average of the pressure at the matrix nodes was suggested by Segura and Carol (2004) as a resource to consider transversal pressure jumps across double-nodded interface elements. They showed that this is a good assumption when the fractures permeability is not so low that they will act as flow barriers. While they make this enforcement for the entire fractured domain, here it is used only at the boundary fracture nodes, so its impact on the global solution is expected to be less significant.

The weak enforcement of the anti-periodicity of fluxes also requires the fluxes at the boundary fracture nodes to be distributed to the mortar nodes. We define $\boldsymbol{q_t^m}$ as the vector containing the fluxes received by the mortar nodes from the fractures and $\boldsymbol{q_f}^{\Gamma}$ as the vector of fluxes at the boundary fracture nodes. They are related by:

$$\boldsymbol{q_t^m} = \boldsymbol{\alpha}^T \boldsymbol{q}_f^{\Gamma} \tag{4.31}$$

So, for fractured domains containing lower-dimensional interface elements, the anti-periodicity condition in (4.27) becomes:

$$\boldsymbol{q}^m + \boldsymbol{A}^T \boldsymbol{q}^n + \boldsymbol{q_t^m} = 0 \tag{4.32}$$

In (4.32) the coefficients in $\boldsymbol{\alpha}$ are used to equally distribute the fluxes in the fracture among its coupled matrix nodes; if these nodes are on the non-mortar side, this flux ends up being redistributed to their master nodes.

We continue with the definition of the coefficients in $\boldsymbol{\alpha}$. In the following, the space Ω_f contains the fracture nodes and the space $\Omega_{m,i}$ contains the pair of matrix nodes coupled to a fracture node i. Two possibilities are considered:

(a) If the fracture node is on the mortar side:

$$\forall i \in \Omega_f \cap \Gamma_m \; \boldsymbol{\alpha}_{ij} = \begin{cases} \frac{1}{2}, & \text{if } j \in \Omega_{m,i} \\ 0, & \text{otherwise} \end{cases} \tag{4.33}$$

(b) If the fracture node is on the non-mortar side, the quantities that would be distributed to their coupled matrix nodes will actually be distributed to the pertinent mortar nodes using the coefficients of matrix $\boldsymbol{A}$ in (4.21); so:

$$\forall i \in \Omega_f \cap \Gamma_n \ \boldsymbol{\alpha}_{ik} = \frac{1}{2} \sum_{j \in \Omega_{m,i}} \boldsymbol{A}_{jk} \tag{4.34}$$

To incorporate these additional considerations in System 4.29, we use the following decomposition of the pressures at the boundary ($\boldsymbol{p}^{\Gamma}$):

$$\boldsymbol{p}^{\Gamma} = \{\boldsymbol{p}_b^m \ \boldsymbol{p}_b^n \ \boldsymbol{p}_f^{\Gamma}\} \tag{4.35}$$

where the subscripts b and f denote bulk and fracture, respectively, and the superscripts are used to identify the location of the nodes. After the imposition of constraints (4.21), (4.27), (4.30) and (4.32), the system for the flux problem containing lower-dimensional elements becomes:

$$\begin{bmatrix} \boldsymbol{K}_f^{ii} & \boldsymbol{K}_f^{in} & \boldsymbol{K}_f^{im} & \boldsymbol{K}_f^{if} & \boldsymbol{K}_f^{ip} \\ \boldsymbol{0} & \boldsymbol{I}_n & -\boldsymbol{A} & \boldsymbol{0} & \boldsymbol{0} \\ \boldsymbol{J}^{mi} & \boldsymbol{J}^{mn} & \boldsymbol{J}^{mm} & \boldsymbol{J}^{mf} & \boldsymbol{J}^{mp} \\ \boldsymbol{0} & \boldsymbol{0} & -\boldsymbol{\alpha} & \boldsymbol{I}_f & \boldsymbol{0} \\ \boldsymbol{0} & \boldsymbol{0} & \boldsymbol{0} & \boldsymbol{0} & \boldsymbol{I}_p \end{bmatrix} \begin{Bmatrix} \boldsymbol{p}^i \\ \boldsymbol{p}_b^n \\ \boldsymbol{p}_b^m \\ \boldsymbol{p}_f^{\Gamma} \\ \boldsymbol{p}^p \end{Bmatrix} = \begin{Bmatrix} \boldsymbol{q}^i \\ [\![\boldsymbol{p}_l^n]\!]_{\Gamma} \\ \boldsymbol{0} \\ [\![\boldsymbol{p}_l^f]\!]_{\Gamma} \\ \overline{\boldsymbol{p}} \end{Bmatrix} \tag{4.36}$$

where

$$\boldsymbol{J} = \begin{bmatrix} \boldsymbol{J}^{mi} & \boldsymbol{J}^{mn} & \boldsymbol{J}^{mm} & \boldsymbol{J}^{mf} & \boldsymbol{J}^{mp} \end{bmatrix} = \boldsymbol{K}^m + \boldsymbol{A}^T \boldsymbol{K}^n + \boldsymbol{\alpha}^T \boldsymbol{K}^{fb} \tag{4.37}$$

and $\boldsymbol{I}_f$ is the identity matrix of size the number of boundary fracture nodes and $\boldsymbol{K}^{fb}$ is the tangent matrix originally assembled to the boundary fracture nodes, that is, before the periodicity constraints are added.

4.2.3 Implementation in DuMu^x

The classes added to DuMu^x to manage the implementation of the periodic boundary conditions have three main functions that need to be called:

1. The function called `setPeriodicMap` maps corresponding nodes, in the strongly periodic case, and builds the virtual integration lines and the mapping matrices in (4.21) and (4.30), in the case of the mortar periodic boundary conditions. This function is called after the FV mesh is initiated;

2. The function `extendJacobianPattern` adds new pairs of rows and columns to the tangent matrices $\boldsymbol{K}_e$ and $\boldsymbol{K}_f$. The pattern of these matrices is configured to store only non-zero entries by identifying which nodes depend on each other because of the mesh connectivity; as the periodic boundary conditions add new dependency relationships between nodes, this original pattern needs to be extended before changing the system.

3. The function `enforceSystemPeriodicConstraints` needs to be called at each iteration after the assembly of the system, so it can be modified by adding the periodicity and anti-periodicity constraints that form systems (4.12), (4.11), (4.28), (4.29) and (4.36).

4.3 Verification of the properties of the boundary conditions

A few tests were made in fractured samples to verify the properties of the three types of boundary conditions mentioned in Section 2.2.1: Neumann, linear Dirichlet and periodic. The permeability and stiffness tensors were obtained for the unit cell of a periodic fractured media and for several REVs of random fractured media. The Neumann boundary conditions are the no-flow restrictions in Figure 2.4 for the flux problem and the constant tractions in Figure 2.5 for the mechanical problem; the Dirichlet boundary conditions are the linear pressures in Figure 2.2 for the flux problem and the linear displacements in Figure 2.3 for the mechanical problems.

4.3.1 Unit cell of periodic media

The fractured domain in Figure 4.4 is assumed to be a unit cell of a periodic media. The permeability and stiffness tensors were obtained for a grid of 1 x 1 to 40 x 40 unit cells with Neumann, linear Dirichlet and mortar periodic boundary conditions. In this latter, Γ_+ was taken as the mortar boundary, and the upper right corner node was prescribed to zero pressure and displacements. The mesh employed for one unit cell is presented in Figure 4.4, as well as one periodic media composed of 5 x 5 cells.

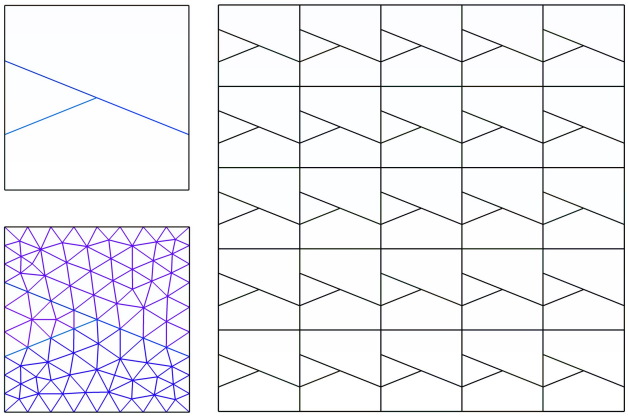

Figure 4.4: Geometry adopted for the experiments on fractured periodic media. On the left side, the unit cell, with fractures in blue, and its mesh are presented; on the right side, there is an example of periodic grid containing 5×5 unit cells.

The permeability tensor was obtained for conductive and blocking fractures. In both cases the permeability of the fractures is equal to $3.5 \times 10^{-10}\ m^2$; but for the first tests the matrix permeability is $1.0 \times 10^{-15}\ m^2$ while it is as high as $1.0 \times 10^{-9}\ m^2$ in the second ones, so the fracture will act as a barrier.

Figure 4.5 shows the pressure fields for the unit cells subjected to an injection in the x-direction with different boundary conditions; this is achieved by imposing a pressure-gradient in the x-direction for the Dirichlet and periodic boundary conditions and by prescribing a unit flux in the x-direction for the no-flow boundary conditions.

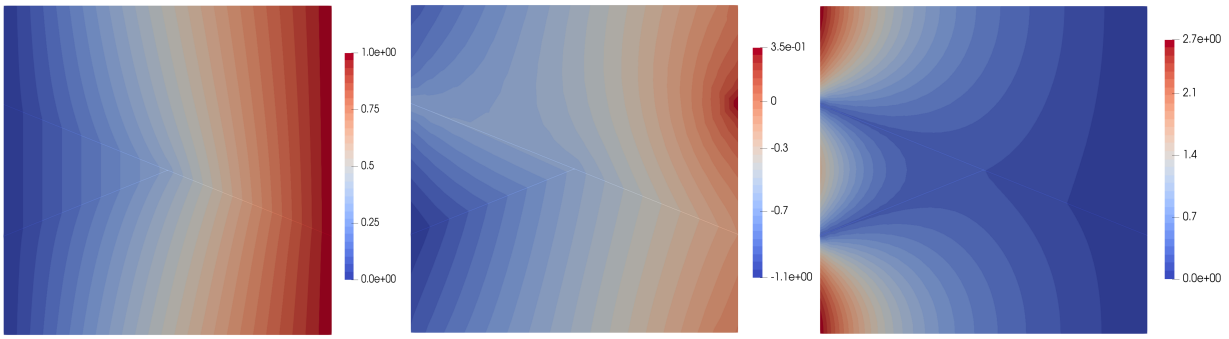

Figure 4.5: Pressure fields of the fractured unit cell for: a pressure gradient in the x direction of 1 kPa/m imposed with linear pressure (left) and periodic (center) boundary conditions and a unit flux of 1e-6 m/s in the x direction imposed with no-flow boundary conditions (right). The intrinsic permeability is $1.0 \times 10^{-15}\ m^2$ for the matrix and $3.5 \times 10^{-10}\ m^2$ for the fractures.

For the periodic boundary conditions, there is a higher localized gradient in the upper portion of the mortar side that is symmetric to the fracture; this results from the anti-periodicity of flux, which imposes the flux at the fracture to be equal to the flux at its opposite matrix node. Indeed, if this cell is repeated periodically, that would be the effect on the pressure gradient in the vicinity of the tip of a conductive fracture. Because of the existence of this non-periodic fracture node, the pressure field for the same gradient imposed with linear Dirichlet boundary conditions is different and overestimates the velocity of the injection in this fracture. The pressure fields for the no-flow boundary conditions can not be directly compared because this cell is subjected to a different pressure gradient, but the symmetric pattern in Figure 4.5 indicates that both fractures at the upstream boundary have the same effect; this is not the case when looking at the bigger picture, since the upper fracture node should not have the same drainage capacity for not being periodically connected to other fracture.

Figure 4.6 shows the pressure fields on the unit cells subjected to a flux in the y-direction for the blocking fracture case. Again, the linear pressure and no-flow boundary conditions can not predict the whole picture using one unit cell only, since they divide the media in three independent blocks as if no connectivity was present between them. The periodic

boundary conditions are more realistic; they provide smoother pressure gradients, since the matrix blocks are actually interconnected when the periodic pattern is considered.

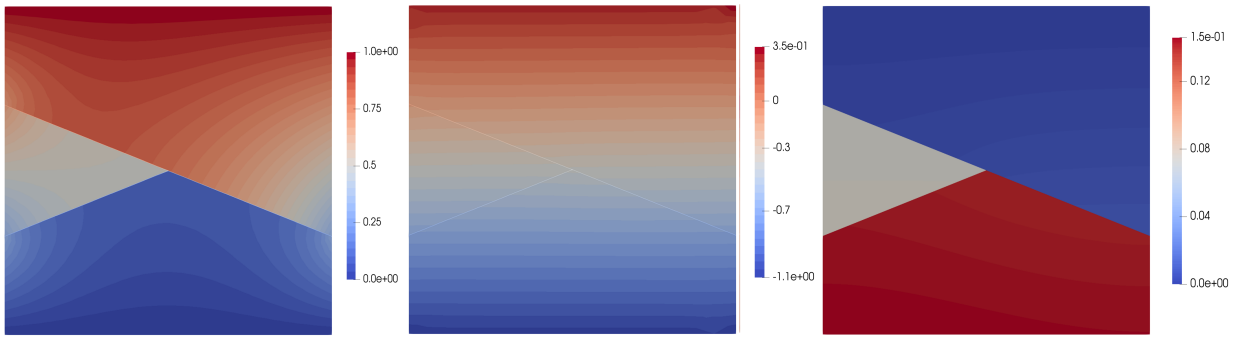

Figure 4.6: Pressure fields of the fractured unit cell for: a pressure gradient in the y direction of 1 kPa/m imposed with linear pressure (left) and periodic (center) boundary conditions and a unit flux of 1×10^{-14} m/s in the y direction imposed with no-flow boundary conditions (right). The intrinsic permeability is 1×10^{-5} m^2 for the matrix and 3.5×10^{-10} m^2 for the fractures.

Following Svenning et al. (2016), we present here the comparison of the constitutive tensors in terms of their eigenvalues. Figures 4.7 and 4.8 present the largest and smallest eigenvalues of the permeability tensor when imposing the three types of boundary conditions to grids containing increasing numbers of unit cells. The results agree with what is theoretically expected, since the periodic boundary conditions result in the final effective properties for one unit cell, while Dirichlet and Neumann boundary conditions give upper and lower bounds, respectively; also, these latter eventually converge to the values obtained with periodic boundary conditions.

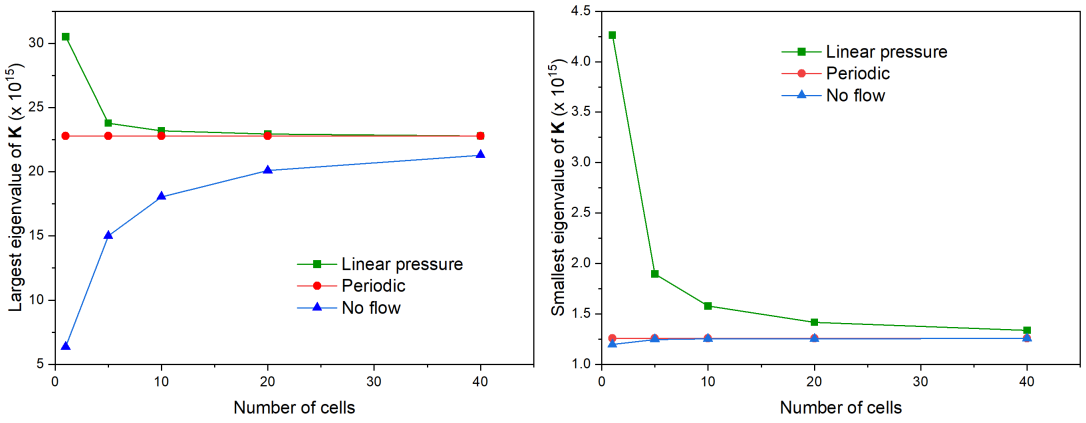

Figure 4.7: Smallest and largest eigenvalues of the upscaled permeability tensor $\boldsymbol{K}$ for the unit cell in subjected to linear pressure, periodic and no flow boundary conditions. The intrinsic permeability is 1e-15 m^2 for the matrix and 3.5e-10 m^2 for the fractures.

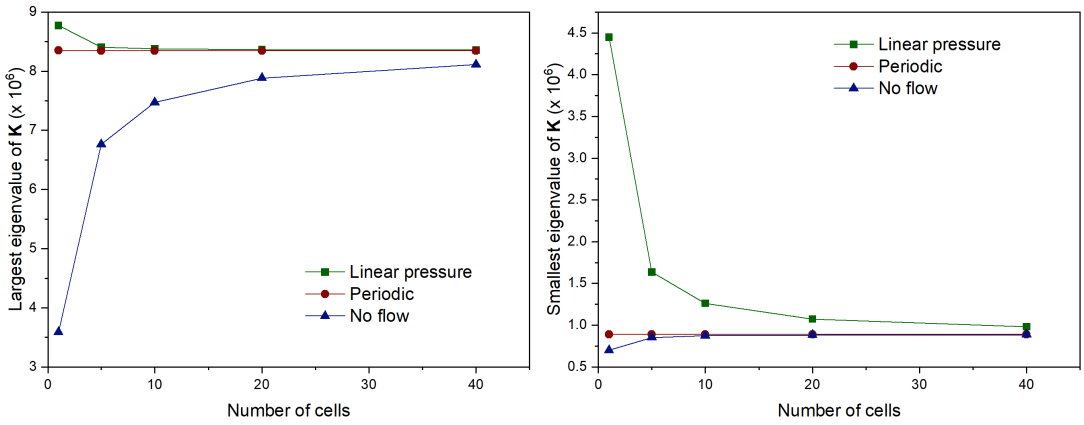

Figure 4.8: Smallest and largest eigenvalues of the upscaled permeability tensor $\boldsymbol{K}$ for the unit cell in Figure 4.4 subjected to linear pressure, periodic and no flow boundary conditions. The intrinsic permeability is 1e-5 m^2 for the matrix and 3.5e-10 m^2 for the fractures.

Figure 4.9 presents the smallest and largest eigenvalues for the upscaled stiffness tensor when using the elastic properties in Table 4.3. As expected, the periodic boundary conditions result in the final effective properties for only one unit cell, while linear displacement boundary conditions converge from above and constant traction boundary conditions converge from below. The linear displacement boundary conditions force the fractures to have zero displacement discontinuities at the boundaries; this reduces the fractures potential to slip under shear, which results in an overstiffness for small numbers of unit cells. In the case of the constant traction boundary conditions, the absence of displacements restrictions makes the mobilization of isolated blocks to be overestimated.

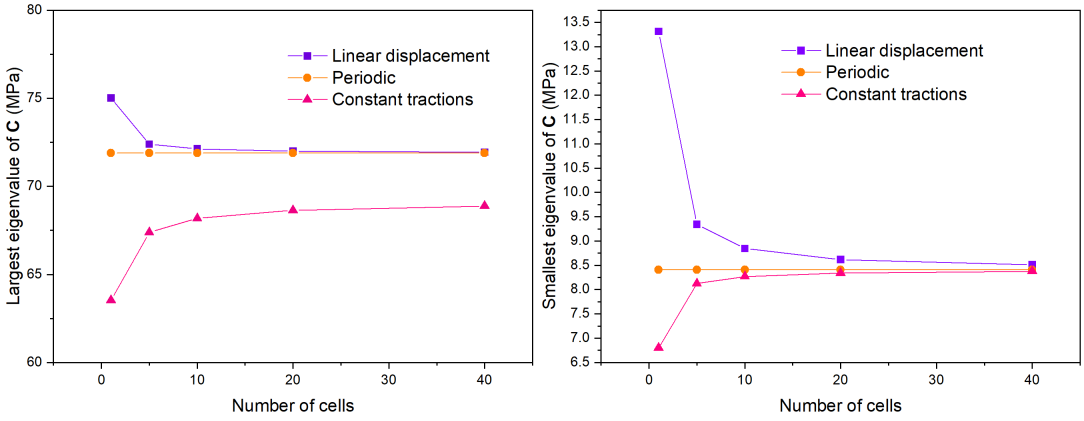

Figure 4.9: Smallest and largest eigenvalues of the upscaled stiffness tensor $\boldsymbol{C}$ for the unit cell in in Figure 4.4 subjected to linear displacements, periodic and constant traction boundary conditions.

4.3.2 Random media

The permeability and stiffness tensors were also obtained for 100 generations of the fracture network described in Table 4.2, which is the same one tested by Yang et al. (2014) to upscale elastic properties. The parameters of the intact rock and the fractures are described in Table 4.3. Five sizes that range from 4 to 20 m were tested.

Table 4.2: Statistical parameters used to generate the random fractured samples to be tested with three different boundary conditions: linear Dirichlet, Neumann and periodic. From Yang et al. (2014).

	Dip orientation			Length			Density
	Type	Mean	Std. Deviation	Type	Mean(m)	Std. Deviation (m)	$(1/m^2)$
Set 1	Normal	150	10.0	Normal	4	1	0.16
Set 2	Normal	50	7.0	Normal	3	0.7	0.25

Table 4.3: Elastic properties and permeability for the intact rock and the fractures used to compare linear Dirichlet, Neumann and periodic boundary conditions.

Intact rock			Fracture		
E (GPa)	ν	$k_m(m^2)$	K_n (GPa/m)	K_t (GPa/m)	$k_f(m^2)$
50.0	0.25	1.0×10^{-14}	50.0	10.0	3.5×10^{-10}

Figure 4.10 shows that the mesh and the geometries are far from being periodic.

A small maximum element area was selected to avoid mesh size effects. As the the mortar method enforces periodicity weakly, the resultant nodal values at the boundaries are sensitive to the size of the elements. Also, if the mesh densities at opposite sides are significantly different, the choice of the mortar and non-mortar boundaries impacts the results. To avoid these effects, we performed mesh tests on ten random samples. The maximum element area was selected based on the convergence of the upscaled properties with mesh size. Also, for the selected mesh size, the upscaled properties were not influenced by the choice of Γ_+ or Γ_- to be the mortar size.

In the tests performed on all the one hundred DFNs, the boundary Γ_+ was taken as the mortar side, so the upper right corner node is prescribed to zero pressure and displacements.

Figures 4.11, 4.12, 4.13 and 4.14 show the average value and the COV of the smallest and largest eigenvalues for the permeability and the stiffness tensors for different REV sizes. For both the mechanical and hydraulic tests, the same trend repeats: the Neumann, periodic and Dirichlet boundary conditions provide lower, intermediate and upper bounds for the average of the properties, respectively. The COVs are also different for smaller sizes, but they converge to approximately the same value faster than the average properties.

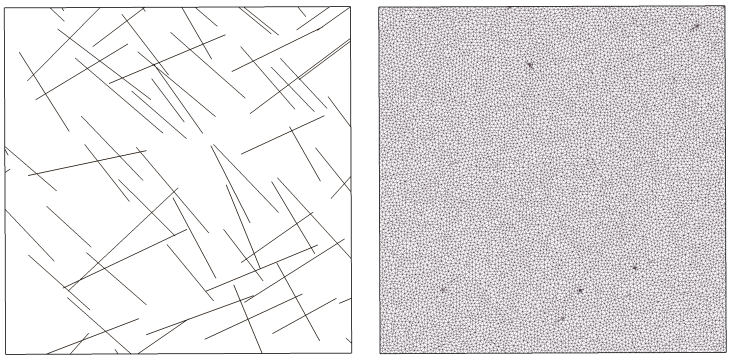

Figure 4.10: Example of one of the DFNs generated to compare the elastic and permeability tensors obtained with three types of periodic boundary conditions: linear Dirichlet, Neumann and mortar periodic. On the right side, the mesh generated for a maximum element area calibrated after convergence tests.

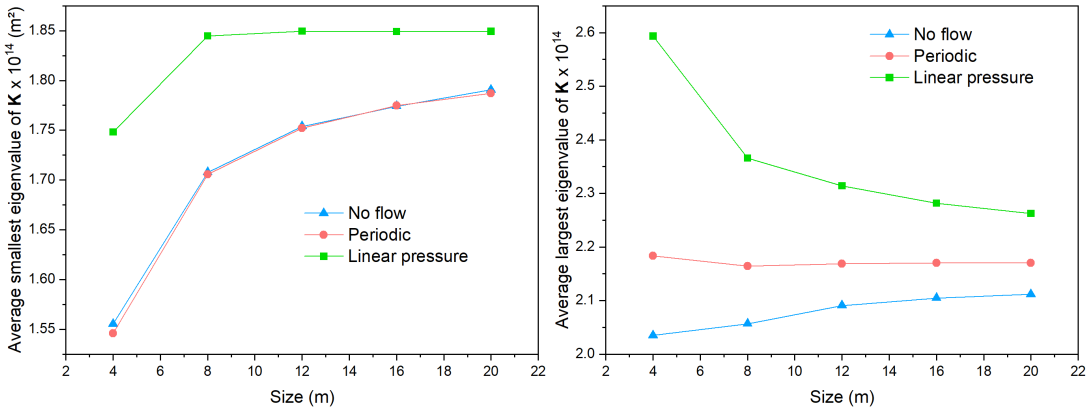

Figure 4.11: Average eigenvalues of the equivalent permeability tensor $\boldsymbol{K}$ for 100 realizations of the fracture network describe in Table 4.2 when using linear pressure, periodic and no-flow boundary conditions.

4.4 Conclusions of the chapter

In this chapter, we presented the methods used to impose periodic boundary conditions in flow and equilibrium problems on fractured domains. They require the addition of constraints of periodicity of the primary variables and anti-periodicity of fluxes and forces to the original systems of equations.

Two methods were implemented to manage the imposition of periodic boundary conditions. The first one requires a periodic mesh to impose a strong periodicity on the domain. Adaptions were proposed to deal with non-periodic geometries containing interface elements; they restrain the discontinuities in these cases. The second method is the mortar element method, which has been recently applied to impose weak periodicity on heterogeneous domains. To our best knowledge this method has not been applied to media containing triple-

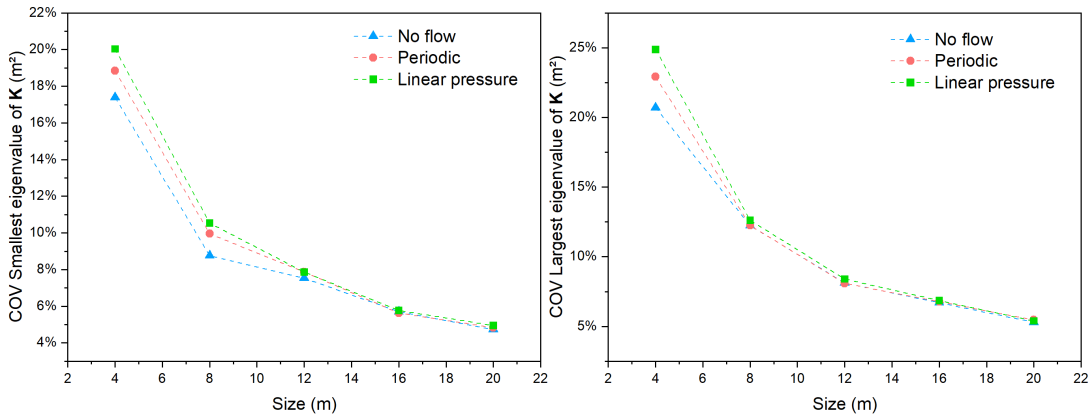

Figure 4.12: Coefficients of variation of the equivalent permeability tensor $\boldsymbol{K}$ for 100 realizations of Network 1 when using linear pressure, periodic and no-flow boundary conditions.

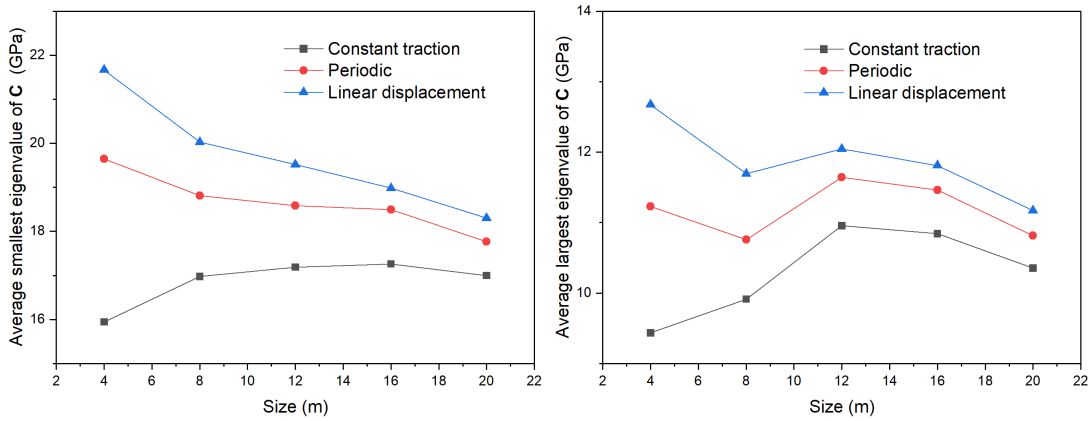

Figure 4.13: Average eigenvalues of the equivalent stiffness tensor $\boldsymbol{C}$ for 100 realizations of Network 1 when using linear displacements, periodic and constant traction boundary conditions.

nodded interface elements, so we proposed modifications to use them in the flux problem.

These new implementations were applied in the upscaling of elastic properties and permeability of periodic and random media. Linear Dirichlet, periodic and Neumann boundary conditions were compared. The results agree with what is reported in the literature, which is that the periodic boundary conditions result in an intermediate value for the equivalent properties, while Dirichlet and Neumann boundary conditions provide upper and lower bounds, respectively. Also, the properties obtained by the different boundary conditions become closer as the REV size increases.

The periodic boundary conditions are not necessarily more efficient in the sense of requiring smaller REVs. The COVs obtained for the equivalent constitutive tensors converge to similar values for all the boundary conditions types; so, if a variability-based criterion such as the COV is to be used, the REV size for the tested DFN would be similar for all

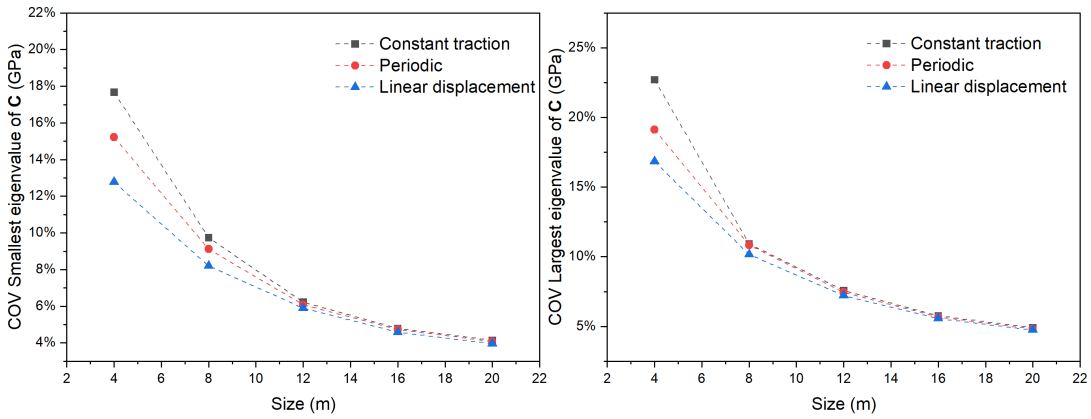

Figure 4.14: Coefficients of variation of the equivalent permeability tensor $\boldsymbol{C}$ for 100 realizations of Network 1 when using linear displacements, periodic and constant traction boundary conditions.

types of boundary conditions.

However, the average values obtained with periodic boundary conditions converge faster to the final effective average properties. Also, for periodic domains the periodic boundary conditions do provide more realistic fields of the studied quantities. So, they are more efficient for the applications that will follow, for which a REV for fractured random media will be considered to periodically repeat itself in the macroscopic domain.

Chapter 5

Statistics-based methodology to select the REV size

Although the fractures measured in the field can be grouped in sets according to their common features and geological history, their geometries always present a variability. As a consequence of the stochastic nature of natural fractures, the hydro-mechanical properties taken from selected samples are also variable, and this should be considered when defining the REV of naturally fractured reservoirs.

A rigorous definition of the REV of random media should be based on the criterion of spatial stationarity (Equation 2.5), which means that the local mean of a property must be invariant for different samples of same size. Of course, the mean value of a property taken from random media is never really invariant, but it can be considered to be approximately constant when its variance is low. Thus, both the mean value and standard deviation of the hydro-mechanical properties are considered to define the REV of fractured media when a statistical approach is used; the coefficient of variation (COV) is one of the most popular criteria to define a minimum size.

Most of the existing works that define the REV of fractured media based on the COV of the equivalent property do not use a large number of samples due to computational limitations and to the difficulty of automatically generating meshes when complex DFNs exist. Also, many of the existing results lack generality and draw conclusions for a specific fracture network measured in the field. Another issue is that the COV does not account for the uncertainty associated to the number of generated REVs, although the calculated mean and standard deviations are less reliable as this number gets smaller.

These issues were addressed in the paper entitled General statistics-based methodology for the determination of the geometrical and mechanical Representative Elementary Volumes of fractured media, published in the Rock Mechanics and Rock Engineering journal (Loyola et al., 2021). This work introduced a statistics-based methodology to calculate the geometrical and mechanical REV sizes of fractured media. The methodology uses the Central Limit Theorem (CLT) to simplify and generalize the procedure of defining the REV based on a

variability-related criterion.

This chapter is dedicated to the presentation of this methodology and of the results obtained in Loyola et al. (2021) for the geometrical and mechanical properties of fractured media. Then, Section 5.5.4 explores the applicability of this methodology to define the REV for permeability considering two scenarios: constant and variable aperture.

5.1 Sampling of the mean and the Central Limit Theorem

Consider a variable x that follows a certain probability distribution $f(x)$. In most practical applications, the true mean μ_x and the true standard deviation σ_x of x are unknown and need to be estimated. For that, a sample S_x must be taken from the population of x, which can be generally represented as:

$$S_x = \{x_1, x_2 ... x_n\} \tag{5.1}$$

Note that S_x is a sample of samples: it contains the samples $x_1 ... x_n$, but, at the same time, it is a sample of the many possible sets of n values that could be taken from the population. The number n is called its sample size. From now on, the word sample will refer to a set S_x such as the one in (5.1); the term sample size will refer to the number n of values of x in S_x and the term component or individual sample will refer to a value such as x_i.

The average $\overline{x}$ and the standard deviation s of the components of S_x provide an estimator for the true mean value and the standard deviation of x . If various samples S_x of size n are repeatedly taken, and for each of them the average $\overline{x}$ is calculated, it is possible to obtain the distribution $f(\overline{x})$. The Central Limit Theorem (CLT), which is the second fundamental theorem of statistics, states that as $n \to \infty$ the distribution $f(\overline{x})$ approaches a normal distribution with mean $\mu_{\overline{x}}$ and standard deviation $\sigma_{\overline{x}}$, where:

$$\mu_{\overline{x}} = \mu_x \tag{5.2}$$

$$\sigma_{\overline{x}} = \frac{\sigma_x}{\sqrt{n}} \tag{5.3}$$

The CLT works when most of the random variables are independent and when important outliers are not present. It is a powerful theorem because it works for variables that follow any distribution; thus, even if x follows a distribution that is far from normal and that may not be described by any known mathematical function, $\mu_{\overline{x}}$ will tend to a normal distribution that is ruled by Equations 5.2 and 5.3. Normality can be observed from a certain sample size. A general rule of thumb states that when $n = 30$, a normal distribution can be observed. However, this size actually depends on the variable's distribution $f(x)$: it can be much bigger if $f(x)$ is far from a normal distribution, or significantly smaller if $f(x)$ is nearly normal.

The CLT does not apply only to the average value, but to any sum A_x of the type:

$$A_x = \frac{1}{T} \sum_{i=1}^{n} x_i \tag{5.4}$$

where T is an arbitrary scaling parameter. In this case, the distribution $f(A_x)$ tends to be normal with mean μ_{A_x} and standard deviation σ_{A_x}, where:

$$\mu_{A_x} = \frac{n}{T} \mu_x \tag{5.5}$$

$$\sigma_{A_x} = \frac{\sqrt{n}}{T} \sigma_x \tag{5.6}$$

If A_x is the average value, $T = n$ and Equations 5.5 and 5.6 become Equations 5.2 and 5.3, respectively. Note that Equation 5.3 states that the standard deviation of the sample's mean decreases when the sample size increases. This is intuitive, since bigger samples are expected to generate estimations that are closer to the true mean.

Based on the normality of the distribution of the sample's mean, the following confidence interval can be built for the average value $\overline{x}$, estimated from N samples S_x:

$$\overline{x} \pm {t^*}_{\alpha,n_d} \frac{s}{\sqrt{N}} \tag{5.7}$$

where ${t^*}_{\alpha,n_d}$ is the t-value associated to the confidence level α and the number of degrees of freedom n_d, where $n_d = N_{\overline{x}} - 1$ and $N_{\overline{x}}$ is the number of samples used to estimate the average. For a degree of confidence $\alpha = 0.05$, for example, a 95% confidence interval is built for the calculated average $\overline{x}$, which means that there is a 95% chance that the true mean is inside this interval.

5.2 Sampling theory applied to REVs

A parallel can be drawn between REVs and the concepts presented in the previous section. The REV of a fractured rock mass can be regarded as a sample of fractures. In this perspective, the sample size is then the number of fractures n_f in the REV, which in turn is directly related to the volume V of the REV as:

$$n_f = V \sum_{s=1}^{n_s} {P_0}^{(s)} = V P_0 \tag{5.8}$$

where n_s is the number of fracture sets, ${P_0}^{(s)}$ and P_0 are the expected fractured density of the s^{th} set and of the network. The fracture density is the number of fractures per unit volume/area, depending on the problem being 2D or 3D.

The statistical theory of the sampling of means provides meaningful insights for studies

on REVs because the REV, by definition, must be representative of the mean constitutive behavior. Thus, a rigorous choice of the REV must be based on the accuracy of the average of the homogenized properties. This was acknowledged by several works on fractured rocks that select the REV based on the COV, which measures variability with respect to the average.

The existing works on fractured media, however, do not propose any general rule for the relationship between REV size and variability. Also, although the COV is a logical criterion, it does not account for the uncertainty related to the number of simulated samples. This would be an important consideration since the number of simulations may face computational limitations. For instance, several works on the REV for mechanical properties of fractured media that use Monte Carlo Simulations (MCS) do not use a large number of realizations: e.g. Min and Jing (2003) and Esmaieli et al. (2010) used no more than ten simulations per size to define the REV based on DEM simulations.

In order to account for the number of tested REVs, the COV can be replaced by a precision error ε_{rel} related to the confidence interval in Equation 5.7 which is obtained by:

$$\varepsilon_{rel} = \frac{\varepsilon_{abs}}{\overline{x}} = t^*{}_{n_d,\alpha} \frac{s(V)}{\overline{x}\sqrt{N}} \tag{5.9}$$

The confidence interval of the average was already suggested by Kanit et al. (2003) as a criterion to select the REV for composites. Note that the standard deviation s is a function of the volume V. In order to define this function, the authors perform a large number of simulations for different REV sizes. Then, if a desired error and a number of realizations N is set, a volume V can be calculated. The REV can be defined as the volume for which one simulation ($N = 1$) is required to obtain a desired precision error. If a 95% degree of confidence is set, this would mean that a REV with the calculated size would have a 95% chance of returning a value for a property that does not differ from the true mean of this property by more than the set error. Alternatively, one can impose a volume and calculate the number of realizations N required to attend the error criterion. This methodology can be readily applied to fractured media studies, as was done by Caspari et al. (2016). The methodology suggested in Loyola et al. (2021) simplifies this procedure by taking advantage of the CLT, as will be explained below.

Consider a property Z of a fractured rock mass. For two different volumes V_1 and V_2, Equation 5.2 states that for both volumes the average $\overline{Z}$ has the same mean value and Equation 5.3 can be used to establish the following relationship:

$$\sigma_{\overline{Z}}(V_2) = \sigma_{\overline{Z}}(V_1) \sqrt{\frac{n_f(V_1)}{n_f(V_2)}} \tag{5.10}$$

The standard deviation $\sigma_{\overline{Z}}(V_i)$ is estimated by $s(V_i)$, which is the standard deviation of the average $\overline{Z}$ taken from N REVs of volume V_i. The number of fractures n_f corresponds to the sample size n.

By replacing the number of fractures in volumes V_1 and V_2 for (5.8) and considering that their P_0 is approximately the same, (5.10) can be reformulated as:

$$\sigma_Z(V_2) = \sigma_Z(V_1)\sqrt{\frac{V_1}{V_2}} \tag{5.11}$$

Equations 5.10 and 5.11 show that it is possible to estimate the standard deviation of $\overline{Z}$ associated to any REV size by obtaining $s_{\overline{Z}}$ for one reference volume (V_1) only, given that this reference volume contains a sample size large enough for $\overline{Z}$ to follow an approximately normal distribution.

A first important property for which Equations 5.10 and 5.11 apply is the crack tensor $\boldsymbol{F}$ in (2.34) and (2.36). All of the components in the fracture tensor, including its first invariant, are a sum S_f of the form:

$$S_f = \sum_{k=1}^{n_f} \frac{Y^{(k)}}{V} \tag{5.12}$$

where $Y^{(k)}$ is a variable obtained from the product of geometrical features of the fracture k such as the normal vector components and area, and V is the volume of the rock mass, which can be replaced by (5.8) to obtain:

$$S_f = F_{ij} = \sum_{k=1}^{n_f} \frac{Y^{(k)} {P_0}^{(V)}}{n_f} = \sum_{k=1}^{n_f} \frac{X^{(k)}}{n_f} \tag{5.13}$$

Thus, each component of the fracture tensor is the average of a variable X that contains information on the geometry of a fracture and on the density over the domain. As such, regardless of what the distribution of Y is, the fracture tensor components tend to a normal distribution, as stated by the CLT, and their mean value and standard deviation can be estimated by Equations 5.2 and 5.3. Also, Equations 5.10 and 5.11 can be used to predict the standard deviations of the fracture tensor components for any volume if the standard deviations for one volume only are known.

There are two main arguments that sustain the idea that the CLT also applies to the hydromechanical properties. Firstly, these properties are calculated from volumetric averages of the stresses and strains (Equation 2.10) and of the pressure gradients and fluxes (Equation 2.15), which, for being averages, theoretically follow the CLT.

A second argument is that there is a reported strong relationship between the hydromechanical properties and the fracture tensor. Functions that relate mechanical and hydraulic properties to the components of the fracture tensor were derived by Oda et al. (1984) and Oda (1985), for example. As long as these functions are continuous, they should respect the Delta Method, which is a well known theorem in statistics that states that any differential function $g(Y)$ of a variable Y that has a limiting normal distribution also tends to a normal distribution. The Delta method uses a Taylor expansion truncated at the second term to calculate the standard deviation of $g(Y)$, whose limiting normal distribution is the following:

$$g(Y) \approx N\left(g(\mu_Y), (g'(\mu_Y))^2 \frac{\sigma_Y^2}{n_Y}\right) \tag{5.14}$$

where μ_Y, σ_Y and n_Y are the mean value, standard deviation and sample size of Y. As the function g becomes closer to linear and the sample size becomes bigger, the truncated Taylor expansion is a better estimation for g and its distribution converges faster to (5.14).

According to the Delta method, if the hydro-mechanical properties are a function of the fracture tensor, they also theoretically tend to a normal distribution. Of course, these properties depend also on other factors, such as the boundary conditions applied to the simulated volume, the current state of the sample and other geometrical aspects that are not captured by the crack tensor. Nonetheless, the following sections will show that the hypothesis of normality and Equations 5.10–5.11 work well for different DFNs and can be used to simplify the definition of a REV for fractured media while accounting for its stochastic nature.

5.3 Methods

This section presents the methodology employed by Loyola et al. (2021) to obtain the geometrical and mechanical REV of two fracture networks. A similar approach was later used in the present work to estimate the REV for permeability estimation, with the main differences being the number of tested REVs, a change in the fracture intensity of one of the networks and the computational tool used to solve the numerical problems. While Loyola et al. (2021) solved the mechanical problems with a FEM code whose functions were later transferred in part to DuMu^X, the equivalent permeability was calculated in this chapter using the Box method in DuMu^X.

Equations 5.10 and 5.11 were tested for the DFNs used by Yang et al. (2014) and Min and Jing (2003), which will be hereinafter referred to as Networks 1 and 2, respectively. Tables 5.1 and 5.2 present the statistical characterization of these networks. For Network 1, the length of the two existing sets follow normal distributions with different means and standard deviations. As was shown by Loyola et al. (2021), the combination of these two sets results in an equivalent distribution for the length that is more skewed than a normal one. As for the lengths in Network 2, they are described by power-laws, which are even further from normal.

Table 5.1: Statistical parameters for Network 1, from Yang et al. (2014).

	Dip orientation			Length			Density
	Type	Mean(°)	Std. Deviation (°)	Type	Mean(m)	Std. Deviation (m)	(1/m^2)
Set 1	Normal	150	10.0	Normal	4	1	0.16
Set 2	Normal	50	7.0	Normal	3	0.7	0.25

Table 5.2: Statistical parameters for Network 2, from Min and Jing (2003). D and k are coefficients of the power-law and Fisher distributions.

	Dip/ Dip direction			Length			Density
	Type	Mean(°/ °)	k	Type	Mean(m)	D	($1/m^2$)
Set 1	Fisher	8/145	5.9	Fractal	0.92	2.2	4.6
Set 2	Fisher	88/148	9.0	Fractal	0.92	2.2	4.6
Set 3	Fisher	76/21	10.0	Fractal	0.92	2.2	4.6
Set 4	Fisher	69/87	10.0	Fractal	0.92	2.2	4.6

Both works calculated the equivalent elastic tensor for the studied rock masses and obtained the REV size for the elastic properties by progressively reducing the sample's volume. A deterministic approach was used for Network 1, while for Network 2 the authors used MCS to generate 10 statistically equivalent samples. A similar approach is used here, with the difference that 1000 samples were generated for each tested size. Figure 5.1 shows the process of generating samples. The stress boundary conditions illustrated in Figure 2.5 were applied to the rock samples and Equations 2.10, 2.25 and 2.32 were used to obtain the elastic compliance tensor.

Network 1 was tested for 11 different square REVs with sizes that range from 2 m x 2 m to 22 m x 22 m. Network 2 was tested for 9 sizes that range from 0.5 m x 0.5 m to 8 m x 8 m. The DFNs were stochastically generated with a Poisson process in an initial large domain and increasingly smaller domains were cut out from the original one while maintaining the same geometrical center. At each size reduction, the fractures whose centers lied outside of the new domain were removed; those whose centers lied inside the new domain but intersected its boundaries had their lengths adjusted. The purpose of the removal of these external fractures is to not consider fractures that would not be generated by an independent Poisson process at each REV (Loyola et al., 2021) and thus to make the fracture density P_0 approximately equal for all sizes. This eliminates the so-called boundary effects demonstrated by Min et al. (2004a) and allow for the use of (5.11). Alternatively, if the common approach of not removing external fractures were used, (5.10) would apply.

Meshes constrained by the DFNs were generated with calls to the software Triangle (Shewchuk, 1996) at the beginning of each simulation. Figure 5.2 shows an example of a generated DFN and its correspondent mesh for each study case.

Then, interface elements were created with the procedure illustrated in Figure 3.2 by calling the open-source code ciGen (Nguyen, 2014), which was modified to duplicate the nodes only at edges where fractures are present. Not all simulations were successful because of the precision of the output files of Triangle, which created overlapping nodes for fractures that were too close from each other. The minimum number of successful simulations was 950 for the 22 m x 22 m REV of Network 1 and 751 for the 8 m x 8 m REV of Network 2.

In the numerical experiments, both the intact rock and the fractures are considered to be

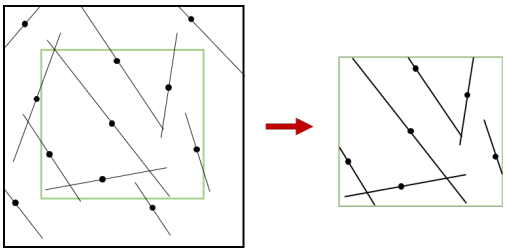

Figure 5.1: Generation of smaller REVs from bigger ones: geometrical center is maintained, external fractures are removed and boundary intersections are adjusted.

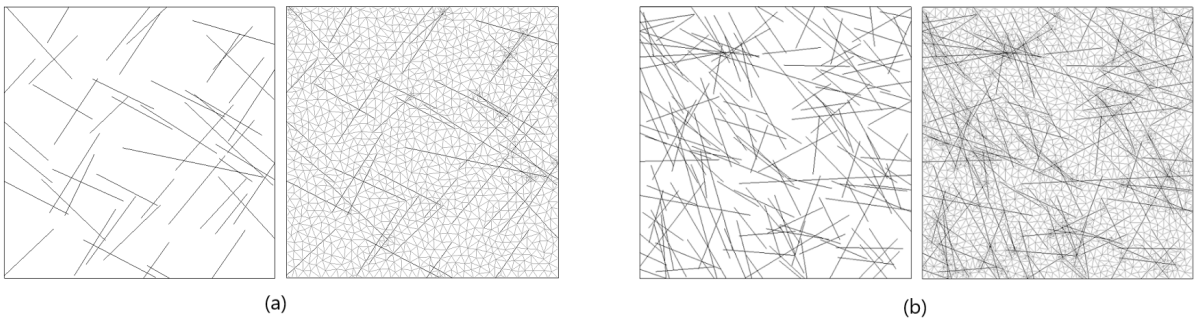

Figure 5.2: Examples of DFNs and conforming meshes for (a) Network 1 and (b) Network 2.

linear elastic materials. Their properties, which were taken from the reference publications, are described in Table 5.3.

Table 5.3: Elastic properties for the intact rock and the fractures of both study cases according to Yang et al. (2014) and Min and Jing (2003).

	Intact rock		Fracture	
	E (GPa)	ν	K_n (GPa/m)	K_t (GPa/m)
Network 1	50.00	0.25	50.00	10.00
Network 2	84.60	0.24	434.00	86.80

5.4 Results for the Geometrical REV

Figures 5.3 and 5.4 show Q-Q plots for the elements of the crack tensor of Networks 1 and 2. It is clear that as the size of the REV increases, the crack tensor approaches a normal distribution. The 2 m x 2 m REV of Network 1 is severely skewed because its size is smaller than the average fracture spacing, and thus some of the tested domains did not contain any

fractures. Figure 5.5 shows the average of the crack tensor components and its first invariant for the tested sizes.

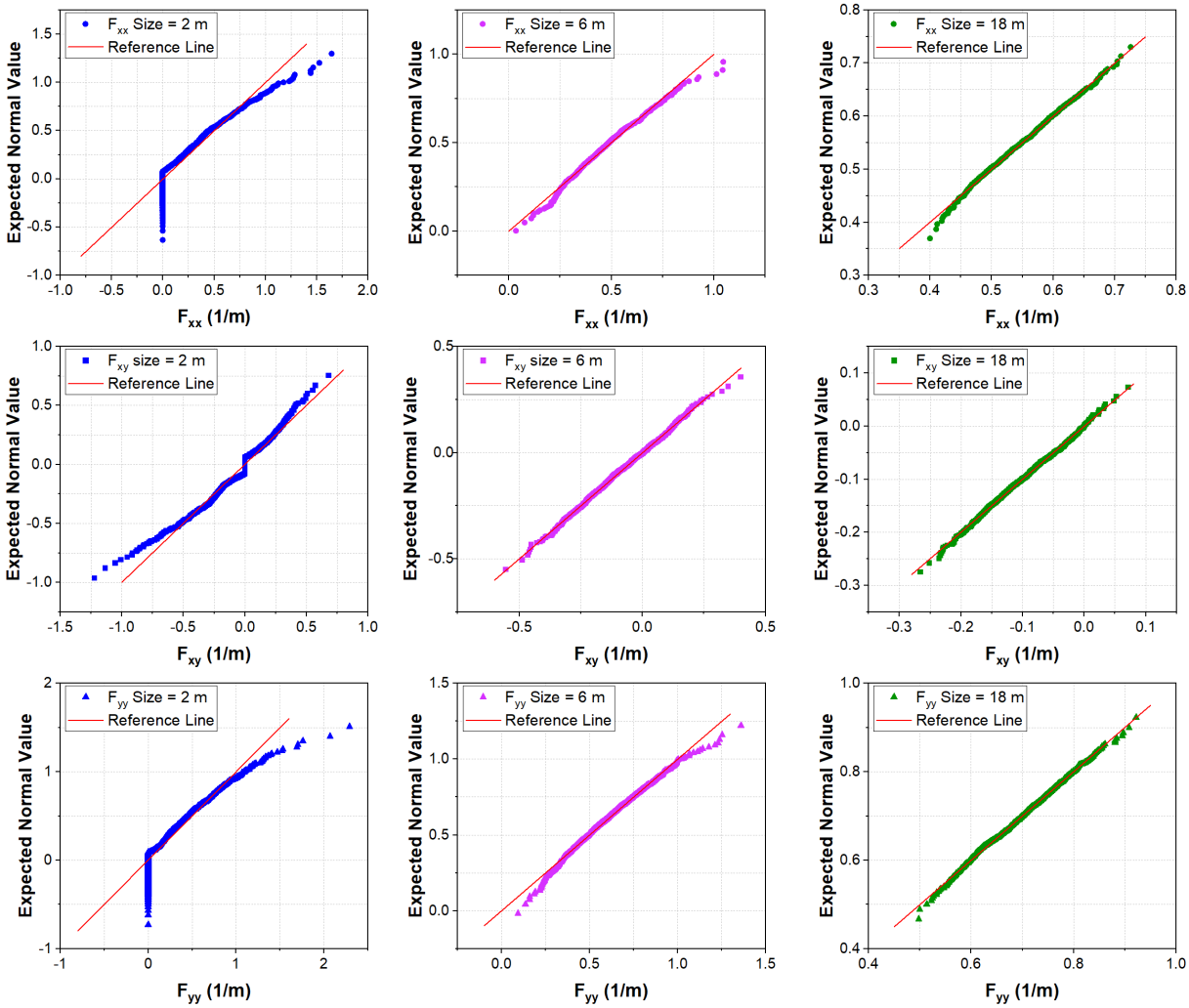

Figure 5.3: Q-Q plots for the fracture tensor of Network 1.

The smallest sizes for which the averages seems to stabilize are 6 m for Network 1 and 3 m for Network 2. Also, these are the first sizes to present maximum absolute values of 0.5 and 1.0 for the skewness and kurtosis, respectively, which are commonly used rules of thumb to attest the normality of a distribution. These criteria are conservative when compared to the confidence intervals built by Jones (1969) for these parameters. From the densities in Tables 5.1 and 5.2, these sizes have an expected number of fractures of 15 and 166, respectively. As Network 2 presents a length distribution that is much further from normality than Network 1, it is unsurprising that it requires a larger sample size to lead to approximately normal distributions of the crack tensor components.

By adopting the sizes of 6 m and 3 m as reference volumes for Network 1 and Network 2, respectively, their standard deviations can be used to predict the standard deviations

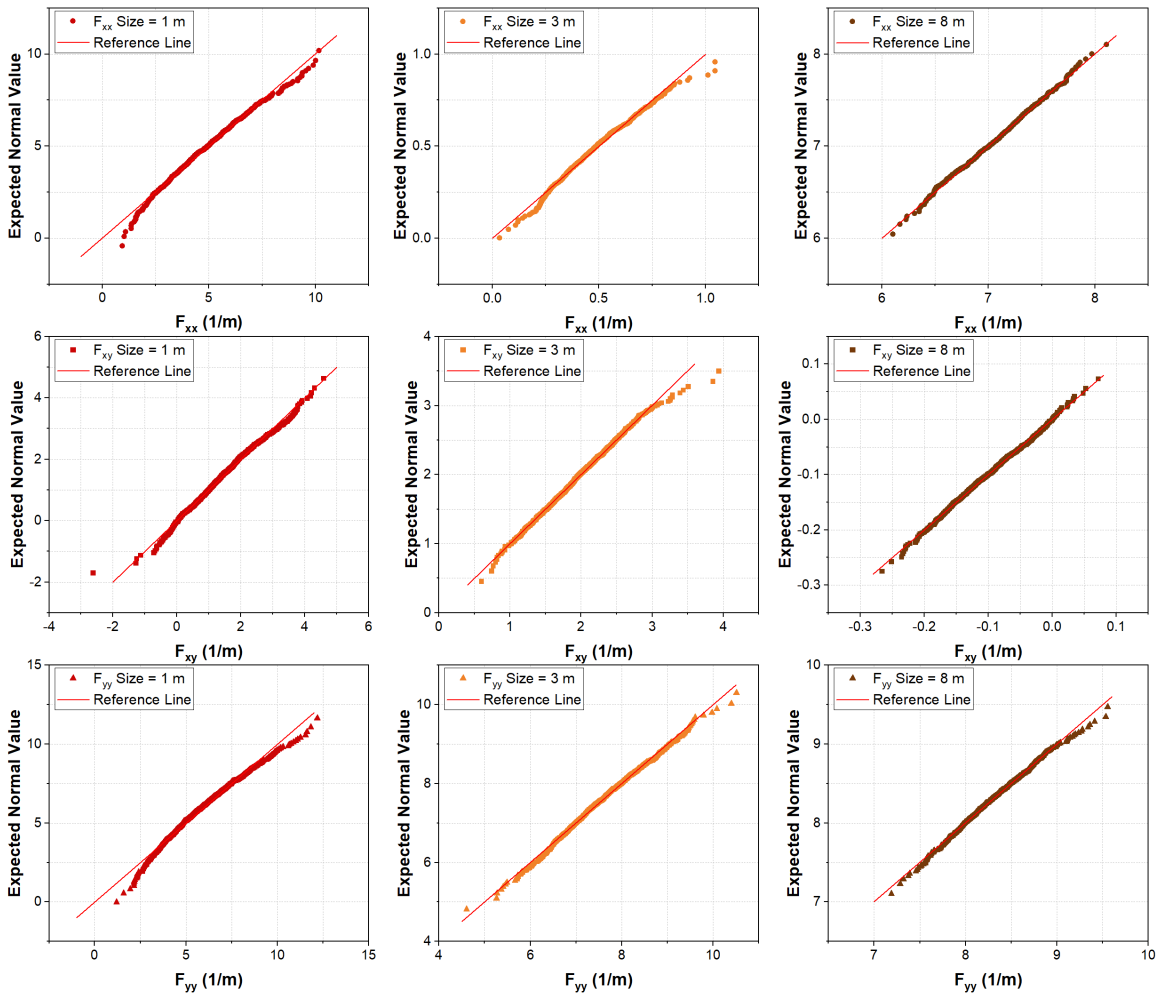

Figure 5.4: Q-Q plots for the fracture tensor of Network 2.

for any other volume using Equation 5.11. Figures 5.6 and 5.7 compare the predicted and calculated standard deviations. Except for the smaller values, for which the distribution of the crack tensor can not be considered to follow a normal distribution yet, the predictions are accurate. Thus, it is proved that if DFNs are generated for a proper reference volume, this volume can be used to calculate the geometrical REV using the error criterion in (5.9), with no need to generate fractured samples of different sizes.

Figures 5.6 and 5.7 show the best fit power laws for the standard deviations as a function of the REV size. By replacing s in (5.9) by the power function aL^b and setting $N = 1$, the size L of the geometrical REV can be calculated as:

$$L = \left(\frac{\overline{x}\, \varepsilon_{rel}}{1.96\, a} \right)^{1/b} \tag{5.15}$$

where 1.96 is the t-value corresponding to the number of samples of the reference volume and to a 95% degree of confidence. If a 10% error is set, the resulting sizes L for the diagonal

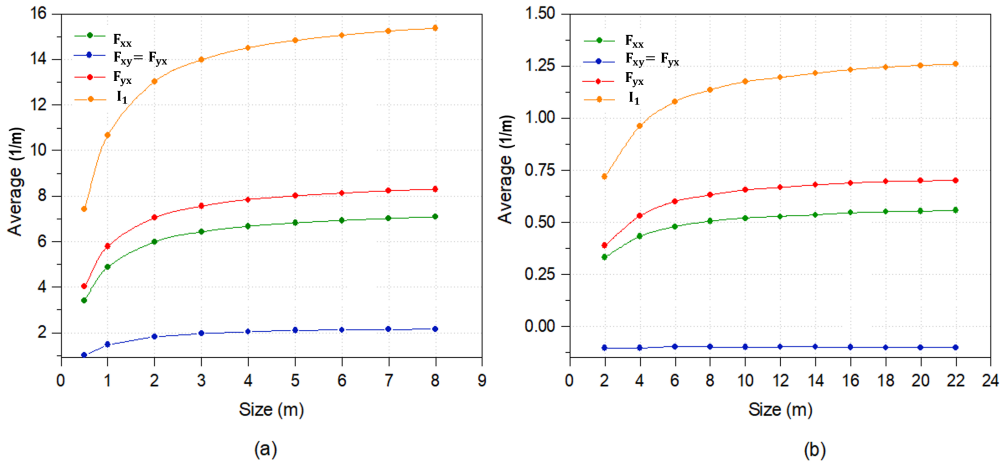

Figure 5.5: Average values of the fracture tensor components for (a) Network 1 and (b) Network 2.

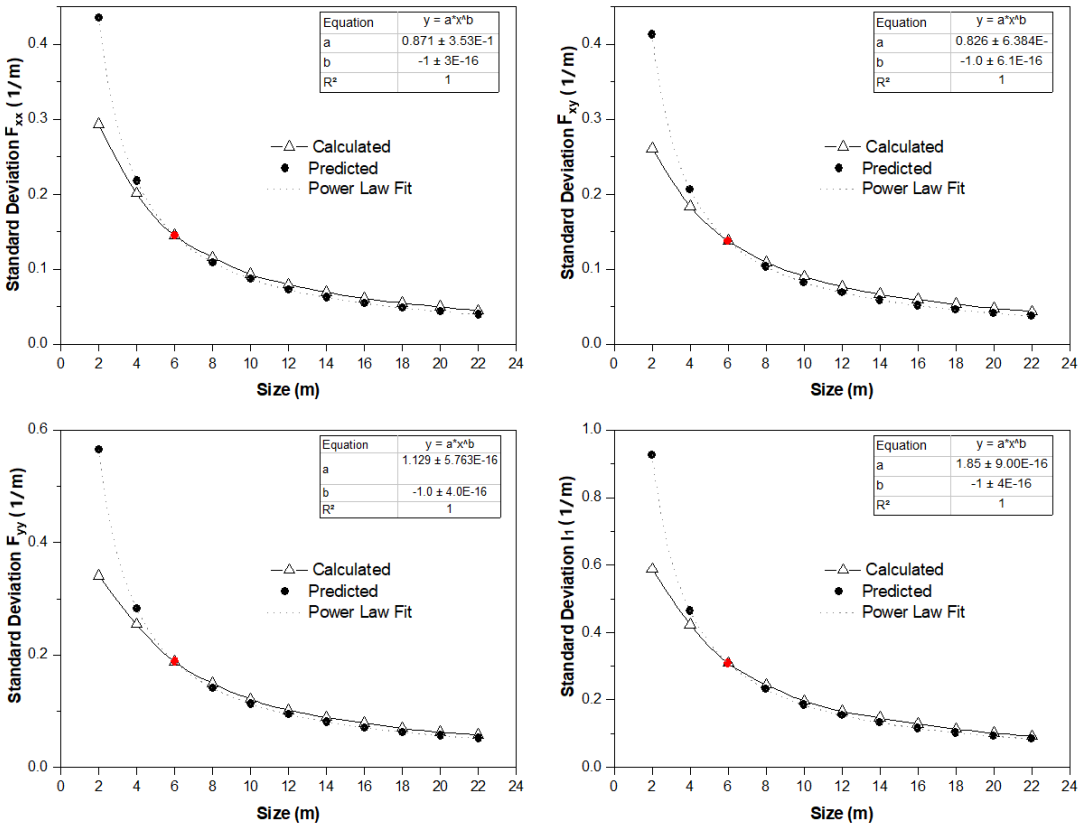

Figure 5.6: Predicted and calculated curves of the standard deviation of the fracture tensor components of Network 1 vs REV size. The red dot signalizes the reference volume.

components F_{ii} of the crack tensor and of its first invariant I_1 are the ones presented in Table 5.4.

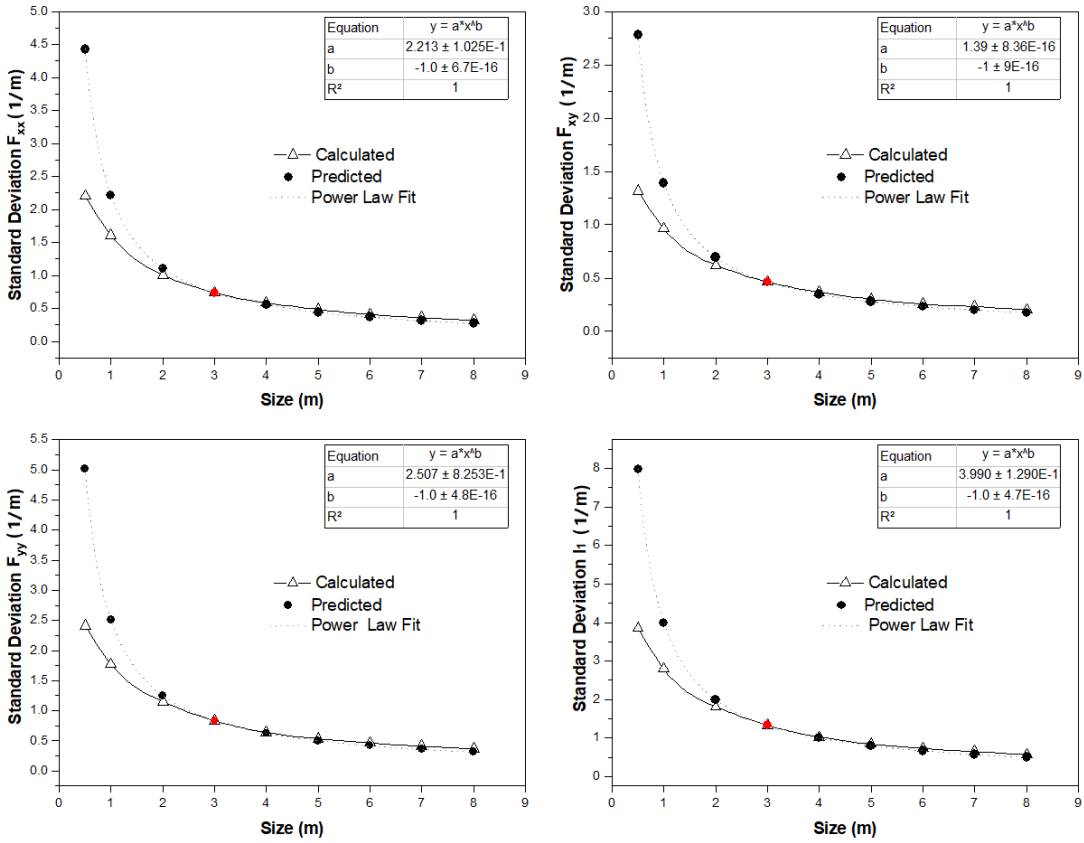

Figure 5.7: Predicted and calculated curves of the standard deviation of the fracture tensor components of Network 2 vs REV size. The red dot signalizes the reference volume.

Table 5.4: Calculated geometrical REVs for a 10% error.

	Network 1			Network 2		
	F_{xx}	F_{yy}	I_1	F_{xx}	F_{yy}	I_1
Size (m)	35.7	37.0	33.7	6.8	6.5	5.6

The diagonal components F_{ii} and the first invariant I_1 were chosen for being strongly related to the mechanical properties, as was discussed in Section 2.3. Based on these quantities and on a 10% error, the geometrical REV size is 37 m for Network 1 and 6.8 meters for Network 2, which both are the largest values for each network. This means that one generation of DFNs in volumes with these dimensions are 95% likely to return geometrical measures that do not dist from their true mean by more than 10%.

5.5 Results for the Mechanical REV

5.5.1 Results for the elastic properties

Loyola et al. (2021) obtained the equivalent elastic tensor for all of the generated REVs, which resulted in 11,000 simulations for Network 1 and 9,000 simulations for Network 2. The focus of the work was the elastic moduli E_x, E_y and G_{xy}. Their results will be presented here.

The explanation for why the CLT applies to the elastic moduli was based on their relationship with the first invariant of the fracture tensor, I_1, which is shown in Figures 5.8 and 5.9. A linear fit is a good estimation for this relationship. It is not perfect for two reasons: firstly, I_1 is not the only factor that affects the elastic moduli, which also depend on other geometrical features, such as the particular intersections between the fractures in each DFN and on their resulting meshes. For that reason, there is a dispersion of the elastic moduli for similar values of I_1. Also, as was early proved by Kulatilake et al. (1993), a power function would be an even better fit for these curves. Figures 5.8 and 5.9 show that the ranges of variation of I_1 are short enough for this power function to be treated as approximately linear; this becomes a better assumption as the REV becomes larger and this range of variation becomes shorter. As stated before, from the Delta method it is possible to infer that, if I_1 follows a normal distribution, so does the elastic moduli. The quasi-linearity of their relationship indicates that the convergence of the elastic moduli to a normal distribution should be fast and almost simultaneous to the convergence of the geometrical properties.

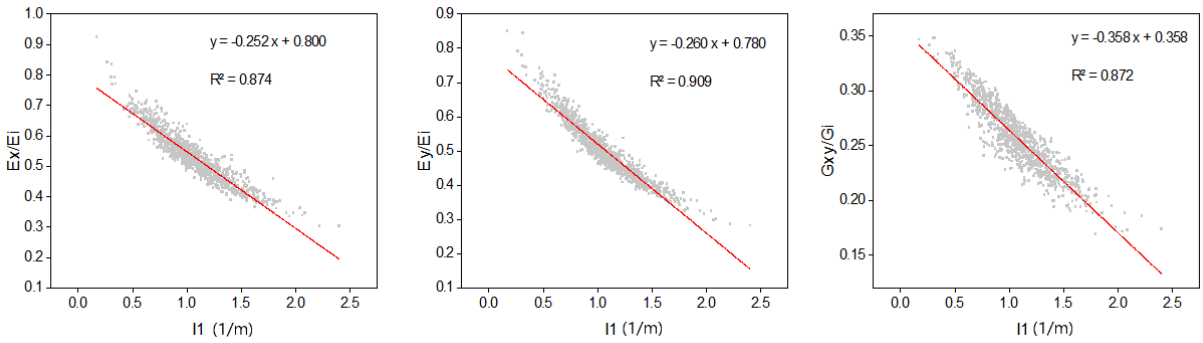

Figure 5.8: Equivalent elastic moduli normalized by the elastic moduli of the intact rock, E_i and G_i, vs first invariant - Network 1.

Figures 5.10 and 5.11 show the QQ-plots for the elastic moduli of the geometrical reference volumes and Figures 5.12 and 5.13 show their extreme and average values. These data indicate that for the reference sizes of 6 m for Network 1 and 3 m for Network 2 the distribution of the elastic moduli are close to normal and their average values become stable. Thus, they seem to follow the same tendency to normality than the fracture tensor. Table 5.5 compares the skewness of the elastic moduli and of I_1 and shows that, for the same size,

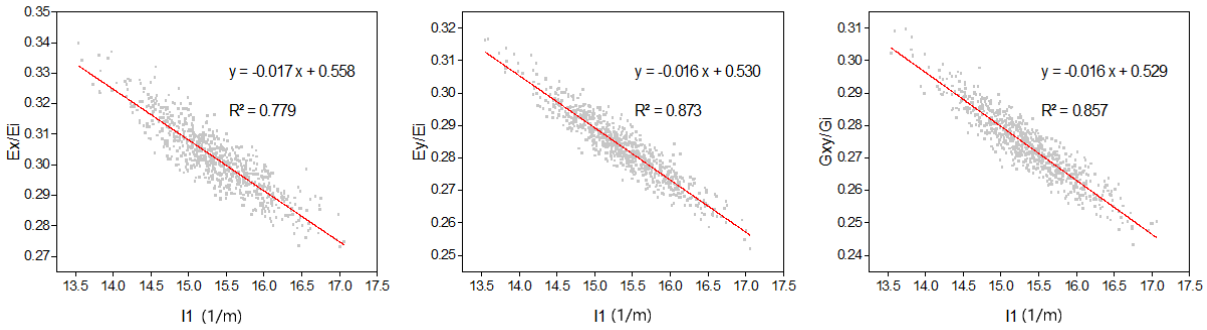

Figure 5.9: Equivalent elastic moduli normalized by the elastic moduli of the intact rock, E_i and G_i, vs first invariant - Network 2.

the latter tends to be less skewed and thus closer to normal. This can be explained by the non-perfect linear relationship between these properties, but yet, the distributions of the elastic moduli can be considered approximately normal. This is further confirmed by the accurate predictions made for the standard deviations of the elastic moduli using (5.11), as shown in Figures 5.14 and 5.15.

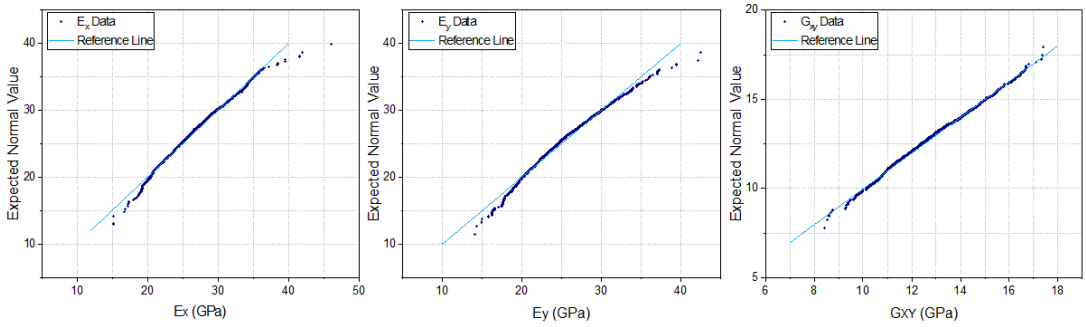

Figure 5.10: Q-Q plots for the elastic moduli of the 6 m x 6 m REVs of Network 1.

By setting a 10% error and using the power law fits in Figures 5.14 and 5.15, Equation 5.15 can be used to calculate the mechanical REV sizes for the elastic moduli, resulting in 19.8 m for Network 1 and 5.2 m for Network 2. For both networks, the mechanical REVs are smaller than the geometrical ones. This suggests that the geometrical REV can be used as a conservative estimation for the REV of the elastic properties. However, this topic is controversial because other studies concluded the opposite (e.g. Esmaieli et al., 2010; Ni et al., 2017), so more DFNs would need to be tested with a large number of experiments before setting any general rule for the relationship between geometrical and mechanical REVs.

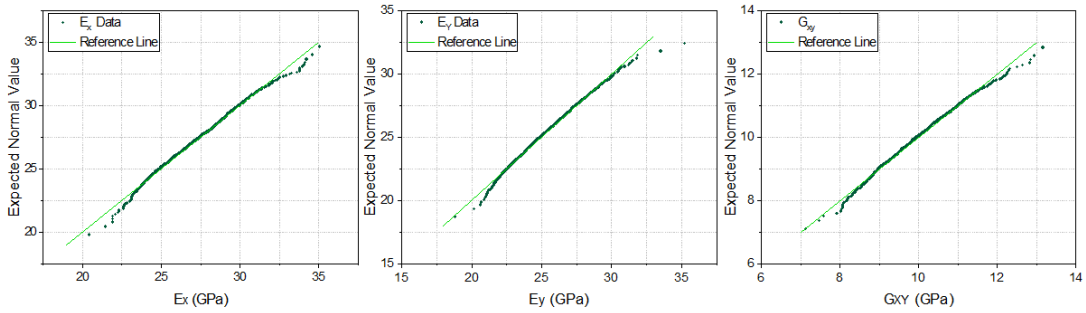

Figure 5.11: Q-Q plots for the elastic moduli of the 3 m x 3 m REVs of Network 2.

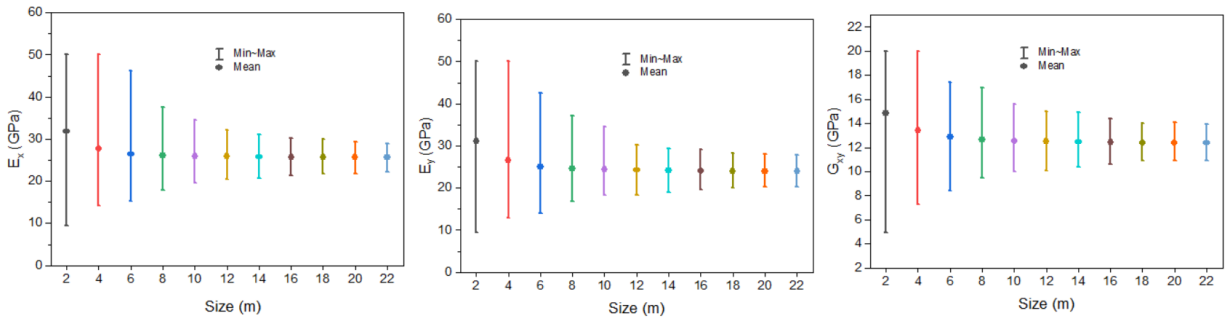

Figure 5.12: Average, minimum and maximum elastic moduli for Network 1.

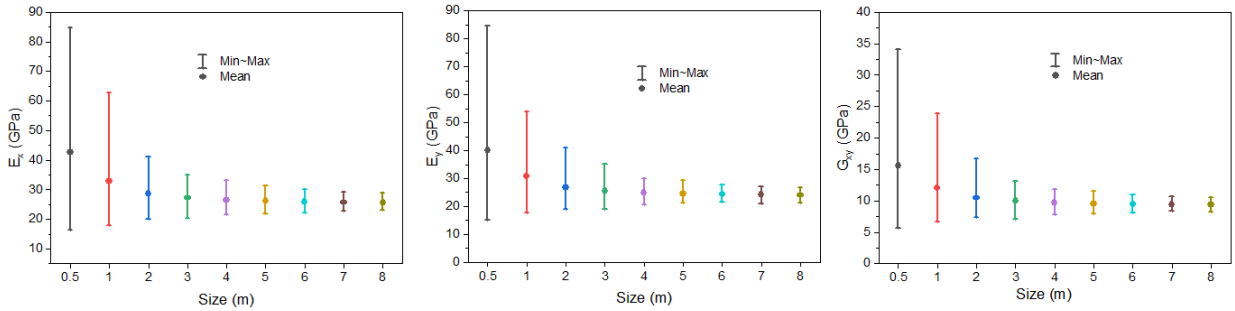

Figure 5.13: Average, minimum and maximum elastic moduli for Network 2.

5.5.2 Applicability to non-elastic problems: a preliminary verification

The fracture network in a rock mass does not affect only its deformability, but also reduces its strength and changes its mechanisms of failure. Since predictions concerning shear failure are of extreme importance to several geomechanical problems, the upscaling of mechanical properties for large scale simulations usually include the determination of models for the equivalent strength.

For that reason, Equations 5.10 – 5.11 were tested for their capability of predicting the

Table 5.5: Skewness of the elastic moduli and the first invariant of the crack tensor of Networks 1 and 2.

Skewness Network 1					Skewness Network 2				
Size	I_1	E_x	E_y	G_{xy}	Size	I_1	E_x	E_y	G_{xy}
2 m x 2 m	0.89	0.36	0.43	-0.11	0.5 m x 0.5 m	0.52	0.87	0.94	0.96
4 m x 4 m	0.60	0.49	0.56	0.01	1 m x 1 m	0.25	0.80	0.64	0.77
6 m x 6 m	0.35	0.42	0.50	0.15	2 m x 2 m	0.25	0.43	0.38	0.50
8 m x 8 m	0.14	0.36	0.49	0.30	3 m x 3 m	0.18	0.24	0.31	0.28
10 m x 10 m	0.19	0.20	0.29	0.14	4 m x 4 m	0.16	0.22	0.21	0.13
12 m x 12 m	0.21	0.11	0.19	0.16	5 m x 5 m	0.09	0.17	0.21	0.21
14 m x 14 m	0.18	0.14	0.17	0.10	6 m x 6 m	0.09	0.19	0.14	0.14
16 m x 16 m	0.09	0.19	0.21	0.11	7 m x 7 m	0.04	0.26	0.11	0.19
20 m x 20 m	0.07	0.14	0.19	0.13	8 m x 8 m	0.01	0.27	0.11	0.15
20 m x 20 m	0.00	0.15	0.24	0.22					
22 m x 22 m	-0.07	0.21	0.29	0.21					

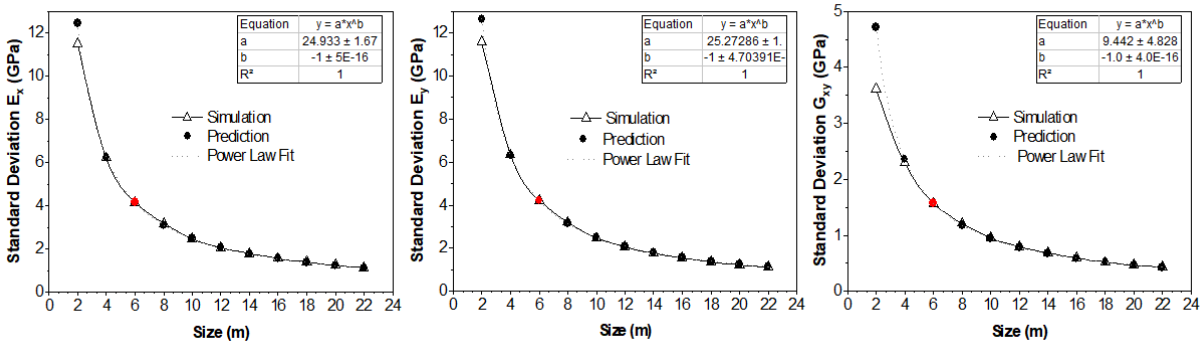

Figure 5.14: Predicted and calculated curves of the standard deviation of the elastic moduli of Network 1 vs REV size. The red dot signalizes the reference volume.

Table 5.6: Calculated mechanical REVs for the elastic moduli for a 10% error.

	Network 1			Network 2		
	E_x	E_y	G_{xy}	E_x	E_y	G_{xy}
Size (m)	18.5	19.8	14.4	5.0	4.9	5.2

standard deviation of the Uniaxial Compression Strength (UCS) of fractured rocks using the data of two publications: Esmaieli et al. (2010) and Farahmand et al. (2018). It is likely that the concepts presented above apply, at least partially, to the upscaling of strength because this property is allegedly related to the fracture tensor by a power function (Wu and Kulatilake, 2012).

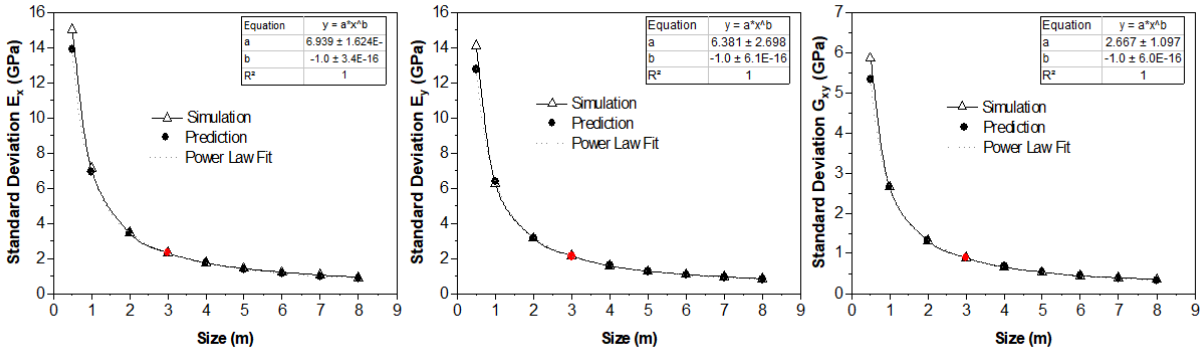

Figure 5.15: Predicted and calculated curves of the standard deviation of the elastic moduli of Network 2 vs REV size. The red dot signalizes the reference volume.

Esmaieli et al. (2010) obtained the equivalent UCS for five 3D samples of each tested size; Farahmand et al. (2018) used 2D samples and considered from three to ten REVs of each tested size. They also considered fracture propagation by the inclusion of a cohesive crack model. A summary of their data is presented in Tables 5.7 and 5.8.

Table 5.7: Data for the Uniaxial Compressive Strength in Esmaieli et al. (2010).

Sample size (m)	Number of samples	Avg. number of fractures	Std. Dev. UCS (MPa)
1.5 m x 1.5 m x 3.0 m	5	30.8	42.7
3.5 m x 3.5 m x 7.0 m	5	197.1	17.8
7.0 m x 7.0 m x 14.0 m	5	1214.4	8.9
10.0 m x 10.0 m x 20.0 m	5	152.1	3.6

Table 5.8: Data for the Uniaxial Compressive Strength in Farahmand et al. (2018). The data was retrieved from Fig.14 of the paper.

Sample size (m)	Number of samples	Std. Dev. UCS (MPa)
5.0 m x 2.0 m	8	25.6
7.0 m x 2.8 m	7	9.2
8.0 m x 3.2 m	5	6.9
9.0 m x 3.6 m	4	4.6
10.0 m x 4.0 m	3	3.7

Figure 5.16 presents the estimations of the standard deviation of the UCS against the values obtained by Esmaieli et al. (2010). Also, it presents the confidence intervals for the standard deviations based on the number of samples in Table 5.7. The estimated standard deviations are all inside the confidence intervals and are close to those obtained by the DEM simulations. Since the authors provided the average number of fractures for each tested size,

Equation 5.10 was used for the predictions. The 3.5 m x 3.5 m x 7.0 m was selected as the reference volume because it is the first size to contain an average number of fractures that is safely above the general rule of thumb of minimum sample size of 30 to observe normality.

Figure 5.17 presents the estimated and calculated standard deviations of the UCS of the rock mass tested by Farahmand et al. (2018). As there is no information on the number of fractures, Equation 5.11 was used. Figure 5.17 shows that reasonable predictions of the standard deviation of the first invariant of the fracture tensor I_1 can be made from the REV of dimensions 5 m x 2 m. Since the non-perfect linear relationship between I_1 and the mechanical properties leads the latter further from a normal distribution, the immediately larger REV of 7 m x 2.8 m was selected as the reference volume for the UCS. Fair predictions were obtained for the volumes larger than the reference REV. For the 5 m x 2 m domain, the estimation is inside the interval of confidence, but distant from the value calculated from the simulations. Besides the small number of samples, this could be explained by the inadequacy of Equation 5.11, because it assumes different REV sizes to have the same fracture density. Equal densities are only attainable with the approach used here to remove external fractures in the generation of the DFNs, which is not a standard procedure in fractured REV studies, Also, as Farahmand et al. (2018) consider fracture propagation, it is even more likely that distinct volumes have differences in their fracture density at failure. Anyhow, the results obtained for the sizes larger than 7 m x 2.8 m are encouraging and tend to show that the methodology here presented can be extended to non-elastic parameters.

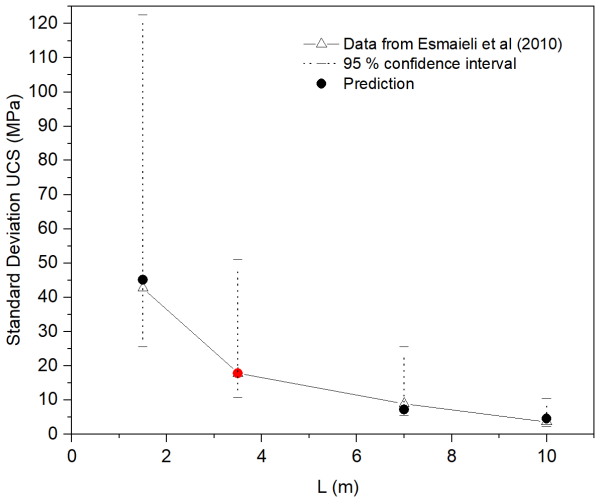

Figure 5.16: Standard deviations of the UCS obtained by Esmaieli et al. (2010) for samples with sizes L x L x 2L and those predicted with (5.10) from the reference volume with L = 3.5 m. The red dot signalizes the reference size of L.

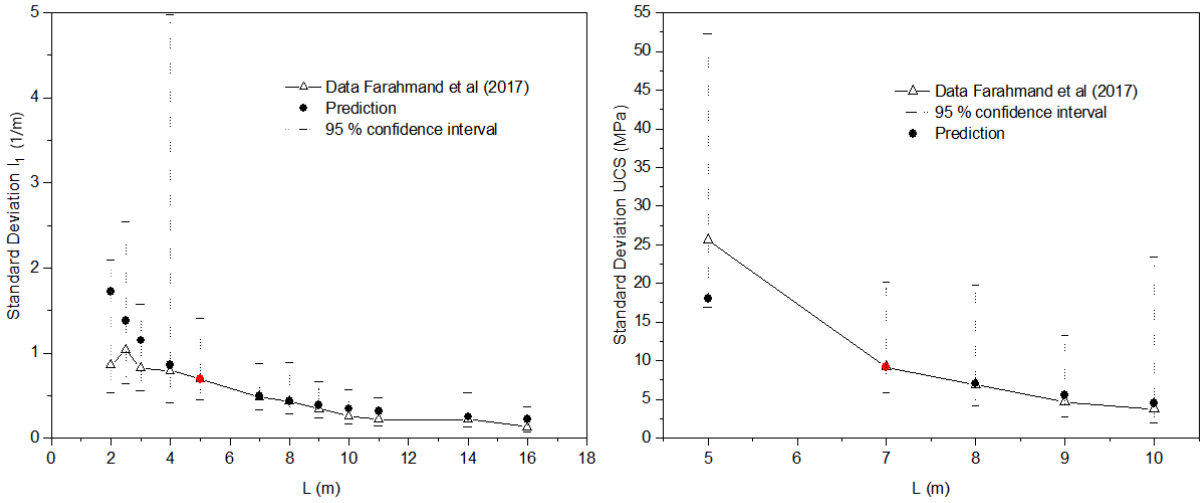

Figure 5.17: Standard deviations of I_1 and of the UCS obtained by Farahmand et al. (2018) for samples with sizes L x 0.4 L and those predicted with (5.11). The red dot signalizes the reference size of L.

5.5.3 Methodology to define the REV size

Based on the results presented above, the following steps were defined by Loyola et al. (2021) to obtain the geometrical and mechanical REV size for fractured rocks:

[1] Choose a reference volume Select a reference volume that returns approximate normal distributions for the properties. An initial guess for the reference volume can be made by using the rule of thumb that defines a minimum sample size of 30; thus, a volume for which there are at least 30 fractures can be used to generate a large sample of DFNs. If the obtained distribution for the fracture tensor is approximately normal, the choice of the geometric reference volume is valid. Since the data for the elastic moduli tends to be more skewed than the first invariant of the fracture tensor, we recommend the reference volume of the numerical experiments to be larger than the geometrical reference volume, specially if the number of REVs to be tested is small. The definition of normality can be made based on a maximum skewness of 0.5 and maximum kurtosis of 1.0 or by the visual inspection of the QQ-plots.

[2] Obtain homogenized properties Perform numerical tests on the REVs to obtain the upscaled properties and their statistical distributions for the reference size.

[3] Predict standard deviations for other sizes Use Equation (5.10) or Equation (5.11) (if the fracture density does not vary significantly between REV sizes) to calculate the standard deviations of the upscaled property for any other REV size. Use Equation (5.9) to

obtain the predicted errors.

[4] Select REV size Set a maximum precision error and select the size of the REV and the number of simulations N that will be used to estimate the average properties.

A large number of REVs was used so: (i) the distribution of the properties could be observed and (ii) their standard deviation could be predicted with accuracy. Using the fact that the standard deviation of a normal variable follows a chi-squared distribution, it is possible to build a confidence interval for the calculated standard deviations and affirm that they are 95% likely to not present an error higher than 6%. However, works on fractured media usually employ a much smaller number of samples. It was shown in Loyola et al. (2021) that a small set of REVs can be selected for the numerical experiments from a larger original population of generated DFNs. Sets of 10 and 50 REVs were selected under the criterion of not returning averages and standard deviations for the fracture tensor elements that differed by 5% or less from those of the original population. These smaller sets yielded accurate estimations, and the higher uncertainty attributed to them is already considered in their higher t-values.

5.5.4 Hydraulic REV

Min et al. (2004a) studied the equivalent permeability for Network 2, described in Table 5.2. They used 10 realizations for some tested sizes and 50 for others, for which they observed the distribution of intrinsic permeability.

The strong relationship between permeability and the fracture tensor, which was discussed in Section 2.3.3, indicates that the methodology presented above could work for the hydraulic REV as well. When observing the distributions obtained by Min et al. (2004a), the possibility of applying the CLT for this particular network is even more evident, since they were shown to be approximately normal. To confirm that, 500 generations of Network 2 were used to upscale permeability using DuMu^X. Following Min et al. (2004a), linear pressure boundary conditions were applied (Figure 2.2). Permeability was calculated using Equations 2.15, 2.21 and 2.33. Although the authors observed a variability in aperture in their field measurements, a constant aperture of 65 μm was adopted for the fractures. From the cubic law, this gives an intrinsic permeability of 3.5×10^{-10} m^2 for these discontinuities.

There are three main differences between the simulations performed here and those from the reference study. While Min et al. (2004a) used the DEM, removed isolated fractures and dead-ends and considered the rock matrix to be impermeable, the experiments here were simulated with the Box method, without any alteration to the generated DFN and considering a 1×10^{-15} m^2 permeability for the rock matrix. This latter avoids a singular matrix when solving the multi-domain system in DuMu^X. For the computation of permeability the external fractures were not removed, so the applicability of Equation 5.10 is demonstrated. Also, the fracture densities used for the generation of the DFNs are half the values presented

in Table 5.2 to assess their effect on the size of the geometrical REV. Because of that, this fracture network will be referred to as modified Network 2.

Figure 5.18 presents the average values of the components of the fracture and permeability tensors. The average values of the fracture tensor seem stable for sizes larger than 2 m. The Q-Q plots in Figure 5.19 confirm that the size of 2 m presents a fairly normal distribution. For that reason, this was selected as the reference size to predict the standard deviations of the fracture tensor components. Figure 5.20 shows there is a good agreement between the predictions and the results obtained from the sample of 500 generations.

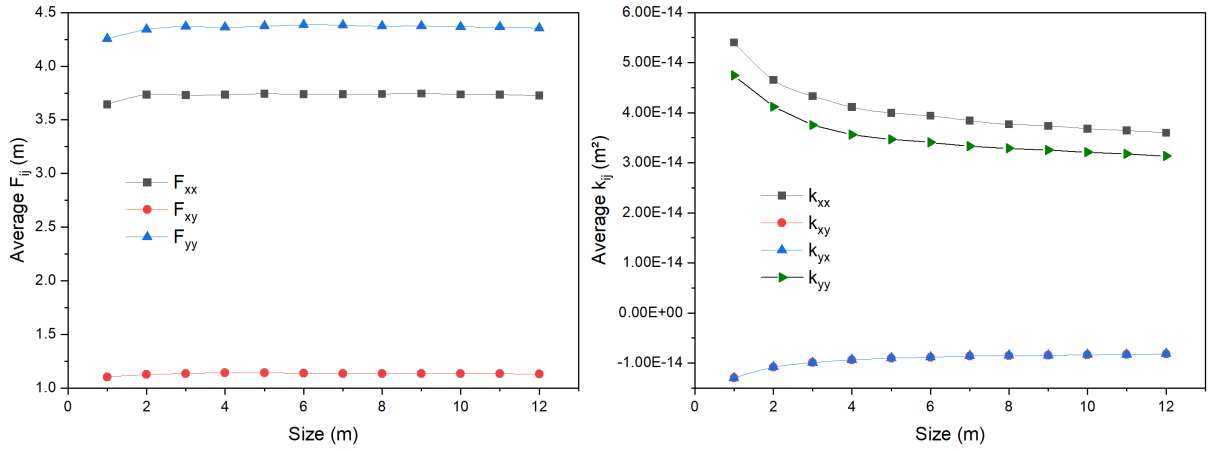

Figure 5.18: Average values of the fracture tensor and permeability tensor components as a function of size - modified Network 2.

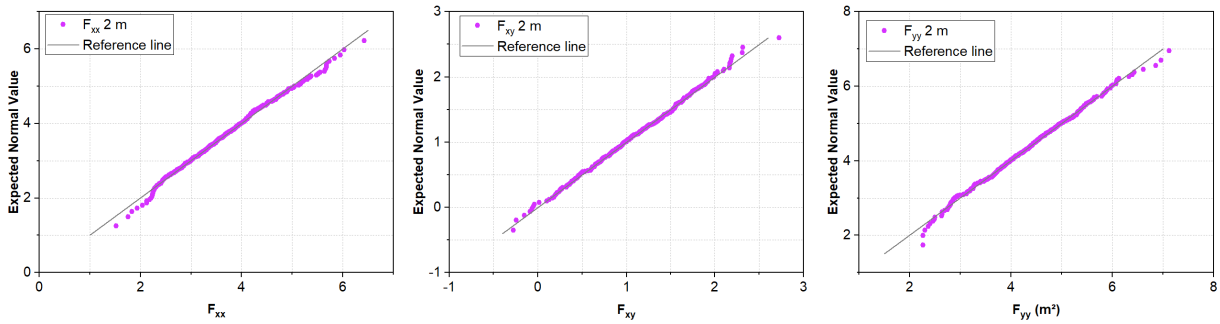

Figure 5.19: Q-Q plots for the fracture tensor of the 2 m x 2 m REVs of modified Network 2.

Since the proposed methodology requires the selection of a reference volume for the upscaled properties without the simulation of various sizes, a first try for the reference volume for permeability could be the size of 3 m. This follows the recommendation in step 1 of Section 5.5.3 to select a volume bigger than the reference volume for the geometrical properties. Figure 5.18 shows that the greatest variations in the average permeabilities

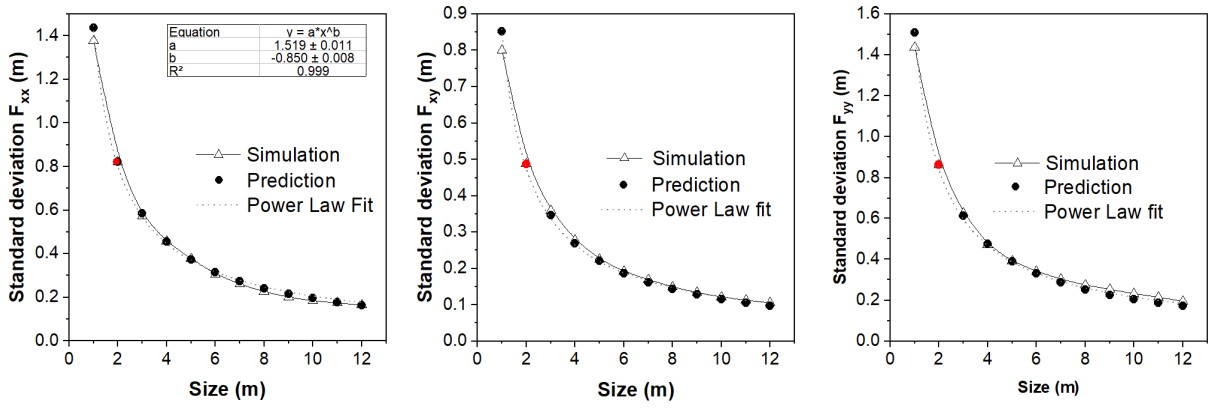

Figure 5.20: Predicted and calculated curves of the fracture tensor components of the modified Network 2 vs REV size. The red dot signalizes the reference volume.

occur for sizes smaller than 3 m. Thus, 3 m seems to be a size for which the permeability distributions are nearly stable.

The Q-Q plots in Figure 5.21 show that the permeability components have approximately normal distributions for the size of 3 m, although there is a more perceptible skewness than in the data for the fracture tensor components (Figure 5.19).

Kulatilake and Panda (2000) showed that permeability for a direction i is related to the diagonal component of the fracture tensor that is normal to i. Figure 5.22 shows that for the studied DFN these relationships are approximately linear, as it occurs for the elastic moduli. This explains the approximate normality of the permeabilities distributions.

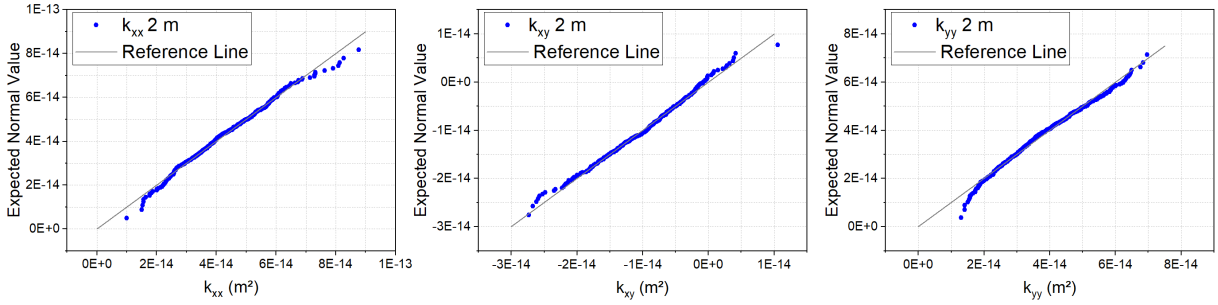

Figure 5.21: Q-Q plots for the permeability tensor of the 2 m x 2 m REVs of modified Network 2.

Figure 5.23 presents the comparison between the predicted and calculated standard deviations of the permeability. The predictions match the results from the simulations satisfactorily. The average difference between the calculated and predicted standard deviations is 7.6 % for k_{xx}, 4.9 % for k_{xy} and 5.6 % for k_{yy}.

Using the power-law fits and adopting a 10% precision error, the geometrical and hydraulic REV sizes in Table 5.9 were obtained. As expected, the decrease in the fracture density makes the REV size bigger. The geometrical REV sizes for the components F_{xx} and

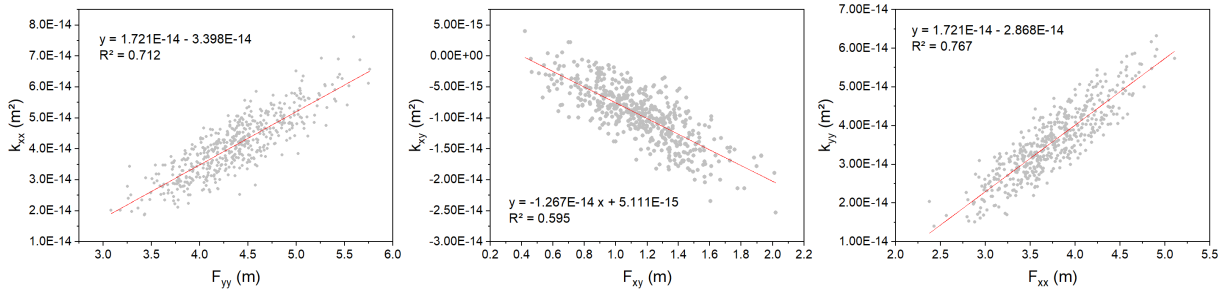

Figure 5.22: Equivalent permeability vs fracture tensor components - modified Network 2.

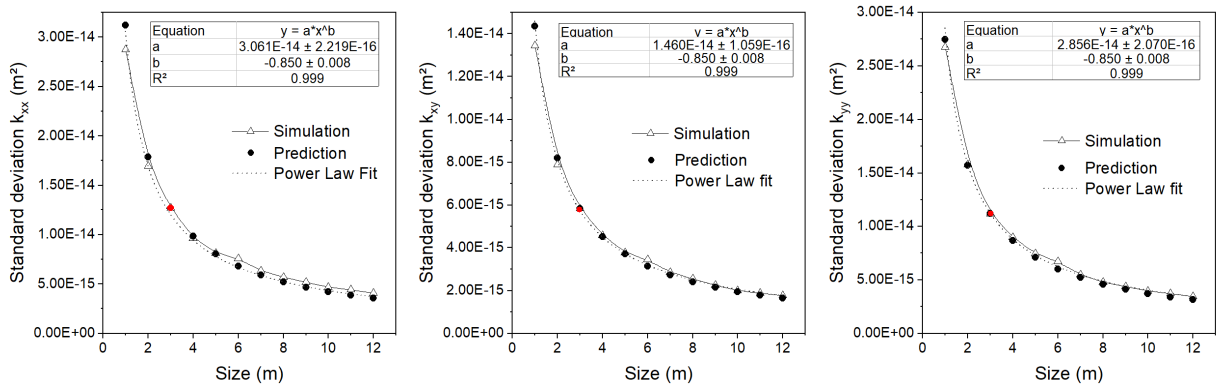

Figure 5.23: Predicted and calculated curves of the permeability tensor components of the modified Network 2 vs REV size. The red dot signalizes the reference volume.

F_{yy} are 47% and 60% larger then for a DFN with fracture intensity twice as big (Table 5.4). The REVs for permeability are significantly larger than those for the geometrical properties; so, in this case, a choice based only on the geometrical properties would not be conservative. Since these sizes may be too large to perform efficient simulations or to respect the principle of separation of scales, an alternative would be to upscale a quantity N of smaller samples (see Equation 5.9).

Table 5.9: Calculated geometrical and hydraulic REVs for a 10% error.

	Modified Network 2					
	F_{xx}	F_{xy}	F_{yy}	k_{xx}	k_{yy}	k_{xy}
Size (m)	10.9	23.9	9.6	22.0	52.2	24.5

5.5.4.1 Varying aperture

Several field measurements show that aperture presents a variability within a fracture set and that it correlates with fracture length. The adoption of a constant aperture is a model simplification that might provide for proper estimations of the averaged permeability (De

Dreuzy et al., 2012). However, since the permeability of a fracture depends highly on its aperture (Equation 2.68), this simplification might give erroneous predictions for the fluid distribution, because it can not consider the possible formation of preferential flow paths that pass through the wider fractures. From this fact alone it is already possible to infer that if a variable aperture is considered, the variability of the upscaled permeability is expected to increase.

Baghbanan and Jing (2007) investigated the size and existence of the REV for the permeability of Network 2 (Table 5.2) when the aperture is variable and follows a log-normal distribution. Three different scenarios were explored: constant aperture, variable aperture with a distribution independent from the length's distribution and variable aperture correlated with length. Using 10 DFN generations for each REV size, they could estimate the COV and average values of the permeability tensor. The upscaled permeabilities when the aperture is variable were significantly higher than those for constant aperture. Also, while for the constant aperture case there was a consistent decrease of the COV with size, the data for variable aperture were more scarred, because of the higher variability of the permeability and also possibly because of the low number of DFN generations.

The case of variable aperture correlated to length will be tested here for a bigger number of DFN generations to observe the distribution of the permeability and to test the statistical methodology proposed above. Fracture aperture w and length l are correlated by truncating their respective log-normal and power law distributions, as detailed by Baghbanan and Jing (2007). The resulting correlation relationship is the following:

$$l = \left(l_{min}^{-D} + \frac{g(w) - g(w_{min})}{g(w_{max}) - g_(w_{min})} (l_{max}^{-D} - l_{min}^{-D}) \right)^{-1/d} \tag{5.16}$$

where l_{min} and l_{max} are the minimum and maximum fracture lengths, respectively; D is the exponent of the power law distribution in Table 5.2; w_{min} and w_{max} are the minimum and maximum apertures, respectively and the function $g(w)$ is equal to:

$$g(w) = \text{erf}\left(\frac{\ln h - \overline{w}_{log}}{\sqrt{2}\sigma_{w_{log}}} \right) \tag{5.17}$$

where erf is the error function and $\overline{w}_{log}$ and $\sigma_{w_{log}}$ are the mean and standard deviation of the log-normal distribution for the fracture aperture. Table 5.10 presents the parameters used to define the relationships (5.16) and (5.17).

Table 5.10: Parameters used by Baghbanan and Jing (2007) to define the log-normal distribution of the aperture and their correlation with length.

$l_{min}(m)$	$l_{max}(m)$	$w_{min}(\mu m)$	$w_{max}(\mu m)$	$\overline{w}_{log}(\mu m)$	$\sigma_{w_{log}}(\mu m)$
0.5	250.0	1.0	200.0	65.0	1.0

The fractures lengths vary in a wide range, as it often does in fractured rock masses.

Due to its power law distribution, the long fractures are rare, which also agrees with usual field conditions. In fact, for this distribution, 95 % of the fractures have lengths smaller than 2 m, and the average fracture length is 0.92 m (Baghbanan and Jing, 2007). The rare fractures that might have a trace-length of tenths or even hundreds of meters are reduced by the REV size and often become discontinuities that cross the entire REV from one end to an other. In the case of constant aperture, this big fractures did not produce important outliers that affected the hypothesis of normality (Figure 5.21) necessary to use Equations 5.10 and 5.11. However, the case of the aperture correlated with length is a good test of the limits of this methodology. In this scenario, the longer fractures, although not frequent, will not only have larger trace lengths, but also a much larger aperture, and thus higher permeability than the others. As a consequence, they have the potential of being outliers in the sense that they alone might contribute to a significant part of the upscaled permeability. To work with a problem that is even harder to homogenize, and also to compare the distribution of the permeability with the constant aperture case, we will use here the modified Network 2, that is, Network 2 with half the fracture intensity. The tested REV sizes lie between 3 m and 25 m and 500 DFN generations were used.

Figures 5.24, 5.25 and 5.26 show the distribution of the permeability components k_{xx}, k_{xy} and k_{yy} and the reference line for a normal distribution for the sizes of 5 m, 11 m and 21 m. In the case of k_{xx} and k_{yy}, the observed distributions are much more skewed than a normal one, and actually would better fit a log-normal distribution. It can be observed, however, that there is a slow convergence towards a normal distribution. The distribution of k_{xy} also starts off far from normal, but converges faster to normality as the size increases.

For comparison purposes, the upscaled permeability was also calculated for 500 generations of the original Network 2, with fracture intensity of $4.6/m^2$. Figure 5.27 compares their distributions of k_{yy}; as expected, the convergence to normality is faster as the fracture density increases. Since what defines the convergence to normality is basically the sample size, this confirms that for larger sizes the modified Network 2 should approach a normal one. Also, this shows how the CLT is theoretically more applicable to larger fracture densities.

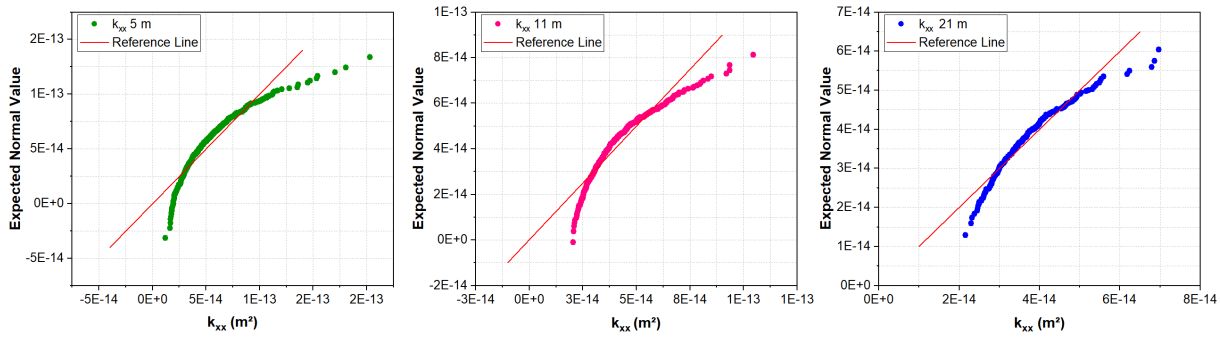

Figure 5.24: QQ-plots fot the permeability k_{xx} of the modified Network 2 with variable aperture for sizes 5 m x 5 m, 11 m x 11 m and 21 m x 21 m.

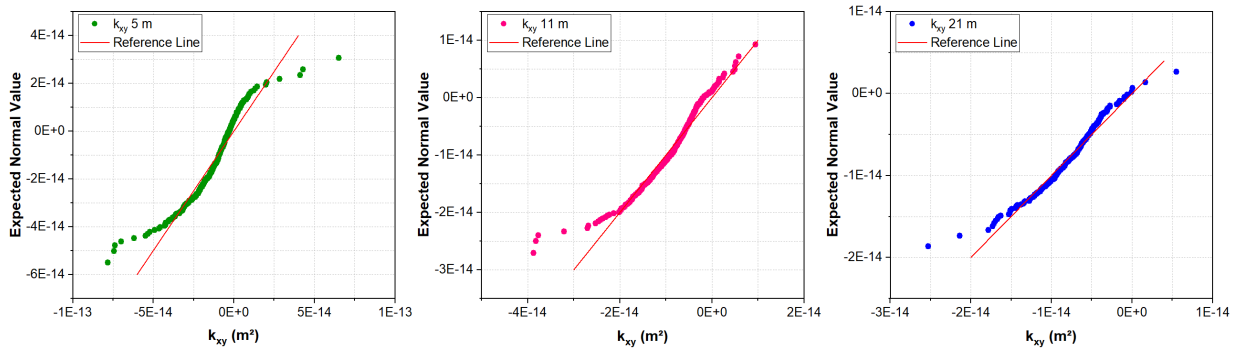

Figure 5.25: QQ-plots for the permeability k_{xy} of the modified Network 2 with variable aperture for sizes 5 m x 5 m, 11 m x 11 m and 21 m x 21 m.

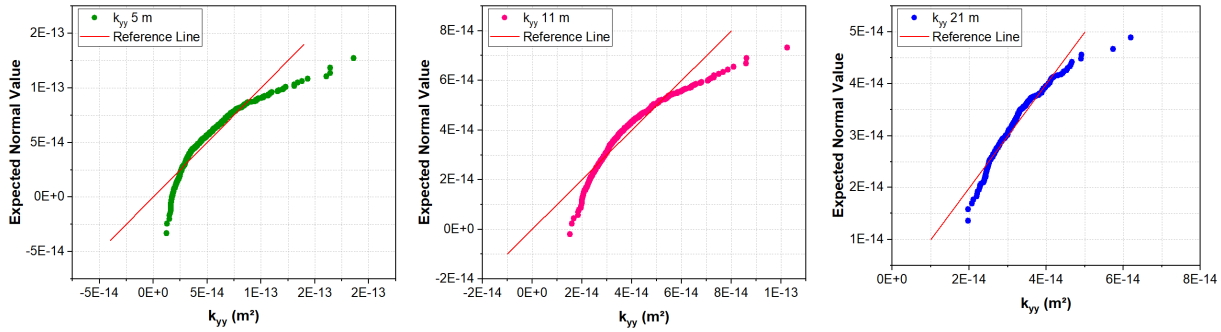

Figure 5.26: QQ-plots for the permeability k_{yy} of the modified Network 2 with variable aperture for sizes 5 m x 5 m, 11 m x 11 m and 21 m x 21 m.

Having in mind these considerations and the non-normality of most of the tested REV sizes for modified Network 2, the methodology described in Section 5.5.3 is used anyway to evaluate the predictability of Equation 5.10.

The first step is to select a reference volume based on the distribution of the crack tensor. The formulation used here is the one in (2.36), which accounts for the cube of the aperture. Figure 5.28 shows that the distributions of this crack tensor approach normality as the size increases. The first size to return a maximum skewness of 0.5 and maximum kurtosis of 1.0 for all the tensor components is 7.0 m. So, this is adopted as the reference REV.

Figure 5.29 shows that the curve of standard deviation versus size can be fairly well predicted for sizes above 7.0 m, despite of the significant skewness of the permeability distribution. The predictions are not as close to the simulated results as for the constant aperture case (Figure 5.23), specially for the smaller sizes. Also, as it occurs in the data obtained by Baghbanan and Jing (2007), there is not a consistent decrease with size of the standard deviations calculated from the simulations. This might be due to the presence of outliers. Still, the average difference between the calculated and predicted standard deviations is 8.2 % for k_{xx}, 6.1 % for k_{xy} and 7.2 % for k_{yy}.

These differences are larger than for the constant permeability case, but can still be

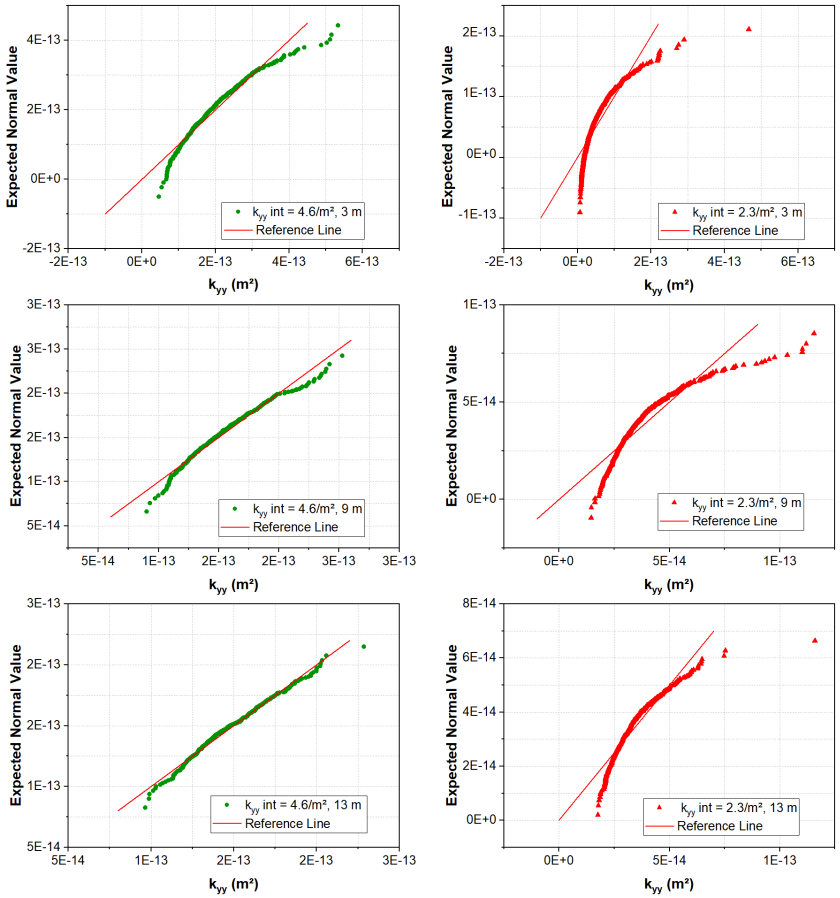

Figure 5.27: Comparison of the QQ-plots for the permeability k_{yy} of modified Network 2 (red), with fracture intensity of 2.3/m², and the original Network 2 (green), with fracture intensity of 4.6/m². The REV sizes are 3 m x 3 m, 9 m x 9 m and 13 m x 13 m.

considered acceptable.

Table 5.11 presents the calculated hydraulic REVs for modified Network 2 considering a precision error of 10%. The sizes are significantly larger than those for the constant aperture case. Hence, a variable aperture makes it harder to obtain a proper REV for homogenization, i.e. a volume that respects the separation of scales.

Table 5.11: Calculated hydraulic REVs for modified Network 2 with variable aperture considering a 10% error.

	k_{xx}	k_{yy}	k_{xy}
Size (m)	71.4	143.0	63.9

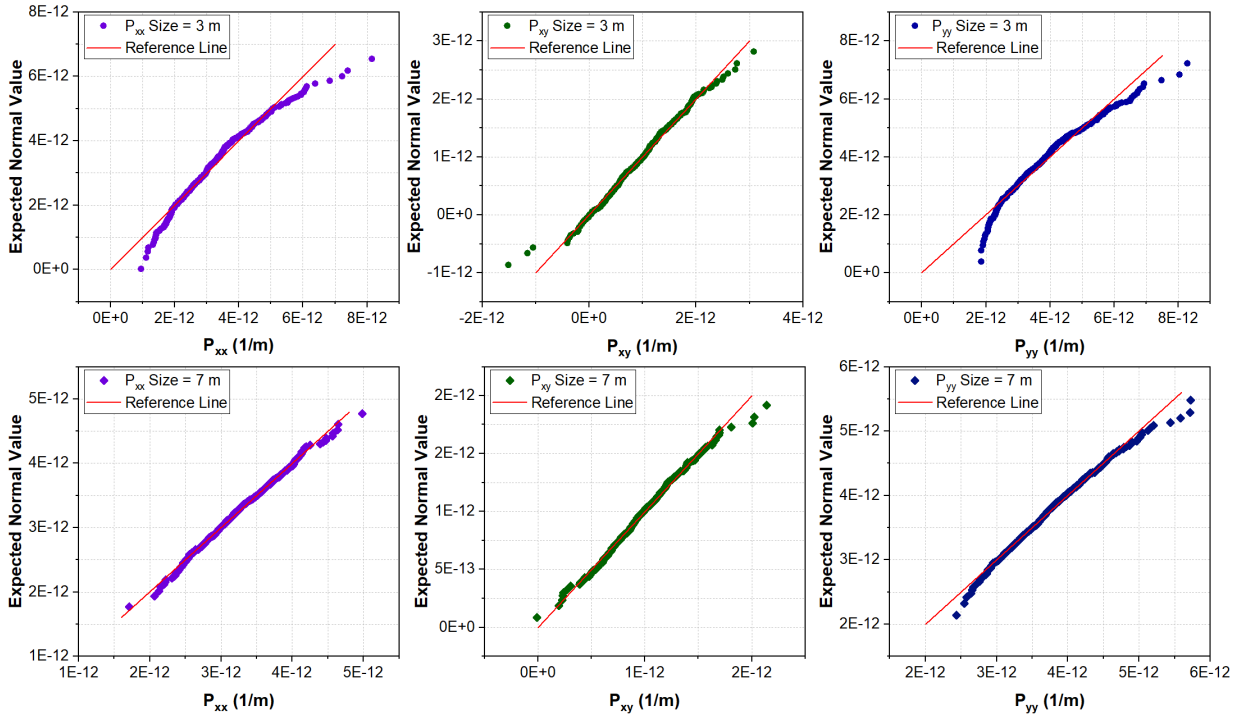

Figure 5.28: QQ-plots for the crack tensor $\boldsymbol{P}$ in Equation 2.36 of the modified Network 2 with variable aperture for sizes 3 m x 3 m, and 7 m x 7 m.

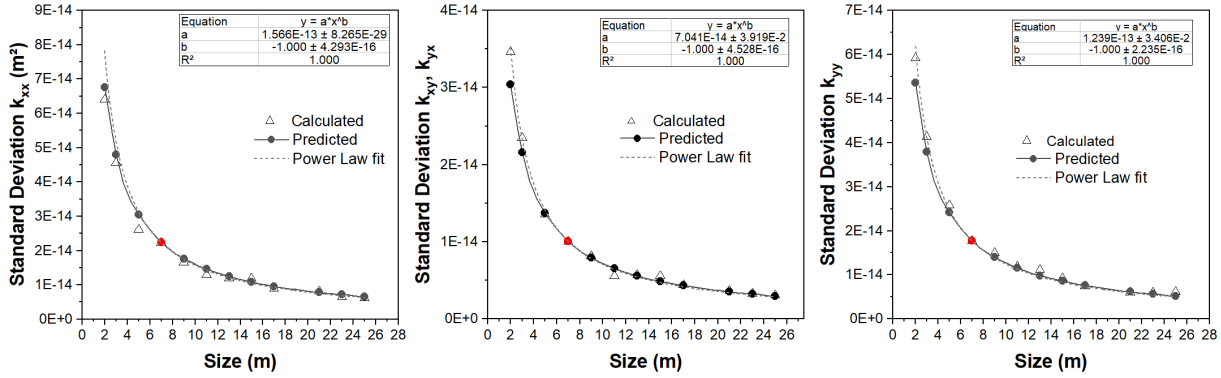

Figure 5.29: Predicted and calculated curves of the permeability of the modified Network 2 with variable aperture vs REV size. The red dot signalizes the reference volume.

5.6 Conclusions of the chapter

A proper REV should return a good estimation of the mean constitutive behavior of the sampled material. For this reason, some works define a REV for random media based on the precision error of the estimated average values of the equivalent properties. We consider this criterion to be more adequate than the COV because it accounts for the number of tested samples.

The process of defining the size of the REV based on a variability-related criterion would

normally require a considerable number of simulations, since a distribution of the studied properties would have to be generated for each tested size. It was shown here that the application of the CLT simplifies this process and makes it general for different DFNs by means of general equations that predict the standard deviation of a property.

The applicability of these equations was tested for two very different fracture networks that were previously studied for the size of their REVs. The geometrical REV was defined based on Oda's crack tensor, which theoretically has a limiting normal distribution. Because of their strong correlation with the crack tensor, the distributions of the equivalent mechanical properties and the intrinsic permeability tend to normal. As a consequence, the proposed equations could be successfully applied to predict the standard deviation of the studied properties based on the data for a reference volume only. It was shown that the decay of these standard deviations depends on the sample size only, which can be represented by the dimensions of the REV or by its average number of fractures.

The last tested scenario was the REV for permeability when the aperture of the fractures is variable and correlated to their lengths. Because of the existence of occasional very large and wide fractures that give an important individual contribution to the calculated permeability, outliers are present. As such, the limits of the applicability of the CLT were tested. Indeed, the calculated standard deviations were more scarred in this case and the approximation to a normal distribution was very slow. In fact, except for the larger tested sizes, a log-normal distribution would be a better fit. Even so, the predicted standard deviations were reasonable.

Log-normal and normal distributions for permeability are commonly reported in the literature. For example, Azizmohammadi and Matthäi (2017) studied the permeability of several DFNs and obtained log-normal distributions for some cases and normal distributions for others. In the case of the log-normal fits, it is unclear whether the authors didn't test sizes that were large enough for normality to be reached or if their limiting distributions were indeed log-normal. Anyway, a log-normal distribution would not be an impediment for the use of the methodology presented here. Indeed, it would only require the log-permeability to be the analyzed property.

About the presence of outliers, they could be removed by selecting a proper scale of study. If the homogenization of the REV is to be used in a large scale simulation, it would be desirable to limit the microscale to a certain size of fractures and to explicitly represent the larger fractures at the macroscale. Here we opted for not setting a maximum length for the fractures to test the limits of the methodology; for that reason, there were many persistent wide fractures in the samples.

For one of the networks, we calculated the REV size for the geometrical properties, the elastic moduli and the permeability. The REV for permeability was the largest and the REV for the mechanical properties was the smallest. These results showed that it is not always possible to define a REV size based on the geometrical properties only. Furthermore, and as expected, the REV for permeability when a variable aperture is considered is significantly larger than for the same network with constant aperture.

The REV sizes obtained for the permeability of Network 2 would be hardly viable in a multiscale simulation because of computational costs. But since the aim of defining a REV is to obtain a precise average constitutive response, a possible alternative would be to pick smaller REVs that return equivalent properties that are close to the mean value and mimic well the behavior of a larger volume, while meeting a chosen error criterion.

Chapter 6

Multiscale simulation: methods and implementation

6.1 Multiscale methods

Engineering models often rely on analytical homogenization and on numerical upscaling to account for small heterogeneities. However, both approaches are limited. Analytical methods can not deal with complex non-linear phenomena and may require a level of abstraction that makes the idealized materials very different from the actual ones.

Numerical upscaling does not have the same drawbacks, but it disregards two important aspects of the materials behaviour. The first one is a possible multi-physics nature, thanks to which different physical laws may be necessary to describe different scales. This is an issue because upscaled solutions require a prior assumption on the form of the large-scale constitutive laws; and sometimes the upscaled response is too complex to fit in any known model.

The second aspect that upscaling may fail to capture is the state-dependent nature of the materials behavior. Since there must be a choice on the boundary conditions used in the numerical experiments, the constitutive properties are obtained only for a limited amount of scenarios. Even if the boundary value problem at the REV is carefully chosen to well represent the macroscale, upscaling will hardly be able to capture all the dynamic aspects of the actual large-scale problem, namely the spatial and time variations in state and the consequent changes in the constitutive behavior.

Several different multi-scale methods have been developed to surpass these limitations and make numerical models more robust. We use the term multiscale method to refer to numerical techniques where multiple scales are solved numerically and coupled to each other by some sort of transfer of information. They have the following advantages:

- They can capture the small-scale effects at the large-scale without the need of resolving all of the small-scale features.

- When using these methods, it is not necessary to formulate a constitutive law for the macroscale; its behavior arises from the simulation of the microscale.
- The boundary conditions of the microscale problem are dynamic and arise from the current state at the large-scale.

The most popular multiscale methods used in the field of engineering were originally formulated with a classical finite-element discretization (e.g. Hou and Wu, 1997; Smit et al., 1998). Since then, other numerical methods have been used with similar methodologies. Some works maintain the FEM at the macroscale but use different methods to solve the microscale (e.g. Wang and Sun, 2019). Others exchange the FEM completely by a more convenient method. For example, Aarnes (2004) introduced the mixed FEM to the original formulation by Hou and Wu (1997) with the objective of adding local mass conservation, which is usually a desired feature in reservoir simulation. Here, we also add local mass conservation to a multiscale method originally formulated with the classical FEM. However, the locally conservative method to be used is the Box, and the multi-scale method to be adapted is the multi-level FEM by Smit et al. (1998).

6.2 Multi-level finite element method

The multi-level finite element method, also called the finite element method squared (FE^2), was first proposed by Smit et al. (1998) and applied to model the mechanical behavior of non-linear heterogeneous materials. As the name suggests, the method uses the FEM to solve both the macro and the microscale problems.

In the multi-level finite element method each integration point of the macroscale consists of a REV or a unit cell for periodic media. Treating the REV as a point implies that its dimensions should be small enough for separation of scales to exist.

The general algorithm for the solution of a hydro-mechanical problem at the microscale is the following:

1. Localization: receive the macroscale displacement and pressure gradients and convert them into consistent boundary conditions.
2. Solve the microscale boundary value problem.
3. Homogenization: return averaged stresses and fluid velocities to the macroscale.

This procedure is nested in the macroscale problem, which is solved with a common iterative method. The difference from a solution with only one-scale is that each computation of stresses and fluxes at the integration points correspond to a simulation of the REV following the procedure described above.

Since Smit's pioneer work, the method has been extended and used in a variety of applications, including the modeling of elastoplastic (e.g Miehe et al., 1999) and viscoelastoplastic

(e.g Feyel and Chaboche, 2000; Kouznetsova et al., 2001a) heterogeneous materials, as well as fracturing media (e.g Wu and Kulatilake, 2012); localization problems were addressed by Kouznetsova et al. (2004), who proposed a second order multi-level finite element that uses a higher order approximation of the macroscopic strains.

The method was first used to model coupled phenomena by Özdemir et al. (2008) in the field of thermo-mechanics. Similar strategies were later applied to hydro-mechanical problems. For instance, Frey et al. (2013) proposed the use of the method to assess the evolution of transmissivity properties of cohesive rocks; their microscale model consists of hyperelastic grains and cohesive interfaces through which a compressible fluid percolates. Their technique was later applied by Marinelli et al. (2016) to model the consolidation of granular solids. More recently, Bertrand et al. (2020) used the method to capture the effects of shrinkage and swelling of fractured coal in the production of gas; in their microscale model, the cleats are explicitly represented and have a stress-dependent permeability. Hydro-mechanical coupling has also been incorporated to second-order computational homogenization by van den Eijnden et al. (2016, 2017), who applied the finite element method squared to model the strain localization during the excavation of a gallery. All of these works assume steady-state flow at the microscale; this is supposed to be a good hypothesis when separation of scales is strong enough for the pressure changes to be considered instantaneous at the REV.

Larsson et al. (2009) tested the hypothesis of quasi-stationarity at the microscale for different REV sizes in a heat conduction problem; their results show that the quasi-stationarity assumption leads to very accurate solutions only when the REV size is between at least 100 and 1000 times smaller than the macroscale characteristic length. They proposed a multi-level finite element method where the problem at the REV is transient, which was later extended to consolidation problems (Larsson et al., 2011b). Since then, other approaches were adopted to consider the microscopic transient terms in hydro-mechanical analyses with one-phase (Khoei and Hajiabadi, 2018) and multiphase flow (Khoei and Saeedmonir, 2021).

6.3 Equations of the macroscale problem

The hydro-mechanical problem at the macroscale is described by the mechanical equilibrium:

$$\nabla \cdot \boldsymbol{\sigma}_M + \boldsymbol{b}_M = 0 \tag{6.1}$$

and the mass conservation equation for one fluid phase:

$$\dot{\Upsilon}_M + \nabla \cdot (\rho_\alpha \boldsymbol{v}_M) - q_M = 0 \tag{6.2}$$

The subscript M denotes the macroscale, $\boldsymbol{\sigma}$ is the total stress tensor, $\boldsymbol{b}$ is the body force vector, M is stored mass of fluid per unit volume, $\boldsymbol{v}$ is the fluid velocity vector and q is a flux source term.

The terms $\boldsymbol{\sigma}_M$, $\dot{\Upsilon}_M$ and $\boldsymbol{v}_M$ are outcomes of the homogenization of the REV. They are

calculated from the volume averages in Equations 2.7, 2.12 and 2.14, which are revisited below for convenience:

$$\boldsymbol{\sigma}_M(\boldsymbol{y},t) = \langle \boldsymbol{\sigma}_m(\boldsymbol{x},t) \rangle \tag{2.7}$$

$$\boldsymbol{v}_{\alpha M}(\boldsymbol{y},t) = \langle \boldsymbol{v}_{\alpha m}(\boldsymbol{x},t) - \boldsymbol{x}\dot{\Theta}_{m\alpha} \rangle \tag{2.12}$$

$$\Upsilon_{M\alpha}(\boldsymbol{y},t) = \langle \Upsilon_{m\alpha}(\boldsymbol{x},t) \rangle = \frac{1}{V}\int_V \rho_{m\alpha}(\boldsymbol{x},t)\Theta_{m\alpha}(\boldsymbol{x},t) \rangle \tag{2.14}$$

The macroscale total stresses in (2.7) can be rewritten in terms of the microscale effective stresses (σ'_m) and pore-pressures (p_m):

$$\boldsymbol{\sigma}_M = \langle \boldsymbol{\sigma}_m \rangle = \langle \boldsymbol{\sigma'}_m + b_m p_m \boldsymbol{\delta} \rangle \tag{6.3}$$

where b_m is the Biot's coefficient at the microscale.

Here, the fluid density will be considered to be constant, so the macroscale storage term in (2.14) becomes:

$$\dot{\Upsilon}_M = \rho_f \dot{\Theta}_M \tag{6.4}$$

For one-phase flow, the volumetric content is equal to the porosity; so, considering (2.62), (2.14) can be rewritten as:

$$\dot{\Theta}_M = \langle \dot{\Theta}_m \rangle = \langle b_m \dot{\boldsymbol{\varepsilon}}_{vm} + \frac{\dot{p_m}}{M_m} \rangle \tag{6.5}$$

where ε_{vm} and M_m are the microscale's volumetric strains and Biot's modulus. Note that the volumetric strain of a fracture is obtained from the aperture variation in (2.65).

Equations (6.1) and (6.2) will be solved as a monolithic system, that is, with a full-coupling scheme. Similarly to the microscale problem, the discretization is made with the Box method. The only difference is that there are no interface elements at the macroscale, because the fractures are explicitly represented only at the level of the REV.

Since the system formed by (6.1) and (6.2) is non-linear, it will be solved with the Newton-Raphson scheme. During this iterative process, the macroscale solution vector, composed of the displacements $\boldsymbol{u}_M$ and the pressures $\boldsymbol{p}_M$, is updated as:

$$\begin{Bmatrix} \boldsymbol{u}_M^{j+1,t} \\ \boldsymbol{p}_M^{j+1,t} \end{Bmatrix} = \begin{Bmatrix} \boldsymbol{u}_M^{j,t} \\ \boldsymbol{p}_M^{j,t} \end{Bmatrix} + \begin{Bmatrix} \boldsymbol{du}_M^{j+1,t} \\ \boldsymbol{dp}_M^{j+1,t} \end{Bmatrix} \tag{6.6}$$

where:

$$(\boldsymbol{J})^{j,t} \begin{Bmatrix} \boldsymbol{du}_M^{j+1,t} \\ \boldsymbol{dp}_M^{j+1,t} \end{Bmatrix} = \begin{Bmatrix} (\boldsymbol{\Psi}_M^s)^{j+1,t} - (\boldsymbol{\Psi}_M^s)^{j,t} \\ (\boldsymbol{\Psi}_M^f)^{j+1,t} - (\boldsymbol{\Psi}_M^f)^{j,t} \end{Bmatrix} \tag{6.7}$$

The vectors $(\boldsymbol{\Psi}_M^s)$ and $(\boldsymbol{\Psi}_M^f)$ store force and flux residuals, respectively, and $\boldsymbol{J}$ is the

Jacobian matrix, given by:

$$\boldsymbol{J} = \begin{bmatrix} \frac{\partial \boldsymbol{\Psi}_M^s}{\partial \boldsymbol{u}_M} & \frac{\partial \boldsymbol{\Psi}_M^s}{\partial \boldsymbol{p}_M} \\ \frac{\partial \boldsymbol{\Psi}_M^f}{\partial \boldsymbol{u}_M} & \frac{\partial \boldsymbol{\Psi}_M^f}{\partial \boldsymbol{p}_M} \end{bmatrix} \tag{6.8}$$

The particularity of the system assemblage in multiscale methods is that $\boldsymbol{\Psi}_M$ and $\boldsymbol{J}$ are computed from the solution of the boundary value problem at REV of each integration point. There are different possible techniques that can be used to compute $\boldsymbol{J}$; the strategy adopted here will be discussed in the following section.

The general algorithm of the multi-level FEM will be adopted in this work. However, the spatial discretization at both scales is made with the Box. So, it is more adequate to refer to the multiscale method we use here as multi-level Box from now on.

6.4 Multi-level Box

The main difference between the multi-level Box and the multi-level FEM is the position of the integration points, and, consequentially, of the REVs. Figure 6.1 indicates these locations for triangular and quadrangular elements; each mid-point of a face that is not located at the boundary and each center of a sub-control volume (SCV) of the domain corresponds to a REV. The REVs are used to compute homogenized stresses and velocities; the REVs at the center of sub-control volumes are used to compute the homogenized storage term.

6.4.1 Localization

The quantities to be passed from the large-scale to the REV are the pressure gradient vector:

$$\nabla_M p_M = \begin{Bmatrix} \frac{\partial p_M}{\partial x} \\ \frac{\partial p_M}{\partial y} \end{Bmatrix} \tag{6.9}$$

the displacements gradient matrix:

$$\nabla_M \otimes \boldsymbol{u}_M = \begin{bmatrix} \frac{\partial u_{Mx}}{\partial x} & \frac{\partial u_{Mx}}{\partial y} \\ \frac{\partial u_{My}}{\partial x} & \frac{\partial u_{My}}{\partial y} \end{bmatrix} \tag{6.10}$$

and the macroscale pressure p_M, which is to ensure that the pressure field at the microscale is compatible with the macroscale. We employ here the following constraint used by (Frey et al., 2013):

$$p_M = \langle p_m \rangle \tag{6.11}$$

These variables are all evaluated at the faces and sub-control volumes centers using the finite element shape functions $\boldsymbol{N}$. For a REV located at the local coordinates (ξ, η) inside

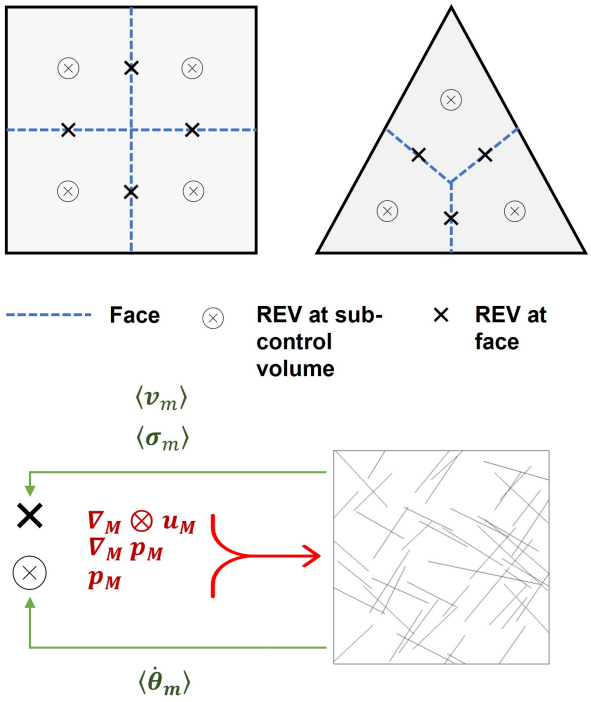

Figure 6.1: Location of the REVs in the multi-level Box method: each center of a face and of a SCV contains a REV. The REV receives the interpolated pressures and gradients at these locations, and sends homogenized fluxes and stresses to the faces and the homogenized storage term to the SCV.

an element ζ:

$$p_M \approx \sum_{k\in\zeta} N^k(\xi,\eta)\hat{p}_{M,k} \tag{6.12}$$

$$\frac{\partial p_M}{\partial x_i}(\xi,\eta) \approx \sum_{k\in\zeta} \frac{\partial N^k}{\partial x_i}(\xi,\eta)\hat{p}_{M,k} \tag{6.13}$$

$$\frac{\partial \boldsymbol{u}_M}{\partial x_i}(\xi,\eta) \approx \sum_{k\in\zeta} \frac{\partial N^k}{\partial x_i}(\xi,\eta)\hat{\boldsymbol{u}}_{M,k} \tag{6.14}$$

where $\hat{p}_{M,k}$ and $\hat{u}_{Mj,k}$ are macroscopic nodal values of pressure and displacement at node k.

Periodic boundary conditions are used to impose (6.9) and (6.10) on the REV. We already presented in Chapter 4 the procedure to add the periodicity constraints on periodic and non-periodic meshes containing interface elements.

Only one additional clarification needs to be made about the prescription of displacements and pressures on the corner nodes. For the mechanical problem the corner nodes have displacement fluctuations prescribed to zero to prevent rigid body motion, as is usually done when the mechanical problem is not dynamic. The prescribed pressures, however, need to

guarantee that (6.11) is fullfilled. So, we adopt here the same procedure used by Frey et al. (2013) and Marinelli et al. (2016). It is the following iterative process:

1. Prescribe the master corner node as equal to p_M.
2. Solve the flux problem and compute $\langle p_m \rangle$
3. If $|p_M - \langle p_m \rangle|$ is below a tolerance ε_{tol}, the flux problem converged; proceed to the next step.
4. If convergence is not reached, prescribe a correction to the master corner equal to $p_M - \langle p_m \rangle$ and return to step 2.

6.4.2 Homogenization and computation of residuals

The solution of the REV boundary value problem has been detailed in Chapter 2. We recall that the fluid percolation and mechanical equations are solved sequentially with a two-way coupling. Darcian flow is assumed for both the fractures and the porous matrix.

After the solution of the REV problem, the homogenized stresses and velocities are calculated with (6.3) and (2.12); then, they are used to compute the acting forces $\boldsymbol{f}_F$ and flow rates q_F at the corresponding face F of the macroscale mesh as:

$$\boldsymbol{f}_F = \mathbf{n}_F \cdot \boldsymbol{\sigma}_M |F| \tag{6.15}$$

$$q_F = \rho_\alpha \boldsymbol{n}_F \cdot \boldsymbol{v}_M |F| \tag{6.16}$$

where $\boldsymbol{n}_F$ is the unit vector normal to F. And at the center of a sub-control volume, the homogenization of the REV returns the average volumetric content (Equation 6.5).

The residuals in a node k are then computed as:

$$\boldsymbol{\Psi}_M^{s,k} = \sum_{F \in B_k} \boldsymbol{f}_F + \overline{\boldsymbol{f}}_k \tag{6.17}$$

$$\Psi_M^{f,k} = \sum_{F \in B_k} q_F + \overline{q}_k + \sum_{V \in B_k} \rho_\alpha \dot{\Theta}_{M,V} \tag{6.18}$$

where B_k is the control volume around node k, V is a sub-control volume, $\overline{\boldsymbol{f}}_k$ and $\overline{q}_k$ are prescribed forces and fluxes at node k.

In the exceptional case of an infinite Biot's modulus and a Biot's coefficient constant and equal to 1.0 in the REV, the REV computations at the sub-control volumes centers are not necessary. This is because the changes of porosity depend only on the macroscale displacements in this case, and so the volumetric strains can be directly computed using the shape functions.

6.4.3 Computation of the macroscopic Jacobian matrix

Since multiscale methods do not involve any assumption on the form of the macroscale constitutive laws, the macroscale tangent operator needs to be determined numerically. Works that use the multi-level FEM usually retrieve the Jacobian matrix with a perturbation method (e.g. Feyel and Chaboche, 2000; Marinelli et al., 2016) or through the static condensation of the microscale global tangent matrix (e.g. Kouznetsova et al., 2001b; Feyel and Chaboche, 2001; Khoei and Hajiabadi, 2018). The former is used in this work because of its easier implementation.

DuMu^x already employs the perturbation method to assemble the tangent matrix using a finite difference scheme. However, in the original code this is done by perturbing each primary variable at each node at a time. A solution to reduce the number of perturbations, and, consequently, of REV simulations, is to perturb directly the values at the integration point. Feyel and Chaboche (2000), for example, perturbed the components of the strain vector instead of the nodal displacements. Here, we brought this idea to hydro-mechanical simulations with the multi-level Box. This means that the quantities evaluated at the faces and sub-control volumes centers are perturbed, which are: p_M (Equation 6.12), $\nabla_M p_M$ (Equation 6.13) and $\nabla_M \boldsymbol{u}_M$ (Equation 6.14).

By provoking a perturbation ε_p in a variable a, the following derivatives are calculated using a forward-difference approximation:

$$\frac{\partial \boldsymbol{f}_F}{\partial a_M} \approx \frac{\boldsymbol{f}_F(a_M + \varepsilon_p) - \boldsymbol{f}_F(a_M)}{\varepsilon_p} \tag{6.19}$$

$$\frac{\partial q_F}{\partial a_M} \approx \frac{q_F(a_M + \varepsilon_p) - q_F(a_M)}{\varepsilon_p} \tag{6.20}$$

$$\frac{\partial \dot{\Theta}_V}{\partial a_M} \approx \frac{\dot{\Theta}_V(a_M + \varepsilon_p) - \dot{\Theta}_V(a_M)}{\varepsilon_p} \tag{6.21}$$

where $\boldsymbol{f}_F$ and q_F are the force vector and mass flux at a face F, computed from (6.15) and (6.16), and $\dot{\Theta}_V$ is the variation in time of the fluid volumetric content, computed from (6.5); the perturbed variable a is either p_M, $\frac{\partial p_M}{\partial x}$, $\frac{\partial p_M}{\partial y}$, $\frac{\partial u_M x}{\partial x}$, $\frac{\partial u_{My}}{\partial y}$ or $\frac{\partial u_{Mx}}{\partial y}$. Due to symmetry conditions, derivatives of forces/fluxes with respect to $\frac{\partial u_{My}}{\partial x}$ are equal to their derivatives with respect to $\frac{\partial u_{Mx}}{\partial y}$. In brief, for each assemblage of the macroscale tangent matrix there are six perturbations per REV.

The computation of the perturbed homogenized quantities requires the solution of a perturbed boundary value problem in the REV. To make this procedure more efficient, the microscale Jacobian matrix is not updated at each perturbation; so, the tangent matrix computed at the end of the calculation of the residuals is used. This categorizes the iterative solution of the perturbed problem as a modified Newton-Raphson. To facilitate convergence, it is important to ensure that the perturbation is small enough for the tangent matrix to remain approximately unchanged.

The derivatives of the residuals in (6.18) and (6.17) with respect to the nodal values are retrieved from (6.19) and (6.21) with the finite element shape functions as:

$$\frac{\partial \boldsymbol{\Psi}^{s,k}_{M,i}}{\partial \boldsymbol{u}_{M,j}} = \sum_{F \in B_k} \frac{\partial \boldsymbol{f}_{F,i}}{\partial(\nabla \boldsymbol{u}_{M,j})} \boldsymbol{B}(\boldsymbol{x}_F) \tag{6.22}$$

$$\frac{\partial \boldsymbol{\Psi}^{s,k}_{M,i}}{\partial \boldsymbol{p}_M} = \sum_{F \in B_j} \frac{\partial \boldsymbol{f}_{F,i}}{\partial \boldsymbol{p}_F} \boldsymbol{N}(\boldsymbol{x}_F) + \frac{\partial \boldsymbol{f}_{F,i}}{\partial(\nabla p_F)} \boldsymbol{B}(\boldsymbol{x}_F) \tag{6.23}$$

$$\frac{\partial \Psi^{f,k}_{M,k}}{\partial \boldsymbol{u}_{M,j}} = \sum_{F \in B_k} \frac{\partial q_F}{\partial(\nabla \boldsymbol{u}_{M,j})} \boldsymbol{B}(\boldsymbol{x}_F) + \sum_{V \in B_k} \frac{\partial \dot{\Theta}_V}{\partial(\nabla \boldsymbol{u}_{M,j})} \boldsymbol{B}(\boldsymbol{x}_V) \tag{6.24}$$

$$\frac{\partial \Psi^{f}_{M,k}}{\partial \boldsymbol{p}_M} = \sum_{F \in B_k} \left(\frac{\partial q_F}{\partial \boldsymbol{p}_F} \boldsymbol{N}(\boldsymbol{x}_F) + \frac{\partial q_F}{\partial(\nabla p_F)} \boldsymbol{B}(\boldsymbol{x}_F) \right) + \sum_{V \in B_k} \left(\frac{\partial \dot{\Theta}_V}{\partial \boldsymbol{p}_V} \boldsymbol{N}(\boldsymbol{x}_V) + \frac{\partial \dot{\Theta}_V}{\partial(\nabla p_V)} \boldsymbol{B}(\boldsymbol{x}_V) \right) \tag{6.25}$$

where the superscript k indicates the corresponding node, $i, j = x, y$, $\boldsymbol{x}_F$ and $\boldsymbol{x}_V$ denote the coordinates of the center of a face F and a sub-control volume V, respectively, and:

$$\boldsymbol{B} = \begin{Bmatrix} \frac{\partial N^k}{\partial x} \\ \frac{\partial N^k}{\partial y} \end{Bmatrix} \tag{6.26}$$

6.4.4 Algorithm

Figure 6.2 presents the general algorithm for the multi-level Box. The assembly of the system is made element by element, and for each element the components of the residual and Jacobian matrix are computed one face at a time, and then one sub-control volume at a time.

Each calculation of fluxes, stresses and storage terms requires a call to the microscale problem. At the level of the REV, the flux and mechanical equations are solved sequentially. The flux problem involves the localization of the interpolated pressure gradients and macroscale pressures with the algorithm described in Section 6.4.1. The mechanical problem involves the localization of the interpolated displacement gradients. It receives the pressures calculated in the flux problem to solve the equilibrium expressed in terms of effective stresses and fluid pressure. Then, the resulting displacements are used to update permeabilities and other strain-dependent parameters. The flux problem is considered to be at steady-state, so scale separation must exist.

6.4.5 Implementation in DuMu^x

A new module called `Multiscale` was added to DuMu^x to include multiscale simulations with the multi-level Box method. Its main components are illustrated in Figure 6.3.

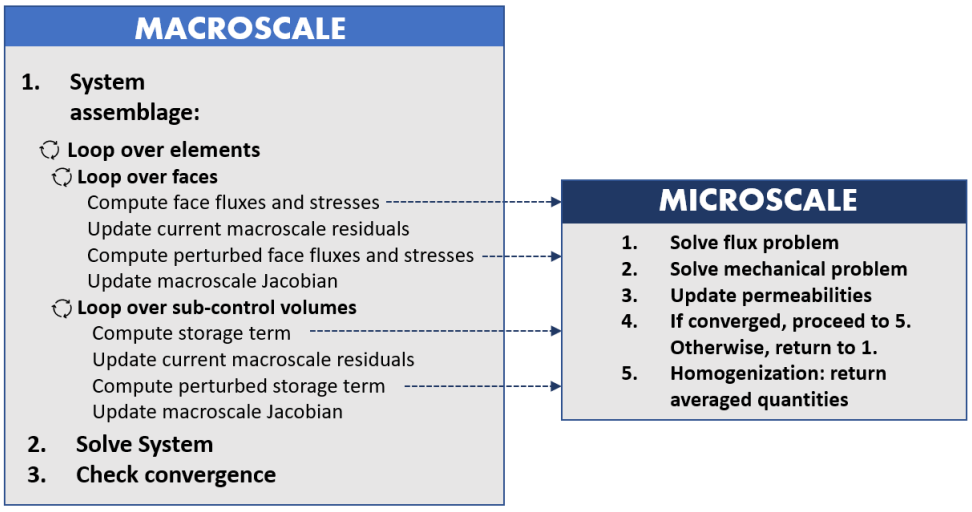

Figure 6.2: General algorithm of the implemented multi-level Box method. Each computation of stress, flux and storage term corresponds to a REV simulation, where the flux and mechanical problems are solved sequentially.

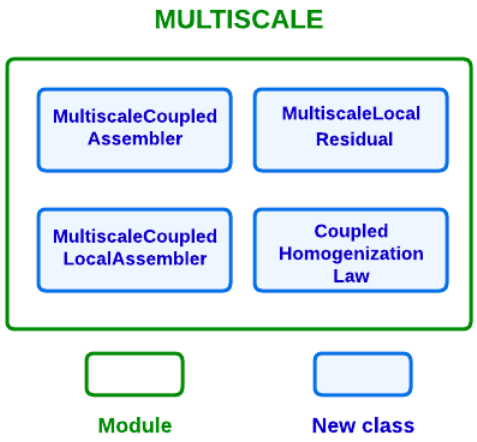

Figure 6.3: The new module called Multiscale in DuMu^x.

The main differences between multiscale simulations and one-scale simulations lie in the assemblage of the system. To deal with these particularities, the new classes `MultiscaleCoupledLocalAssembler` and `MultiscaleCoupledAssembler` were created. The original assembly classes in DuMu^x could not be used because they provoke perturbations in the nodal variables; the new class for multi-scale analyses updates the Jacobian matrix by perturbing the variables interpolated at the faces and sub-control volumes center. Also, the original classes used to compute residuals require a constitutive law to be provided. To overcome

this, a the new class `CoupledHomogenizationLaw` was created to calculate residuals. This is where the REV problem is called and where the homogenized quantities are received to compute forces, fluxes and storage terms. Finally, the new base class `MultiscaleProblem` was created. It is similar to all the other problem classes in DuMu^x, with the difference that, instead of receiving an object that contains the definition of constitutive properties, it must receive an object that belongs to the `Microscale` class.

The `Microscale` class must be completely defined by the user and contains two mandatory functions: one for initialization, which creates the REV mesh and establishes the mappings between nodes necessary to couple different domains and to impose periodic boundary conditions; and a function that solves the localization boundary value problems and returns homogenized quantities. The microscale problem contains all the ingredients for a multi-domain problem described in Section 3.1.1.

6.5 Validation

To verify the accuracy and good implementation of the coupled multi-level Box method, a Terzaghi-like consolidation problem was simulated. The geometry and boundary conditions are the same of the validation case described in Figure 3.7 and Table 3.2. However, the domain now is a fractured medium composed of two persistent and perpendicular sets of fractures. The fractures have a constant spacing of 5 mm between them. As this is a regular periodic domain, its REV reduces to the 1 cm unit cell illustrated in Figure 6.4. Periodic boundary conditions were imposed with the coupling manager for strong periodicity.

The domain was discretized in 10 squares of dimensions 10 cm x 10 cm. So, the macroscopic element is 10 times larger than the microscale's unit cell. The mesh of the unit cell is shown in Figure 6.4. A reference solution was obtained by solving the same problem with an explicit representation of all fractures; in this case, the mesh is composed of 1000 unit cells with the mesh of Figure 6.4. For this reference solution, the fixed-stress split was adopted to handle the hydro-mechanical coupling.

The minimum time step that can be used depends on the size of the mesh. So, naturally, the minimum time step for the macroscale problem is larger than that of the reference solution. For the multiscale simulation, the minimum time step to not provoke spurious oscillations was 100 s; for the reference solution, this time step is 10 s. The total time of the simulation is 3000 s.

Table 6.1 describes the material parameters used in this analysis.

Figure 6.5 compares the reference solution with the multiscale solution. A maximum difference of 8 % was observed in this test. The multiscale solution underestimates the pressures along the vertical axis. Nonetheless, it is satisfactory, specially when considering the major differences from the reference solution, which are the mesh and time step sizes and the assumption of stationarity at the level of the REV.

This loss of accuracy seems reasonable when considering the computation time that was

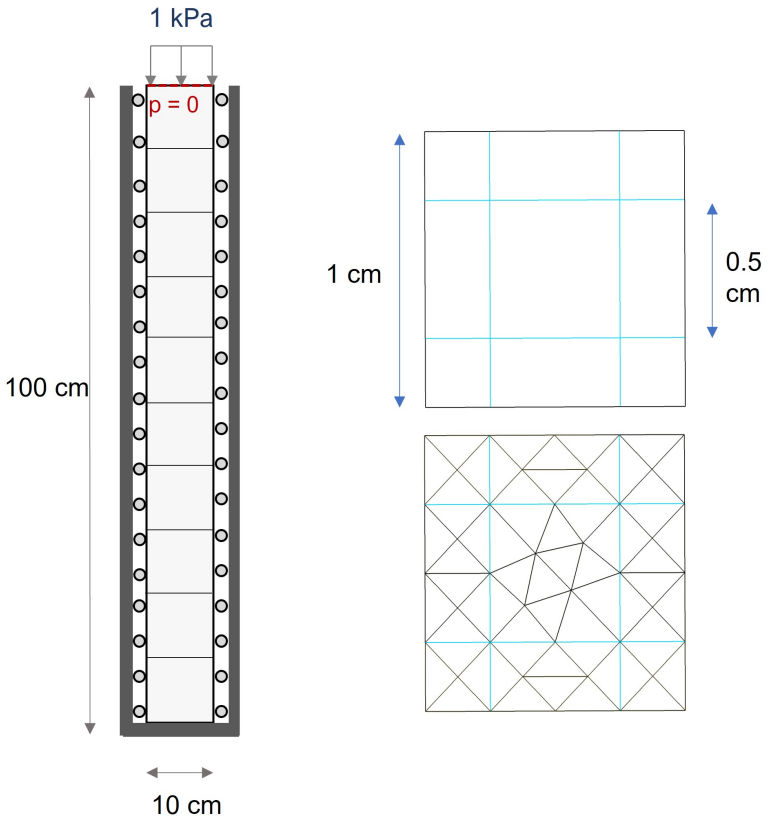

Figure 6.4: Consolidation problem used to validate the multi-level Box. On the left, the macroscale domain, its mesh and boundary conditions. On the right, the fractured unit cell and its mesh are presented, with fractures in blue.

Table 6.1: Fracture and porous matrix parameters adopted in the validation case of the multi-level Box, described in Figure 6.4.

Quantity	Unity	Value
Matrix Young's modulus (E)	kPa	1000
Matrix Poisson's ratio (ν)	-	0.25
Matrix Permeability (k_s)	m^2	1.16×10^{-9}
Matrix Biot's coefficient (b)	-	1.0
Matrix Biot's modulus (M)	kPa	∞
Fracture Normal Stiffness (K_n)	kPa/m	50000
Fracture Tangent Stiffness (K_t)	kPa/m	10000
Fracture Permeability (k_t)	m^2	1.0×10^{-7}
Fracture Biot's coefficient (b_f)	-	1.0
Fracture Biot's modulus (M_f)	kPa	∞

saved with the multiscale simulation. The multiscale simulation took on average 4.8 s and three iterations to solve each time step, which results in an average of 1.6 s per time step.

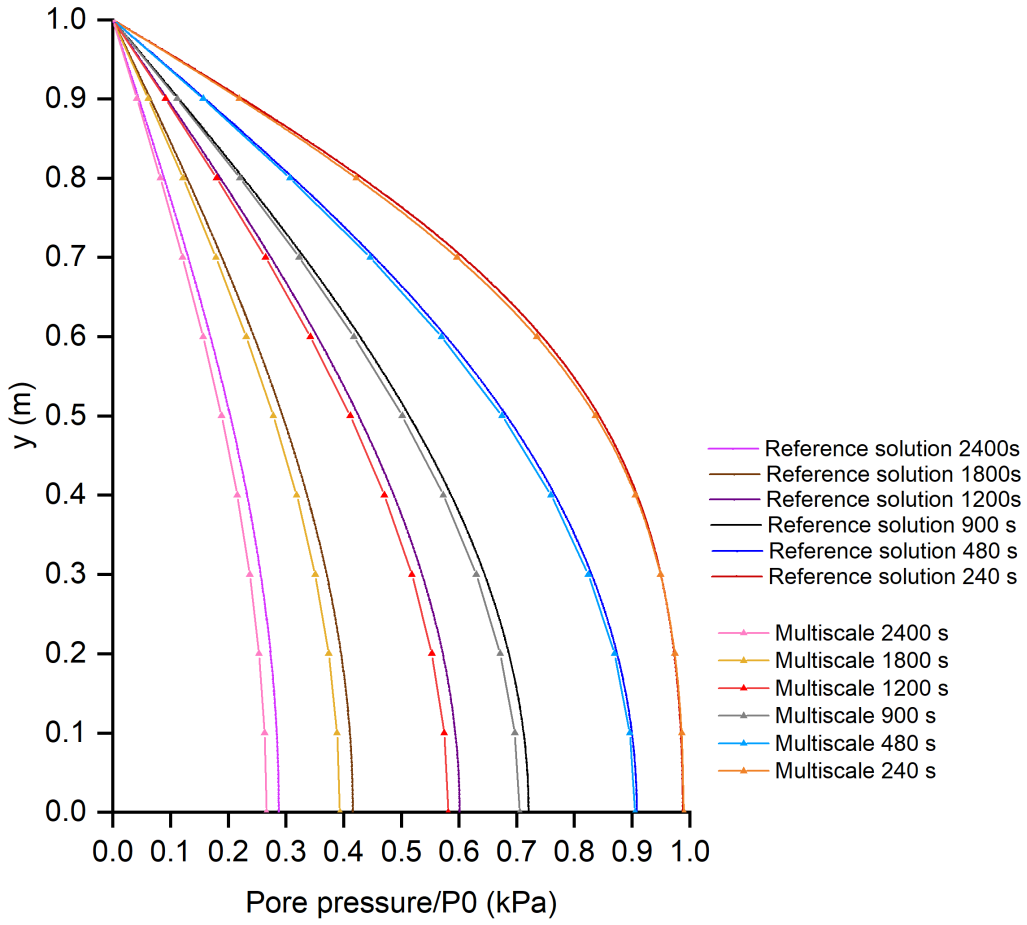

Figure 6.5: Comparison of the solutions of the consolidation problem in a fractured domain with the multi-level box and the reference solution with explicit representation of all the fractures.

As for the reference solution, it took on average 24.3 s and 4 iterations to solve each time step, that is, 6.1 s per time step.

6.6 Conclusions of the chapter

Multicale methods are more robust than the equivalent property (upscaling) approach because they do not require the assumption of a constitutive law for the macroscale and the conditions of the microscale problem do not need to be chosen, but arise from the large-scale simulation.

We adapted the framework of a multiscale method called the finite element method squared to create an adaption called the multi-level Box method. The main impact of this modification is the addition of local mass conservation to the original method. Each center of a face and of a sub-control volume corresponds to a REV computation where homogenized

quantities are obtained. The macroscopic Jacobian matrix is computed with a perturbation method.

The multi-level Box method was implemented in DuMu^x in a new module called Multiscale. The implemented algorithm was verified for a consolidation problem in a regular fractured domain, and despite the assumption of stationary flow at the REV, of the coarser mesh and of the larger time step, the results agree well with the direct solution of a coupled transient problem in the fractured domain.

Chapter 7

Multiscale simulation of a fractured reservoir: a case study

7.1 Introduction

The tools and methods developed in this thesis will be applied to a case study inspired by the Ekofisk reservoir, a chalk reservoir located in the North Sea. Despite of having a high average porosity of 32%, the carbonate in the Ekofisk reservoir has a permeability of only 1 mD. However, well tests indicated that permeability could get as high as 150 mD because of the existence of conductive fractures. Teufel and Farrell (1990) classified the fractures of the Ekofisk field in four classes: healed, isolated, stylolite-associated and tectonic. Only the tectonic fractures form a well connected conductive path for the fluids. These are planar shear discontinuities that appear sometimes in conjugate pairs. They dip from 65 to 80 and their orientations are usually aligned with those of large faults that occur in the reservoir (Toublanc et al., 2005). The average spacing of the tectonic fractures ranges between 15 and 100 cm. In zones of higher intensity, the typical spacing can reach 5 cm. Since they can not be captured by seismic methods, but are larger than the extracted cores, their lengths are very uncertain. However, from their average spacing and from investigations of analogues it is possible to infer that their sizes range from tenths of centimeters to meters (Teufel and Farrell, 1990).

The tectonic fractures in the Ekofisk field are good candidates for a multiscale analysis. Firstly, because their dimensions are much smaller than those of the reservoir and also than the typical size of a cell in a reservoir simulator, which has at least tenths of meters (Bourbiaux, 2010; Christie, 1996). Secondly, because they are connected and frequent enough to influence the performance of some regions of the reservoir. And lastly, because this influence is dynamic and hard to capture with equivalent properties.

In the multi-scale model to be presented, the microscale's fractures replicate one of the typical patterns of the tectonic fractures in the Ekofisk reservoir. Also, the initial pore pressures and stresses were taken from the average values reported by Teufel and Farrell

(1990). The adoption of this reference case had the sole purpose of building a realistic synthetic case, with no intention of representing the actual reservoir, which has many other complexities that are not considered in our simplified model.

7.2 Modeling of the REV

7.2.1 Generation of the DFNs

The orientation, dip and intensities of the tectonic fractures in Ekofisk are relatively well known thanks to a number of geological studies that were made in the area (Teufel and Farrell, 1990; Toublanc et al., 2005). However, there is no public information on the ranges of the lengths of these fractures, or on the statistical distributions of their geometrical features. So, to generate the DFNs that replicate their typical configuration, we used as a reference the work by Gutierrez et al. (1994) . They performed mechanical numerical experiments on representative fractured samples of the Ekofisk chalk; these samples are squared with size of 2 m. We used their third sample, called "model of a 40% porosity chalk with natural fractures", to define a mean fracture intensity and a mean fracture length.

The reference sample is made of conjugate pairs of shear fractures. The lengths of the dominant shear fractures range between 0.7 m and 1.4 m and their average intensity is of 4 fractures/m^2. As for their conjugates, they have lengths that vary from 0.13 m to 0.82 m and mean intensity of 2.6 fractures/m^2. The actual rock probably has tectonic fractures that are larger than those, as Teufel and Farrell (1990) mentioned that these fractures could have up to 10 m. However, as fracture lengths usually follow a power-law like distribution, these largest fractures are probably rare; and since there is no other data on their sizes, we will stick only to what can be observed in the samples by Gutierrez et al. (1994).

With a notion of the average lengths, intensities and dips (which range from 65° to 80°), it is possible to generate stochastic DFNs if an assumption is made on the statistical distribution of these features. In the lack of these data, we assume a normal distribution for the lengths and dips. Since the lengths in the reference models do not vary in large ranges, they should be well represented by a normal distribution. The standard deviations of the properties were estimated using the three-sigma rule: based on the fact that 99.7 % of the values in a normal distribution lie within three standard deviations from the mean, the standard deviation can be estimated as the size of the range between the maximum and minimum observed values divided by six. Table 7.1 presents a summary of the geometrical features used to generate the DFNs. We developed a code to randomly generate the fractures; their centers were generated with a Poisson process. Then, the meshes were generated with the open source software Triangle (Shewchuk, 1996), which divides the domain in triangular finite elements.

Using the distributions in Table 7.1, 100 random generations were performed for 10 different sample sizes that range from 1 m to 10 m. Figure 7.1 shows an example of a 8 m

Table 7.1: Average and standard deviations of the geometrical features of the DFN used in the case study. A normal distribution is assumed for the lengths and the dips.

	Dominant Set		Conjugate Set	
	Average	Std. Deviation	Average	Std. Deviation
Length (m)	1.05	0.12	0.48	0.12
Dip (°)	72.5	4.2	72.5	4.2
Intensity ($1/m^2$)	4.0	-	2.6	-

sample.

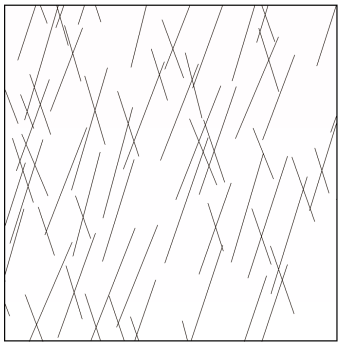

Figure 7.1: Example of one of the generated DFNs that replicate the pattern of the tectonic fractures in the Ekofisk reservoir. There is a main sub-vertical set of larger fractures, which are sometimes associated to conjugate smaller fractures.

Figure 7.2 shows the averages of the crack tensor components (Equation 2.34) as a function of sample size. Since the fractures are almost vertical, the average F_{xx}, which gives the projection of the fractures lengths in the y-direction, is much higher than F_{yy}.

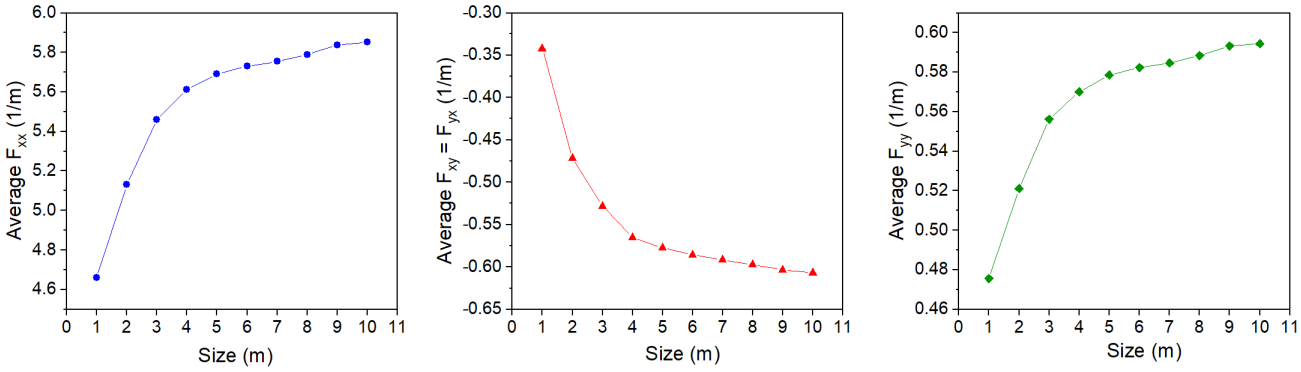

Figure 7.2: Average of the crack tensor components of the DFN used in the study case as a function of sample size.

7.2.2 Constitutive models for the fractures and intact rock

The intact rock is considered to be linear elastic and the elastic behavior of the fractures follows the Barton and Bandis law (Barton et al., 1985), according to which:

$$K_n = \frac{K_{ni}}{\left(1 - \frac{u_n}{u_{max}}\right)^2} \tag{7.1}$$

where K_n is the fractures normal stiffness, K_{ni} is the initial normal stiffness, u_n is the normal displacement jump (positive for compression or closure) and u_{max} is the fractures maximum closure. The fractures tangent stiffness is considered to be constant here, which is a simplification since this stiffness tends to be damaged when shear failure occurs or when the fracture opens.

When their elastoplastic behavior is considered, the fractures and the intact rock are modelled with a perfectly plastic Mohr-Coulomb criterion. Table 7.2 describes the intact rock and fracture constitutive parameters. The mechanical parameters used in this study are the same as those adopted by Gutierrez et al. (1994). These authors, however, adopt a strain-dependent Mohr-Coulomb yield surface with cap for the intact rock.

Gutierrez et al. (1994) obtained the properties of the rock matrix were obtained by fitting the experimental results on cores taken from the Ekofisk. For the fractures, Table 7.2 presents directly the initial normal stiffness, tangent stiffness and initial fracture opening. But these data are calculated from the Joint Roughness Coefficient (JRC) and Joint Compressive Strength (JCS) with the relationships proposed by Bandis et al. (1983). Gutierrez et al. (1994) estimated the JRC from tilt tests on fractured cores taken from the Ekofisk reservoir. JCS was estimated from the unconfined compressive strength of the intact rock, and the residual friction angle is assumed to be equal to the internal friction angle of the intact rock.

The permeability of the matrix is constant and equal to 1×10^{-15} or 1 mD. The permeability of the fractures (k_f) is a function of their aperture following the cubic law:

$$k_f = \frac{w^2}{12} \tag{7.2}$$

where w is the fracture's aperture.

7.2.3 Generation of the initial state

Prior to the multiscale simulations, it is necessary to set the initial stress state of the REV. According to Teufel and Farrell (1990), the average initial pore pressure in the Ekofisk was 48 MPa and the total overburden stress 62 MPa. Thus, the initial effective vertical stresses are 14 MPa. As for the horizontal stresses, they are much more uncertain and vary a lot. In-situ experiments indicate that the initial K_0 (ratio of effective horizontal stress to effective vertical stress) ranged between 0.2 and 0.5. So the effective horizontal stresses range between 2.8 MPa and 7 MPa.

Table 7.2: Fracture and intact rock parameters adopted in the case study.

Intact rock		Fractures	
Young's modulus, E(GPa)	1.4	Initial Normal Stiffness, K_{ni} (GPa/m)	10
Poisson's ratio, ν	0.2	Initial aperture, w_0 (mm)	1.8
Cohesion, c (MPa)	4.1	Tangent Stiffness, K_t (GPa/m)	50
Friction angle, φ (°)	24	Cohesion, c_f (MPa)	2
Dilation angle, ψ (°)	0	Friction angle, φ_f (°)	14
Biot's coefficient b	1.0	Dilation angle, ψ_f (°)	14
Permeability, k_m (m^2)	1×10^{-15}	Biot's coefficient, b_f	1.0
		Permeability, k_f	Function
		Minimum aperture, w_{min} (m)	5×10^{-7}

Here, the directions x, y and z will refer to the horizontal, vertical and out-of-plane directions, respectively.Following Gutierrez et al. (1994), an initial K_0 of 0.2 was selected, which means an initial horizontal stress of 2.8 MPa. Plane-strain conditions are assumed.

In order to impose these initial stress conditions to the fractured samples, these latter were submitted to the loads illustrated in Figure 7.3. This loading was divided in 100 steps and a fully drained behavior was assumed.

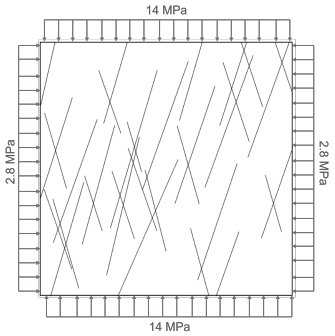

Figure 7.3: Stress boundary conditions used to set the initial stress state of the REVs in the case study.

Apart from generating the initial distribution of stresses, this procedure also generates the initial apertures, which in turn define the initial fracture permeabilities and stiffness in the large-scale simulation. The initial average aperture is 8.2×10^{-5} m and the minimum aperture is $5.6 \times 10^{-5} m$.

7.2.4 Upscaling of the initial properties and REV size

Gutierrez et al. (1994) used 2 m samples to perform their numerical experiments, but they did not perform REV studies to define the actual size of the REV or to verify how reliable are the estimations obtained from the size they selected.

The methodology described in Chapter 5 was used to define the REV for our replica of the tectonic fracture network in the Ekofisk field. The first step is to select a reference volume to perform the upscaling in a sample of REVs. Figure 7.2 shows that the average geometrical properties stabilize above a size of 4 m, so this was selected as the reference volume. All 4 m samples were firstly subjected to the loading in Figure 7.3, so their initial apertures were generated. In any of these samples the initial stress conditions were sufficient to make neither the fractures nor the intact rock reach the yielding surface. Then, the equivalent constitutive tensors were obtained. This upscaling was performed by imposing mortar periodic boundary conditions with the procedure described in Section 4.2.2. The permeability tensor of the intact rock ($\boldsymbol{k}_i$) is the following:

$$\boldsymbol{k}_i = \begin{bmatrix} k_{xx} & k_{xy} \\ k_{yx} & k_{yy} \end{bmatrix} = \begin{bmatrix} 1 \times 10^{-15} & 0 \\ 0 & 1 \times 10^{-15} \end{bmatrix} m^2 \tag{7.3}$$

And the stiffness tensor $\boldsymbol{C}_i$ of the intact rock is the following:

$$\boldsymbol{C}_i = \begin{bmatrix} C_{11} & C_{12} & C_{13} & C_{14} \\ C_{21} & C_{22} & C_{23} & C_{24} \\ C_{31} & C_{31} & C_{33} & C_{34} \\ C_{41} & C_{42} & C_{43} & C_{44} \end{bmatrix} = \begin{bmatrix} 1555.6 & 388.9 & 388.9 & 0 \\ 388.9 & 1555.6 & 388.9 & 0 \\ 388.9 & 388.9 & 1555.6 & 0 \\ 0 & 0 & 0 & \end{bmatrix} MPa \tag{7.4}$$

Figures 7.4 and 7.5 present the QQ-plots for the components of the equivalent permeability and stiffness tensors, $\boldsymbol{k}$ and $\boldsymbol{C}$ for the fractured 4 m samples. In all experiments the upscaled tensors were symmetrical, so only half of the off-diagonal terms is presented. The third row and columns of $\boldsymbol{C}$ are not shown because the normal stresses in the direction z are calculated from the plane-strain assumption, and not upscaled like the other components.

The anisotropic behavior caused by the fractures is clear. Because the main fractures dip almost vertically, the permeability k_{yy} is one order of magnitude larger than k_{xx} and two orders of magnitude larger than the permeability of the intact rock. Also, the component k_{xy} is on average larger than k_{xx}, which means that, in the initial conditions, a pressure gradient in the x-direction provokes a higher specific flux in the y-direction than in the x-direction.

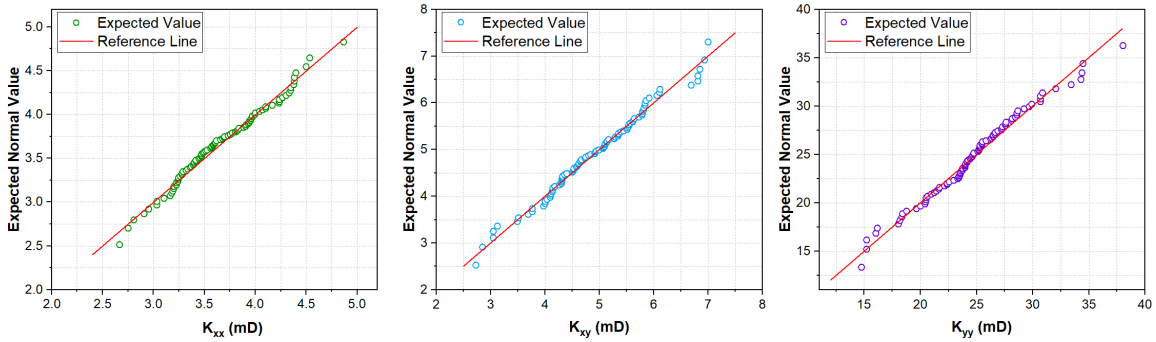

Figure 7.4: QQ-plots for the equivalent permeability tensor of the 4 m samples generated for the case study.

Anisotropy also manifests in the equivalent stiffness tensor; the components C_{14} and C_{24}

are non-zero, which means that shear strains are associated to normal stress increments and vice versa. However, their values are insignificant when compared to the other components. As for the diagonal components, C_{11} is much more significantly reduced than C_{22}, which remains very close to the value for the intact rock. As the fractures are nearly vertical, their apertures suffer larger variations when submitted to a normal stress in the x-direction.

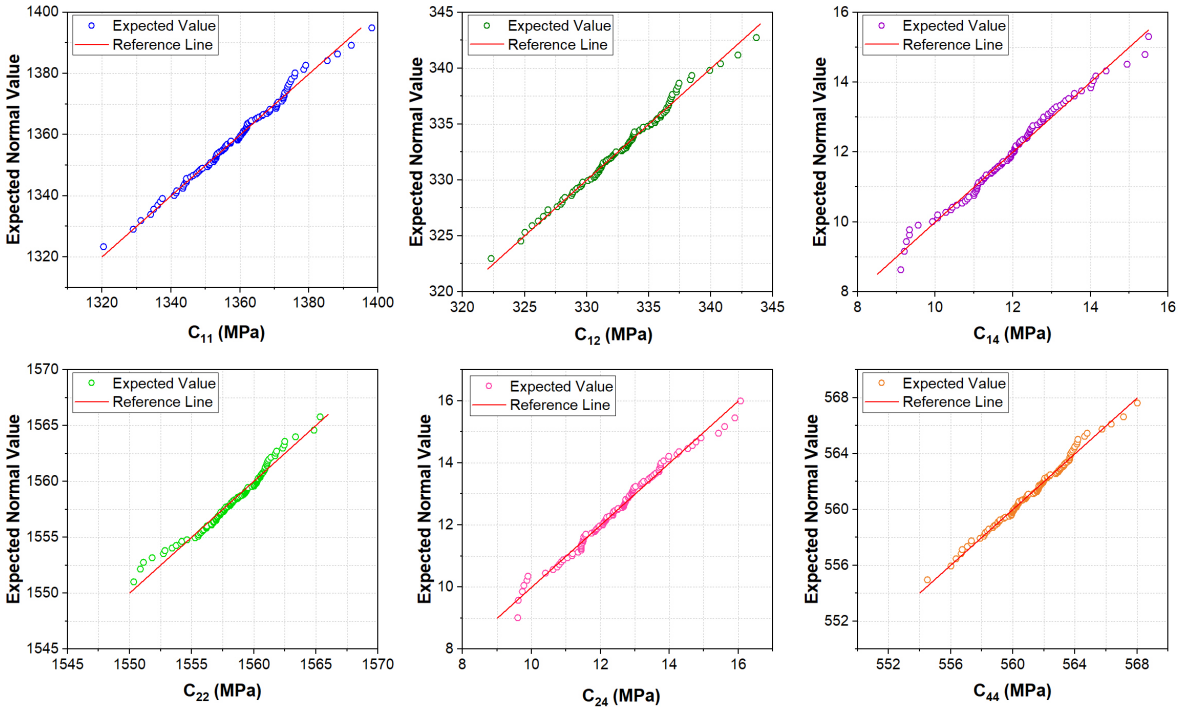

Figure 7.5: QQ-plots for the equivalent stiffness tensor of the 4 m samples generated for the case study.

Figures 7.4 and 7.5 show that the distribution of the constitutive tensors for the 4 m samples are nearly normal. So, these data can be used to calculate the REV using Equation 5.10. Table 7.3 shows the minimum sizes calculated for a maximum precision error of 10 %, a confidence level of 95% and one REV generation (N = 1 in Equation 5.10).

The small sizes obtained for most of the elastic parameters can not be used as the actual size of the REV, since they are smaller than the average fracture lengths. Also, some are smaller than the average fracture spacing, which means that random generations of this size could return samples with no fractures. So, the smallest possible sample that represents well the fracture network geometry should be selected in this case. Although C_{14} and C_{24} returned a minimum size of 8.7 m, they are one to two orders of magnitudes smaller than the other components, so they are too insignificant to dictate the REV size. The critical parameter is permeability, which returned a minimum size of 10 m.

In a multiscale simulation, the size of the REV has a big impact on the computation time. As Equation 5.10 suggests, a reliable estimation of the average permeability can be

Table 7.3: Calculated REVs for a 10% error and one generation - Case study.

Geometrical						
	F_{xx}	F_{xy}	F_{yy}			
REV size (m)	5.5	8.8	5.5			
Permeability						
	k_{xx}	k_{xy}	k_{yx}	k_{yy}		
REV size (m)	6.1	10.0	10.0	8.6		
Elastic Stiffness Tensor						
	C_{11}	C_{12}	C_{14}	C_{22}	C_{24}	C_{44}
REV size (m)	0.8	0.9	8.7	0.15	8.7	0.35

obtained with either 1 REV of 10 m or from the average of 5 REVs of 2 m, for example. Since the order of computation time of each system at the REV boundary value problem is the square of the number of degrees of freedom, it would probably be more efficient to perform 5 multiscale simulations with a REV of 2 m. So, to minimise the computation time, we selected the size of 2 m for the REV that will be carried out to the multiscale simulations.

Equation 5.10 presupposes that the N REV generations are random. The process can be made less random by selecting smaller REVs that are known to return constitutive properties that are close to the average ones. To be able to have a good notion of the average behavior of the reservoir with one multiscale simulation only, one sample of 2 m was selected using the procedure that will be presented hereinafter.

7.2.5 Selection of the REV

Firstly, we obtained the upscaled constitutive tensors of a random 10 m sample to be used as a reference REV. According to the theory presented in Chapter 5, there is a 95% chance that this sample will return values that do not dist more than 10% from their true mean. This is true for the permeability k_{xy}, for which the minimum REV size was the largest; the size of 10 m is expected to return values that are even closer to the true mean for the other properties.

Then, a few 2 m samples who had crack tensor components close to those of the reference REV were tested for their properties. We selected the 2 m sample that returned properties that were the closest to those of the 10 m sample. Table 7.4 presents the upscaled properties of both the selected and reference REVs.

Figure 7.2 presents the selected 2 m REV and the mesh used in the multiscale simulations, which is composed of 736 nodes. This mesh was selected after a test of convergence of the upscaled properties when using mortar periodic boundary conditions.

Table 7.4: Properties of the 2 m REV selected for the case study and the reference 10 m REV.

Crack tensor (1/m)						
	F_{xx}	F_{xy}	F_{yy}			
10 m REV	5.88	-0.63	0.59			
2 m REV	5.35	-0.58	0.57			
Difference	9.0%	12.7%	3.4%			
Permeability ($\times 10^{-15}$ m^2)						
	k_{xx}	k_{xy}	k_{yx}	k_{yy}		
10 m REV	3.49	5.03	5.03	24.1		
2 m REV	3.34	4.53	4.53	23.6		
Difference	4.1%	9.9%	9.9%	2.3%		
Elastic Stiffness Tensor (MPa)						
	C_{11}	C_{12}	C_{14}	C_{22}	C_{24}	C_{44}
10 m REV	1348.5	330.4	13.0	1557.0	13.6	559.6
2 m REV	1399.9	344.2	12.31	1566.3	12.7	568.5
Difference	3.8%	4.3%	5.4%	0.6%	6.7%	1.6%

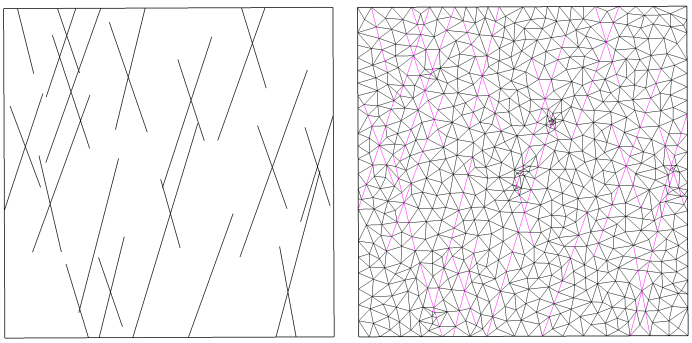

Figure 7.6: REV of size 2 m that was selected to carry out the multiscale simulations (left) and its mesh (right).

7.3 Multiscale simulations

7.3.1 Macroscale model

Figure 7.7 describes the synthetic case to be simulated with the multi-level Box method. The section of the reservoir is 200 m deep and an extension of 600 m is considered. The displacement restrictions at the bottom suggest that the reservoir is set over a very stiff rock.

The mesh at the reservoir scale is composed of 200 elements of dimensions 30 m x 20 m. The zone of production in Figure 7.7 indicates a well where the pressure is controlled. The initial pore pressure in the reservoir is 48 MPa. Two pressures were tested at the production

zone: 43 MPa and 38MPa. The fluid in the reservoir is incompressible water.

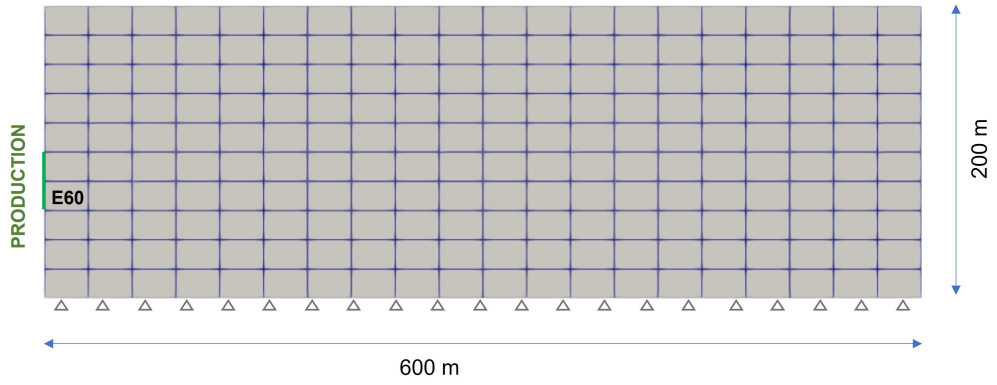

Figure 7.7: Mesh and boundary conditions of the synthetic case study.

7.3.2 Simulation of depletion

Neither the initial load nor the depletion were sufficient to make the rock matrix or the fractures reach their yielding surface. So, in the simulation of the depletion of the reservoir their behavior is elastic. For comparison purposes, three types of simulations were performed for the depletion with a bore hole pressure of 43 MPa. The first scenario is a static case, where the permeability and normal stiffness of the fractures are considered to be constant and equal to the initial values in Table 7.4. In a second scenario, the fractures permeability is dynamic and updated during the simulation with the cubic law (Equation 7.2). The third case considers both the fractures permeability and stiffness are dynamic; this latter is updated with the Bartis-Bandis law (Equation 7.1).

Figure 7.8 presents the flux rates and cumulative production for the three scenarios during one year of production. The use of only the initial properties significantly overestimates the flux rates. As a result, the predicted cumulative production at the end of one year is also overestimated by approximately 17%. The comparison between the scenario with dynamic permeability and stiffness and the scenario with dynamic permeability only shows that the production is quite sensitive to the fractures normal stiffness.

Figure 7.9 compares the pore pressure distribution of the static and dynamic scenarios after 100 days of production when the well pressure is 43 MPa. In the static scenario, the anisotropic permeability of the domain is clear; the pressure distribution is oriented with the main fracture set of the REV (see Figure 7.6) and favors the flux in the y-direction. However, the multiscale simulation of the dynamic scenario shows that this tendency changes in the zones that are reached by significant pore pressure reductions. This happens because, as the fractures start to close, the anisotropy of the equivalent permeability tensor becomes progressively less accentuated. The effect of this dynamic behavior is clear near the well, where the pore pressure distribution is perturbed in comparison with the static case. This

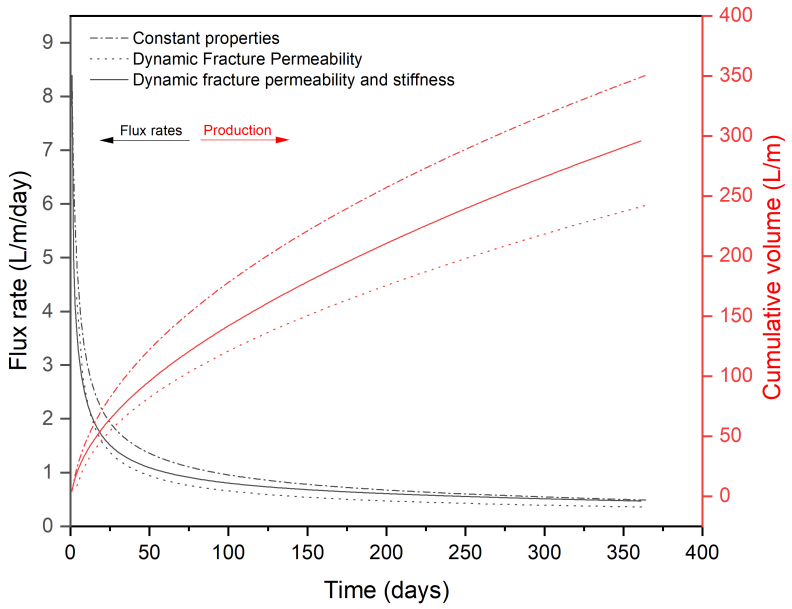

Figure 7.8: Comparison of the flux rates and cumulative production during one year of production for three scenarios: constant fracture properties, dynamic fracture permeability and dynamic fracture permeability and normal stiffness.

effect is more visible when the well pressure is 38 MPa (Figure 7.10).

Figure 7.11 shows this effect at the level of the microscale. The pressure increments and fracture apertures at the REV of one of the faces of element 60 (indicated as E60 in Figure 7.7) are compared for 40 and 160 days of production. As the depletion continues, the upstream fractures close and reach the minimum aperture value of 5×10^{-7} m. As a result, the distribution of the pressure increments become less influenced by the fractures sub-vertical orientation.

These changes can be quantitatively evaluated in Figure 7.12, which shows the evolution of the permeability tensor normalized by its initial values as a function of the pore pressure variation during depletion. While the off-diagonal terms of the permeability tensor vanish after a pore pressure variation of -2 MPa, while k_{xx} and k_{yy} decrease to 51 % and 9 % of their original values, respectively. These values stabilize because of the consideration of a minimum aperture in the model. Since the reduction in the component k_{yy} is more significant, the y-direction becomes less of a preferential direction for flow during depletion. For that reason, the pore pressure fields change as the fractures close.

Figure 7.13 compares the dynamic and static scenarios for the predicted cumulative volume of water after 200 days of production when the pressure at the well is 43 MPa and 38 MPa. While the use of constant permeability makes this 5 MPa reduction in the well seem more than twice as effective, the dynamic case shows that the gain in productivity is less significant, of the order of 67%. This happens because, as the initial well pressure gets lower, the fractures also close more rapidly and more considerably. Thus, the consideration

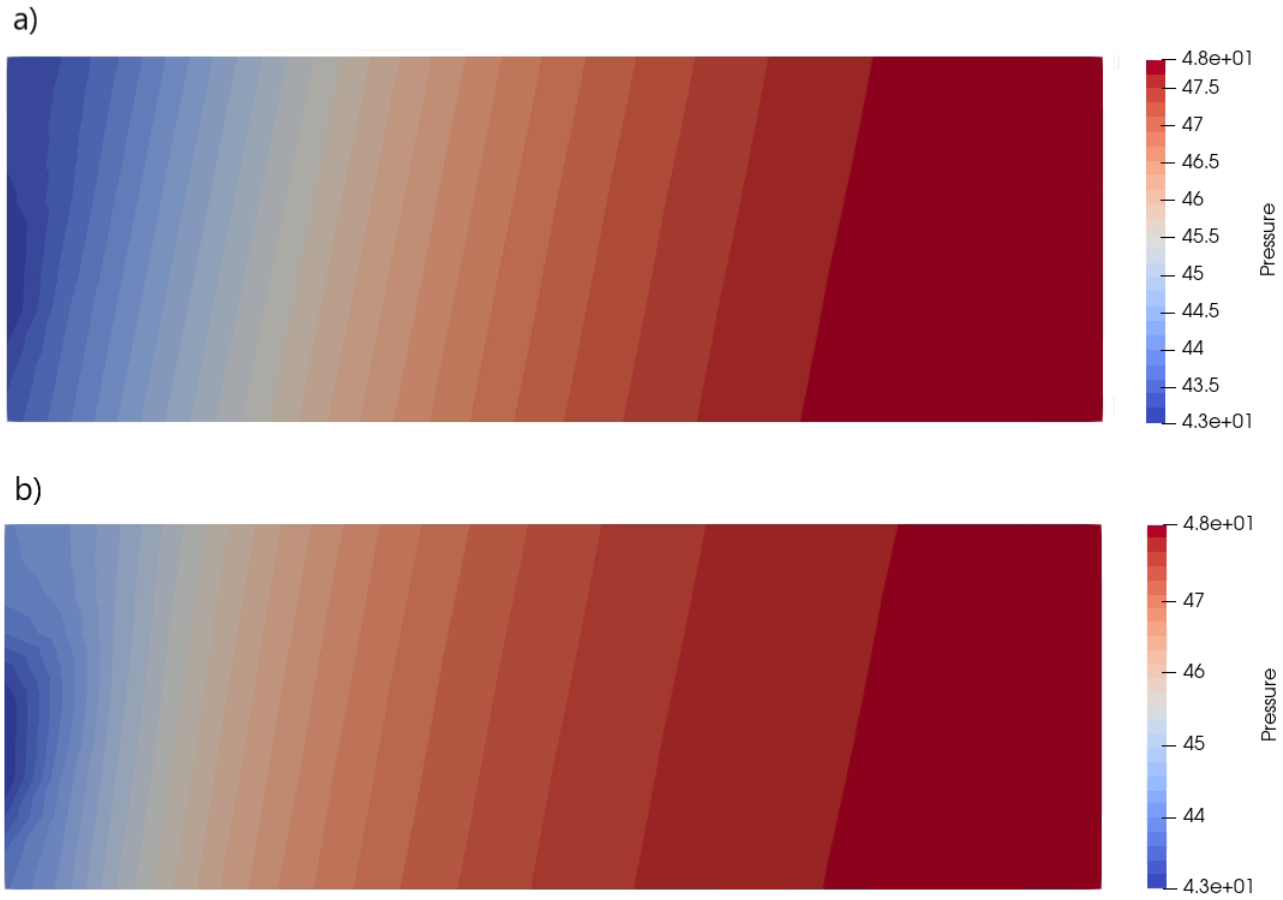

Figure 7.9: Pore pressure distribution in the reservoir after 100 days of production for a) the static case and b) the dynamic case. The well pressure is 43 MPa.

of dynamic permeabilities when setting the well pressure may also be useful to maintain the reservoir's permeability and productivity.

7.3.3 Evaluation of the separation of scales

The accuracy of the results obtained with the multiscale simulations is expected to improve as the scale separation gets stronger, specially because of the assumption of stationary flow at the REV. The pressure variations are the driver of the field changes in the reservoir during depletion. As a consequence, we can evaluate the scale factor in Equation 2.4 by using the pressure as the characteristic physical quantity Ψ, as was done by Bertrand et al. (2020).

To get conservative results, the most critical pressure gradient will be estimated as the difference between the pressure in the well and the initial reservoir pressure (48 MPa) divided by the minimum dimension of the element at the well, which is 20 m. Thus, the critical pressure gradient is 0.25 MPa/m when the well pressure is 43 MPa and 0.5 MPa/m when

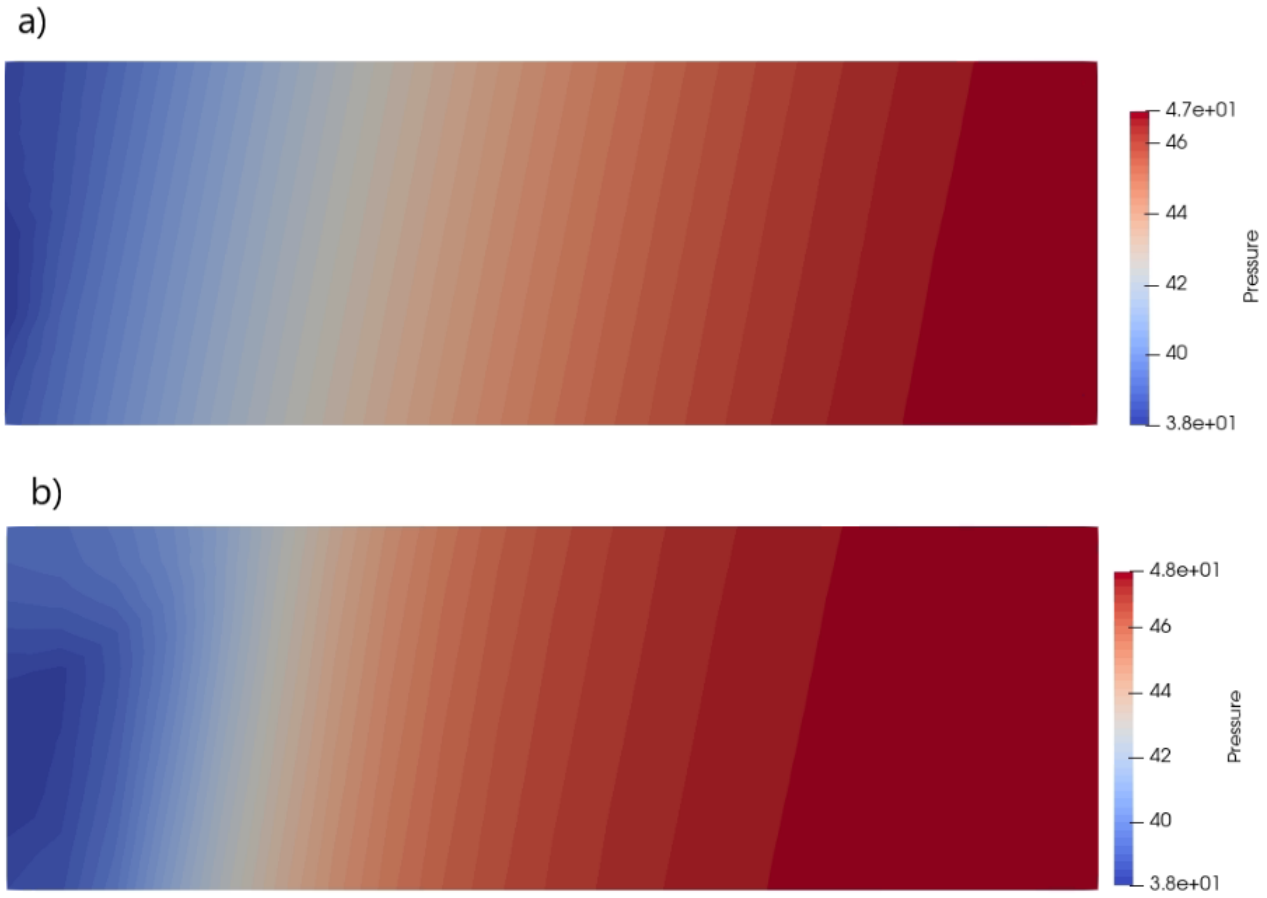

Figure 7.10: Pore pressure distribution in the reservoir after 100 days of production for a) the static case and b) the dynamic case. The well pressure is 38 MPa.

the well pressure is 38 MPa. The quantity Ψ in Equation 2.4 will also be estimated, in a conservative manner, as the well pressure, which is the minimum possible pressure.

Hence, recalling that the characteristic length l_c of the REV has been set to 2 m, when the well pressure is 43 MPa:

$$\varepsilon = \frac{0.25 \text{ MPa/m}}{43 \text{ MPa}} \times 2 \text{ m} = 0.012 \tag{7.5}$$

and when the well pressure is 38 MPa:

$$\varepsilon = \frac{0.5 \text{ MPa/m}}{38 \text{ MPa}} \times 2 \text{ m} = 0.026 \tag{7.6}$$

This means that at the REV the imposed pressures can vary up to 1.2% and 2.6% for the pressures of 43 MPa and 38 MPa, respectively. If the REV was really a point at the macroscale, this variation would be zero. But the maximum scale parameters obtained in our simulations are small enough to affirm that a separation of scales exists.

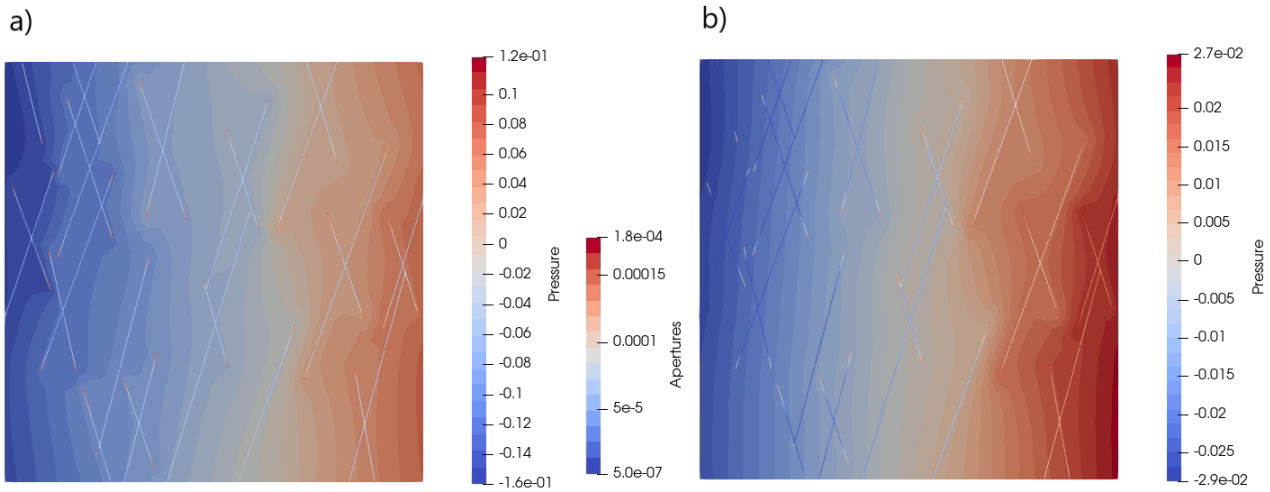

Figure 7.11: Comparison of the distribution of the pressure increments and of the fracture apertures (presented in the lower-dimensional elements) after a) 40 days and b) 160 days of production.

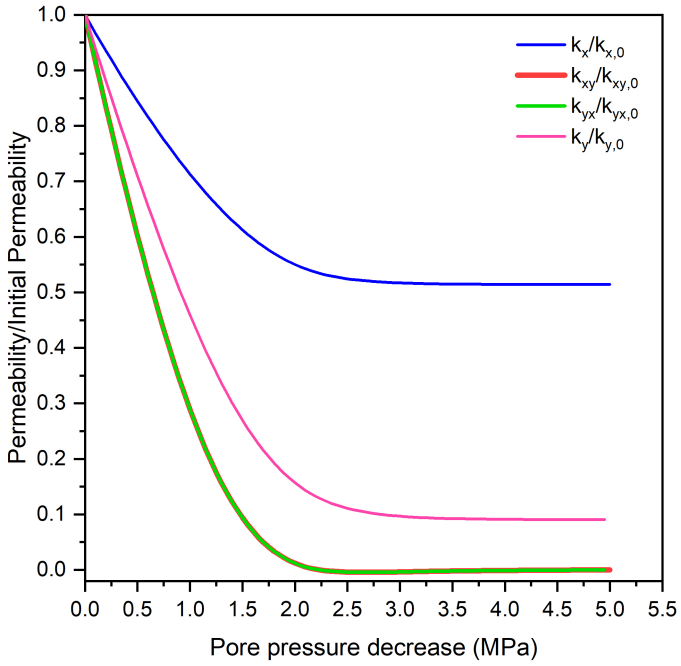

Figure 7.12: Equivalent permeabilities normalized by their initial values as a function of pore pressure decrease during depletion.

7.4 Points for optimization

While multiscale methods were shown to be an option to incorporate the dynamic behavior of small fractures, there are two main issues that need to be addressed for them to be

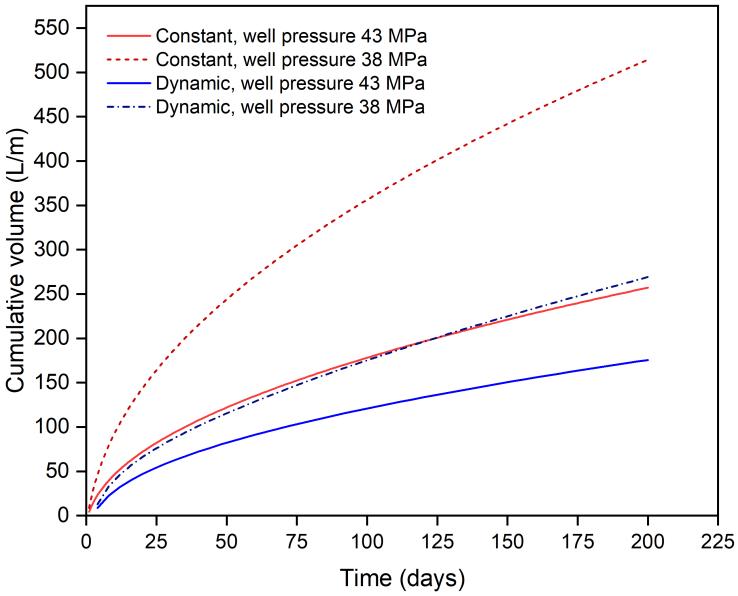

Figure 7.13: Cumulative production predicted for 200 days of production for the static and dynamic scenarios for two well pressures: 43 MPa and 38 MPa.

considered as a viable tool in larger scale and more realistic reservoir simulations. The first issue is related to the computation time, and the second one to the separation of scales.

The resolution of each time step of the multiscale simulation of the reservoir's depletion took on average 120 minutes and 3 iterations, that is, on average 40 minutes per iteration. Clearly, it is very computationally expensive to solve several boundary-values problems numerically at each integration point of the domain, specially in such non-linear problems as the hydro-mechanical simulation of media where the constitutive properties are solution-dependent. There are computational resources and numerical strategies that can be used to optimize this solution and make multiscale simulations more competitive.

The first and most obvious one is the parallelization of the problem. In multiscale simulations, most of the computation time is spent assembling the system; as in finite-element based methods this assembly is made element by element, it is simple to divide the elements among the existing processors so they can assemble different parts of the domain simultaneously. Parallelization strategies for the finite element method squared have been proposed by Matsui et al. (2004) and Lopes et al. (2018), for example, to speed up the computations. The simulations presented here could not be run in parallel because the multi-domain module of DuMu^x does not support parallelization. So, this is a first point for optimization in the implemented code. Another simple strategy that could be tested is to use a modified Newton-Raphson to solve the large-scale problem, so the assembly of the system would have to be made only once at each time step.

These strategies would not whatsoever completely solve the problem of computation time in real reservoir simulations, because these models can have hundreds of thousands to

millions of cells. So, the multiscale approach should also ideally be used only in regions of the reservoir where they really can be useful, like the zones where the constitutive behavior is very dynamic. Hajiabadi and Khoei (2018) have employed this approach to simulate the consolidation of a fractured domain with a sugar cube microstructure. They used the finite element method squared in the zones of higher pressure gradient, and the classical dual-porosity model elsewhere. These results matched well with those obtained using the multiscale method over the entire domain.

Another possible solution is to associate machine learning to multiscale methods. This was achieved, for example, by Wang and Sun (2019). They developed a hydro-mechanical multiscale method where the macroscale is solved with the FEM, the mechanical response of the REV is solved with the DEM and the hydraulic behavior is obtained from a neural network trained with data from numerical experiments with the Lattice-Boltzmann method. So, if a large amount of data is collected by upscaling the constitutive behavior of the fractured REVS in the reservoir with different boundary conditions, machine learning methods could replace many of the REV computations that are performed to assemble the system.

The respect of the separation of scales is the second issue that needs to be addressed to make multiscale simulations more applicable to reservoir simulation. While the fractures tested in this case study have lengths that range from tenths of centimeters to only a few meters, subseismic fractures can reach even tenths of meters and still be too small to be explicitly represented in large-scale simulations. At the same time, the REVs for these larger fractures may not attend a reasonable level of separation of scales. For these cases, it would be interesting to find approaches that can overcome this limitation. A first solution would be to drop the assumption of stationarity at the REV and solve the microscale for transient flow. The comparisons made by Khoei and Hajiabadi (2018) between the multiscale and the direct solution of a consolidation problem on heterogeneous media showed that introducing dynamic effects at the REV can significantly improve the solution when the separation of scales is not strong enough. Of course, this approach requires an extra amount of computational efforts, so it should be considered along with optimization methods. Ways of surpassing the restrictive assumption of separation of scales have also been addressed in mechanical problems. They led to the development of the second order multi-level FEM, to the use of enriched kinematics at the level of the REV (e.g Feyel, 2003) and to the proposal of relocalization techniques (e.g Feyel and Chaboche, 2001). These latter refer to the interpolation of quantities from the REV at the macroscale when the size of the heterogeneities is significant.

Finally, here the random fractured domain was replaced by an equivalent periodic media for which the unit cell returns good estimations of the average constitutive behavior. The actual accuracy of the estimated average quantities should be tested, which is only possible by averaging several multiscale simulations where the REVs at each integration point are randomly generated. Thus, this is also a very costly task that will be possible if combined with efficient optimization methods.

7.5 Conclusions of the chapter

The methods developed in the previous chapters were applied to the modeling of a synthetic case study. The methodology presented in Chapter 5 was used to perform REV studies on fractured networks similar to the tectonic fractures in the Ekofisk reservoir. The mortar periodic conditions presented in Chapter 4 were used to upscale the hydro-mechanical properties and to solve the boundary value problem of the REV in the multiscale simulations.

The multiscale method called multi-level Box method, described in Chapter 7, was used to simulate the depletion of the reservoir. The results of the multiscale simulation for the predicted flux rates, cumulative production and pore pressure fields were compared with a scenario where the hydro-mechanical properties are static. The results showed that static fracture properties significantly overestimate the predicted flux rates and cumulative production, and disregard the evolution of the level of anisotropy in the reservoir.

While the developed multiscale method is a robust tool to consider the dynamic behavior of the reservoir, the computational costs associated to the application of this technique on more realistic reservoir simulations may be too high. Thus, optimization techniques should be developed for complex reservoir models to benefit from the better predictability of multiscale simulations.

Chapter 8

Conclusions and perspectives

8.1 Concluding remarks

Because of the strong hydro-mechanical coupling of their properties, fractures have a dynamic impact on the behavior of naturally fractured reservoirs during production. While sub-seismic fractures may be frequent enough for this influence to be significant, they are also usually too small to be all explicitly represented in numerical models. Traditional upscaling can not consider the geometrical complexity and the state-dependent behavior of these fracture networks. So, this thesis presented multiscale methods as an alternative to model the hydro-mechanical behavior of reservoirs containing complex networks of small fractures. Contributions were made to the different parts of this modeling process.

Much of the complexity of this modeling is at the level of the REV, where the fractures are generated stochastically and explicitly represented. A first problem that arises because of this complex geometry is the imposition of periodic boundary conditions, which are usually preferred in numerical homogenization studies. Chapter 4 approached this issue by proposing adaptions to the mortar method, which is traditionally used in contact problems and was recently applied to the imposition of periodic boundary conditions on non-fractured domains. The mortar periodic boundary conditions were tested for the upscaling of random and periodic fractured media and were shown to have the theoretically expected properties when compared to Dirichlet and Neumann boundary conditions.

Another problematic related to the randomness and complexity of the fracture networks is the definition of the size of the REV. Chapter 5 presented a methodology that uses the Central Limit Theorem to make this process general and efficient. The geometrical and hydro-mechanical properties of any fracture network were shown to converge to a normal distribution if no important outliers are present. Because of that, it is possible to predict the standard deviation of a property for any REV size from the simulation of one REV size only. After this prediction, the results can be used to define the REV based on a maximum tolerated error for the average value. Thus, the ultimate purpose of this methodology is to have a good estimation of the average constitutive behavior, or at least to quantitatively

estimate how far off one can be from this true mean by selecting a certain REV size.

After dealing with the REV problem, a contribution was made to the field of multiscale simulations. Chapter 6 presents an adaption of the multi-level FEM that was called the multi-level Box method. In this novel approach, the Box method is used to solve both the macroscale and the microscale. Differently from the multi-level FEM, the multi-level Box method is locally conservative. As a consequence, it may be advantageous for reservoir simulations if the method is to be adapted to multi-phase flow problems, for example.

All of these developments resulted in the extension of an existing open-source code, which can now be used to perform hydro-mechanical multiscale (and, obviously, one-scale) simulations of elastoplastic fractured media.

The application of the developed techniques to a case study showed that considering the dynamic behavior of small fractures may be important to correctly predict the performance of the reservoir. The methods developed here can be readily applied in case studies like this to assess, in a simplified manner, how production can be optimized considering the interplay between stress state, the geometry and the coupled constitutive properties of small fractures. Nonetheless, the introduction of multiscale approaches in complex reservoir simulations still requires more work. Once these techniques are optimized, the quality of recovery plans and the predictability of numerical models can benefit from their robustness.

8.2 Perspectives and improvements for future works

The code that was implemented in this thesis can be improved with the following additions:

- Parallelization of the multiscale simulations. This requires low-level changes in DuMu^x, whose multi-domain module currently does not support computations in parallel.
- Implementation of more sophisticated constitutive models for the intact rock and for the fractures.
- Adaptation of the multi-level Box method to multi-phase flow.

Also, to reach a better understanding and applicability of the computational methods applied here, we envision to work on the following topics:

- Gather a large amount of data from numerical experiments on fractured media to test the applicability of the Central Limit Theorem to their constitutive properties.
- Explore in details the accuracy of the multi-level Box method by comparing it to the direct solution of fractured domains. The influence of the size of the REV with respect to the size of the domain should be evaluated, as well as the limits of the assumption of stationarity at the REV need to be better understood.

- Perform multiscale simulations where the REVs at the integration points are randomly generated. Then, compare the average resulting fields with those of a multiscale simulation performed with one REV only that well represents the average constitutive behavior.
- Develop reliable methods to optimize the multiscale methods. The more efficient way of doing this seems to mix multiscale and one-scale approaches in the same domain, by using the former only when necessary. For that, proper criteria to turn multiscale on and off need to be studied and validated.

Bibliography

Aarnes JE (2004) On the use of a mixed multiscale finite element method for greater flexibility and increased speed or improved accuracy in reservoir simulation. Multiscale Modeling and Simulation 2(3):421–439 (Cited on pages: 2, 4, and 110)

Auriault JL, Boutin C, Geindreau C (2009) Homogenization of Coupled Phenomena in Heterogeneous Media. John Wiley & Sons, Ltd (Cited on pages: 12, 58)

Azizmohammadi S, Matthäi SK (2017) Is the permeability of naturally fractured rocks scale dependent? Water Resources Research 53(9):8041–8063 (Cited on page: 107)

Baghbanan A, Jing L (2007) Hydraulic properties of fractured rock masses with correlated fracture length and aperture. International Journal of Rock Mechanics and Mining Sciences 44(5):704–719 (Cited on pages: xviii, 24, 102, 103, and 104)

Bagheri M, Settari A (2008) Modeling of Geomechanics in Naturally Fractured Reservoirs. SPE Reservoir Evaluation Engineering 11(01):108–118 (Cited on page: 6)

Bandis S, Lumsdent A, Barton N (1983) Fundamentals of rock joint deformation 20:249–268 (Cited on page: 126)

Barker JW, Dupouy P (1999) An analysis of dynamic pseudo-relative permeability methods for oil-water flows. Petroleum Geoscience 5(4):385–394 (Cited on page: 23)

Barton N, Bandis S, Bakhtar K (1985) Strength, deformation and conductivity coupling of rock joints. International Journal of Rock Mechanics and Mining Sciences Geomechanics Abstracts 22(3):121–140 (Cited on pages: 5, 126)

Beck M, Rinaldi A, Flemisch B, Class H (2020) Accuracy of fully coupled and sequential approaches for modeling hydro- and geomechanical processes. Computational Geosciences 24:1707–1723 (Cited on pages: 35, 36)

Berkowitz B (2002) Characterizing flow and transport in fractured geological media: A review. Advances in Water Resources 25(8-12):861–884 (Cited on page: 2)

Bertrand F, Buzzi O, Bésuelle P, Collin F (2020) Hydro-mechanical modelling of multiphase flow in naturally fractured coalbed using a multiscale approach. Journal of Natural Gas Science and Engineering 78:103303 (Cited on pages: 7, 111, and 134)

Bisdom K, Bertotti G, Nick HM (2016) The impact of in-situ stress and outcrop-based fracture geometry on hydraulic aperture and upscaled permeability in fractured reservoirs. Tectonophysics 690:63–75 (Cited on pages: 23, 24)

Blunt M, Rubin B (1992) Implicit flux limiting schemes for petroleum reservoir simulation. Journal of Computational Physics 102(1):194–210 (Cited on page: 29)

Bourbiaux B (2010) Fractured reservoir simulation: a challenging and rewarding issue. Oil and Gas Science and Technology 65(2):227–238 (Cited on pages: 1, 2, and 123)

Brooks R, AT C (1966) Properties of porous media affecting fluid flow. Journal of the Irrigation and Drainage Division 92(2):61–87 (Cited on page: 3)

Caspari E, Milani M, Rubino J, Müller T, Quintal B, Holliger K (2016) Numerical upscaling of frequency-dependent p- and s-wave moduli in fractured porous media. Geophysical Prospecting 64:1166–1179 (Cited on page: 82)

Castelletto N, White J, Tchelepi H (2015) Accuracy and convergence properties of the fixed-stress iterative solution of two-way coupled poromechanics. International Journal for Numerical and Analytical Methods in Geomechanics 39(14):1593–1618 (Cited on page: 50)

Chalhoub M, Pouya A (2008) Numerical homogenization of a fractured rock mass: A geometrical approach to determine the mechanical Representative Elementary Volume. Electronic Journal of Geotechnical Engineering 13:1–12 (Cited on page: 22)

Chalon F, Mainguy M, Longuemare P, Lemonnier P (2004) Upscaling of elastic properties for large scale geomechanical simulations. International Journal for Numerical and Analytical Methods in Geomechanics 28(11):1105–1119 (Cited on page: 19)

Chen HY, Teufel LW (1997) Coupling fluid-flow and geomechanics in dual-porosity modeling of naturally fractured reservoirs. SPE Annual Technical Conference and Exhibition, San Antonio, Texas (Cited on page: 6)

Chen T, Clauser C, Marquart G, Willbrand K, Mottaghy D (2015) A new upscaling method for fractured porous media. Advances in Water Resources 80:60–68 (Cited on page: 19)

Chen Y, Durlofsky LJ, Gerritsen M, Wen XH (2003) A coupled local-global upscaling approach for simulating flow in highly heterogeneous formations. Advances in Water Resources 26(10):1041–1060 (Cited on pages: 3, 4, and 23)

Christie M (1996) Upscaling for Reservoir Simulation. Journal of Petroleum Technology 48(11):1004–1010 (Cited on pages: 2, 123)

Christie MA (2001) Flow in porous media - Scale up of multiphase flow. Current Opinion in Colloid and Interface Science 6(3):236–241 (Cited on page: 23)

Clauser C (1992) Permeability of crystalline rocks. Eos, Transactions American Geophysical Union 73(21):233–238 (Cited on page: 24)

Crisfield MA (1987) Plasticity computations using the mohr—coulomb yield criterion. Engineering Computations 4(4):300–308 (Cited on page: 45)

Daley TM, Schoenberg MA, Rutqvist J, Nihei KT (2006) Fractured reservoirs: An analysis of coupled elastodynamic and permeability changes from pore-pressure variation. Geophysics 71:33–41 (Cited on page: 7)

De Dreuzy JR, Méheust Y, Pichot G (2012) Influence of fracture scale heterogeneity on the flow properties of three-dimensional discrete fracture networks (DFN). Journal of Geophysical Research B: Solid Earth 117(11):1–21 (Cited on pages: 23, 101)

de Sousa Junior LC, dos Santos LO, de Souza Rios V, Araújo C, Celes W, Sepehrnoori K (2016) Methodology for geomechanically controlled transmissibility through active natural fractures in reservoir simulation. Journal of Petroleum Science and Engineering 147:7–14 (Cited on page: 6)

Dean R, Xiuli G, Stone C, Minkoff S (2013) A comparison of techniques for coupling porous flow and geomechanics. SPE Journal 11:132–140 (Cited on page: 35)

Dias-Da-Costa D, Alfaiate J, Sluys LJ, Júlio E (2010) A comparative study on the modelling of discontinuous fracture by means of enriched nodal and element techniques and interface elements. International Journal of Fracture 161(1):97–119 (Cited on page: 25)

Dormieux L, Kondo D, U FJ (2006) Microporomechanics. John Wiley & Sons (Cited on page: 15)

Duncan JM, Goodman RE (1968) Finite element analyses of slopes in jointed rock: A report of an investigation. Tech. Rep. S-68-3, U.S. Army Corps of Engineers (Cited on pages: 20, 47)

Durlofsky LJ (1991) Numerical calculation of equivalent grid block permeability tensors for heterogeneous porous media. Water Resources Research 27(5):699–708 (Cited on page: 23)

Durlofsky LJ (2005) Upscaling and gridding of fine scale geological models for flow simulation. 8th International Forum on Reservoir Simulation pp 1–59 (Cited on page: 23)

Esmaieli K, Hadjigeorgiou J, Grenon M (2010) Estimating geometrical and mechanical REV based on synthetic rock mass models at Brunswick Mine. International Journal of Rock Mechanics and Mining Sciences 47:915–926 (Cited on pages: xiv, xvii, 22, 82, 92, 94, 95, and 96)

Farahmand K, Vazaios I, Diederichs MS, Vlachopoulos N (2018) Investigating the scale-dependency of the geometrical and mechanical properties of a moderately jointed rock using a synthetic rock mass (SRM) approach. Computers and Geotechnics 95:162–179 (Cited on pages: xv, xvii, 22, 94, 95, 96, and 97)

Feyel F (2003) A multilevel finite element method (fe2) to describe the response of highly non-linear structures using generalized continua. Computer Methods in Applied Mechanics and Engineering 192:3233–3244 (Cited on page: 138)

Feyel F, Chaboche JL (2000) FE 2 multiscale approach for modelling the elastoviscoplastic behaviour of long fibre SiC/Ti composite materials. Computer Methods in Applied Mechanics and Engineering 183(3-4):309–330 (Cited on pages: 58, 111, and 116)

Feyel F, Chaboche JL (2001) Multi-scale nonlinear fe 2 analysis of composite structures: Damage and fiber size effects. Revue Européenne des Éléments Finis 10:449–472 (Cited on pages: 116, 138)

Firoozabadi A (2000) Recovery mechanisms in fractured reservoirs and field performance. Journal of Canadian Petroleum Technology 39(11):13–17 (Cited on pages: 1, 2)

Flemisch B, Berre I, Boon W, Fumagalli A, Schwenck N, Scotti A, Stefansson I, Tatomir A (2018) Benchmarks for single-phase flow in fractured porous media. Advances in Water Resources (111):239–258 (Cited on page: 29)

Frey J, Chambon R, Dascalu C (2013) A two-scale poromechanical model for cohesive rocks. Acta Geotechnica 8:107–124 (Cited on pages: 111, 113, and 115)

Gan Q, Elsworth D (2016) Production optimization in fractured geothermal reservoirs by coupled discrete fracture network modeling. Geothermics 62:131–142 (Cited on page: 7)

Geiger S, Roberts S, Matthäi SK, Zoppou C, Burri A (2004) Combining finite element and finite volume methods for efficient multiphase flow simulations in highly heterogeneous and structurally complex geologic media. Geofluids 4(4):284–299 (Cited on page: 26)

Goodman R, Taylor R, Brekke T (1968) A model for the mechanics of jointed rock. Journal of the Soil Mechanics and Foundations Division 94 (Cited on page: 25)

Gutierrez M, Tunbridge L, Hansteen H, Makurat A, Barton N, Landa GH (1994) Modelling of the compaction behaviour of fractured chalk All Days, sPE-28130-MS (Cited on pages: 124, 126, and 127)

Hajiabadi MR, Khoei A (2018) A bridge between dual porosity and multiscale models of heterogeneous deformable porous media. International Journal for Numerical and Analytical Methods in Geomechanics 43(1):212–238 (Cited on page: 138)

Harthong B, Scholtès L, Donzé FV (2012) Strength characterization of rock masses using a coupled DEM-DFN model. Geophysical Journal International 191(2):467–480 (Cited on page: 22)

Helmig R (1997) Multiphase flow and transport processes in the subsurface: a contribution to the modeling of hydrosystems. Springer-Verlag, Berlin, Germany (Cited on page: 26)

Hoek E, Brown ET (1997) Practical estimates of rock mass strength. International Journal of Rock Mechanics and Mining Sciences 34(8):1165–1186 (Cited on page: 20)

Hou TY, Wu XH (1997) A multiscale finite element method for elliptic problems in composite materials and porous media. Journal of Computational Physics 134(1):169–189 (Cited on page: 110)

Hudson J, Harrison J (2000) Engineering rock mechanics: an introduction to the principles. Elsevier, Amsterdam (Cited on page: 11)

Indelman P, Dagan G (1993) Benchmarks for single-phase flow in fractured porous media. Water Resources Research 29(4):917–923 (Cited on page: 13)

JianPing Y, WeiZhong C, DianSen Y, JingQiang Y (2015) Numerical determination of strength and deformability of fractured rock mass by FEM modeling. Computers and Geotechnics 64:20–31 (Cited on page: 22)

Jones TA (1969) Skewness and kurtosis as criteria of normality in observed frequency distributions. Journal of Sedimentary Research 39(4):1622–1627 (Cited on page: 87)

Kanit T, Forest S, Galliet I, Mounoury V, Jeulin D (2003) Determination of the size of the representative volume element for random composites: statistical and numerical approach. International Journal of Solids and Structures 40:3647–3679 (Cited on pages: 10, 59, and 82)

Khoei A, Hajiabadi MR (2018) Fully coupled hydro-mechanical multi-scale model with micro-dynamic effects. International Journal for Numerical Methods in Engineering 115(3):1–35 (Cited on pages: 13, 111, 116, and 138)

Khoei A, Saeedmonir S (2021) Computational homogenization of fully coupled multiphase flow in deformable porous media. Computer Methods in Applied Mechanics and Engineering 376:113660 (Cited on page: 111)

Kim J, Tchelepi H, Juanes R (2011) Stability and convergence of sequential methods for coupled flow and geomechanics: Fixed-stress and fixed-strain splits. Computer Methods in Applied Mechanics and Engineering 200(13):1591–1606 (Cited on pages: 34, 35, 37, and 38)

Koch T, Gläser D, Weishaupt K, Ackermann S, Beck M, Becker B, Burbulla S, Class H, Coltman E, Emmert S, Fetzer T, Grüninger C, Heck K, Hommel J, Kurz T, Lipp M, Mohammadi F, Scherrer S, Schneider M, Seitz G, Stadler L, Utz M, Weinhardt F, Flemisch B (2020) DuMux 3 – an open-source simulator for solving flow and transport problems in porous media with a focus on model coupling. Computers and Mathematics with Applications 81:423–443 (Cited on pages: 8, 41)

Kouznetsova V, Brekelmans W, Baaijens F (2001a) Approach to micro-macro modeling of heterogeneous materials. Computational Mechanics 27:37–48 (Cited on page: 111)

Kouznetsova V, Brekelmans W, Baaijens F (2001b) Approach to micro-macro modeling of heterogeneous materials. Computational Mechanics 27:37–48 (Cited on page: 116)

Kouznetsova V, Geers M, Brekelmans W (2004) Multi-scale second-order computational homogenization of multi-phase materials: a nested finite element solution strategy. Computer Methods in Applied Mechanics and Engineering 193(48):5525–5550 (Cited on page: 111)

Kulatilake PHS, Panda BB (2000) Effect of block size and joint geometry on jointed rock hydraulics and rev. Journal of Engineering Mechanics 126(8):850–858 (Cited on pages: 23, 24, and 100)

Kulatilake PHSW, Wang S, Stephansson O (1993) Effect of finite size joints on the deformability of jointed rock in three dimensions. Int J Rock Mech Min Sci & Geomech 30:479–501 (Cited on pages: 21, 22, and 91)

Kulatilake PHSW, Malama B, Wang J (2001) Physical and particle flow modeling of jointed rock block behavior under uniaxial loading. International Journal of Rock Mechanics & Mining Sciences 38:641–657 (Cited on page: 22)

Larsson F, Runesson K, Su F (2009) Variationally consistent computational homogenization of transient heat flow 81:1659 – 1686 (Cited on page: 111)

Larsson F, Runesson K, Saroukhani S, Vafadari R (2011a) Computational homogenization based on a weak format of micro-periodicity for rve-problems. Computer Methods in Applied Mechanics and Engineering 200(1):11–26 (Cited on page: 64)

Larsson F, Runesson K, Su F (2011b) Computational homogenization of uncoupled consolidation in micro-heterogeneous porous media. International Journal for Numerical and Analytical Methods in Geomechanics 34:1431 – 1458 (Cited on page: 111)

Lei Q, Latham JP, Xiang J, Tsang CF, Lang P, Guo L (2014) Effects of geomechanical changes on the validity of a discrete fracture network representation of a realistic two-dimensional fractured rock. International Journal of Rock Mechanics and Mining Sciences 70:507–523 (Cited on page: 23)

Lei Q, Latham JP, Tsang CF (2017) The use of discrete fracture networks for modelling coupled geomechanical and hydrological behaviour of fractured rocks. Computers and Geotechnics 85:151–176 (Cited on pages: 24, 25)

Li J, Lei Z, Qin G, Gong B (2015) Effective local-global upscaling of fractured reservoirs under discrete fractured discretization. Energies 8(9):10178–10197 (Cited on page: 4)

Liu C, Reina C (2016) Discrete Averaging Relations for Micro to Macro Transition. Journal of Applied Mechanics 83(8) (Cited on page: 19)

Liu Y, Wang Q, Chen J, Song S J Zhan, Han X (2018) Determination of geometrical revs based on volumetric fracture intensity and statistical tests. Appl Sci 8(800):1–18 (Cited on page: 20)

Lohr T, Krawczyk CM, Tanner DC, Samiee R, Endres H, Thierer PO, Oncken O, Trappe H, Bachmann R, Kukla PA (2008) Prediction of subseismic faults and fractures: Integration of three-dimensional seismic data, three-dimensional retrodeformation, and well data on an example of deformation around an inverted fault. American Association of Petroleum Geologists Bulletin 92(4):473–485 (Cited on page: 1)

Long JC, Remer JS, Wilson CR, Witherspoon PA (1982) Porous media equivalents for networks of discontinuous fractures. Water Resources Research 18(3):645–658 (Cited on pages: 15, 19)

Lopes I, Pires F, FJP R (2018) A mixed parallel strategy for the solution of coupled multi-scale problems at finite strains. Computational Mechanics 61:157–180 (Cited on page: 137)

Loyola A, Pereira J, Cordão Neto M (2021) General statistics-based methodology for the determination of the geometrical and mechanical representative elementary volumes of fractured media. Rock Mechanics and Rock Engineering 54(4):1821–1841 (Cited on pages: xii, 22, 44, 79, 80, 82, 84, 85, 91, 97, and 98)

Mandel J (1953) Consolidation des sols (Étude mathématique). Géotechnique 3(7):287–299 (Cited on pages: 36, 50)

Marinelli F, van den Eijnden B, Sieffert Y, Chambon R, Collin F (2016) Modeling of granular solids with computational homogenization: Comparison with biot's theory. Finite Elements in Analysis and Design 119:45–62 (Cited on pages: 111, 115, and 116)

Massart T, Selvadurai P (2012) Stress-induced permeability evolution in a quasi-brittle geomaterial. Journal of Geophysical Research (Solid Earth) 117:B07207 (Cited on page: 24)

Matsui K, Terada K, Yuge K (2004) Two-scale finite element analysis of heterogeneous solids with periodic microstructures. Computers Structures 82(7):593–606 (Cited on page: 137)

Matthäi SK, Mezentsev A, Belayneh M (2007) Finite element-node-centered finite-volume two-phase-flow experiments with fractured rock represented by unstructured hybrid-element meshes. SPE Reservoir Evaluation and Engineering 10(6):740–756 (Cited on pages: 1, 3, and 23)

Miehe C (2003) Computational micro-to-macro transitions for discretized micro-structures of heterogeneous materials at finite strains based on the minimization of averaged incremental energy. Computer Methods in Applied Mechanics and Engineering 192(5):559–591 (Cited on page: 58)

Miehe C, Schröder J, Schotte J (1999) Computational homogenization analysis in finite plasticity simulation of texture development in polycrystalline materials. Computer Methods in Applied Mechanics and Engineering 171(3):387–418 (Cited on page: 110)

Min K, Jing L (2003) Numerical determination of the equivalent elastic compliance tensor for fractured rock masses using the distinct element method. International Journal of Rock Mechanics and Mining Sciences 40:795–816 (Cited on pages: xvii, 21, 22, 82, 84, 85, and 86)

Min KB, Jing L, Stephansson O (2004a) Determining the equivalent permeability tensor for fractured rock masses using a stochastic REV approach: Method and application to the field data from Sellafield, UK. Hydrogeology Journal 12(5):497–510 (Cited on pages: 23, 24, 85, and 98)

Min KB, Rutqvist J, Tsang CF, Jing L (2004b) Stress-dependent permeability of fractured rock masses: A numerical study. International Journal of Rock Mechanics and Mining Sciences 41(7):1191–1210 (Cited on page: 24)

Nelson R (2001) Geologic Analysis of Naturally Fractured Reservoirs, 2nd edn. Gulf Professional Publishing, DOI 10.1016/b978-0-88415-317-7.x5000-3 (Cited on page: 1)

Neuman SP (1994) Generalized scaling of permeabilities: Validation and effect of support scale. Geophysical Research Letters 21(5):349–352 (Cited on page: 24)

Nguyen VD, Béchet E, Geuzaine C, Noels L (2012) Imposing periodic boundary condition on arbitrary meshes by polynomial interpolation. Computational Materials Science 55:390–406 (Cited on pages: 60, 62)

Nguyen VP (2014) An open source program to generate zero-thickness cohesive interface elements. Advances in Engineering Software 74:27–39 (Cited on pages: 64, 85)

Ni P, Wang S, Wang C, Zhang S (2017) Estimationf of the REV size for fractured rock mass based on damage coefficient. Rock Mechanics and Rock Engineering 50:555–570 (Cited on pages: 22, 92)

Oda M (1982) Fabric tensor for discontinuous geological materials. Soils and Foundations 22:96–108 (Cited on page: 20)

Oda M (1985) Permeability tensor for discontinuous rock masses. Géotechnique (4):483–495 (Cited on pages: 3, 20, 21, 23, and 83)

Oda M (1988) A new method for evaluating the representative elementary volume based on joint survey of rock masses. Canadian Geotechnical Journal 25:440–447 (Cited on page: 20)

Oda M, Suzuki K, Maeshibu T (1984) Elastic compliance for rock-like materials with random cracks. Soils and Foundations 24:27–40 (Cited on page: 83)

Panda BB, Kulatilake PHS (1999) Relations between fracture tensor parameters and jointed rock hydraulics. Journal of Engineering Mechanics 125(1):51–59 (Cited on page: 23)

Pouya A (2015) A finite element method for modeling coupled flow and deformation in porous fractured media. International Journal for Numerical and Analytical Methods in Geomechanics (39):1836–1852 (Cited on page: 25)

Pouya A, Fouché O (2009) Permeability of 3D discontinuity networks: New tensors from boundary-conditioned homogenisation. Advances in Water Resources 32(3):303–314 (Cited on page: 19)

Pouya A, Ghoreychi M (2001) Determination of rock mass strength properties by homogenization. International Journal for Numerical and Analytical Methods in Geomechanics 25(13):1285–1303 (Cited on page: 21)

Preisig M, Prevost J (2011) Coupled multi-phase thermo-poromechanical effects. case study: Co 2 injection at in salah, algeria. International Journal of Greenhouse Gas Control 5:1055–1064, DOI 10.1016/j.ijggc.2010.12.006 (Cited on pages: 35, 36, and 50)

Rahman M, Rahman S (2013) Studies of hydraulic fracture-propagation behavior in presence of natural fractures: Fully coupled fractured-reservoir modeling in poroelastic environments. International Journal of Geomechanics 13(6):809–826 (Cited on page: 5)

Rahman M, Hossain M, Rahman S (2002) A shear-dilation-based model for evaluation of hydraulically stimulated naturally fractured reservoirs. International Journal for Numerical and Analytical Methods in Geomechanics 26:469 – 497 (Cited on page: 6)

Rasmussen LL, de Farias MM, de Assis AP (2018) Extended Rigid Body Spring Network method for the simulation of brittle rocks. Computers and Geotechnics 99:31–41 (Cited on page: 22)

Reichenberger V, Jakobs H, Bastian P, Helmig R (2006) A mixed-dimensional finite volume method for two-phase flow in fractured porous media. Advances in Water Resources 29(7):1020–1036 (Cited on page: 29)

Reis F, Andrade Pires F (2014) A mortar based approach for the enforcement of periodic boundary conditions on arbitrarily generated meshes. Computer Methods in Applied Mechanics and Engineering 274:168–191 (Cited on pages: 62, 64, 65, and 67)

Rodrigues Lopes I, Ferreira B, Andrade Pires F (2021) On the efficient enforcement of uniform traction and mortar periodic boundary conditions in computational homogenisation. Computer Methods in Applied Mechanics and Engineering 384:113930 (Cited on pages: 64, 67)

Salimi H, Bruining J (2010) Improved prediction of oil recovery from waterflooded fractured reservoirs using homogenization. SPE Reservoir Evaluation and Engineering 13(1):44–55 (Cited on page: 3)

Segura J, Carol I (2004) On zero-thickness elements for diffusion problems. International Journal for Numerical and Analytical Methods in Geomechanics 28:947 – 962 (Cited on pages: 53, 69)

Segura J, Carol I (2008) Coupled HM analysis using zero-thickness interface elements with double nodes. part i: Theoretical model. International Journal for Numerical and Analytical Methods in Geomechanics (32):2083–2101 (Cited on pages: xii, xvii, 25, 33, 36, 52, 53, and 54)

Shahbazi A, Saeidi A, Chesnaux R (2020) A review of existing methods used to evaluate the hydraulic conductivity of a fractured rock mass. Engineering Geology 265:105438 (Cited on page: 22)

Shewchuk JR (1996) Triangle: Engineering a 2D Quality Mesh Generator and Delaunay Triangulator. In: Applied Computational Geometry: Towards Geometric Engineering,

Lecture Notes in Computer Science, vol 1148, Springer-Verlag, pp 203–222, from the First ACM Workshop on Applied Computational Geometry (Cited on pages: 85, 124)

Sloan S (1987) Substepping schemes for the numerical integration of elastoplastic stress-strain relations. International Journal for Numerical Methods in Engineering 24:893–911 (Cited on page: 49)

Smit R, Brekelmans W, Meijer H (1998) Prediction of the mechanical behavior of nonlinear heterogeneous systems by multi-level finite element modeling. Computer Methods in Applied Mechanics and Engineering 155(1):181–192 (Cited on page: 110)

Svenning E, Fagerström M, Larsson F (2016) Computational homogenization of microfractured continua using weakly periodic boundary conditions. Computer Methods in Applied Mechanics and Engineering 299:1–21 (Cited on pages: 58, 59, 64, and 73)

Szymkiewicz A (2013) Modelling Water Flow in Unsaturated Porous Media: Accounting for Nonlinear Permeability and Material Heterogeneity. Springer-Verlag Berlin Heidelberg (Cited on page: 26)

Tao Q, Ghassemi A, Ehlig-Economides CA (2011) A fully coupled method to model fracture permeability change in naturally fractured reservoirs. International Journal of Rock Mechanics and Mining Sciences 48(2):259–268 (Cited on page: 6)

Terada K, Hori M, Kyoya T, Kikuchi N (2000) Simulation of the multi-scale convergence in computational homogenization approaches. International Journal of Solids and Structures 37(16):2285–2311 (Cited on page: 58)

Teufel L, Farrell HE (1990) In situ stress and natural fracture distribution in the Ekofisk field, North Sea. AAPG Annual Conference pp 1–33 (Cited on pages: 123, 124, and 126)

Teufel L, Rhett D (1991) Geomechanical Evidence for Shear Failure of Chalk During Production of the Ekofisk Field. SPE Annual Technical Conference and Exhibition, Dallas, Texas SPE-22755-MS (Cited on page: 6)

Teufel L, Rhett D, Farrell H, Lorenz J (1993) Control of Fractured Reservoir Permeability by Spatial and Temporal Variations in Stress Magnitude and Orientation. SPE Annual Technical Conference and Exhibition (Cited on pages: 5, 6)

Toublanc A, Renaud S, Sylte J, Clausen K, Eiben T, Nadland G (2005) Ekofisk field: fracture permeability evaluation and implementation in the flow model. Petroleum Geoscience 11:321–330 (Cited on pages: 123, 124)

van den Eijnden A, Bésuelle P, Chambon R, Collin F (2016) A fe2 modelling approach to hydromechanical coupling in cracking-induced localization problems. International Journal of Solids and Structures 97-98:475–488 (Cited on page: 111)

van den Eijnden A, Bésuelle P, Collin F, Chambon R, Desrues J (2017) Modeling the strain localization around an underground gallery with a hydro-mechanical double scale model; effect of anisotropy. Computers and Geotechnics 85:384–400 (Cited on page: 111)

Van Genuchten M (1980) A closed-form equation for predicting the hydraulic conductivity of unsaturated soils 1. Soil Science Society of America Journal 44:892–898 (Cited on page: 3)

Wang K, Sun W (2019) An updated lagrangian lbm–dem–fem coupling model for dual-permeability fissured porous media with embedded discontinuities. Computer Methods in Applied Mechanics and Engineering 344:276–305 (Cited on pages: 110, 138)

Wang S, Huang R, Ni R P Gamage, Zhang M (2013) Fracture behavior of intact rock using acoustic emission: experimental observation and realistic modeling. Geotechnical Testing Journal 36(6):903–914 (Cited on page: 21)

Wang Z, Li W, Bi L, Qiao L, Liu R, Liu J (2018) Estimation of the REV Size and Equivalent Permeability Coefficient of Fractured Rock Masses with an Emphasis on Comparing the Radial and Unidirectional Flow Configurations. Rock Mechanics and Rock Engineering 51(5):1457–1471 (Cited on page: 24)

Warren J, Root P (1963) The Behavior of Naturally Fractured Reservoirs. Society of Petroleum Engineers Journal 3(03):245–255 (Cited on pages: xi, 3)

Witherspoon P, JSY W, Iwai K, Gale J (1980) Validity of cubic law for fluid flow in a deformable rock fracture 16(6):1016–1024 (Cited on page: 5)

Wohlmuth B (2000) A mortar finite element method using dual spaces for the lagrange multiplier. SIAM Journal on Numerical Analysis 38:1–23 (Cited on page: 67)

Wu Q, Kulatilake PHSW (2012) REV and its properties on fracture system and mechanical properties, and an orthotropic constitutive model for a jointed rock mass in a dam site in China. Computer and Geotechnics 43:124–142 (Cited on pages: 22, 94, and 111)

Xia L, Zheng Y, Yu Q (2016) Estimation of the REV size for blockiness of fractured rock masses. Computers and Geotechnics 76:83–92 (Cited on page: 20)

Yang J, Chen W, Y D, Yu H (2014) Numerical determination of elastic compliance tensor of fractured rock masses by finite element modeling. International Journal of Rock Mechanics and Mining Sciences 70:474–482 (Cited on pages: xvii, 21, 22, 75, 84, and 86)

Zareidarmyian A, Parisio F, Makhnenko R, Salari H, Vilarrasa V (2021) How equivalent are equivalent porous media? Geophysical Research Letters 48(9):e2020GL089163 (Cited on page: 4)

Zhang L, Einstein H (2000) Estimating the intensity of rock discontinuities. International Journal of Rock Mechanics and Mining Sciences 37:819–837 (Cited on page: 20)

Zhang W, Chen JP, Liu C, Huang R, Li M, Zhang Y (2011) Determination of geometrical and structural representative volume elements at the Baihetan dam site. Rock Mechanics and Rock Engineering 45:409–419 (Cited on page: 20)

Zienkiewicz OC, Taylor R (2000) The Finite Element, Volume 1 – The Basis, 5th edn. Butterworth-Heinemann, Oxford, United Kingdom (Cited on page: 29)

Özdemir I, Brekelmans W, Geers M (2008) Fe2 computational homogenization for the thermo-mechanical analysis of heterogeneous solids. Computer Methods in Applied Mechanics and Engineering 198(3):602–613 (Cited on pages: 58, 111)

Appendices

Appendix A

Upscaling of the elastic constitutive tensors

We show here the upscaling of the elastic constitutive tensors for 2D plane-strain conditions ($\varepsilon_z = 0$).

A.1 Constant tractions

The imposition of the linearly independent constant tractions in Figure 2.5 allow the direct calculation of the equivalent elastic compliance tensor. The stress-strain relationship for linear elastic anisotropic media can be expressed as:

$$\boldsymbol{\varepsilon} = \boldsymbol{S}\boldsymbol{\sigma} \tag{A.1}$$

We consider here the equivalent compliance tensor of a fractured rock mass where the intact rock has Young modulus E_r and Poisson ratio ν_r. In the two-dimensional space, the constitutive tensor S_{ijkl} can be expressed in terms of the equivalent elastic moduli as:

$$S_{ijkl} = \begin{bmatrix} S_{11} & S_{12} & S_{13} & S_{14} \\ S_{21} & S_{22} & S_{23} & S_{24} \\ S_{31} & S_{32} & S_{33} & S_{34} \\ S_{41} & S_{42} & S_{43} & S_{44} \end{bmatrix} = \begin{bmatrix} \frac{1}{E_x} & -\frac{\nu_{yx}}{E_y} & -\frac{\nu_{zx}}{E_z} & \frac{\eta_{x,xy}}{G_{xy}} \\ -\frac{\nu_{xy}}{E_x} & \frac{1}{E_y} & -\frac{\nu_{zy}}{E_z} & \frac{\eta_{y,xy}}{G_{xy}} \\ -\frac{\nu_{xz}}{E_x} & -\frac{\nu_{yz}}{E_y} & \frac{1}{E_z} & \frac{\eta_{z,xy}}{G_{xy}} \\ \frac{\eta_{xy,x}}{E_x} & \frac{\eta_{xy,y}}{E_y} & \frac{\eta_{xy,z}}{E_z} & \frac{1}{G_{xy}} \end{bmatrix} \tag{A.2}$$

where E_i are the elastic moduli, ν_{ij} are Poisson ratios, $\eta_{i,jk}$ are coefficients of mutual inflience of the first kind and $\eta_{ij,k}$ are coefficients of mutual influence of the second kind. Considering that the fractures have strikes in the direction z, they do not affect the deformations in this direction; thus, $E_z = E_r$, $\nu_{xz} = \nu_{yz} = \nu_r$, and the components S_{31}, S_{32} and S_{33} are then equal to those of the compliance tensor of the intact rock. Also, since the shear stress σ_{xy} does not affect deformations in z, S_{34} is equal to zero. Considering the symmetry conditions,

$S_{13} = S_{31}$, $S_{23} = S_{32}$ and $S_{34} = S_{43}$. Hence, there are 7 components of the tensor which are known a priori because of the assumption of bidimensionality.

For plane-strain conditions, the relationship in (A.1) reduces to:

$$\begin{Bmatrix} \varepsilon_x \\ \varepsilon_y \\ 0 \\ \gamma_{xy} \end{Bmatrix} = \begin{bmatrix} S_{11} & S_{12} & {S_{13}}^r & S_{14} \\ S_{21} & S_{22} & {S_{23}}^r & S_{24} \\ {S_{31}}^r & {S_{32}}^r & {S_{33}}^r & 0 \\ S_{41} & S_{42} & 0 & S_{44} \end{bmatrix} \begin{Bmatrix} \sigma_x \\ \sigma_y \\ \sigma_z \\ \tau_{xy} \end{Bmatrix} \tag{A.3}$$

Three linearly independent boundary conditions are necessary to obtain the unknowns of the elastic compliance tensor. That means that three boundary-value problems are solved to obtain $\boldsymbol{S}$. In this paper, we used the applied stresses illustrated in Figure 2.5, where at each step only one of the stress components $\boldsymbol{\sigma}_x$, $\boldsymbol{\sigma}_y$ and $\boldsymbol{\tau}_{xy}$ have non-zero values. So, at each step one row of $\boldsymbol{S}$ is entirely computed.

The displacement gradients are calculated from the integral boundaries in (2.32). They are used to calculate strain vector $\boldsymbol{\varepsilon}_i$.

The stress σ_z can be calculated from the applied stresses and the properties of the intact rock as:

$$\sigma_z = -\frac{{S_{31}}^r \sigma_x + {S_{32}}^r \sigma_y}{{S_{33}}^r} \tag{A.4}$$

And the tensor components are calculated using (A.4) and the system formed by lines 1, 2 and 4 in (A.3)

If the equivalent stiffness tensor $\boldsymbol{C}$ is desired, one can obtain it by inverting the equivalent compliance tensor:

$$\boldsymbol{C} = \boldsymbol{S}^{-1} \tag{A.5}$$

The equivalent elastic moduli are obtained by inverting the diagonal terms of $\boldsymbol{S}$.

A.2 Periodic and linear displacement

Both periodic and linear displacement boundary conditions (Figures 2.3 and 2.6) are used to impose a macroscopic strain vector $\boldsymbol{\varepsilon}$. They allow the direct computation of the stiffness tensor $\boldsymbol{C}$, where:

$$\begin{Bmatrix} \sigma_x \\ \sigma_y \\ \sigma_z \\ \tau_{xy} \end{Bmatrix} = \begin{bmatrix} C_{11} & C_{12} & C_{13} & C_{14} \\ C_{21} & C_{22} & C_{23} & C_{24} \\ C_{31} & C_{32} & {C_{33}}^r & C_{34} \\ C_{41} & C_{42} & C_{43} & C_{44} \end{bmatrix} \begin{Bmatrix} \varepsilon_x \\ \varepsilon_y \\ 0 \\ \gamma_{xy} \end{Bmatrix} \tag{A.6}$$

Each component of the strain vector is kept non-zero at a time to compute the columns 1, 2 and 4 of $\boldsymbol{C}$. The third column, which corresponds to the strain $\varepsilon_z = 0$, is computed by

assuming the component $\boldsymbol{C}_{33}$ to be equal to the one of the intact rock, that is:

$$\boldsymbol{C}_{33} = \frac{E_r(1-\nu_r)}{(1+\nu_r)(1-2\nu_r)} \tag{A.7}$$

and the off-diagonal terms are obtained from the assumption of symmetry, that is, $C_{j3} = C_{3j}$, where $j = 1, 2, 4$.

If the equivalent compliance tensor $\boldsymbol{C}$ is desired, one can obtain it by inverting the equivalent stiffness tensor:

$$\boldsymbol{S} = \boldsymbol{C}^{-1} \tag{A.8}$$